RAMAN SPECTROSCOPIC APPLICATIONS TOWARDS THE MANAGEMENT OF TRAUMATIC INJURIES TO THE CENTRAL NERVOUS SYSTEM

By

CLARISSA ANGELA STICKLAND

A thesis submitted to the University of Birmingham for the degree of DOCTOR OF PHILOSOPHY

Advanced Nano-Materials, Structures and Applications Group

School of Chemical Engineering

College of Engineering and Physical Sciences

University of Birmingham

December 2024

ABSTRACT

Traumatic central nervous system (CNS) injuries, or CNS trauma, are a leading cause of morbidity and mortality worldwide, with high-complication rates, prolonged post-traumatic neuro-disorders requiring long-term care, and are associated with important socio-economic costs such as prolonged medical care, rehabilitation costs, and loss of productivity and economic contribution. CNS trauma often affects individuals at their most economically active, yet no primary disease modifying interventions. Therapeutic strategies continue to be explored, including photobiomodulation (PBM). Given the limited regenerative capacity of CNS tissue, early insights into the biochemical changes that occur following trauma are essential for developing effective interventions. Traumatic brain injury (TBI) in particular, presents with notoriously inconsistent symptoms, complicating the development of reliable diagnostic tools. However, current hospital-based diagnostic modalities are often too slow or costly to support timely clinical decision-making in acute care settings, creating significant barriers to effective TBI management. This thesis aims to ascertain the use of Raman spectroscopy as a method of biochemical detection on CNS tissue to identify potential therapeutic pathways.

Here, we have developed an unprecedented Raman spectroscopy library of eighteen potential TBI biomarkers recorded on four laser wavelengths. Paired with the development of a probe as a portable technology capable of rapidly detecting TBI biochemical changes in the brain via Raman spectroscopy-based measurements of brain tissue, the biomarker library is a tool capable identifying therapeutic targets for TBI

primary injuries, as well as an experimental guide for researchers in the field of Raman diagnostics for CNS trauma. Using established and emergent cranial access in secondary care, we have successfully demonstrated the use of the probe to classify healthy from injured tissue to an accuracy of 94.5% (±0.03), temporally tracking the injury pathology and evolution. Using a 3D printed intracranial bolt, the developed probe-device demonstrates the differentiation between injured and healthy controls, classifying injury severities via the Self-Optimising Kohonen Index Network, and quantitatively attributing changes to the underlying biochemistry in a murine model of simulated TBI impact. An additional novel approach to transcranial Raman spectroscopy is featured in its early stages, yielding a preliminary 92.8% (±0.06) accuracy of classification between distinct brain biochemical environments. Real-time direct spectroscopy of rat brain tissue post-TBI enables improved interrogation of injury heterogeneity and subtypes, greater target management strategies, identification of novel targets for intervention, and allows for a clearer understanding of the fundamental biochemistry evolution and pathological dysregulation. Overall, this device demonstrates the feasibility for real-time optical brain spectroscopic interface. This technology can thus be directly translated for integration into current standards of CNS trauma care and is applicable in the research of primary disease modifying interventions.

Following the identification of therapeutic targets, Raman spectroscopy has been established as a monitoring tool to track PBM treatment efficacy for spinal cord injury. Through the examination of spinal cord tissue, dorsal root ganglia (DRG), and brain tissue, PBM was ascertained to accelerate dendrite growth and axonal regeneration in the DRG and showed evidence of recovering injured spinal cord tissue towards a healthy baseline.

~

To Attila Koppanyi, who passed away peacefully in my first year of study at the University on the 31st of October 2017.

~

To Angela Koppanyi, who passed away peacefully in my final year of study at the University on the 27th of July 2024.

~

I can't thank you both enough

ACKNOWLEDGEMENTS

First of all, I must express my most profound gratitude to the Advanced Nano-Materials, Structure and Applications group, led by Professor Pola Goldberg Oppenheimer. Coming from a purely biochemistry background, under Pola's supervision I was able expand my breadth of knowledge beyond biochemistry and was allowed to creatively think about research in a way I wouldn't have been able to experience otherwise. I've been presented with such great opportunities and have learnt so much. For this, I thank you.

I would like to acknowledge everyone I met in the office along the way, both in the ANMSA group and out, with several special mentions. Dr Alex Brean, who became a close friend, a great housemate, and has always been positive influence to be around. The Gym Mice, for the many cheese & board games nights and the early morning sessions that kept us going. An extra special mention to Mr Jarrod Thomas, for the friendship, endless coffees and chats, for taking the time to proof-read my chapters, and the encouragement at the most difficult times, thank you.

Finally, in the most cliché of endings, I would like to thank my family and friends outside of the office, who were so understanding and encouraging whilst I was in my "thesis world". My mother, Lyn, who showed me strength and always made sure I knew I had a place to call home. My father, David, who never had a doubt and made sure I knew it. My sister, Rachel, for the phone calls and motivation. Damola, for always being there. Kate, Sydney, Morayo, and Rose, I can finally visit more!

Thank you all so much.

CONTENTS LISTINGS

- Papers and Abstracts
- Table Of Contents
- List Of Figures Included
- List Of Tables Included
- List Of Abbreviations

PAPERS AND ABSTRACTS

This thesis is based off the following research papers:

- Harris, G., **C. A. Stickland**, M. Lim and P. Goldberg Oppenheimer (2023). "Raman Spectroscopy Spectral Fingerprints of Biomarkers of Traumatic Brain Injury." Cells 12(22): 2589.
- **C. A. Stickland**, Z. Sztranyovszky, J. J. S. Rickard, P. Goldberg Oppenheimer (2023). "Validation of Optimised Intracranial Spectroscopic Probe for Instantaneous In-Situ Monitoring and Classification of Traumatic Brain Injury". Experimental Neurology

Additionally, the following review was published:

- Stevens, A. R., **C. A. Stickland**, G. Harris, Z. Ahmed, P. Goldberg Oppenheimer, A. Belli and D. J. Davies (2022). "Raman Spectroscopy as a Neuromonitoring Tool in Traumatic Brain Injury: A Systematic Review and Clinical Perspectives." Cells 11(7): 1227.

And these abstracts were accepted as conference presentations:

- **C. A. Stickland**, P. Goldberg Oppenheimer (2023). "Development of a portable Raman device for monitoring and classification of traumatic brain injury in murine species". 2nd International Conference on Medical Devices: Materials, Mechanics and Manufacturing, Corfu, Greece (Presentation)
- **C. A. Stickland**, Z. Sztranyovszky, J. J. S. Rickard, P. Goldberg Oppenheimer (2023). "Validation of an Intracranial Raman Spectroscopic Probe for In-Situ

Monitoring of Traumatic Brain Injury". Healthcare Technologies Institute Winter Symposium, Birmingham, UK, (Poster)

- **C. A. Stickland**, Z. Sztranyovszky, J. J. S. Rickard, P. Goldberg Oppenheimer (2024). "Validation of an Intracranial Raman Spectroscopic Probe for In-Situ Monitoring of Traumatic Brain Injury". N-CODE EXPO, Birmingham, UK, (Poster)
- **C. A. Stickland**, Z. Sztranyovszky, J. J. S. Rickard, P. Goldberg Oppenheimer (2024). "Validation of an Intracranial Raman Spectroscopic Probe for In-Situ Monitoring of Traumatic Brain Injury". Sensors, Barcelona, Spain (Presentation)

Table of Contents

1. Chapter 1: Thesis Overview 1

1.1 Research Motivation 2

1.2 Thesis Scope 3

1.3 References 5

2. Chapter 2: Introduction 6

2.1 Introduction 7

2.2 Raman Spectroscopy 8

2.3 Raman Instrumentation 11

2.4 Pathophysiology of TBI 12

2.4.1 Excitotoxicity 13

2.4.2 Mitochondrial Dysfunction 14

2.4.3 Oxidative Stress 15

2.4.4 Neuroinflammation 15

2.4.5 Axonal Damage 16

2.4.6 Apoptosis 17

2.5 TBI Predictive Biomarkers 18

2.6 Current sTBI Assessment 19

2.6.1 Glasgow Coma Scale 20

2.6.2 Imaging 21

2.7 Surgical Interventions for sTBI 23

2.7.1 ICP Monitoring 23

2.7.2 Decompressive Craniectomies 24

2.8 Raman Diagnostics for Brain Tissue 25

2.9 References 28

3. Chapter 3: Raman Spectroscopy Spectral Fingerprints of Biomarkers of Traumatic Brain Injury 37

3.1 Abstract 38

3.2 Introduction 40
3.3 Materials and Methods 43
3.3.1 TBI Biomarkers 43
3.3.2 Reference Chemicals 44
3.3.3 Raman Spectroscopy 45
3.3.4 Data Analysis 45
3.4 Results and Discussion 46
3.4.1 Acute Phase 54
3.4.2 Sub-Acute Phase 59
3.4.3 Chronic Phase 65
3.4.4 Laser Specific Ratio Analysis 72
3.5 Current Challenges and Future Outlook 75
3.6 Conclusions 79
3.7 References 81
4. Chapter 4: Validation of Optimised Intracranial Spectroscopic Probe for Instantaneous In-Situ Monitoring and Classification of Traumatic Brain Injury ____ 95
4.1 Abstract 96
4.2 Introduction 97
4.3 Methods and Materials 102
4.3.1 Materials and Biomarkers 102
4.3.2 Spiked Brain Tissue Sample Preparation 102
4.3.3 SCI Rat Brains 103
4.3.4 Raman Spectra Acquisition and Analysis 103
4.3.5 Multivariate Data Analysis and AI Classification 104
4.3.6 Finite Element Analysis 105
4.4 Results and Discussion 105
4.4.1 Intra-RSP Bolt Design for ICP Catheter Insertion 105
4.4.2 Biomarker Spiked Brain Tissue 109

4.4.3 Transcranial Brain Spectra Acquisition 114
4.4.4 Classification of brain tissue extracted from spinal cord injured animals 116
4.5 Conclusions 121
4.6 References 124
5. Chapter 5: Efficacy of Raman Spectroscopy as a Neuromonitoring Tool for the Treatment of SCI Using Photobiomodulation ____ 129
5.1 Abstract 130
5.2 Introduction 131
5.3 Methods 134
5.3.1 Surgical Procedures 134
5.3.2 Photobiomodulation 135
5.3.3 Raman Spectroscopy 135
5.3.4 Data Processing 136
5.4 Results and Discussion 136
5.4.1 Raman Spectroscopy on SCI Tissue 136
5.4.2 SCI Biomarkers 149
5.5 Conclusion 152
5.6 References 154
6. Chapter 6: Conclusions and Future Outlook ____ 158
6.1 Summary 159
6.2 Future Outlook 161
7. Appendices ____ 163
A Raman Spectroscopy Spectral Fingerprints of Biomarkers of Traumatic Brain Injury ____ 164
B Validation of optimised intracranial spectroscopic probe for instantaneous in-situ monitoring and classification of traumatic brain injury ____ 193
C Raman Spectroscopy as a Neuromonitoring Tool in Traumatic Brain Injury: A Systematic Review and Clinical Perspectives ____ 208

List of Figures

Figure 2-1 – Jablonski diagram demonstrating energy shifts during absorption, emission, Rayleigh scattering and Raman scattering (Stokes and Anti-Stokes) _____10

Figure 2-2 – Raman vibrational modes _____11

Figure 2-3 – Depiction of portable Raman spectroscopy probe application _____26

Figure 3-1 – Schematic timeline overview of the TBI biomarkers and their phases _____44

Figure 3-2 – Characteristic Raman fingerprints of acute-phase TBI biomarkers _____56

Figure 3-3 – Characteristic Raman fingerprints of sub-acute-phase TBI biomarkers ___63

Figure 3-4 – Characteristic Raman fingerprints of chronic-phase TBI biomarkers_____67

Figure 3-5 – Characteristic peak ratios identified from spectral fingerprints per each studied TBI – indicative biomarker _____74

Figure 4-1– Portable Intracranial Raman Spectroscopy Probe overview_____99

Figure 4-2 – Schematic of cranial bolt_____108

Figure 4-3 – Spectral Analysis of Spiked Brain Tissue _____110

Figure 4-4 – Spectral Analysis of Transcranial Brains _____115

Figure 4-5 – Spectral Brain tissue Analysis of SCI Injured Rodents _____118

Figure 5-1 – SCI iunjured spinal cord tissue spectral analysis_____140

Figure 5-2 – SCI injured DRG tissue spectral analysis_____143

Figure 5-3 – SCI injured brain tissue spectral analysis _____145

Figure 5-4 – Differences in SCI spectral intensities _____148

Figure 5-5 – SCI biomarker spectra _____150

Figure 5-6 – Percentage differences in relative intensity ratios of injured and treated spinal cord intensities against healthy _____151

List of Tables

Table 2-1 – Glasgow Coma Scale guide for initial TBI diagnosis _____21

Table 3-1 – Overview of the studied TBI biomarker cohort with the corresponding physiological significance _____47

Table 3-2 – Acute TBI phase associated Raman bands and their assignments _____57

Table 3-3 – Peak assignments of significant peaks present in the sub-acute TBI biomarker phase _____64

Table 3-4 – Peak assignments of significant peaks present in the chronic TBI biomarkers phase _____70

Table 4-1 – TBI biomarkers and their physiological effect following trauma _____101

Table 4-2 – Outputs from finite element analysis including torque and the corresponding safety factors _____108

Table 4-3 – SOMDI scores for control, BS1 and BS2 brain tissue with the corresponding assignments of the identified characteristic peaks_____113

Table 4-4 – SOMDI scores for SCI injured rat brains and the corresponding spectral assignments _____119

Table 5-1 – Associated Raman bands and their assignments _____137

Table 5-2 – 10-fold cross validation scores for identification of number of PBM treated spinal cord spectra classified as healthy_____140

Table 5-3 – 10-fold cross validation scores for identification of number of DRG spectra from PBM treated samples classified as healthy _____143

Table 5-4 – 10-fold cross validation scores for identification of number of brain spectra from PBM treated samples classified as healthy _____145

List of Abbreviations

Central Nervous System	CNS	N-Acetyl-Aspartic Acid	NAA
Traumatic Brain Injury	TBI	Glutathione	GSH
Spinal Cord Injury	SCI	Interleukin-6	IL-6
Severe Traumatic Brain Injury	sTBI	Interleukin-18	IL-18
Blood Brain Barrier	BBB	Neurofilament Light Chain	NFL
N-Methyl-D-Aspartate	NMDA	Neuron Specific Enolase	NSE
A-Amino-3-Hydroxy-5-Methyl-4-Isoxazolepropionic Acid	AMPA	Emergency Department	ED
Electron Transport Chain	ETC	Mild Traumatic Brain Injury	mTBI
Adenosine Triphosphate	ATP	Vibration	vib
Mitochondrial Reactive Oxygen Species	mtROS	Stretching	v
Mitochondrial Permeability Transition Pore	mPTP	Bending	δ
Reactive Nitrogen Species	RNS	Twisting	τ
Intracranial Pressure	ICP	Rocking	ρ
Traumatic Axonal Injury	TAI	Wagging	ω
Apoptosis Inducing Factor	AIF	Symmetric	s
Cerebrospinal Fluid	CSF	Asymmetric	a
Glial Fibrillary Acidic Protein	GFAP	Aromatic	arom
Ubiquitin Carboxy-Terminal Hydrolase L1	UCHL-1	Skeletal	skel
Glasgow Coma Scale	GCS	Ring Breathing Vibration	Δ
Computerised Tomography	CT	Intracranial Raman Spectroscopy Probe	Intra-RSP

Magnetic Resonance Imaging	MRI
Diffusion Tensor Imaging	DTI
Decompressive Craniectomy	DC
Self-Optimizing Kohonen Index Network	SKiNET
Self-Organising Map Discriminant Index	SOMDI
Self-Organising Map	SOM
Biomarker Solution 1	BS1
Biomarker Solution 2	BS2
Transcranial Brain	TB
Spiked Transcranial Brain	sTB
Photobiomodulation	PBM
Dorsal Root Ganglia	DRG
Peripheral Nervous System	PNS
Thoracic Level 8	T8
Glycosaminoglycan	GAG
Chondroitin Sulphate Proteoglycan	CSPG

Chapter 1: Thesis Overview

1.1 Research Motivation

Traumatic central nervous system (CNS) injuries, or CNS trauma, is the designated name attributable to both traumatic brain injury (TBI) and spinal cord injury (SCI). The Global Burden of Diseases, Injuries and Risk Factors study estimated that in 2016 there was a 55.5 million global prevalence of TBI and 27 million for SCI [1]. Traumatic CNS injuries range from short-term mild injuries to long-term debilitating injuries, and sometimes death, therefore present as a massive socio-economic burden worldwide [2]. As the tissues affected are widely recognised as non-regenerative, both types of traumatic injuries have therefore gained traction in research over the years, however, there remain many unknowns about both diseases in terms of diagnosis, precise understanding of physiological changes, and treatment. Direct access to the spinal cord and brain is restricted to necessary preventative medical procedures, and most diagnostic tests rely on imaging and compositions of alternative biofluids.

Diagnostics tests directly on the injured tissue would elucidate the extent of the primary injuries, and aid in the development of direct treatments of the damage, thus reducing the possibility of future CNS trauma related complications and improving patient outcomes. Currently, TBI and SCI treatments mostly provide symptomatic relief [3, 4]. Left unattended, secondary injuries to the brain can progress to cognitive decline over time, higher risk for dementia, increased neurodegeneration, and emerging diseases such as chronic traumatic encephalopathy [5-7]. In the case for SCI, chronic respiratory, cardiovascular, or urinary and bowel complications are commonly reported, as well as pain syndromes and spasticity, to name but a few, all leading to increased morbidity,

decreased quality of life for patient and family, and a great burden for the healthcare industry [8, 9].

The aim of this research is to establish the use of Raman spectroscopy, an emerging analytical technique in the field of diagnostics [10-14], for i) the initiation of the development of a rapid, portable device to aid in the identification of key biochemical changes occurring in the brain following TBI, and ii) as a monitoring tool for a proposed SCI therapy and the tracking of treatment efficacy in various tissue types [15].

1.2 Thesis Scope

The main aim of this research was the development of a portable probe for TBI monitoring; as such, the thesis has a bias towards TBI related research. The following chapters include an introduction and three research articles, which have been published or submitted to review during the duration of this doctorate:

- **Chapter 2**: An introduction to brain-based changes in TBI, current methods for diagnostics and treatments, and the potential for Raman spectroscopy to fit into the existing procedures as a diagnostic tool.
- **Chapter 3**: The building of a Raman spectral library of predictive TBI biomarkers and their associated characterisations.
- **Chapter 4**: Validation of the Intracranial Raman Spectroscopic Probe for instantaneous monitoring and classification of TBI, and novel approaches and

applications of Raman spectroscopy for transcranial TBI detection in animal models.

- **Chapter 5**: Evaluating the efficacy of Raman spectroscopy as a neuromonitoring tool for the treatment of SCI derived effects via photobiomodulation in the spinal cord, dorsal root ganglia, and the brain in *in vivo* animal models.

The thesis is then summarised in **Chapter 6**, where future considerations and prospects for this research are outlined.

1.3 References

[1] S. L. James *et al.*, "Global, regional, and national burden of traumatic brain injury and spinal cord injury, 1990–2016: a systematic analysis for the Global Burden of Disease Study 2016," *The Lancet Neurology,* vol. 18, no. 1, pp. 56-87, 2019.

[2] F. H. Kobeissy *et al.*, "Autoantibodies in central nervous system trauma: new frontiers for diagnosis and prognosis biomarkers," in *Biomarkers for Traumatic Brain Injury*: Elsevier, 2020, pp. 431-451.

[3] M. Galgano, G. Toshkezi, X. Qiu, T. Russell, L. Chin, and L.-R. Zhao, "Traumatic brain injury: current treatment strategies and future endeavors," *Cell transplantation,* vol. 26, no. 7, pp. 1118-1130, 2017.

[4] D. W. Cadotte and M. G. Fehlings, "Spinal cord injury: a systematic review of current treatment options," *Clinical Orthopaedics and Related Research®,* vol. 469, no. 3, pp. 732-741, 2011.

[5] H. M. Bramlett and W. D. Dietrich, "Long-term consequences of traumatic brain injury: current status of potential mechanisms of injury and neurological outcomes," *Journal of neurotrauma,* vol. 32, no. 23, pp. 1834-1848, 2015.

[6] B. E. Masel, D. S. DeWitt, H. Levin, D. Shum, and R. Chan, "Traumatic brain injury disease: long-term consequences of traumatic brain injury," *Understanding traumatic brain injury: Current research and future directions,* vol. 28, 2014.

[7] H. S. Levin, D. Shum, and R. C. Chan, "Understanding traumatic brain injury: current research and future directions," 2014.

[8] N. Sezer, S. Akkuş, and F. G. Uğurlu, "Chronic complications of spinal cord injury," *World journal of orthopedics,* vol. 6, no. 1, p. 24, 2015.

[9] H. Frankel *et al.*, "Long-term survival in spinal cord injury: a fifty year investigation," *Spinal cord,* vol. 36, no. 4, 1998.

[10] E. Buchan, M. Hardy, P. d. C. Gomes, L. Kelleher, H. O. M. Chu, and P. G. Oppenheimer, "Emerging Raman spectroscopy and saliva-based diagnostics: from challenges to applications," *Applied Spectroscopy Reviews,* vol. 59, no. 3, pp. 277-314, 2024.

[11] J. M. Surmacki, L. Ansel-Bollepalli, F. Pischiutta, E. R. Zanier, A. Ercole, and S. E. Bohndiek, "Label-free monitoring of tissue biochemistry following traumatic brain injury using Raman spectroscopy," *Analyst,* 10.1039/C6AN02238C vol. 142, no. 1, pp. 132-139, 2017, doi: 10.1039/C6AN02238C.

[12] G. Harris *et al.*, "Emerging Eye-Based Diagnostic Technologies for Traumatic Brain Injury," *IEEE reviews in biomedical engineering,* vol. 16, pp. 530-559, 2022.

[13] C. Banbury *et al.*, "Spectroscopic detection of traumatic brain injury severity and biochemistry from the retina," *Biomedical optics express,* vol. 11, no. 11, pp. 6249-6261, 2020.

[14] J. Desroches *et al.*, "Characterization of a Raman spectroscopy probe system for intraoperative brain tissue classification," *Biomedical optics express,* vol. 6, no. 7, pp. 2380-2397, 2015.

[15] A. R. Stevens *et al.*, "Implantable and transcutaneous photobiomodulation promote neuroregeneration and recovery of lost function after spinal cord injury," *Bioengineering & Translational Medicine,* p. e10674, 2024.

Chapter 2: Introduction

2.1 Introduction

Traumatic brain injuries are a prevalent worldwide socio-economic burden. These injuries can result from various external physical forces, including impacts to the skull, skull penetration, or rapid acceleration or deceleration. The resulting conditions range from mild concussions to fatal or long-term debilitating disabilities [1]. The heterogeneity of the disease means that the progression and presentation of the injury will be different in each patient, and tools for diagnosis and treatment are challenging to standardize universally. The lack of treatments available to treat the primary injuries are the cause of the financial burden from the first response, immediate medical care and any future disabilities and secondary injuries; addressing the primary injury at any severity could reduce these costs in the future. The American Congress of Rehabilitation Medicine's diagnostic criteria for mild TBI (mTBI) classify it based on symptoms, clinical examination, and neuroimaging, aiming to standardize assessment and improve consistency in both clinical care and research [2]. Given that the mechanisms of injury are unique to each patient, symptoms of different intensities will present in diverse ways, resulting in the non-conformity of response protocols, leading to presumptuous dismissals of severe injuries [3]. Generally, TBIs are classified as mild, moderate, or severe. Given the nature of the research, only severe TBI (sTBI) will be discussed as the biochemical environment of brain tissue is only accessible in cases of severe injury.

2.2 Raman Spectroscopy

The interaction of light with matter can have three outcomes [4]. The first being the photon is absorbed, and the molecule excited, promoting it to a higher energy state. The second outcome is photon scattering, where they interact with the molecules and polarise the electron cloud. The polarisation, or distortion, of this cloud creates a short lived and unobservable quantum state, called a virtual energy state, allowing for a brief but recordable energy transfer. Lastly, the photon may not interact with matter altogether, and just traverse through. Raman spectroscopy relies on the inelastic scattering of light, a concept first evidenced in 1928 by its namesake when a spectrogram of monochromatic light shone on benzene showed two distinct spectral lines, the implication being a gain in energy by a photon following interaction with the molecule [5]. Raman spectroscopy is a sensitive, non-destructive, and label-free analytical chemistry technique, with a recent surge in popularity for its potential in disease diagnostics due to its ability to detect trace quantities of a molecule [6-13].

This inelastic scattering of light relies on photons from a monochromatic light source to undergo a specific energy shift following their interaction with the virtual electronic states of a sample, which are influenced by the molecule's vibrational mode [5, 14, 15]. These virtual states, depicted in Figure 2-1 are temporary, non-quantized energy levels that do not correspond to actual electronic transitions but instead represent short-lived distortions of the electron cloud during photon interaction [16]. The effect recorded is due

to a molecule's change in vibrational energy state, enabled by variations in its polarizability during the interaction [4]. Vibrational energy states refer to the discrete levels of energy a molecule possesses due to the atoms vibrating relative to one another; these vibrations occur at specific frequencies depending on the molecule's structure and bonding. Upon interaction with a photon, the vibrational modes can become excited or relaxed, resulting in a measurable energy difference [4]. The polarizability of a molecule is typically defined as the molecule's tendency to procure a dipole moment following induction of an electric field [17]. In the case for elastic scattering, or Rayleigh scattering, an excited photon is raised to a virtual state and is returned with no shift in energy. Inelastic scattering, or Raman scattering, infers a change in energy, either from the photon being raised from the ground vibrational energy state and returned at a higher energy (Stokes), or starting in a higher vibrational energy state and returning to a lower one (Anti-Stokes), as depicted in Figure 2-1.

At ambient conditions, an increased likelihood exists for the molecular vibrations to be in their ground state, rendering Stokes more probable and therefore more intense than Anti-Stokes [4, 18]. For this reason, most research, and this thesis included, proceed using Stokes scattering. Raman spectroscopy is not to be confused with other common vibrational methods, such as infrared spectroscopy, which defines functional groups by the wavenumber (cm^{-1}) at which it experiences a vibrational mode, absorption, to which the electron is raised from its ground state to a higher vibrational energy level, or fluorescence, also named emission or phosphorescence. In this instance, a photon is lost at a higher virtual state before the molecule's return to its ground state [19, 20]. These

latter two examples require for the molecule to be excited, enabling the change in vibrational energy levels to be recorded.

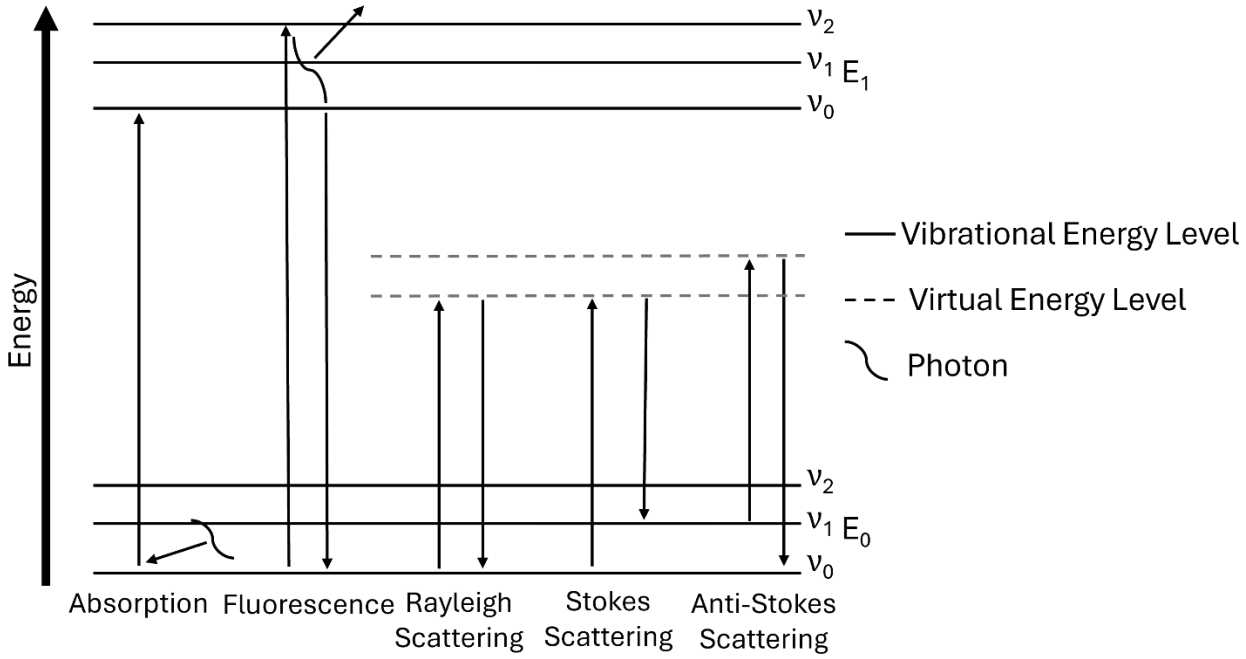

Figure 2-1 – Jablonski diagram demonstrating energy shifts during absorption, emission, Rayleigh scattering and Raman scattering (Stokes and Anti-Stokes).

Since Raman is coupled to the polarisation of electrons within a molecule, the deformation of the electron clouds dictates the vibration types observed. Bonds can experience stretching, rocking, wagging or twisting, in either a symmetric or asymmetric fashion, shown in Figure 2-2. A Raman spectrum records bands positioned according to the vibration frequency of each of these bonds, measured in terms of intensity (A.U.) against spatial frequency (cm^{-1}) [4]. Raman spectroscopy can therefore provide a unique biomolecular spectral fingerprint of target biomarkers as a rapid analytical response [21, 22]. These spectroscopic barcodes have been shown to identify various diseases from direct tissue sampling and collected biofluids [10, 23-28]. Raman spectroscopy has the

advantage of requiring no sample preparation or biopsy, and is non-destructive and biocompatible, making it an ideal choice for CNS tissue evaluation over other spectral techniques such as infrared or fluorescence spectroscopy.

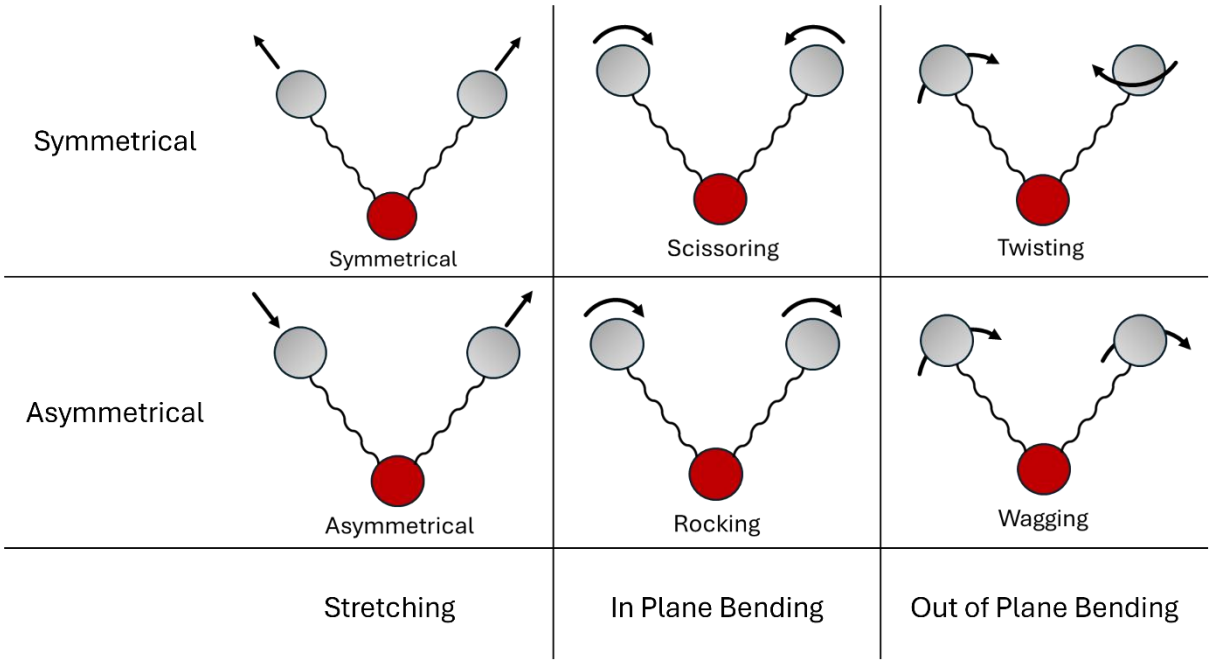

Figure 2-2 - Raman vibrational modes. Vibrational modes are dependent on the polarizability of a molecule, and therefore a function of the deformation of electron clouds. Bonds specifically experience stretching and bending in symmetric and asymmetric manners, both in plane and out of plane.

2.3 Raman Instrumentation

In Raman spectroscopy, lasers are almost always used as the excitation source. The choice of laser wavelength is dependent on the molecules or sample of interest, frequent options being in the regions of 514, 633, 785, 830 and 1064 nm due to their commercial availability, cost-effectiveness and versatility across ranges of sample types. Despite the

promising potential for Raman spectroscopy, the small number of inelastically scattered photons makes it an inherently weak effect. The simpler the molecule, the higher the quality of the spectrum. Organic samples tend to experience increased autofluorescence, and therefore worsen the signal to noise ratio, lowering the overall quality of the acquired spectra [29, 30]. The 785 nm laser is an industrial standard used for fresh biological samples. Lying in the near infrared region allows for a reduced autofluorescence and the risk of burning the samples (e.g. photothermal damage), due to longer wavelengths than other common Raman laser sources, at the expense of higher intensity signal the shorter wavelengths could provide [29].

The light is focussed on the sample in different ways depending on the instrument. Confocal Raman spectroscopy utilises the microscope objective to precisely direct the light, whereas most handheld devices will use a variety of filters and a lens to guide the light. Back-scattered light is collected at a calculated angle through the same lens, where dichroic beamsplitters usually redirect the light so as to keep it separate from the excitation light. The collected light is filtered for Rayleigh scattering, and a diffraction grating spatially disperses the remaining light towards a spectrometer, commonly a charge coupled device [4].

2.4 Pathophysiology of TBI

Following TBI, an immediate cascade of events occurs impacting a myriad of brain functions. Many of these processes are initially triggered as neuroprotective features,

however, depending on the degree of injury, degrade into disorderly responses, many of which impact further responses in a circular fashion.

2.4.1 Excitotoxicity

Damage to the blood-brain barrier (BBB) triggers a host of events, including the uncontrolled release of the brain's primary neurotransmitter, glutamate, into extracellular fluids [31]. The immediate effect of increased glutamate is the overexcitement of N-methyl-D-aspartate (NMDA) and α-amino-3-hydroxy-5-methyl-4-isoxazolepropionic acid (AMPA) receptors causing a dysregulation in intracellular Na^+, K^+ and Ca^{2+} concentrations. NMDA and AMPA receptors work together, in which AMPA receptors influence short-term alterations in synaptic strength and NMDA receptors control the genes necessary for the long-term maintenance of these changes [32]. Under normal circumstances, the receptor overexcitement would be corrected for by astrocytic glutamate transporters. In injury, however, the excessive levels of glutamate become neurotoxic, coining the term excitotoxicity [31]. Measuring glutamate levels has been found to be indicative of outcome, although there is a lack of accessible equipment to routinely determine levels [31, 33]. The result of excessive intracellular calcium can be dysfunction of calcium-dependent proteins, leading to apoptosis [34]. Studies investigating treatments into receptor antagonists have not been as successful as predicted, necessitating research into new insights into the excitotoxicity pathway [35, 36]. Untreated increased Ca^{2+} has further consequences regarding mitochondrial dysfunction and oxidative stress [37, 38].

2.4.2 Mitochondrial Dysfunction

Cytosolic Ca^{2+} levels are regulated by its uptake through uniports in the inner mitochondrial membrane against a concentration gradient, generating a membrane potential driving the electron transport chain (ETC) and adenosine triphosphate (ATP) production [39]. Although efficient, the ETC and energy production mechanisms suffer from energy loss from electron leakage, producing mitochondrial reactive oxygen species (mtROS) [40, 41]. Whilst excessive mtROS production is usually controlled via specific scavengers, important roles for regulated levels of mtROS in gene expression, cell signalling, and general physiological and pathological performance have been elucidated as well [42-47]. The uniporters regulating Ca^{2+} levels have a limit to their efficacy, and exceeding this limit causes the mitochondrial permeability transition pore (mPTP) to open [48]. An open mPTP depolarises the mitochondria, uncouples the ETC from ATP production, swells the matrix and ruptures the outer mitochondrial membrane, releasing apoptotic proteins signalling cellular death, and increases complex III based ROS production [49-55]. This consequence in neurons has been identified as a potential trigger for neurodegenerative diseases later in life [39]. The overall repercussions of mitochondrial dysfunction circles back to unregulated Ca^{2+} levels, linking mitochondrial damage to oxidative stress from increased ROS and excitotoxicity [37, 38].

2.4.3 Oxidative Stress

Increases in ROS and reactive nitrogen species (RNS) production are a consequence of increased metabolic rate from a higher oxygen demand in the brain post injury [56]. Brain parenchyma contains significant amounts of free-radical sensitive components, namely unsaturated and polyunsaturated fatty acids, and iron [57]. Mitochondrial function is disrupted by oxidative stress through free radical interactions with polyunsaturated fatty acids causing lipid peroxidation on mitochondrial membranes, leading to chronic inflammations and synaptic dysfunctions [56, 58]. The cellular Ca^{2+} increases promote production of NO and its subsequent reactions with free radical superoxides to form peroxynitrite, a cytotoxic derivative of NO whose inhibition has been shown to be beneficial following injury [59-61]. The abundance of ROS accumulating in the brain eventually has negative impacts on proteins, DNA, and cellular membranes [59-62]. The extended excitotoxicity means there is a constant release of ROS and lipid peroxidation, causing reduced cerebral blood flow and brain plasticity [63]. Promising studies for treatments have been attempted using scavenging molecules and antioxidants to correct for the ROS [56, 64-66].

2.4.4 Neuroinflammation

Studies conducted on both humans and rodents show presence of polymorphonuclear leukocytes and cytokines within 24 hours of trauma, upregulated in cascades following

primary and secondary injuries [67-70]. Prolonged cytokine upregulation induces multiple inflammatory responses, initially as a neuroprotective feature, but the maintenance of the inflammation can eventually do more harm than good [71]. Prolonged inflammation is also indicative of a disrupted BBB and vascular system, allowing red and white blood cells to penetrate the brain tissue and initiate communication between inflammatory cytokines, ultimately leading to neurological defects and increased intracranial pressure (ICP) [72].

2.4.5 Axonal Damage

Neurons experiencing diffuse axonal idiopathic injuries, or more modernly referred to as traumatic axonal injury (TAI), can severely damage or destroy the axonal cytoskeleton [73]. Originally, TAI was thought to be shearing and tearing as a result of direct mechanical force on the brain tissue, following by the formation of visible retraction bulbs [74]. It has since been evidenced that this is only the primary injury the axon endures, named primary axotomy. Following from the primary axotomy, mitochondrial respiration and glycolysis processes are dysregulated, lowering ATP levels [75]. Secondary axotomy is triggered through a cascade of molecular events, causing long term axonal inflammatory and eventually cellular and oligodendrocyte apoptotic responses [76]. Secondary axotomy and its implications of energetic failures is generally regarded as the main cause of axonal degeneration [77]. The degree of axon damage can be further assessed through degree of

degradation observed of the myelin sheath, accumulations of axonal transport proteins, as well as changes in axonal transport [76].

2.4.6 Apoptosis

Neuronal cell death can be seen for up to a year following injury [78]. Apoptosis can occur via two main pathways. Intrinsically, pro-apoptotic proteins can be released from the mitochondrial intermembrane in response to increased ROS production; Cytochrome C depolarised by the mitochondria activates caspase 3 through the modulation of caspases 8 and 9 [79, 80]. The caspases activity is dictated by the Bcl-2 proteins and are a good indicator of prognosis [80]. Specifically, higher caspase 8 levels in blood are associated with higher chances of mortality [81], and higher levels of activated caspase 9 can be indicative of neurological outcomes, however Darwish and Amiridze's study does not support that the intrinsic apoptotic pathway in its whole contributes majorly to secondary TBI injuries [82]. The extrinsic pathway is a result of extracellular signals causing TNF to integrate with the Fas cellular death receptors [79]. Clinical trials into anti-TNF drugs have been proposed for clinical trials as possible TBI treatments to reduce the numerous aspects of the pathology they influence [83]. Caspase induced apoptosis is more visible in mild TBI, where mitochondrial energy levels are within normal limits [84]. Caspase independent apoptosis is induced through the release of apoptosis inducing factor (AIF) and flavoprotein with NADH oxidase from the mitochondria into the cytosol as a result of the membrane permeabilization from mitochondrial dysfunction [85, 86]. The

translocation of the AIF into the cell nucleus causes cellular death. Caspase-independent apoptosis can occur in energy impaired states, meaning it is more probable to be a mitigating factor in TBI induced apoptosis where cerebral ischemia is more likely [87, 88].

2.5 TBI Predictive Biomarkers

Biological molecules indicative of normal or abnormal physiological processes are referred to as biomarkers. Isolating biomarker changes following injuries help identify affected processes and predict further injuries, and therefore provide a basis for therapeutic targets. Currently, assays for TBI diagnostics rely heavily on blood-based biomarkers, with some research investigating complimentary biofluids such as saliva or urine [89-92]. Cerebrospinal fluid (CSF) has been used as an accurate source due to its proximity to the area of impact, however most consider it too invasive as a biofluid to access [93].

S100B is a formally acknowledged mild TBI biomarker, recognised for diagnostics use in Scandinavia in the ALERT-TBI scheme [94, 95]. S100B is a calcium binding protein involved in mitochondrial function most commonly found in astrocytes, but observable in blood, brain tissue and CSF, which if overexpressed contributes to calcium homeostatic disruption and indicates cellular structural damage and death [96, 97]. Although S100B has been integrated as a clinical marker in Scandinavia, there are further quantitative studies which have shown it is not specific enough as a single marker, as its increase has been observed in various other neuronal and non-neuronal diseases alike, such as

Alzheimer's disease, Parkinson's disease, multiple sclerosis, psychiatric disorders, inflammatory bowel disease and COVID-19 [98-100]. Due to the nature of the injury, the specificity of a biomarker is important in determining if its increase is the result of the TBI, or any other injuries the patient will have incurred at the same time.

Glial fibrillary acidic protein (GFAP) is an intermediate filament III protein found in white and grey matter, tasked to maintain the cytoskeleton of glial cells, neurons and the BBB [101]. GFAP is overexpressed as a result of TBI-induced cellular hypertrophy and can cause glial scars on brain tissue, delaying axonal regeneration, making it a viable candidate as an indicator of damage and predictive of outcomes [102]. Ubiquitin carboxy-terminal hydrolase L1 (UCHL1) is a regulatory enzyme for axonal transport, structure and synapsis [103]. UCHL1 is brain-specific and selectively increased post brain injury in correlation with axonal damage [104]. The specificity of UCHL1 makes it a powerful component as a diagnostical tool. The assessment of a panel of biomarkers used in conjunction with each other ensures increased specificity to TBI and can provide a more accurate appraisal of the degree of injury. Further research towards the approval of clinically useful biomarkers to facilitate effective decision-making and improve patient stratification has the potential to drive non-imaging modalities based diagnostic platforms.

2.6 Current sTBI Assessment

2.6.1 Glasgow Coma Scale

The Glasgow coma scale (GCS) is an internationally recognised standard of initial assessment for head injuries developed in the 70s [105]. The GCS uses eye opening, motor responses and verbal activities, shown in Table 2-1, to provide a global outlook of affected brain regions. The GCS is scored between 15 and 3; scores between 3-8 are considered severe, 9-12 are moderate and 13 and over are mild [106, 107]. Although the test is subjective to the healthcare provider or emergency service worker, differences in scores of up to 2 points are acceptable.

Table 2-1 -Glasgow Coma Scale guide for initial TBI diagnosis. Each behaviour assessed indicates the probable site of injury, while the patient's response indicates the degree of injury [105].

Target Behaviour	Response	Score (points)
Eye Opening	Spontaneously	4
	To verbal command / speech	3
	To pain stimulus	2
	No eye opening	1
Verbal Response	Oriented	5
	Confused	4
	Inappropriate	3
	Incomprehensible	2
	No verbal response	1
Motor Response	Obeys movement command	6
	Moves to localised pain stimulus	5
	Withdraws from pain stimulus	4
	Spastic / abnormal flexing, decorticate	3
	Rigid / abnormal extension, decerebrate	2
	No motor response	1

Mild TBI: 15-13 points **Moderate TBI**: 12-9 points **Severe TBI**: 8-3 points

2.6.2 Imaging

In most cases, the first point of call for a closed head injury with a GCS score lower than 13 would be a non-contrast computerised tomography (CT) scan [106] to identify any emergency requiring neurosurgery. Amongst others, neurosurgical emergencies can include herniations, hydrocephalus, and hematomas in the brain. However, non-contrast CT scans can depreciate the importance of any parenchymal contusions, TAI, or hypertension.

Magnetic resonance imaging (MRI) scans can complement what the already highly sensitive CT scan cannot accurately record. MRI susceptibility weighted imaging can allow for comparison between the magnetic susceptibility of tissues and identify microhaemorrhages through a 3D gradient-echo sequence that can be particularly sensitive to blood and blood products [108]. Mechanical changes in the brain following TBI can be recorded through magnetic resonance elastography, which uses low-frequency vibrations to visualise tissue that has been compressed out of its elastic range [109].

Development of the QuickBrain MRI protocol, a rapid MRI of the brain, for paediatric cases has been studied for hydrocephalus detection and has a sensitivity towards TBI as well, removing the risks associated with ionizing radiation from CT scans and anaesthesia from longer MRI scans [110]. The QuickBrain MRI has not been implemented as a standard of care yet but shows promise as a more efficient tool than a traditional MRI.

Diffusion Tensor Imaging (DTI) is advanced MRI-based technique that visualises white matter structure and connectivity through the measurement of water molecule diffusion. Water tends to diffuse more easily along the direction of axonal fibres than across them, a property known as anisotropic diffusion [111]. DTI captures the direction and the magnitude of this movement, allowing to detect disruptions and abnormalities in the white matter pathways [112]. Compared to CT scans or conventional MRI, DTI is more sensitive to subtle changes in white matter integrity and can therefore contribute to assessing injury severity and predicting clinical outcomes. However, it is still not a

standard diagnostic tool in most clinical settings and continues to evolve in its clinical applications [112].

2.7 Surgical Interventions for sTBI

Surgical intervention for TBI management is indicated on a patient-to-patient basis. The nature of the injury triggers a specific recommendation for its type.

2.7.1 ICP Monitoring

Invasive monitoring of the brain can be required depending on the severity of the injury. Intraparenchymal catheters measure the ICP or, more commonly, intraventricular catheters record the ICP and drain any excess CSF buildup to reduce pressure [113]. Monitoring cerebral perfusion can serve as a useful guide in determining whether further surgical intervention is required. In accordance with the Monro-Kellie Hypothesis, which states that the sum of the constituents within the brain (tissue, blood, and CSF) must remain constant, a substantial increase in ICP can have dangerous consequences such as herniation or cerebral ischemia [114]. Between April 2014 and June 2015, a total of 1136 ICP insertion procedures were performed in England and Wales, from a sample of 15 820 patients across 187 hospitals, 26 of which had specialist neurosurgical services [115].

2.7.2 Decompressive Craniectomies

Neuroinflammation, whilst initially a protective feature, results in more space being taken up in the skull than is available, and ultimately causes more structural damage to the brain. To resolve this, a decompressive craniectomy (DC) can be performed, a procedure in which a minimum of 11 cm of the bone flap is removed to allow the brain to swell without incurring further damage against the skull and to adequately reduce the ICP. The size of the bone flap removed ultimately depends on the patient's condition. Whilst a DC reduces the ICP, the procedure exposes the patient to infection, haemorrhaging, and operative complications, and patients often come out with significant permanent disabilities. The decision to continue with a DC must therefore be heavily indicated and is considered last-tier therapy [116]. Between 2014 and 2019, the Hospital Episode Statistics recorded 4627 DC procedures in England [117].

Despite evidence of trephination dating back to Neolithic period and by Hippocrates in the Greek era, the first methods description and indications recorded was established by Italian physician and engineer Berengario da Carpi in the 16th century, who successfully performed a craniotomy on three patients [118-121]. This success has been followed by various randomized clinical trials from the 1900s to the 1980s of conflicting outcomes, eventually pausing the progress in the use of DC [122-130]. The improvement of ICP monitoring in the 1990s proved to be a game changer in determining the indications for DC. Clinical trials implementing DC in conjunction with ICP monitoring does eventually decrease mortality for TBI patients with a GCS score under 7 and no signs of irreversible

brain damage where intensive medical care has failed, thus putting DCs back on the therapeutic map [116, 131-134].

2.8 Raman Diagnostics for Brain Tissue

Brain-based tissue TBI biomarkers are under-represented in research due to blood-based diagnostic analysis techniques being more readily available, however crucial understanding of the damage being incurred in the brain itself may be misrepresented by the time biomarkers are circulating through the blood. Previous work by Harris and colleagues, represented in **Chapter 3** of this thesis, has produced an unparalleled Raman based TBI biomarker library [12], elucidating the Raman spectra for a panel of eighteen blood, CSF, and tissue-based biomarkers in both their raw state and in aqueous solutions at four commonly employed Raman spectroscopy laser wavelengths.

The implementation of Raman devices for invasive brain monitoring following TBI has been investigated by Surmacki and colleagues, in which brains from mice inflicted with TBI were assessed for spectroscopic changes in different areas of the brain at day 2 and 7 post injury [6]. Raman spectroscopy was sensitive to biochemical changes relating to both proteins and lipids in the mice brains at both day 2 and 7, as well as in the contralateral region from the injury. Potential repair mechanisms underway at day 7 were observed through cholesterol levels and signals related to bleeding observed at day 2 were absent by day 7. This research provides a basis for the potential of Raman

spectroscopy as a tool to precisely analyse the brain following TBI, introduced in Figure 2-3.

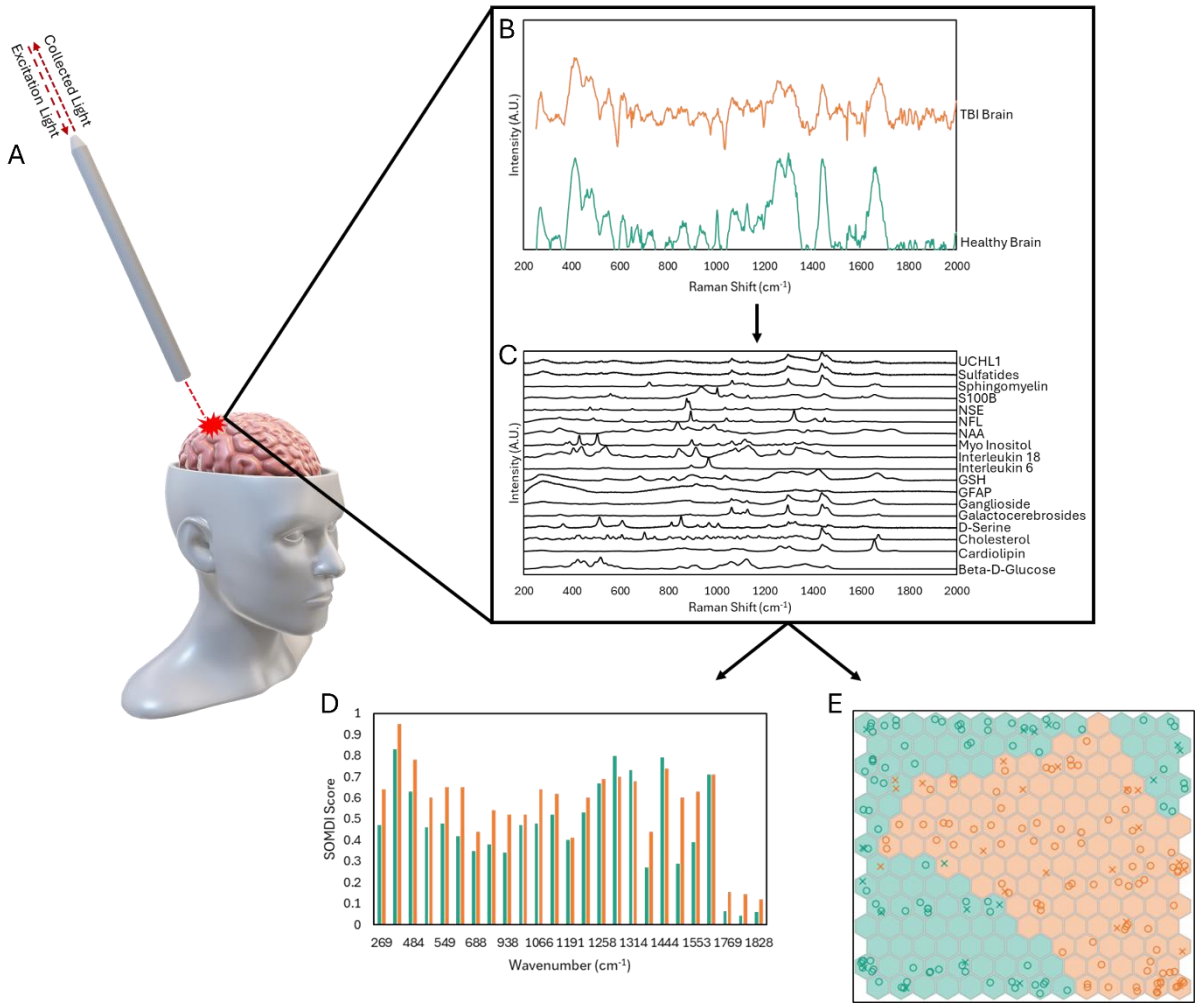

Figure 2-3 – Depiction of portable Raman spectroscopy probe application. A) Probe showing light path onto contusion point in brain. B) Collected spectra from different conditions are analysed against C) TBI biomarker Raman profiles. Machine learning multivariate analysis yields a D) self-organising map discriminant index (SOMDI), used to identify key wavenumbers used to distributed spectra on the E) self-organising map (SOM), a dimensionally reduced representation of the spectral differences.

Our group has previously employed a Raman spectroscopy probe paired with a 785 nm laser and commercial confocal Raman spectrometer (Renishaw, Inc.) to distinguish TBI brains from healthy in murine species [8]. This proof-of-concept discusses the potential

for a fully portable probe, described in Figure 2-3**A**, to be included in brain monitoring surgeries such as ICP placements and decompressive craniectomies. Considerations such as size requirements, brain herniation, and biocompatibility are all accounted for when designing the probe clip employed to stabilise the device, all the while ensuring a high signal to noise ratio [135]. Initial probe results indicate differences in certain spectral ratios, relating to specific biomarker shifts, discussed further in **Chapter 4**. With the help of a machine learning multivariate analysis tool developed by Banbury and colleagues (Figure 2-3**D-E**) [136], a fully portable *in situ* biomarker-based classification of sTBI using Raman spectroscopy is a feasible area of research, and thus opens the door towards patient-specific targeted therapies.

2.9 References

[1] A. I. Maas, N. Stocchetti, and R. Bullock, "Moderate and severe traumatic brain injury in adults," *The Lancet Neurology,* vol. 7, no. 8, pp. 728-741, 2008.

[2] N. D. Silverberg *et al.*, "The American congress of rehabilitation medicine diagnostic criteria for mild traumatic brain injury," *Archives of physical medicine and rehabilitation,* vol. 104, no. 8, pp. 1343-1355, 2023.

[3] T. J. Orr *et al.*, "Traumatic brain injury: a comprehensive review of biomechanics and molecular pathophysiology," *World neurosurgery,* vol. 185, pp. 74-88, 2024.

[4] E. Smith and G. Dent, *Modern Raman spectroscopy: a practical approach*. John Wiley & Sons, 2019.

[5] C. Raman and K. Krishnan, "The negative absorption of radiation," *Nature,* vol. 122, no. 3062, pp. 12-13, 1928.

[6] J. M. Surmacki, L. Ansel-Bollepalli, F. Pischiutta, E. R. Zanier, A. Ercole, and S. E. Bohndiek, "Label-free monitoring of tissue biochemistry following traumatic brain injury using Raman spectroscopy," *Analyst,* 10.1039/C6AN02238C vol. 142, no. 1, pp. 132-139, 2017, doi: 10.1039/C6AN02238C.

[7] C. Banbury, G. Harris, M. Clancy, R. J. Blanch, J. J. S. Rickard, and P. Goldberg Oppenheimer, "Window into the mind: Advanced handheld spectroscopic eye-safe technology for point-of-care neurodiagnostic," *Science Advances,* vol. 9, no. 46, p. eadg5431, 2023.

[8] M. Mowbray, C. Banbury, J. J. Rickard, D. J. Davies, and P. Goldberg Oppenheimer, "Development and Characterization of a Probe Device toward Intracranial Spectroscopy of Traumatic Brain Injury," *ACS biomaterials science & engineering,* vol. 7, no. 3, pp. 1252-1262, 2021.

[9] J. Desroches *et al.*, "Characterization of a Raman spectroscopy probe system for intraoperative brain tissue classification," *Biomedical optics express,* vol. 6, no. 7, pp. 2380-2397, 2015.

[10] E. Buchan, M. Hardy, P. d. C. Gomes, L. Kelleher, H. O. M. Chu, and P. G. Oppenheimer, "Emerging Raman spectroscopy and saliva-based diagnostics: from challenges to applications," *Applied Spectroscopy Reviews,* vol. 59, no. 3, pp. 277-314, 2024.

[11] G. Harris *et al.*, "Emerging Eye-Based Diagnostic Technologies for Traumatic Brain Injury," *IEEE reviews in biomedical engineering,* vol. 16, pp. 530-559, 2022.

[12] G. Harris, C. A. Stickland, M. Lim, and P. Goldberg Oppenheimer, "Raman Spectroscopy Spectral Fingerprints of Biomarkers of Traumatic Brain Injury," *Cells,* vol. 12, no. 22, p. 2589, 2023.

[13] A. R. Stevens *et al.*, "Raman Spectroscopy as a Neuromonitoring Tool in Traumatic Brain Injury: A Systematic Review and Clinical Perspectives," *Cells,* vol. 11, no. 7, p. 1227, 2022.

[14] D. A. Long and D. Long, *The Raman effect: a unified treatment of the theory of Raman scattering by molecules*. Wiley Chichester, 2002.

[15] J. A. Koningstein, *Introduction to the Theory of the Raman Effect*. Springer Science & Business Media, 2012.

[16] T. Wenzel, *Molecular and atomic spectroscopy*. LibreTexts, 2021.

[17] G. Vishwakarma, A. Sonpal, A. Pradhan, M. Haghighatlari, M. A. F. Afzal, and J. Hachmann, "Design of organic materials with tailored optical properties: Predicting quantum-chemical polarizabilities and derived quantities," in *Quantum Chemistry in the Age of Machine Learning*: Elsevier, 2023, pp. 653-674.

[18] P. Vandenabeele, *Practical Raman spectroscopy: an introduction*. John Wiley & Sons, 2013.

[19] L. H. Lajunen and P. Perämäki, *Spectrochemical analysis by atomic absorption and emission*. Royal Society of Chemistry, 2004.

[20] N. Jadhav, M. Yan, C. Vetter, S. Kasisomayajula, and V. Gelling, "Infrared spectroscopy (IR)," *Encyclopedia of Tribology,* pp. 1829-1829, 2013.

[21] E. Hanlon *et al.*, "Prospects for in vivo Raman spectroscopy," *Physics in Medicine & Biology,* vol. 45, no. 2, p. R1, 2000.

[22] S. Guo, T. Bocklitz, and J. Popp, "Optimization of Raman-spectrum baseline correction in biological application," *Analyst,* vol. 141, no. 8, pp. 2396-2404, 2016.

[23] E. Ryzhikova *et al.*, "Raman spectroscopy and machine learning for biomedical applications: Alzheimer's disease diagnosis based on the analysis of cerebrospinal fluid," *Spectrochimica Acta Part A: Molecular and Biomolecular Spectroscopy,* vol. 248, p. 119188, 2021.

[24] R. Sathyavathi *et al.*, "Raman spectroscopy provides a powerful, rapid diagnostic tool for the detection of tuberculous meningitis in ex vivo cerebrospinal fluid samples," *Journal of biophotonics,* vol. 6, no. 8, pp. 567-572, 2013.

[25] C. Chen *et al.*, "Urine Raman spectroscopy for rapid and inexpensive diagnosis of chronic renal failure (CRF) using multiple classification algorithms," *Optik,* vol. 203, p. 164043, 2020.

[26] V. Kavuru, R. S. Senger, J. L. Robertson, and D. Choudhury, "Analysis of urine Raman spectra differences from patients with diabetes mellitus and renal pathologies," *PeerJ,* vol. 11, p. e14879, 2023.

[27] H. J. Koster, A. Guillen-Perez, J. S. Gomez-Diaz, M. Navas-Moreno, A. C. Birkeland, and R. P. Carney, "Fused Raman spectroscopic analysis of blood and saliva delivers high accuracy for head and neck cancer diagnostics," *Scientific reports,* vol. 12, no. 1, p. 18464, 2022.

[28] C. Camerlingo *et al.*, "Characterization of human tear fluid by means of surface-enhanced Raman spectroscopy," *Sensors,* vol. 19, no. 5, p. 1177, 2019.

[29] A. Synytsya, M. Judexova, D. Hoskovec, M. Miskovicova, and L. Petruzelka, "Raman spectroscopy at different excitation wavelengths (1064, 785 and 532 nm) as a tool for diagnosis of colon cancer," *Journal of Raman Spectroscopy,* vol. 45, no. 10, pp. 903-911, 2014.

[30] A. Downes and A. Elfick, "Raman spectroscopy and related techniques in biomedicine," *Sensors,* vol. 10, no. 3, pp. 1871-1889, 2010.

[31] R. Chamoun, D. Suki, S. P. Gopinath, J. C. Goodman, and C. Robertson, "Role of extracellular glutamate measured by cerebral microdialysis in severe traumatic brain injury," *Journal of neurosurgery,* vol. 113, no. 3, pp. 564-570, 2010.

[32] V. R. Rao and S. Finkbeiner, "NMDA and AMPA receptors: old channels, new tricks," *Trends in neurosciences,* vol. 30, no. 6, pp. 284-291, 2007.

[33] R. Bullock *et al.*, "Factors affecting excitatory amino acid release following severe human head injury," *Journal of neurosurgery,* vol. 89, no. 4, pp. 507-518, 1998.

[34] M. M. Folkerts, E. A. Parks, J. R. Dedman, M. A. Kaetzel, B. G. Lyeth, and R. F. Berman, "Phosphorylation of calcium calmodulin—dependent protein kinase II following lateral fluid percussion brain injury in rats," *Journal of neurotrauma,* vol. 24, no. 4, pp. 638-650, 2007.

[35] P. M. Lea IV and A. I. Faden, "Traumatic brain injury: developmental differences in glutamate receptor response and the impact on treatment," *Mental retardation and developmental disabilities research reviews,* vol. 7, no. 4, pp. 235-248, 2001.

[36] C. Ikonomidou and L. Turski, "Why did NMDA receptor antagonists fail clinical trials for stroke and traumatic brain injury?," *The Lancet Neurology,* vol. 1, no. 6, pp. 383-386, 2002.

[37] J.-H. Yi and A. S. Hazell, "Excitotoxic mechanisms and the role of astrocytic glutamate transporters in traumatic brain injury," *Neurochemistry international,* vol. 48, no. 5, pp. 394-403, 2006.

[38] S. A. Susin, N. Zamzami, and G. Kroemer, "Mitochondria as regulators of apoptosis: doubt no more," *Biochimica et Biophysica Acta (BBA)-Bioenergetics,* vol. 1366, no. 1-2, pp. 151-165, 1998.

[39] R. Abeti and A. Y. Abramov, "Mitochondrial Ca2+ in neurodegenerative disorders," *Pharmacological research,* vol. 99, pp. 377-381, 2015.

[40] A. Boveris and B. Chance, "The mitochondrial generation of hydrogen peroxide. General properties and effect of hyperbaric oxygen," *Biochemical Journal,* vol. 134, no. 3, pp. 707-716, 1973.

[41] H. P. Indo *et al.*, "Evidence of ROS generation by mitochondria in cells with impaired electron transport chain and mitochondrial DNA damage," *Mitochondrion,* vol. 7, no. 1-2, pp. 106-118, 2007.

[42] F. Scialo and A. Sanz, "Coenzyme Q redox signalling and longevity," *Free Radical Biology and Medicine,* vol. 164, pp. 187-205, 2021.

[43] D. Herrero *et al.*, "Redox-dependent BMI1 activity drives in vivo adult cardiac progenitor cell differentiation," *Cell Death & Differentiation,* vol. 25, no. 4, pp. 809-822, 2018.

[44] E. T. Chouchani, L. Kazak, and B. M. Spiegelman, "Mitochondrial reactive oxygen species and adipose tissue thermogenesis: Bridging physiology and mechanisms," *Journal of Biological Chemistry,* vol. 292, no. 41, pp. 16810-16816, 2017.

[45] J. Bastin, M. Sroussi, I. Nemazanyy, P. Laurent-Puig, S. Mouillet-Richard, and F. Djouadi, "Downregulation of mitochondrial complex I induces ROS production in colorectal cancer subtypes that differently controls migration," *Journal of Translational Medicine,* vol. 21, no. 1, p. 522, 2023.

[46] L. Han *et al.*, "Retrograde regulation of mitochondrial fission and epithelial to mesenchymal transition in hepatocellular carcinoma by GCN5L1," *Oncogene,* vol. 42, no. 13, pp. 1024-1037, 2023.

[47] H. Kinugasa *et al.*, "Mitochondrial SOD2 regulates epithelial–mesenchymal transition and cell populations defined by differential CD44 expression," *Oncogene,* vol. 34, no. 41, pp. 5229-5239, 2015.

[48] A. Y. Baev, A. Y. Vinokurov, I. N. Novikova, V. V. Dremin, E. V. Potapova, and A. Y. Abramov, "Interaction of mitochondrial calcium and ROS in neurodegeneration," *Cells,* vol. 11, no. 4, p. 706, 2022.

[49] P. Bernardi *et al.*, "The mitochondrial permeability transition," *Biofactors,* vol. 8, no. 3-4, pp. 273-281, 1998.

[50] P. Sullivan, A. Rabchevsky, P. Waldmeier, and J. Springer, "Mitochondrial permeability transition in CNS trauma: cause or effect of neuronal cell death?," *Journal of neuroscience research,* vol. 79, no. 1-2, pp. 231-239, 2005.

[51] I. Szabo, P. Bernardi, and M. Zoratti, "Modulation of the mitochondrial megachannel by divalent cations and protons," *Journal of Biological Chemistry,* vol. 267, no. 5, pp. 2940-2946, 1992.

[52] L. Scorrano, V. Petronilli, and P. Bernardi, "On the voltage dependence of the mitochondrial permeability transition pore: a critical appraisal," *Journal of Biological Chemistry,* vol. 272, no. 19, pp. 12295-12299, 1997.

[53] R. A. Haworth and D. R. Hunter, "The Ca2+-induced membrane transition in mitochondria: II. Nature of the Ca2+ trigger site," *Archives of biochemistry and biophysics,* vol. 195, no. 2, pp. 460-467, 1979.

[54] M. Crompton, "The mitochondrial permeability transition pore and its role in cell death," *Biochemical journal,* vol. 341, no. 2, pp. 233-249, 1999.

[55] T. Briston *et al.*, "Mitochondrial permeability transition pore: sensitivity to opening and mechanistic dependence on substrate availability," *Scientific reports,* vol. 7, no. 1, p. 10492, 2017.

[56] A. Fesharaki-Zadeh, "Oxidative stress in traumatic brain injury," *International journal of molecular sciences,* vol. 23, no. 21, p. 13000, 2022.

[57] V. Herbert, S. Shaw, E. Jayatilleke, and T. Stopler-Kasdan, "Most free-radical injury is iron-related: it is promoted by iron, hemin, holoferritin and vitamin C, and inhibited by desferoxamine and apoferritin," *Stem Cells,* vol. 12, no. 3, pp. 289-303, 1994.

[58] A. Ayala, M. F. Muñoz, and S. Argüelles, "Lipid peroxidation: production, metabolism, and signaling mechanisms of malondialdehyde and 4-hydroxy-2-nonenal," *Oxidative medicine and cellular longevity,* vol. 2014, no. 1, p. 360438, 2014.

[59] C. Szabó, H. Ischiropoulos, and R. Radi, "Peroxynitrite: biochemistry, pathophysiology and development of therapeutics," *Nature reviews Drug discovery,* vol. 6, no. 8, pp. 662-680, 2007.

[60] R. Radi, A. Cassina, R. Hodara, C. Quijano, and L. Castro, "Peroxynitrite reactions and formation in mitochondria," *Free Radical Biology and Medicine,* vol. 33, no. 11, pp. 1451-1464, 2002.

[61] Y. Deng, B. M. Thompson, X. Gao, and E. D. Hall, "Temporal relationship of peroxynitrite-induced oxidative damage, calpain-mediated cytoskeletal degradation and neurodegeneration after traumatic brain injury," *Experimental neurology,* vol. 205, no. 1, pp. 154-165, 2007.

[62] A. K. Ryan, W. Rich, and M. A. Reilly, "Oxidative stress in the brain and retina after traumatic injury," *Frontiers in neuroscience,* vol. 17, p. 1021152, 2023.

[63] K. Thapa, H. Khan, T. G. Singh, and A. Kaur, "Traumatic brain injury: mechanistic insight on pathophysiology and potential therapeutic targets," *Journal of Molecular Neuroscience,* vol. 71, no. 9, pp. 1725-1742, 2021.

[64] J. D. Pierce *et al.*, "Ubiquinol treatment for TBI in male rats: Effects on mitochondrial integrity, injury severity, and neurometabolism," *Journal of neuroscience research,* vol. 96, no. 6, pp. 1080-1092, 2018.

[65] E. D. Hall, M. R. Detloff, K. Johnson, and N. C. Kupina, "Peroxynitrite-mediated protein nitration and lipid peroxidation in a mouse model of traumatic brain injury," *Journal of neurotrauma,* vol. 21, no. 1, pp. 9-20, 2004.

[66] V. Di Pietro *et al.*, "Antioxidant therapies in traumatic brain injury," *Antioxidants,* vol. 9, no. 3, p. 260, 2020.

[67] J. Goodman, M. Van, S. Gopinath, and C. Robertson, "Pro-inflammatory and pro-apoptotic elements of the neuroinflammatory response are activated in traumatic brain injury," in *Acta Neurochirurgica Supplements*, 2009: Springer, pp. 437-439.

[68] B. D. Semple, N. Bye, M. Rancan, J. M. Ziebell, and M. C. Morganti-Kossmann, "Role of CCL2 (MCP-1) in traumatic brain injury (TBI): evidence from severe TBI patients and CCL2−/− mice," *Journal of Cerebral Blood Flow & Metabolism,* vol. 30, no. 4, pp. 769-782, 2010.

[69] G. Lotocki *et al.*, "Alterations in blood-brain barrier permeability to large and small molecules and leukocyte accumulation after traumatic brain injury: effects of post-traumatic hypothermia," *Journal of neurotrauma,* vol. 26, no. 7, pp. 1123-1134, 2009.

[70] T. Frugier, M. C. Morganti-Kossmann, D. O'Reilly, and C. A. McLean, "In situ detection of inflammatory mediators in post mortem human brain tissue after traumatic injury," *Journal of neurotrauma,* vol. 27, no. 3, pp. 497-507, 2010.

[71] D. W. Simon, M. J. McGeachy, H. Bayır, R. S. Clark, D. J. Loane, and P. M. Kochanek, "The far-reaching scope of neuroinflammation after traumatic brain injury," *Nature Reviews Neurology,* vol. 13, no. 3, pp. 171-191, 2017.

[72] J. M. Ziebell and M. C. Morganti-Kossmann, "Involvement of pro-and anti-inflammatory cytokines and chemokines in the pathophysiology of traumatic brain injury," *Neurotherapeutics,* vol. 7, no. 1, pp. 22-30, 2010.

[73] T. M. Andriessen, B. Jacobs, and P. E. Vos, "Clinical characteristics and pathophysiological mechanisms of focal and diffuse traumatic brain injury," *Journal of cellular and molecular medicine,* vol. 14, no. 10, pp. 2381-2392, 2010.

[74] P. Reier, L. Zholudeva, and M. Lane, "Axonal degeneration and regeneration in the peripheral and central nervous systems," in *Conn's Translational Neuroscience*: Elsevier, 2017, pp. 553-575.

[75] G. F. Bruggeman, I. K. Haitsma, C. M. Dirven, and V. Volovici, "Traumatic axonal injury (TAI): definitions, pathophysiology and imaging—a narrative review," *Acta neurochirurgica,* vol. 163, pp. 31-44, 2021.

[76] U. Fünfschilling *et al.*, "Glycolytic oligodendrocytes maintain myelin and long-term axonal integrity," *Nature,* vol. 485, no. 7399, pp. 517-521, 2012.

[77] C. S. Hill, M. P. Coleman, and D. K. Menon, "Traumatic axonal injury: mechanisms and translational opportunities," *Trends in neurosciences,* vol. 39, no. 5, pp. 311-324, 2016.

[78] D. H. SMITH *et al.*, "Progressive atrophy and neuron death for one year following brain trauma in the rat," *Journal of neurotrauma,* vol. 14, no. 10, pp. 715-727, 1997.
[79] K. Niizuma *et al.*, "Mitochondrial and apoptotic neuronal death signaling pathways in cerebral ischemia," *Biochimica et Biophysica Acta (BBA)-Molecular Basis of Disease,* vol. 1802, no. 1, pp. 92-99, 2010.
[80] A. Zhang *et al.*, "The role of caspase family in acute brain injury: the potential therapeutic targets in the future," *Current Neuropharmacology,* vol. 20, no. 6, p. 1194, 2022.
[81] L. Lorente *et al.*, "Low blood caspase-8 levels in survivor patients of traumatic brain injury," *Neurological Sciences,* pp. 1-6, 2021.
[82] R. S. Darwish and N. S. Amiridze, "Detectable levels of cytochrome C and activated caspase-9 in cerebrospinal fluid after human traumatic brain injury," *Neurocritical care,* vol. 12, pp. 337-341, 2010.
[83] Y. Zhou, R. Fan, B. O. Botchway, Y. Zhang, and X. Liu, "Infliximab can improve traumatic brain injury by suppressing the tumor necrosis factor alpha pathway," *Molecular Neurobiology,* vol. 58, no. 6, pp. 2803-2811, 2021.
[84] F.-Q. Zhou, "Genetic study of axon regeneration with cultured adult dorsal root ganglion neurons," *JoVE (Journal of Visualized Experiments),* no. 66, p. e4141, 2012.
[85] X. Zhang *et al.*, "Intranuclear localization of apoptosis-inducing factor (AIF) and large scale DNA fragmentation after traumatic brain injury in rats and in neuronal cultures exposed to peroxynitrite," *Journal of neurochemistry,* vol. 82, no. 1, pp. 181-191, 2002.
[86] S. P. Cregan, V. L. Dawson, and R. S. Slack, "Role of AIF in caspase-dependent and caspase-independent cell death," *Oncogene,* vol. 23, no. 16, pp. 2785-2796, 2004.
[87] C. C. Alano, W. Ying, and R. A. Swanson, "Poly (ADP-ribose) polymerase-1-mediated cell death in astrocytes requires NAD+ depletion and mitochondrial permeability transition," *Journal of Biological Chemistry,* vol. 279, no. 18, pp. 18895-18902, 2004.
[88] Y. Akamatsu and K. A. Hanafy, "Cell death and recovery in traumatic brain injury," *Neurotherapeutics,* vol. 17, no. 2, pp. 446-456, 2020.
[89] A. Rodríguez-Rodríguez *et al.*, "Role of S100B protein in urine and serum as an early predictor of mortality after severe traumatic brain injury in adults," *Clinica chimica acta,* vol. 414, pp. 228-233, 2012.
[90] S. V. Caswell, N. Cortes, K. Mitchell, L. Liotta, and E. F. Petricoin, "Development of nanoparticle-enabled protein biomarker discovery: implementation for saliva-based traumatic brain injury detection," *Advances in Salivary Diagnostics,* pp. 121-129, 2015.
[91] J. J. Rickard, V. Di-Pietro, D. J. Smith, D. J. Davies, A. Belli, and P. G. Oppenheimer, "Rapid optofluidic detection of biomarkers for traumatic brain injury via surface-enhanced Raman spectroscopy," *Nature biomedical engineering,* vol. 4, no. 6, pp. 610-623, 2020.
[92] F. G. Strathmann, S. Schulte, K. Goerl, and D. J. Petron, "Blood-based biomarkers for traumatic brain injury: evaluation of research approaches, available methods

and potential utility from the clinician and clinical laboratory perspectives," *Clinical biochemistry,* vol. 47, no. 10-11, pp. 876-888, 2014.

[93] J. Zhang, V. Puvenna, and D. Janigro, "Biomarkers of traumatic brain injury and their relationship to pathology," 2015.

[94] O. Calcagnile, A. Anell, and J. Undén, "The addition of S100B to guidelines for management of mild head injury is potentially cost saving," *BMC neurology,* vol. 16, pp. 1-7, 2016.

[95] J. Undén, T. Ingebrigtsen, B. Romner, and S. N. Committee, "Scandinavian guidelines for initial management of minimal, mild and moderate head injuries in adults: an evidence and consensus-based update," *BMC medicine,* vol. 11, pp. 1-14, 2013.

[96] H. Nishiyama, T. Knöpfel, S. Endo, and S. Itohara, "Glial protein S100B modulates long-term neuronal synaptic plasticity," *Proceedings of the National Academy of Sciences,* vol. 99, no. 6, pp. 4037-4042, 2002.

[97] A. Goyal *et al.*, "S100b as a prognostic biomarker in outcome prediction for patients with severe traumatic brain injury," *Journal of neurotrauma,* vol. 30, no. 11, pp. 946-957, 2013.

[98] F. Michetti *et al.*, "Growing role of S100B protein as a putative therapeutic target for neurological-and nonneurological-disorders," *Neuroscience & Biobehavioral Reviews,* vol. 127, pp. 446-458, 2021.

[99] F. Michetti *et al.*, "The S100B protein in biological fluids: more than a lifelong biomarker of brain distress," *Journal of neurochemistry,* vol. 120, no. 5, pp. 644-659, 2012.

[100] D. Janigro, S. Mondello, J. P. Posti, and J. Unden, "GFAP and S100B: what you always wanted to know and never dared to ask," *Frontiers in neurology,* vol. 13, p. 835597, 2022.

[101] Z. Yang and K. K. Wang, "Glial fibrillary acidic protein: from intermediate filament assembly and gliosis to neurobiomarker," *Trends in neurosciences,* vol. 38, no. 6, pp. 364-374, 2015.

[102] M. V. Sofroniew, "Molecular dissection of reactive astrogliosis and glial scar formation," *Trends in neurosciences,* vol. 32, no. 12, pp. 638-647, 2009.

[103] H. Liu *et al.*, "Role of UCHL1 in axonal injury and functional recovery after cerebral ischemia," *Proceedings of the National Academy of Sciences,* vol. 116, no. 10, pp. 4643-4650, 2019.

[104] S. Shahjouei *et al.*, "The diagnostic values of UCH-L1 in traumatic brain injury: a meta-analysis," *Brain injury,* vol. 32, no. 1, pp. 1-17, 2018.

[105] G. Teasdale and B. Jennett, "Assessment of coma and impaired consciousness: a practical scale," *The Lancet,* vol. 304, no. 7872, pp. 81-84, 1974.

[106] L. G. Smith *et al.*, "Advanced neuroimaging in traumatic brain injury: an overview," *Neurosurgical Focus,* vol. 47, no. 6, p. E17, 2019.

[107] P. Guide, "VA/DoD CLINICAL PRACTICE GUIDELINE FOR THE MANAGEMENT OF CONCUSSION-MILD TRAUMATIC BRAIN INJURY," 2016.

[108] S. W. Atlas, *Magnetic resonance imaging of the brain and spine*. Lippincott Williams & Wilkins, 2009.

[109] T. Boulet, M. L. Kelso, and S. F. Othman, "Microscopic magnetic resonance elastography of traumatic brain injury model," *Journal of neuroscience methods,* vol. 201, no. 2, pp. 296-306, 2011.
[110] D. C. Sheridan, C. D. Newgard, N. R. Selden, M. A. Jafri, and M. L. Hansen, "QuickBrain MRI for the detection of acute pediatric traumatic brain injury," *Journal of Neurosurgery: Pediatrics,* vol. 19, no. 2, pp. 259-264, 2017.
[111] K. L. Main *et al.*, "DTI measures identify mild and moderate TBI cases among patients with complex health problems: a receiver operating characteristic analysis of US veterans," *NeuroImage: Clinical,* vol. 16, pp. 1-16, 2017.
[112] D. B. Douglas *et al.*, "Diffusion tensor imaging of TBI: potentials and challenges," *Topics in magnetic resonance imaging,* vol. 24, no. 5, pp. 241-251, 2015.
[113] H. Adams, A. G. Kolias, and P. J. Hutchinson, "The role of surgical intervention in traumatic brain injury," *Neurosurgery Clinics,* vol. 27, no. 4, pp. 519-528, 2016.
[114] B. Mokri, "The Monro–Kellie hypothesis: applications in CSF volume depletion," *Neurology,* vol. 56, no. 12, pp. 1746-1748, 2001.
[115] T. Lawrence, A. Helmy, O. Bouamra, M. Woodford, F. Lecky, and P. J. Hutchinson, "Traumatic brain injury in England and Wales: prospective audit of epidemiology, complications and standardised mortality," *BMJ open,* vol. 6, no. 11, p. e012197, 2016.
[116] Z. Rossini, F. Nicolosi, A. G. Kolias, P. J. Hutchinson, P. De Sanctis, and F. Servadei, "The history of decompressive craniectomy in traumatic brain injury," *Frontiers in neurology,* vol. 10, p. 458, 2019.
[117] H. Mee *et al.*, "Decompressive craniectomy to cranioplasty: a retrospective observational study using Hospital Episode Statistics in England," *BMJ Surgery, Interventions, & Health Technologies,* vol. 6, no. 1, p. e000253, 2024.
[118] I. G. Panourias, P. K. Skiadas, D. E. Sakas, and S. G. Marketos, "Hippocrates: a pioneer in the treatment of head injuries," *Neurosurgery,* vol. 57, no. 1, pp. 181-189, 2005.
[119] J. W. Moon and D. K. Hyun, "Decompressive craniectomy in traumatic brain injury: a review article," *Korean journal of neurotrauma,* vol. 13, no. 1, p. 1, 2017.
[120] A. Di Ieva, P. Gaetani, C. Matula, C. Sherif, M. Skopec, and M. Tschabitscher, "Berengario da Carpi: a pioneer in neurotraumatology: Historical vignette," *Journal of neurosurgery,* vol. 114, no. 5, pp. 1461-1470, 2011.
[121] J. B. da Carpi, *Tractatus de fractura calve sive cranei*. Impressum per Hieronymum de Benedictis.
[122] R. N. Kjellberg and A. Prieto, "Bifrontal decompressive craniotomy for massive cerebral edema," *Journal of neurosurgery,* vol. 34, no. 4, pp. 488-493, 1971.
[123] K. G. Jamieson and J. D. Yelland, "Surgically treated traumatic subdural hematomas," *Journal of neurosurgery,* vol. 37, no. 2, pp. 137-149, 1972.
[124] A. Gerl and S. Tavan, "Bilateral craniectomy in the treatment of severe traumatic brain edema," *Zentralblatt fur Neurochirurgie,* vol. 41, no. 2, pp. 125-138, 1980.
[125] D. A. Fell, S. Fitzgerald, R. H. Moiel, and P. Caram, "Acute subdural hematomas: Review of 144 cases," *Journal of Neurosurgery,* vol. 42, no. 1, pp. 37-42, 1975.

[126] K. Clark, T. M. Nash, and G. C. Hutchison, "The failure of circumferential craniotomy in acute traumatic cerebral swelling," *Journal of neurosurgery,* vol. 29, no. 4, pp. 367-371, 1968.
[127] R. H. Britt and R. D. Hamilton, "Large decompressive craniotomy in the treatment of acute subdural hematoma," *Neurosurgery,* vol. 2, no. 3, pp. 195-200, 1978.
[128] H. Cushing, "I. Subtemporal decompressive operations for the intracranial complications associated with bursting fractures of the skull," *Annals of surgery,* vol. 47, no. 5, p. 641, 1908.
[129] G. Horrax, "Some of Harvey Cushing's contributions to neurological surgery," *Journal of neurosurgery,* vol. 54, no. 4, pp. 436-447, 1981.
[130] P. R. Cooper, H. Hagler, K. W. Clark, and P. Barnett, "Enhancement of experimental cerebral edema after decompressive craniectomy: implications for the management of severe head injuries," *Neurosurgery,* vol. 4, no. 4, pp. 296-300, 1979.
[131] D.-S. Yoo, D.-S. Kim, K.-S. Cho, P.-W. Huh, C.-K. Park, and J.-K. Kang, "Ventricular pressure monitoring during bilateral decompression with dural expansion," *Journal of neurosurgery,* vol. 91, no. 6, pp. 953-959, 1999.
[132] R. S. Polin *et al.*, "Decompressive bifrontal craniectomy in the treatment of severe refractory posttraumatic cerebral edema," *Neurosurgery,* vol. 41, no. 1, pp. 84-94, 1997.
[133] W. K.-W. Guerra, M. R. Gaab, H. Dietz, J.-U. Mueller, J. Piek, and M. J. Fritsch, "Surgical decompression for traumatic brain swelling: indications and results," *Journal of neurosurgery,* vol. 90, no. 2, pp. 187-196, 1999.
[134] I. Timofeev *et al.*, "Effect of decompressive craniectomy on intracranial pressure and cerebrospinal compensation following traumatic brain injury," *Journal of neurosurgery,* vol. 108, no. 1, pp. 66-73, 2008.
[135] D. Tuschel, "Photoluminescence spectroscopy using a Raman spectrometer," 2016.
[136] C. Banbury *et al.*, "Development of the self optimising Kohonen index network (SKiNET) for Raman spectroscopy based detection of anatomical eye tissue," *Scientific reports,* vol. 9, no. 1, p. 10812, 2019.

Chapter 3: Raman Spectroscopy Spectral Fingerprints of Biomarkers of Traumatic Brain Injury

This chapter was submitted to and published by Cells as a research article. All work including conceptualisation, methodology, data acquisition, data curation, formal analysis and writing was primarily carried out by the co-first authors, Dr G. Harris and **Miss C. A. Stickland**. Additional author contributions include Prof P. Goldberg Oppenheimer (conceptualisation, resources, reviewing, editing) and Mr M. Lim (data acquisition). Parts of the introduction were altered to avoid repetition and improve clarity.

3.1 Abstract

Traumatic brain injury (TBI) affects millions of people of all ages around the globe. The immediate severity of TBI is notoriously hard to diagnose at the point of care, resulting in incorrect patient management, further neurodegenerative complications, and increased costs. It is vital to develop timely, alternative diagnostics for TBI to assist triage and clinical decision making, complementary to current techniques such as neuroimaging and cognitive assessment. These could deliver rapid, quantitative TBI detection, by obtaining information on biochemical changes from patient's biofluids. If available, this would reduce mis-triage, save healthcare providers costs (both over- and under-triage are expensive) and improve outcomes by guiding early management. Herein, we utilize Raman spectroscopy-based detection to profile a panel of 18 raw (human, animal, and synthetically derived) TBI-indicative biomarkers (N-acetyl-aspartic acid (NAA), Ganglioside, Glutathione (GSH), Neuron Specific Enolase (NSE), Glial Fibrillary Acidic

Protein (GFAP), Ubiquitin C-terminal Hydrolase L1 (UCHL1), Cholesterol, D-Serine, Sphingomyelin, Sulfatides, Cardiolipin, Interleukin-6 (IL-6), S100B, Galactocerebrosides, Beta-D-(+)-Glucose, Myo-Inositol, Interleukin-18 (IL-18), Neurofilament Light Chain (NFL) and their aqueous solution. The subsequently derived unique spectral reference library, exploiting four excitation lasers of 514, 633, 785, and 830 nm, will aid the development of rapid, non-destructive, and label-free spectroscopy-based neuro-diagnostic technologies. These biomolecules, released during cellular damage, provide additional means of diagnosing TBI and assessing the severity of injury. The spectroscopic temporal profiles of the studied biofluid neuro-markers are classed according to their acute, sub-acute, and chronic temporal injury phases and we have further generated detailed peak assignment tables for each brain specific biomolecule within each injury phase. The intensity ratios of significant peaks, yielding the combined unique spectroscopic barcode for each brain-injury marker, are compared to assess variance between lasers, with the smallest variance (σ^2) found for UCHL1 ($\sigma^2 = 0.000164$) and the highest for sulfatide ($\sigma^2 = 0.158$). Overall, this work paves the way for defining and setting the most appropriate diagnostic time window for detection following brain injury. Further rapid and specific detection of these biomarkers, from easily accessible biofluids, would not only enable the triage of TBI, predict outcomes, indicate the progress of recovery, and save healthcare providers costs, but also cement the potential of Raman-based spectroscopy as a powerful tool for neurodiagnostics.

3.2 Introduction

Recent research [1-6] has been focusing on establishing the temporal profile of TBIs and the associated biomarkers including their emergence (i.e., acute phase), crucial for early-stage diagnostics, persistence, and decline (sub-acute and chronic phases)—indicative of the longer-term effects and prognosis as well as development of new therapeutics. TBI biomarkers have been shown to have a characteristic timeframe of acute (<24 h), sub-acute (1 day–3 weeks) and chronic (3 weeks–6 months), as the initial insult causes acute damage to the brain, is typically followed by a biochemical cascade leading to secondary injuries over the following month [7-9]. This indicates that identifying TBI in the acute phase and intervening before further damage occurs is vital for long-term neurological recovery. However, despite the important time window alongside an estimate of 69 million people suffering from TBI each year worldwide, the development of point-of-care, timely TBI diagnostic technologies remains an unmet need and there is no definite triaging and therapeutic patient pathway [10].

The main challenge lies in the fact that pre-hospital and emergency department (ED) assessment is predominantly based on insensitive GCS and history acquisition with guidance on CT being often vague and costly. mTBI is often underdiagnosed if not identified rapidly at the point of injury, with 90% of acute cases requiring medical attention going undetected and not admitted to ED [11, 13, 14]. Therefore, development of successful TBI biomarker diagnostics from blood [15], or other biofluids, i.e., CSF [6],

saliva [16], urine [17], and tears [18], would lead to improved triage of severe and high-risk injuries and improve outcomes, whilst appropriate classification of low-risk and mTBI patients would allow for the focusing of resources on those who need it the most. Furthermore, reduced resource demand would mitigate the relatively low costs of the investigation in comparison to ED assessment, CT imaging and hospital admission, and have distinct yet complementary use cases. In the pre-hospital space, improved triage of TBI as mild will support decision-making by pre-hospital healthcare providers to reduce referral to hospital care, reducing the number of ED visits.

Concurrently, Raman spectroscopy has been increasingly used in medical and diagnostic applications for producing non-destructive chemical information [19]. In contrast to the in vitro bioassays, the availability of inexpensive, portable Raman devices makes this technique particularly attractive for point-of-care testing, analysis, and screening of biofluids. There is limited yet growing research in the development of Raman spectroscopy for biofluid-based neurodiagnostics [31-35]. Whilst research continues to unravel new technologies for rapid point-of-care technologies for TBI diagnostics from biofluids and tissue, it is imperative to establish fingerprints of the inherent characteristics of TBI biomarkers in various injury phases, where the detected changes via Raman spectroscopy could, in the long-term, be attributed to underpinning the variations in TBIs with various severity and as a function of temporal evolution.

Herein, we consistently study a broad panel of TBI biomarkers via Raman spectroscopy profiling and establish a spectral reference library for the interpretation of the Raman fingerprints of TBI-indicative biomarkers via biologically applicable laser excitation

wavelengths in different post-injury phases. A carefully selected cohort of TBI-indicative biomarkers are classed into three main injury phases with spectra in the raw and reconstituted (mimicking the biomarker biofluid) state forms acquired via a range of Raman-applicable laser excitation wavelengths of 514, 633, 785, and 830 nm. Subsequently, for each post-TBI phase, Raman spectroscopy temporal-phase biomarker-profiling establishes an important baseline library in the form of a "multi-biochemical barcode", yielding a characteristic tool for ongoing and future spectroscopic studies for diagnostic applications.

Awareness of the spectroscopic temporal profiles of TBI biomarkers provides an essential pathway for defining and setting the most appropriate diagnostic time window for sampling after injury. The derived Raman fingerprints, combined with the identified biochemical peaks, closely matching notable biomarker characteristics, equip us with the knowledge of the molecule's physiological role. This could not only improve the treatment of TBI through specific targeting of the damage in contrast to current methods, which mostly rely on symptomatic relief [36], but could also provide a further panel of candidate first-line screening TBI-indicative biomarkers. This lays the platform for defining their functionality in the complex TBI aetiology and, in the longer term, cements Raman spectroscopy as a powerful technique for future biomarker discovery in both neurodiagnostics as well as for other detrimental diseases with many ramifications.

3.3 Materials and Methods

3.3.1 TBI Biomarkers

The selected raw biomarkers were purchased without purification and tested in both solid and solution states. These were divided into three main groups of acute, sub-acute, and chronic phases (Figure 3-1). The TBI cohort selection was based on an extensive literature overview of recent research on TBI biomarkers (animal and human) and temporal courses studied in a range of biofluids including blood, plasma, CSF, urine, and the key biomarkers of neuroinflammation [1, 37-44]. Biomarkers included in the panel were obtained in the purest form without any active additives, to avoid impacting spectral signatures. This yielded a cohort of 18 biomarkers including the N-acetyl-L-aspartic acid (NAA), ganglioside, glutathione (GSH), neuron-specific enolase (NSE), glial fibrillary acidic protein (GFAP), ubiquitin carboxyl-terminal hydrolase isozyme L1 (UCHL1), cholesterol, D-serine, sphingomyelin, sulfatide, cardiolipin, interleukin-6 (IL-6), S100B, galactocerebroside, glucose, myo-inositol, interleukin-18 (IL-18), and Neurofilament light chain (NFL). Subsequently, reconstituted biomarker samples were prepared following the technical details provided in the individual data sheets. Typically, this included centrifugation at 8 G for 2 min prior to adding the solvent of distilled H_2O (18.2 MΩ) or chloroform/ethanol, yielding 1:1 *v/v* solutions. After 20 min, to allow full dissolvement, 3 µL samples of each biomarker were deposited onto an aluminium slide and dried in an ambient environment for Raman measurement.

3.3.2 Reference Chemicals

Human-form biomarkers included the S100B (HY-P70659, Cambridge Bioscience, Cambridge, UK), IL-6 (H7416-10UG, Merck, Darmstadt, Germany), NSE (13219-H08E-SIB-50 ug, Stratech, Ely, UK), GFAP (C227-10 ug, Generon, Slough, UK), IL-18 (CSB-YP614514HU, Antibodies.com, Cambridge, UK), NFL (pro-2584-10 ug, Generon), and UCHL1 (UC1-H5140-50 ug, Generon). Animal derived biomarkers included the galactocerebroside (C4905-10MG, Merck), sphingomyelin (1051-25 mg, Cambridge Bioscience), ganglioside (860053P-10MG, Scientific Laboratory Supplies, Nottingham, UK), sulfatide (56-1085-7-LAO-25 mg, Stratech), and cardiolipin (C0563-10MG, Merck). Synthetically produced biomarkers included the NAA (00920-5G, Merck), cholesterol (C8667-1G, Generon), glucose (CAY23733-50, Cambridge Bioscience), D-serine (A11353.06, VWR International, Lutterworth, UK), myo-inositol (A13586.22, VWR International), and GSH (G4251-300MG, Merck)

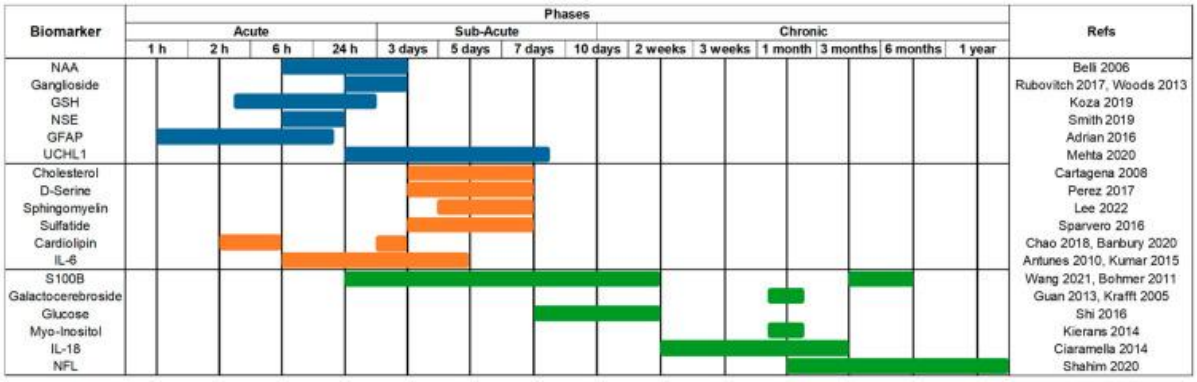

Figure 3-1 - Schematic timeline overview of the TBI biomarkers and their phases, acute (blue), sub-acute (orange), and chronic (green), during which each biomarker has been reported to either increase, persist, or decline post-injury [2, 7, 39, 43, 45-63]. Biomarkers: N-Acetyl-L-aspartic acid (NAA), Glutathione (GSH), Neuron-Specific Enolase (NSE), Glial fibrillary acidic protein (GFAP), Ubiquitin carboxyl-terminal hydrolase isozyme L1 (UCHL1), Interleukin-6 (IL-6), Interleukin-18 (IL-18), and Neurofilament light chain (NFL).

3.3.3 Raman Spectroscopy

Raman measurements were carried out using the InVia Qontor confocal Raman system (Renishaw) equipped with four excitation lasers, which were adjusted for optimal throughput, fluorescence control, and sensitivity. Optical measurements were carried out with a specially adapted research-grade microscope (Leica [Wetzlar, Germany] DM 2700M) equipped with an incoherent white light source, allowing confocal measurements with a 2.0 µm depth resolution. Four excitation wavelengths of 514, 633, 785, and 830 nm were employed in this study to enable a breadth of spectral profiles. To avoid photochemical effects in the spectra, sample damage or degradation, extended spectral Raman scans were acquired over a range of 200–3200 cm^{-1}, 50× objective lens, and an acquisition time of 10 s with 5 accumulations. All Raman spectra were collected at ambient temperature.

3.3.4 Data Analysis

The acquired Raman spectra were collected using Renishaw WiRE 5.2 (Renishaw Plc, Wotton-under-Edge, UK) and cosmic rays were removed during baseline subtraction with a polynomial order of 11 and a 1.5 noise tolerance. Extended spectra were subsequently averaged per biomarker, taking into account the laser excitation wavelength as well as the raw and reconstituted states. The Peak Pick tool (WiRE 5.2) was utilised across the x-axis range to select the six characteristic bands for each assignment, while the slope

detection method was utilised with 15 smooth points and a peak threshold height of 500 counts.

3.4 Results and Discussion

The Raman spectrum is commonly referred to in terms of discrete regions, the low wavenumber region (100–200 cm^{-1}), the fingerprint region (500–2000 cm^{-1}), and the high wavenumber region (2000–4000 cm^{-1}) [64, 65]. In this study, Raman spectra were collected in the extended spectral regions of 200–3200 cm^{-1}, however, only the fingerprint region from 200 to 1800 cm^{-1} was used where the main bands of interest were identified. The biomarkers studied, based on references to TBIs in the literature, were classified within three main injury phases as acute, sub-acute, and chronic (Figure 3-1), the corresponding detailed information for each biomarker, including the accessible biofluid source, physiological function, post-TBI response, and the role they play in head injuries along with the associated phase behaviour are summarised in Table 3-1. Spectral profiles for each biomarker were acquired for both solids as well as of the solute forms, with the former inherently yielding better resolved, sharper Raman peaks. It is well-established that Raman band frequencies are more complex and shifted in the liquid phase, relative to the solid, due to the higher variability of the intermolecular forces and molecular collisions in the liquid phase, which shift the frequencies of intra-molecular vibrations and broaden the bands, relative to the highly regular and stable solid structures. Since the behaviour of biomarkers in aqueous solutions is of particular importance, given that

an aqueous medium is a natural environment for biological molecules, we have identified the spectral signatures of the reconstituted solutions of TBI biomarkers classified by injury state (Figure 3-2, Figure 3-3, Figure 3-4).

Table 3-1 - Overview of the studied TBI biomarker cohort with the corresponding physiological significance. Source refers to the biofluid in which the biomarker has been analysed in the literature. N-Acetyl-L-aspartic acid (NAA); Glutathione (GSH); Neuron-Specific Enolase (NSE); Glial fibrillary acidic protein (GFAP); Ubiquitin carboxyl-terminal hydrolase isozyme L1 (UCHL1); Inter-leukin-6 (IL-6); Interleukin-18 (IL-18); and Neurofilament light chain (NFL). Increase in concentration (↑), decrease in concentration (↓).

Biomarker	Source	Physiological Function	TBI Role	TBI Response	Reference
NAA	Blood CSF	Synthesised in neurons, specific to the nervous system. Has roles in maintaining myelin lipid synthesis and in promoting neuronal mitochondria ATP production.	Marks injury type. Depletion in grey matter and white matter represent neuronal loss and axonal damage, respectively. Rate of replenishment is inversely proportional to injury severity.	↓	[32, 66, 67]
Ganglioside	Serum CSF Brain	Cellular signalling, protein, and ion channel modulator. Main carrier of sialic acid in the nervous system, improving intercellular communications.	Functional disruption causes neurodegeneration, cellular dysfunctions and promotes disease pathogenesis.	↑	[68]

Biomarker	Source	Physiological Function	TBI Role	TBI Response	Reference
GSH	Blood CSF	Essential antioxidant, converted from its reduced state (GSH) to its oxidised form to regulate free radicals from the brain.	GSH depletion coupled with neuroinflammation leads to build-up of free radicals, further damaging the brain and neurons.	↓	[60, 69]
NSE	CSF	Tissue-specific cytosol-based enzymes, upon stimulation they translocate to the cell surface to act as a plasminogen receptors.	The degree of damage is directly correlated to the amount of NSE expressed.	↑	[70]
GFAP	Blood CSF	Intermediate filament III protein. Maintains glial cytoskeleton structure, neighbouring neurons, and blood-brain barrier (BBB).	Post-trauma, astroglial cells undergo astrogliosis, causing cellular hypertrophy and increased GFAP expression. Excess GFAP can cause glial scars in brain tissue which delays axon regeneration.	↑	[71-73]
UCHL1	Blood CSF	A brain-specific enzyme features in the ubiquitin-proteasome	Selectively increases upon axonal damage, utilised to	↑	[74, 75]

Biomarker	Source	Physiological Function	TBI Role	TBI Response	Reference
		pathway to maintain axonal protein integrity. Regulates axonal transport, structure, and synapsis.	remove damaged and defective proteins from axons.		
Cholesterol	CSF Brain Serum	Key component of the cellular membrane, maintaining structure and fluidity. Cholesterol and phospholipids are transported to nerve cells for repair, upkeep and to promote neurite proliferation.	Increased cholesterol is in proportion to cellular damage. Removing excess cholesterol has an anti-inflammatory effect. Dysregulation of brain cholesterol negatively affects neuronal and glial function. Cholesterol builds up from dysregulation causes cellular toxicity.	↑	[63, 76-79]
D-Serine	Brain CSF Blood	*α*-amino acid, abundant in the brain. Binds to N-methyl-d-aspartate (NMDA) and δ_2 glutamate receptors to contribute to	Reactive glial cells become D-Serine synthesisers under inflammatory conditions, causing NMDA	↑	[80]

Biomarker	Source	Physiological Function	TBI Role	TBI Response	Reference
		learning and memory function.	receptor hyperactivation, and leading to hippocampal synaptic damage.		
Sphingomyelin	CSF Blood	Vital in regulation of cellular growth rate, differentiation, and death in the central nervous system. Supports myelination in the brain, and aids in cognitive maturation and regulation of inflammatory responses.	Increased levels are reported in the hippocampus over 12 months after TBI, contributing to neurological disease pathogenesis. Breakdown products regulate the sphingomyelin cycle which inhibits protein kinase c, regulating neuronal signal transduction and function.	↑	[81-85]
Sulfatides	Brain CSF Serum	Abundant in myelin sheath and myelinating cells. Negatively regulates and improves oligodendrocyte differentiation and survival.	Effects functional properties of the membrane, and dysregulation of sulfatides can lead to seizures.	↓	[86]

Biomarker	Source	Physiological Function	TBI Role	TBI Response	Reference
		Maintains myelin and axonal-glial signalling.			
Cardiolipin	Inner Mitochondrial Membrane	Involved in regulating mitochondrial metabolism. The structural component of mitochondrial membranes regulates protein and enzyme activity central to mitochondrial function.	Damaged mitochondria trigger neuronal death when oxidised. Cardiolipin acts as an elimination signal for damaged mitochondria, thus limiting neuronal damage and preserving cognitive functions.	↑	[87-89]
IL-6	CSF Serum Blood	Pleiotropic cytokine with operations in immunity regulation, regeneration processes, neural functions, and cardiovascular protective mechanisms.	Usually undetectable in healthy brain parenchyma but present within an hour following TBI. Upregulated production following trauma from inflammatory cascades to salvage neurons. Sustained inflammation is ultimately damaging.	↑	[51, 90-92]

Biomarker	Source	Physiological Function	TBI Role	TBI Response	Reference
S100B	Blood CSF Brain	Calcium-binding protein involved in long-term synaptic plasticity modulation, cellular growth and structure, calcium concentration maintenance, and energy metabolism. Mitigates mitochondrial failure through calcium modulation.	Overexpression leads to disrupted calcium homeostasis. Increased levels indicate structural damage and cellular death.	↑	[93, 94]
Galactocerebroside	CSF Brain	Major lipid component in the brain, which maintains myelin sheath structure and stability. Important for development of normal myelin in the central nervous system.	Galactosylceridase dysfunction prevents Galactocerebroside from degrading, instead it accumulates in globoid cells in the brain, leading to white matter diseases.	↑	[54, 95, 96]
Glucose	Blood	Main energy source to the brain, used for action potential and postsynaptic potential generation.	Early low glucose levels and low lactate/glucose ratio post-TBI are associated with poor	↓	[97-99]

Biomarker	Source	Physiological Function	TBI Role	TBI Response	Reference
		Synthesises BBB-regulated neuroactive compounds and sustains brain homeostasis.	outcomes. Not associated with ischemia.		
Myo-Inositol	CSF Blood	Regulates glial and neuronal activity and participates in intracellular signalling pathways. Regulates intracellular [Ca^{2+}] and membrane permeability.	Increased levels are correlated to glial proliferation, increased rate of membrane turnover, and myelin sheath damage. Correlated to astrogliosis and dysregulation of cellular osmotic functions.	↑	[100-103]
IL-18	CSF	Inducer of inflammatory cytokines; synthesised as an inactive precursor in microglia and activated by caspase-1 in a forward loop.	Has roles in neuroinflammation and neurodegeneration. Induces respiratory burst and degranulation of polymorphonuclear leukocytes resulting in a release of neurotoxic enzymes.	↑	[104, 105]
NFL	CSF Blood	Integral in maintaining	NFL levels rapidly	↑	[106-108]

Biomarker	Source	Physiological Function	TBI Role	TBI Response	Reference
		axonal cytoskeleton through radial growth. Larger myelinated axons result in more NFL, leading to faster conduction speed.	increase following trauma to account for damaged axons and NFL is released into the interstitial space and integrated into CSF. Indicates significant axonal damage and progression rate of disease.		

3.4.1 Acute Phase

Acute TBI biomarkers have been shown to be applicable in triaging, diagnosing, and eliminating the presence of TBI at the earliest stages (i.e., golden-hour biomarkers) and are thus particularly important for the development of diagnostic point-of-care modalities as well as intervention for TBI [109, 110]. Therefore, biochemical changes and concentration variations in biomarkers are reflected through the spectral information when comparing healthy control cohorts to acute, sub-acute, and chronic phases, which are vital for PoC diagnostics and injury monitoring. Representative average spectra of acute TBI biomarkers are presented in Figure 3-2 alongside peak assignment provided in Table 3-2. Each biomarker produced unique and distinctive spectral features. Strong

characteristic peaks of NAA are found in the 949–957 cm^{-1} and 987–992 cm^{-1} regions for the four-excitation laser used (Figure 3-2**A**), with the main peaks being associated with the C-N stretching as well as CH_2-CH wagging [111]. NAA is an amino acid derivative located in neurons where the decreasing levels are proportional to neuronal loss and axonal damage [68] and, thus, a decrease in characteristic Raman peak intensity can be an important indicator following brain trauma. The most intense peaks of ganglioside, a sialic acid-bearing glycosphingolipid [59], are detected at 1297–1298 cm^{-1} and 1437–1442 cm^{-1} (Figure 3-2**B**). The bands at 1297 and 1440 cm^{-1} are assigned to bending and twisting of CH_2 bonds [112], which optimally could be employed relative to other characteristic peaks of ganglioside post-TBI [113]. These peak intensities have been reported to decrease in counts in tandem with cell loss [113], in contrast to the other characteristic peaks of ganglioside (Table 3-2), which are typically shown to increase in response to neurodegeneration and cellular dysfunction (Table 3-1) [68]. GSH, a non-enzymatic antioxidant tripeptide present in cells to protect membranes from oxidative damage [114], exhibits the most intense peaks located at 1420–1424 cm^{-1} and 1660–1662 cm^{-1} (Figure 3-2**C**), attributed to the -CH_2 bending mode of proteins [115], and symmetrical stretching of the carboxylic acid COO^- [116], and the Amide I region, indicative of amino acids [117], respectively. Post-TBI apoptosis could lead to GSH depletion and thus a reduction in characteristic peak intensity which, when coupled with neuroinflammation, results in TBI secondary injury due to free radical build-up further damaging neurons and the brain (Table 3-1) [69]. NSE is a glycolytic tissue-specific enzyme associated with neuronal damage and post-traumatic inflammation [40, 62], increasing in expression with injury severity [70]. The strongest peak for NSE (Figure 3-2**D**) at 875–877 cm^{-1} at all four

employed excitation wavelengths is assigned to the stretching of C-C bonds and the asymmetric stretching of C-N bonds [54, 118] associated with phenylalanine. A secondary peak of interest at 1077–1082 cm^{-1} is attributed to the stretching of C-O and C-C bonds [119] along with the twisting of CH_2 bonds [120]. NSE is plausible for monitoring post-TBI changes since it is only expressed in a direct correlation to the degree of damage and translocated from the cytosol to cell surface upon stimulation, acting as a plasminogen receptor [61, 70, 121].

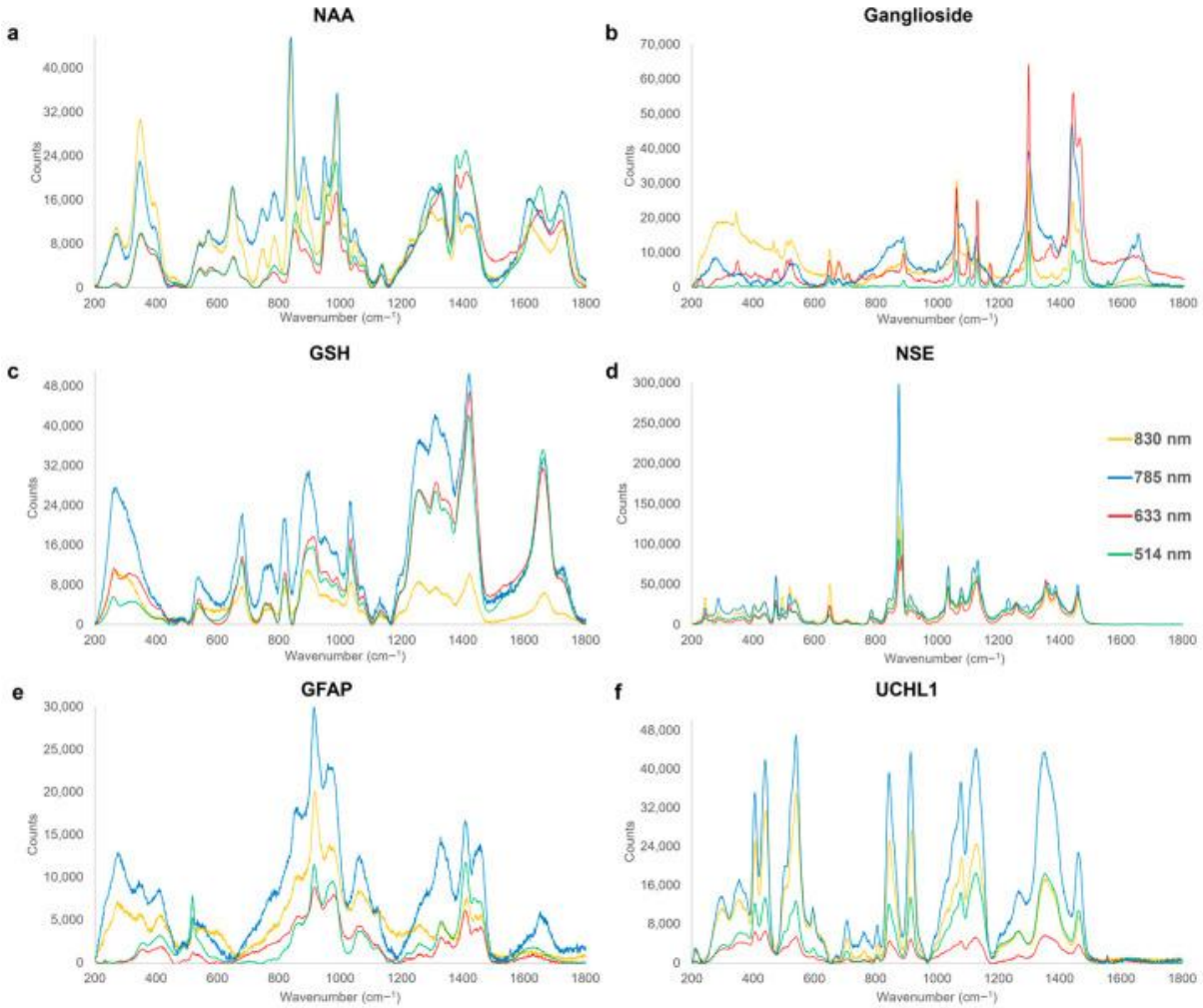

Figure 3-2 - Characteristic Raman spectra fingerprints of acute-phase TBI biomarkers, acquired at excitation wavelengths of 514 nm (green), 633 nm (red), 785 nm (blue), and 830 nm (yellow). Significant Raman peak assignments for each are summarized in Table . N-Acetyl-L-aspartic acid

(NAA); Glutathione (GSH); Neuron-Specific Enolase (NSE); Glial fibrillary acidic protein (GFAP); and Ubiquitin carboxyl-terminal hydrolase isozyme L1 (UCHL1).

GFAP is a structural filament protein of astrocytes [13], with its levels known to increase in response to astrogliosis post-trauma, as discussed in Table 3-1. The most intense detected spectral bands are found in the region of 914–918 cm^{-1} (Figure 3-2**E**), assigned to C-N stretching [118], and asymmetric vibration of the pyranose ring [111], also present in the UCHL1 spectrum (Figure 3-2**F**), increasing in response to TBI, and thus might collectively be an important candidate peak of interest for TBI Raman-based diagnostics.

Table 3-2 - Acute TBI phase associated Raman bands and their assignments. vib = vibration; *v* = stretching; *δ* = bending; *τ* = twisting; *ρ* = rocking; *ω* = wagging; *s* = symmetric; *a* = anti-symmetric; *arom* = aromatic; *skel* = skeletal.

Wavenumber (cm^{-1})	**Assignment**	**Origin**	**Reference**
347–353	v_{skel}(C-C)	NAA	[111]
473–475	*v*(S-S)	NSE	[124]
518–521	C(OH), *Ring deformation*	GFAP	[111, 118]
647–651	*v*(C-S), *τ*(C-C), *Ring breathing*	NAA, NSE, Ganglioside	[118, 125, 126]
679–682	*v*(C-S)	GSH	[118]
705–708	*Ring deformation*	UCHL1	[118]
806	v_s(C-N-C)	UCHL1	[111]
819–821	CH *deformation*	GSH	[111]
843–845	*δ*(H(C-O-H)), *ρ*(H(C-O-H))	UCHL1	[118]
875–877	*v*(C-C), v_a(C-N)	NSE	[54, 118]
889–891	v_{arom}(C-O), *v*(C-C), *ω*(CH_2)	Ganglioside	[127-129]
914–918	*v*(C-N), vib_a(*pyranose ring)*	GFAP, UCHL1	[111, 118]
949–957	*v*(C-N)	NAA	[111]
974–980	v_a(C-C), *ρ*(CH_2)	GFAP	[118, 130]

Wavenumber (cm^{-1})	Assignment	Origin	Reference
987–992	ν(C-N), ω(CH_2- CH)	NAA	[111]
1031–1037	δ(C-H), ν(C-C), ν_a(C-C-N^+)	GSH, NSE	[131, 132]
1060–1068	ν(C-O), ν_{skel}(C-C), τ(NH_2)	Ganglioside, GFAP	[118, 123, 133]
1077–1082	ν(C-O), ν(C-C), τ(CH_2)	NSE, UCHL1	[119, 120]
1127–1130	ν(C-N), ν(C-C)	Ganglioside, UCHL1	[134, 135]
1131–1138	ν(C-C)	NAA	[136]
1297–1298	τ(CH_2)	Ganglioside	[113]
1311–1315	δ(C-H)	GSH	[137]
1328–1336	ω(CH_2), τ(CH_2)	GFAP	[118]
1352–1354	τ(CH_2)	UCHL1	[120]
1378–1383	ν_s(COO^-)	NAA	[138]
1408–1410	δ(C-H), ν_s(COO^-)	GFAP	[118, 122]
1420–1424	δ(CH_2), ν_s(COO^-), ν_s(CO_2)	GSH	[115, 116, 137]
1437–1442	δ(CH_2), τ(CH_2)	Ganglioside	[112]
1458–1460	δ(CH_2)	NSE	[139]
1660–1662	ν(C-N(H)-C=O), ν(C=C)	GSH	[111]

A further sharp peak present in the 1408–1410 cm^{-1} region is assigned to the bending of C-H bonds and symmetrical stretching of COO^- bonds [118, 122], along with a wider band at 1060–1068 cm^{-1}, assigned to the skeletal stretching of C-C bonds and indicative of changes in protein levels [123]. GFAP has been shown to increase after brain trauma because of reactive astrogliosis. Its overexpression, causing scarring of the brain, can be used to distinguish between the healthy and damaged tissue, giving an indication of the amount of damage, and delaying the axonal regeneration [72].

UCHL1, a cytoplasmic enzyme found in neurons, is selectively increased following axonal trauma to remove damaged and defective proteins from axons [74, 140]. Unfortunately,

the glycerol-environment buffer of this protein dominates the spectral fingerprint with aliphatic chains [120, 141] and, therefore, only smaller peaks in the 600–800 cm^{-1} region are identified to be unique to the UCHL1 marker (Figure 3-2**F**) with the 705–708 cm^{-1} band assigned to ring deformation [118], and the 806 cm^{-1} peak assigned to the symmetrical stretching of C-N-C bonds present in amino acids [111].

3.4.2 Sub-Acute Phase

Detection of sub-acute TBI biomarkers is vital for multiple-level diagnostics when the patient is admitted to hospital and a complementary rapid diagnostic technique is required alongside structural neuroimaging. This lays the platform for not only enabling timely TBI management at ED, A&E, etc. for early neuroprotective measures but also for the correct transfer to the most appropriate neurological facility. Rapid diagnosis in the early clinical phase will lay a platform for a range of improvements in personalised medicine and management, reduce strain on the healthcare system, and enable better-quality post-neurotraumatic care. Similarly, in the military context, where neurosurgical support is not routinely deployed and TBI management often requires evacuation, the ability to diagnose and assess TBI severity pre-hospital would avoid unnecessary strategic evacuation and maintain operational effectiveness. Representative average spectra of sub-acute TBI solute-form biomarkers are shown in Figure 3-3 with the corresponding peak assignments summarised in Table 3-3.

Cholesterol's sterol-centred structure presents a unique and large number of intense peaks (Figure 3-3**A**), including the 700 cm^{-1} band of the in-plane deformation of its B ring [142], as well as a sharp peak at 1673 cm^{-1}, assigned to the B ring C=C stretching [143]. Cholesterol is structurally important in the cellular membrane with its increases following TBI proportionally related to the cellular damage [144]. As a response to neuro-inflammation, apolipoprotein E transports cholesterol and phospholipids by forming a protein–lipid complex to damaged nerve cells to assist the cellular damage as well as to increase neurite proliferation [76, 77]; whilst cholesterol removal is associated with the anti-inflammatory response [63, 78]. If left unchecked, the dysregulation of cholesterol in the brain can negatively affect neuronal and glial functions and in due course, leading to cellular toxicity [79].

D-serine is a non-essential polar amino acid, which serves as a precursor to purines and pyrimidines, and is an important neurotransmitter [145]. The characteristic fingerprint of D-serine (Figure 3-3**B**) exhibits strong peaks in the range of 917–923 cm^{-1}, attributed to its C-C backbone stretching [139], as well as at 1327–1336 cm^{-1} from the twisting of its CH_2 groups [118]. Serine is a co-ligand activator of NMDA receptors and of δ2 glutamate receptors, which have regulatory roles in synaptic plasticity and long-term potentiation [80]. Increases in serine following TBI is caused by reactive glial cells, which under inflammatory conditions turn into D-serine synthesisers. An increase in D-serine leads to hyperactivation of NMDA receptors, which damages hippocampal synapsis and is known to disrupt learning and memory formation [45, 80]. Blocking D-serine production under inflammatory conditions has been related to improved outcome following brain trauma [80].

Sphingomyelin can be spectrally identified by a characteristic set of peaks in the range of 717–720 cm^{-1} and 1295–1299 cm^{-1}, due to the symmetric stretching of C-N and the twisting of CH_2, respectively [113, 118] (Figure 3-4**C**). Sphingomyelin is a prominent sphingolipid, found in the plasma membrane with a distribution ratio correlating specifically with cholesterol for suitable membrane function [146]. This lipid plays vital roles within the CNS in terms of cellular growth, differentiation, and death [81]. In the brain, sphingomyelin is also associated with improved cognitive maturation, brain myelination, and regulation of inflammatory responses [82, 147]. Levels of sphingomyelin have been shown to increase following TBIs for over 12 months, rendering it a neuro-marker for both sub-acute as well as chronic phases [83]. Disruption of sphingomyelin metabolism is known to dysregulate the mitochondrial energy pathways, slowing the healing process and increasing the risk of secondary injuries, contributing to the overall TBI pathogenesis [148].

Sulfatides are a class of sulfo-lipids, abundantly present in brain tissue and are a main feature in myelin sheath and within myelinating cells [86]. Spectral characteristic fingerprints of sulfatides are shown in Figure 3-4**D**. These representative peaks include the stretching of the C-OH from the sulphated pyranose ring and C-C backbone along with the CH_2 wagging in the range of 888–893 cm^{-1} [127-129], with the anti-symmetric stretching of the SO_4 group identified at 1107–1111 cm^{-1} [149]. Sulfatides, directly derived from galactocerebrosides, constitute promising candidate TBI biomarkers due to their roles in protein trafficking, neuronal transduction, and negative regulation in oligodendrocyte differentiation [150]. Following TBI, sulfatide levels decrease in the brain subsequently, allowing the oligodendrocyte production to occur at a higher rate, thus

providing axonal myelin wrapping with improved action potential and transmission. However, due to the functional role of sulfatides within the membrane, the dysregulation can lead to physiological responses such as seizures [86].

Cardiolipin, a mitochondrial-specific phospholipid, which signals damaged mitochondria [87] (Figure 3-4**E**), is found to exhibit dominant PO_4 vibrations at 959–964 cm^{-1} and C-O stretching from the linoleic acid groups in the range of 1266–1268 cm^{-1} [151, 152]. Cardiolipin is known to be central to mitochondrial function, with roles in both regulation of metabolism and membrane structure maintenance [87], with damaged and dysregulated mitochondria triggering neuronal death [88, 89]. Cardiolipin is externalised from the inner mitochondrial membrane to signal damaged mitochondria and promote mitophagy, ultimately limiting further neuronal damage and retaining cognitive functions [89], resulting in increases in its concentration linked to the extent of mitochondrial damage [88, 89].

IL-6, an inflammatory cytokine, yields a distinctive spectral signature (Figure 3-4**F**) with peptide bonds bending within the protein detected in the 520–525 cm^{-1} region [111], and a sharp peak at 959–964 cm^{-1}, associated with the symmetric stretching of the C-N-C bonds of proteins [111]. The pleiotropic IL-6 is involved in immunity, regeneration, and neural functions [92]. Whilst in healthy brain tissue it is not typically detectable, it has been found to be present within an hour of brain injury, making it a reliable marker of TBI-induced damage [90, 91]. IL-6 is further upregulated during inflammatory cascades to help healing including the salvation of neurons; however, a prolonged detection of this

biomarker is indicative of sustained inflammation, resulting in more damage over healing [89].

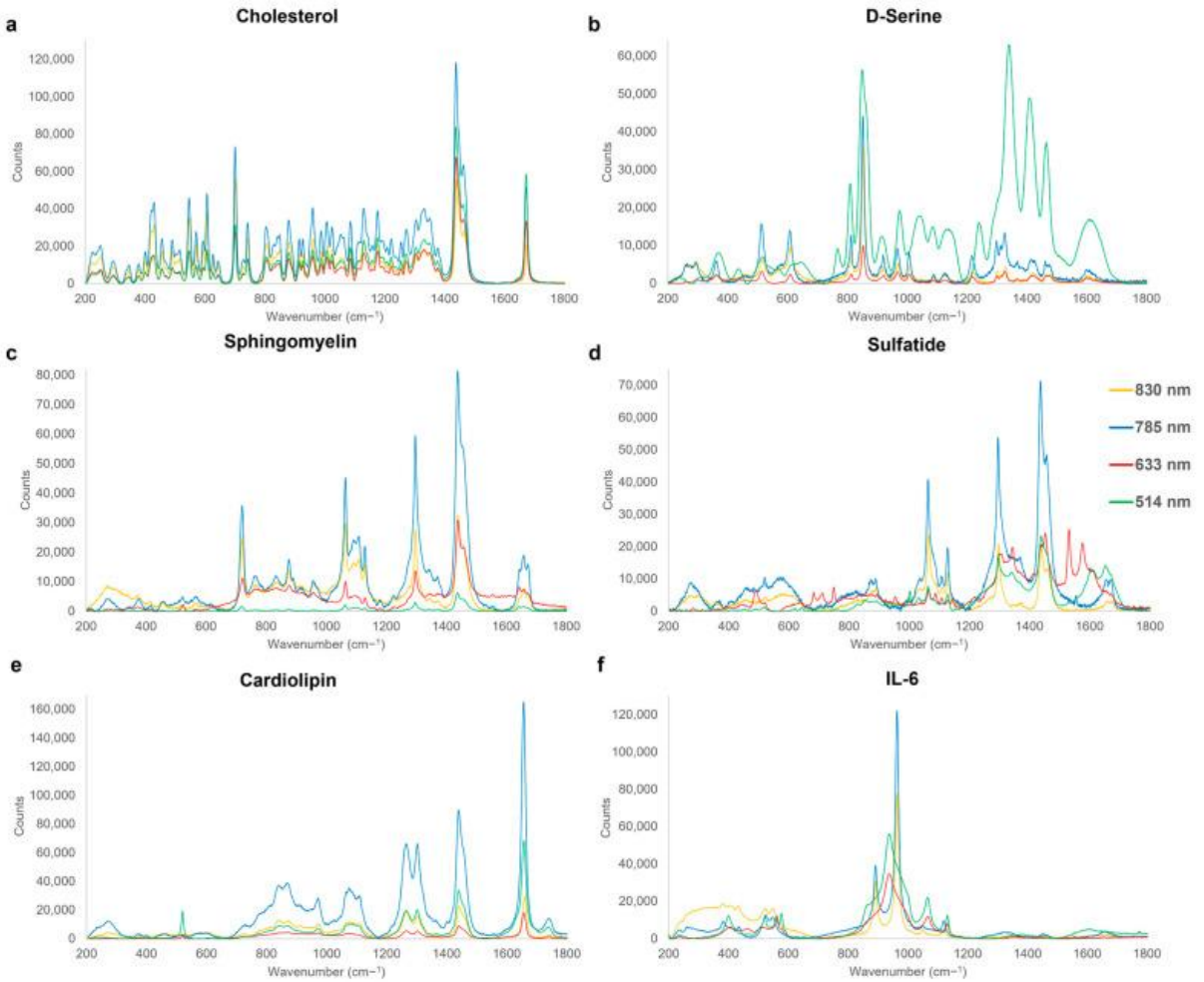

Figure 3-3 - Characteristic Raman spectra fingerprints of sub-acute-phase TBI biomarkers, acquired at excitation wavelengths of 514 nm (green), 633 nm (red), 785 nm (blue), and 830 nm (yellow). Significant Raman peak assignments for each are summarised in Table 3-3.

Table 3-3 - Peak assignments of significant peaks present in the sub-acute TBI biomarker phase. vib = vibration; ν = stretching, δ = bending, τ = twisting, ρ = rocking, ω = wagging, *s* = symmetric, *a* = anti-symmetric, *arom* = aromatic, *skel* = skeletal.

Wavenumber (cm^{-1})	**Assignment**	**Origin**	**References**
512–516	$\rho(COO^-)$	D-Serine	[139]
520–525	δ(N-C=O)	IL-6	[111]
549	δ(N-C-S)	IL-6	[111]
561	-OH *out of plane deformation*	IL-6	[111]
700–702	*In-plane deformation of B ring*	Cholesterol	[142]
717–720	ν_s(C-N)	Sphingomyelin	[118]
809–815	ν(C-C)	D-Serine	[111]
850–854	$\rho(CH_2)$	D-Serine	[139]
888–893	$\nu_{arom}(C\text{-}O)_4$, ν(C-C), $\omega(CH_2)$	Sulfatide	[127-129]
917–923	ν(C-C)	D-Serine	[139]
959–964	*vib*(PO_4), ν_s(C-N-C), δ(C-H)	Cholesterol, IL-6, Cardiolipin	[111, 151]
970–974	ν(C-N)	D-Serine	[139]
1062–1067	ν(C-O), ν(C-C), $\tau(NH_2)$	Sphingomyelin, Sulfatide, IL-6	[118, 123, 133]
1107–1111	$\nu_a(SO_4)$, ν(C-N), ν(C-C), ν(C-OH),	Sulfatide, Cardiolipin	[22, 149]
1127–1130	ν(C-N), ν(C-C), ν_{skel}(C-C)	Sphingomyelin, Sulfatide, IL-6	[134, 135]
1176–1179	ν_{skel}(C-C)	Cholesterol	[143]
1266–1268	ν(C –O)	Cardiolipin	[152]
1295–1299	$\tau(CH_2)$	Sphingomyelin, Sulfatide	[113]
1302–1304	$\tau(CH_2)$	Cardiolipin	[142]
1327–1336	$\omega(CH_2)$, $\tau(CH_2)$	Cholesterol, D-Serine	[118]
1436–1441	$\delta(CH_2)$, $\tau(CH_2)$, $\nu(CH_2/CH_3)$	Cholesterol, Sphingomyelin, Sulfatide, Cardiolipin	[112, 153]

Wavenumber (cm^{-1})	Assignment	Origin	References
1656–1660	*v*(C=O), *v*(C=C)	Sphingomyelin, Cardiolipin	[117, 154]
1672–1674	*v*(C=C)	Cholesterol	[143]

3.4.3 Chronic Phase

Chronic TBI biomarkers span a larger timeframe and are particularly important in cases of undiagnosed mTBI, frequently causing patients long-term effects. Certain chronic biomarkers are expressed in the early phase, during the acute phase, and continue to be expressed in the longer-term [39, 52, 55]. The chosen representative chronic biomarkers (Figure 3-1) provide important underpinning spectral fingerprints, contributing towards ongoing investigations on chronic biomarkers and their post-TBI mechanisms and, once confirmed, the emerging findings would enable the detected biomarker levels at late time points to be used to identify TBI survivors who are at high risk of progressive neurological damage, triggered by their initial TBI. Rapid detection and an in-depth understanding of chronic TBI biomarkers would aid the development of TBI therapeutics and enable in situ tracking of TBI pathology and injury evolution at hospital. Real-time spectroscopy for TBI monitoring would further improve target management and understanding of injury heterogeneity, evolution, penetrance of pharmacological agents, identify novel targets for intervention, and could lead to the development of modalities for tactful therapeutic modifying therapies in TBIs. Representative average spectra of chronic, TBI, solute form biomarkers are shown in Figure 3-4 with the corresponding peak assignments summarised in Table 3-4.

S100B is a calcium-binding protein expressed in astrocytes and is the first brain biomarker to be recognised and utilised within clinical practice guidelines [13, 155]. S100B, known to be neuroprotective and neurotrophic, is regarded as a suitable marker due to its involvement in the modulation of long-term synaptic plasticity and energy metabolism by maintaining calcium concentration and ensuring correct mitochondrial function [93, 94]. Characteristic dominant spectral peaks are identified for S100B throughout the entire 200–1800 cm^{-1} region (Figure 3-4 and Table 3-4). The most intense bands are at 936–937 cm^{-1}, assigned to stretching of the C-C bond of proline and valine [156], and at 1002–1004 cm^{-1}, due to aromatic phenyl breathing of the C-C bond of the phenylalanine [118, 157]. Post-TBI, increased S100B levels accompany structural damage and cellular death [94]. This would result in higher intensity of identified Raman peaks, posing it as a promising marker for Raman-based neuro-diagnostics. Physiologically, the implication of increased S100B levels disrupts the correct calcium homeostasis, leading to mitochondrial failures and damaging long-term hippocampal potentiation [93, 94].

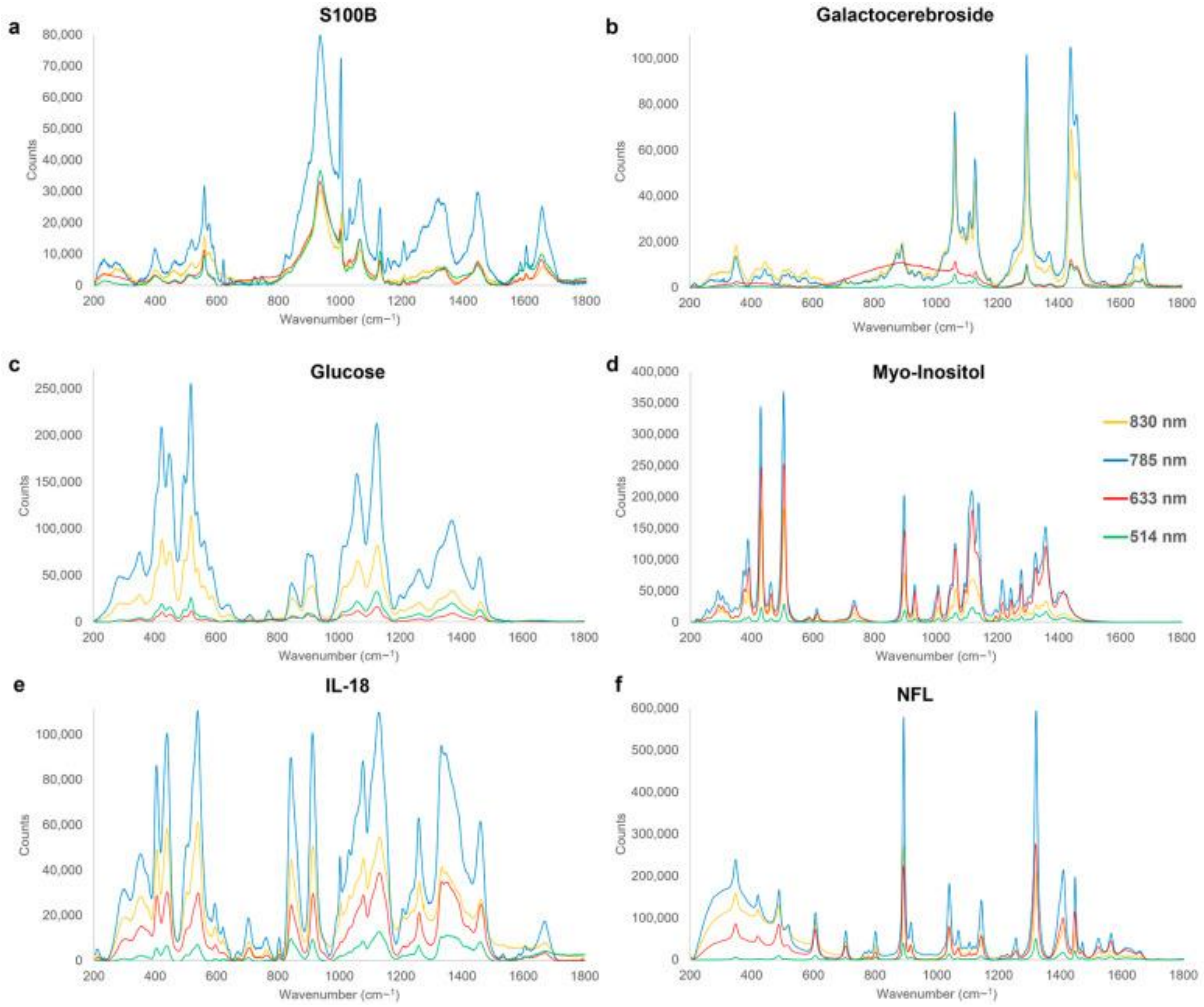

Figure 3-4 - Characteristic Raman spectra fingerprints of chronic-phase TBI biomarkers, acquired at excitation wavelengths of 514 nm (green), 633 nm (red), 785 nm (blue), and 830 nm (yellow). Significant Raman peak assignments for each are summarised in Table 3-4.

Galactocerebrosides are a major glycolipid of the myelin within the CNS and the most abundant glycolipid component of myelin [158, 159]. Figure 3-4**B** exhibits dominant spectral peaks in the fingerprint spectrum, particularly, above the 1000 cm^{-1} region. A characteristic peak in the 1128–1133 cm^{-1} range is assigned to the C-N stretching of the amine bond in the acyl chain [118], and the C-C bond skeletal stretching of the acyl backbone common to lipids [135], and further in the 1295–1298 cm^{-1} region, assigned to

the twisting of CH_2 bonds of lipids [113]. This biomarker accumulates in the brain in globoid cells when there is galactosylcerimidase dysfunction, preventing galactocerebrosides from degrading, potentially leading to a long-term white matter disease (Table 3-1).

Overall, peaks in the range of 1295–1299 cm^{-1} are also present in the spectra of sphingomyelin, sulfatide and ganglioside, creating a potential band of interest for the detection of chronic TBI biomarkers via Raman spectroscopy as well as to assess post-TBI recovery and response to interventions.

Glucose is the predominant and preferred energy source of the mammalian brain, with levels present indicating metabolism in astrocytes [55, 99]. Overall, biomarkers in the chronic phase had a larger number of characteristic peaks identified in the lower wavenumber and fingerprint regions 200–800 cm^{-1} than the earlier phases with two intense bands determined from the glucose spectrum (Figure 3-4**C**) in the 422–424 and 517–520 cm^{-1} regions, with the former attributed to the in-plane aromatic bending of the C-OH bond [111] and the latter assigned to C-OH bond deformation (Table 3-4) [111]. Decreases in glucose levels post-TBI have been shown to be associated with poor outcomes due to the indication of an increased need for energy for tissue repair. Glucose metabolism post-trauma has also been shown to lead to an increase in anaerobic glycolysis; however, this has been specifically proven to be a result of ischemia. Furthermore, glucose levels can be compared to other metabolites downstream in the glycolytic pathway such as the ratio of pyruvate (aerobic product) to lactate (anaerobic product). A larger ratio typically correlates to more glycolytic than mitochondrial activity

and is associated with worse outcomes, due to an indication that neurons might be too damaged to take up lactate for the TCA cycle [99].

Myo-inositol, a sugar derivative, has been reported to increase in proportion with TBI severity [160], and in correlation with glial proliferation, membrane turnover, and myelin sheath damage (Table 3-1). Spectral peaks of myo-inositol are highly consistent across the four excitation wavelengths used (Figure 3-4**D**) with the most intense bands at 504–506 cm^{-1}, assigned to out-of-plane deformation of -OH bonds and further in 1116–1121 cm^{-1} and 1217–1218 cm^{-1} regions, attributed to stretching of the C-C bonds [161-163]. Further intense peaks at 896–899 cm^{-1} and 1357–1359 cm^{-1} arise from CH bending within the aliphatic structure of myo-inositol [111]. Increases in myo-inositol levels post TBI provide a good marker of proliferation of glial cells, membrane turnover, myelin sheath damage as well as astrogliosis and cellular osmotic dysregulation [100-103].

Table 3-4 - Peak assignments of significant peaks present in the chronic TBI biomarkers phase. *v* = stretching, *δ* = bending, *τ* = twisting, *ρ* = rocking, *ω* = wagging, *s* = symmetric, *a* = anti-symmetric, *arom* = aromatic, *skel* = skeletal, Δ = ring breathing vibration.

Wavenumber (cm^{-1})	**Assignment**	**Origin**	**References**
422–424	*In-plane* δ_{arom}(C-OH)	Glucose	[111]
504–506	OH *out-of-plane deformation*	Myo-Inositol	[111]
517–520	C-OH *deformation*	Glucose	[111]
559–560	OH *out-of-plane deformation*	S100B	[164]
606–607	CCC *in-plane deformation*	NFL	[165]
804–807	v_s (C-N-C)	IL-18	[111]
842–844	*Out-of-plane* δ_{arom}(CH), ρ (H(C-O-H))	IL-18	[118, 141]
891–893	$v_s(COO^-)$, *v*(C-C)	NFL	[166, 167]
896–899	$v_{aliphatic}$(C-H)	Myo-Inositol	[111]
912–914	*v*(C-CH_3)	IL-18	[168]
936–937	*v*(C-C)	S100B	[156, 169]
1002–1004	Δ_{arom}(C-C)	S100B	[118, 170]
1008–1010	Δ_{arom}(C-C)	Myo-Inositol	[171]
1040–1041	*v*(C-CH_3), *v*(C-C), *δ*(CH)	NFL	[157, 172]
1058–1066	*v*(C-O), v_{skel}(C-C), *τ*(NH_2)	S100B, Galactocerebroside, Glucose	[123, 133]

Wavenumber (cm^{-1})	Assignment	Origin	References
1077–1080	ν(C-C), ν(C-O)	IL-18	[118, 119]
1116–1121	δ(CH), ν(C-C),	Myo-Inositol	[160, 173]
1124–1127	ν(C-C)	Glucose	[134]
1128–1133	ν_{skel}(C-C), ν(C-N)	S100B, Galactocerebroside, IL-18	[118, 134, 135]
1143–1146	ν(C-N), δ(CH)	NFL	[137, 174, 175]
1217–1218	ν(C-C)	Myo-Inositol	[162]
1259–1261	Amide III (ν(CN) δ(NH)	IL-18	[176, 177]
1295–1298	$\tau(CH_2)$	Galactocerebroside	[113]
1321–1323	δ(CH), $\tau(CH_2)$,	NFL (glycine)	[178, 179]
1357–1359	$\nu_{aliphatic}$(CH)	Myo-Inositol	[111]
1368–1371	$\delta(CH_2)$	Glucose	[180]
1409–1411	ν(C-C), δ(C-H)	NFL	[118]
1439–1441	$\nu(CH_2/CH_3)$	Galactocerebroside	[153]
1458–1464	ω(C-H), $\delta(CH_3)$, ν(C=O), ν_{arom}(C=C)	Galactocerebroside, Glucose, IL-18	[181-183]
1603–1608	$\nu_a(COO^-)$, ν(C=C), ν(C=O)	S100B	[118, 137, 184]
1672–1676	ν(C=C)	Galactocerebroside	[143]

IL-18 is a pro-inflammatory cytokine, produced by microglia and stored in the cytosol as an inactive precursor (Figure 3-4**E**) [104]. The most representative fingerprint peaks of IL-18 are identified at 1259–1261 cm^{-1}, from the amide III stretching of C-N and bending of N-H, specific to proteins [176, 177], and a sharp peak at 806 cm^{-1}, assigned to the protein specific symmetrical stretch of C-N-C bonds [111]. Following TBI, IL-18 is known to externalise and bind to the plasma membrane. Uncontrolled or dysregulated IL-18 can lead to releases of neurotoxic enzymes as well as cause chronic inflammatory diseases, whilst IL-18 inhibition has been shown to prevent further damage [105, 185].

Finally, the NFL marker has been shown to play a role in maintaining the axonal cytoskeleton [106], and although not necessarily specific to TBI, its rapid increase in CSF is indicative of a considerable axonal injury with change in its concentration correlating the severity of damage [107]. It has been therefore suggested that monitoring the NFL levels is useful for determining the extent of trauma as well as the response to any therapeutic interventions [108]. This marker exhibits a characteristic spectral fingerprint consisting of sharp peaks (Figure 3-4**F**), with the most prominent at 891–893 cm^{-1}, due to symmetrical stretching of carboxylic acids and C-C bonds [166, 167], and the 1321–1323 cm^{-1}, attributed to CH bending and CH_2 twisting modes [178, 179].

3.4.4 Laser Specific Ratio Analysis

Further to the spectral assignments of brain-specific molecular species, it is of importance to consider the identified and selected group of correlative changes in Raman peak ratios with key features of these representing quantifiable biochemical changes. The use of characteristic Raman peak ratios allows for the important information to be easily extracted from spectra (particularly, for multiplex mixtures in complex biological

environments such as the body fluid or brain tissue) to gain more information and in conjunction with multivariate analysis methods, the ratio-metric inspection and assignment of Raman spectra can be used to identify spectral changes informed by chemical and spectroscopic knowledge, showing clear systematic trends with identifiable features of biomolecules. With these key Raman peak ratios correlating with structural and quantitative biomarker information, analysis of fingerprint spectra could be performed more accurately than the individual peak changes, which could be often masked in complex biofluids. We have thus utilised dominant peak ratios of the solute state TBI biomarkers, which also allows comparison of their variation across the four excitation wavelength lasers (Figure 3-5). Characteristic peaks were selected without bias from the six assigned bands identified via the peak pick method for each studied biomarker in acute, sub-acute and chronic phases, generating the unique intensity ratios barcode in the fingerprint region. The use of the relative peak ratio intensity provides more accurate and reproducible information over the absolute Raman intensity, which differs among different Raman devices and changing conditions, and is of further importance for multivariate analysis methods often employed in conjunction with Raman spectroscopy detection and analysis [186, 187]. These peak ratios yield the combined unique spectroscopic barcode for each brain-injury marker, which could be used as a reference for rapid and accurate diagnostics of TBI in easily accessible biofluids as well as allow to easier quantify the performance of emerging spectroscopic techniques via the standard variation of the ratios between the amplitudes of two Raman bands from a given biomarker over repeated measurements (Figure 3-5).

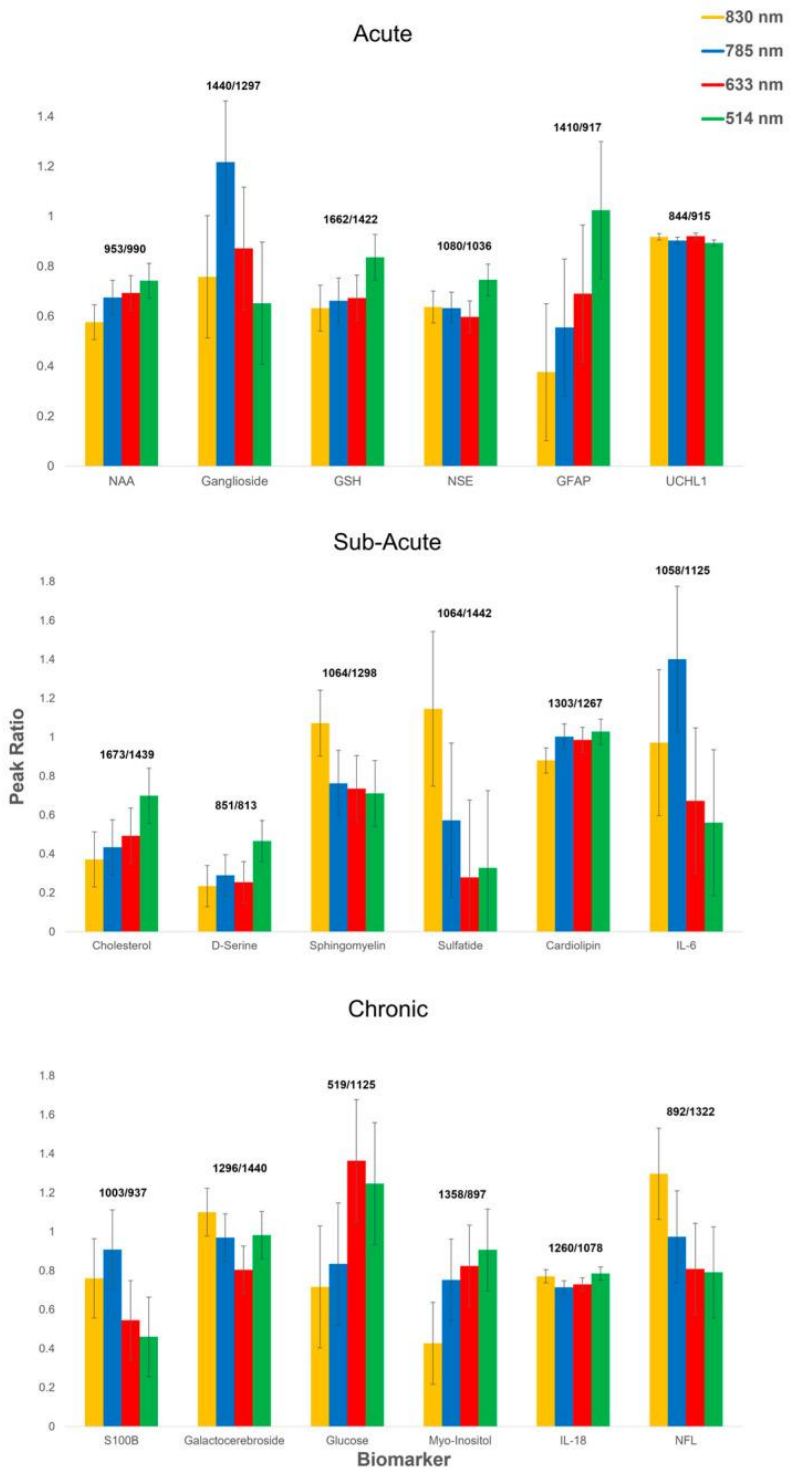

Figure 3-5 - Characteristic peak ratios identified from spectral fingerprints per each studied TBI-indicative biomarker at four excitation wavelengths of 514 nm (green), 633 nm (red), 785 nm (blue), and 830 nm (yellow). ($p < 0.0001$, one-way ANOVA). N-acetyl-L-aspartic acid (NAA); Glutathione (GSH); Neuron-specific enolase (NSE); Glial fibrillary acidic protein (GFAP); Ubiquitin carboxyl-terminal hydrolase isozyme L1 (UCHL1); Interleukin-6 (IL-6); Interleukin-18 (IL-18); and Neurofilament light chain (NFL).

For the majority of the biomarkers, within the experimental error, there was no significant difference in the identified peak ratios when varying the excitation laser except for GFAP, sulfatide and glucose (p *** < 0.0001, one-way ANOVA), which had the largest variance per phase group, with sulfatide having the highest variance (σ^2) of the entire cohort (σ^2 = 0.158). This suggests that greater consideration should be given to the choice of the Raman excitation laser to detect this biomarker, since the molecular bonds of interest are excited at varied intensity strengths depending on the laser wavelength. Conversely, UCHL1, cardiolipin, and IL-18 exhibited the lowest variance within their corresponding phase group, with the lowest overall cohort variance found to be for UCHL1 (σ^2 = 0.000164) with the highest peak agreement amongst the four excitation lasers.

3.5 Current Challenges and Future Outlook

Overall, Raman based diagnosis of TBI pathologies via biofluid detection is emerging as a promising tool for rapid point-of-care diagnostics, and with the addition of the identified molecular profiles, a simple process of a ‘spectroscopic barcode’ will ensure variation due to the presence and/or change in the level of a particular TBI-indicative biomarker and, further, therapeutic treatments and various underlying conditions will be taken into account and reduce the error in the data interpretation of the associated changes, leading towards improved diagnostic accuracy.

It is worth noting, however, that whilst important progress has been accomplished herein via Raman spectroscopy spectral fingerprints of biomarkers of TBI, several limitations and

challenges remain. Firstly, in terms of study design, biomarkers were sourced with the intention to avoid Raman-active additives such as buffers, which would impact the accuracy of the characters' fingerprint. This has, therefore, removed several candidate biomarkers identified in the literature since pure forms were not available. Furthermore, we used a varied source of human/animal TBI biomarkers, with five out of the overall eighteen investigated biomarkers derived from animals, due to limitations in availability. Whilst animal model systems frequently share similarities of specific aspects of TBIs, providing the opportunity to target specific biomarkers, animal neuromarker models, however, can occasionally recapitulate only parts of the pathology observed in human TBI [188-193]. Recognising the opportunities and limitations of translational biomarkers is therefore critical to advancing human TBI therapies. Importantly, this study aims to bridge the gap between preclinical and clinical research as well as to better demonstrate interactions between central expression of TBI pathological markers and peripheral examinations, which could subsequently be used for diagnosis and evaluation of treatment efficacy. Nevertheless, it is important to note, that we did not carry out spectroscopic detection and classification of TBI vs. healthy biomarkers but rather established the characteristic fingerprints for each chosen biomarker, which is a standalone spectroscopic barcode for either human- or animal-derived neuromarkers. In each case, there is a value and significance to having the 'baseline' fingerprint data, as in the case of a rapidly evolving and multifaceted pathology such as TBI, they may provide integrative and complementary clinically useful information, or may be useful for different investigations, time points, or settings. For instance, animal biomarker models provide a major advantage for investigating preclinical measures of therapeutic efficacy [188, 189].

Faster and less expensive results can be garnered from these allowing only the most promising candidates to advance to more costly clinical trials (e.g., Sabbagh et al. [194]) and represent an important approach to exploring the translational utility of a novel compound. In preclinical systems, animal biomarkers could also be effective for valuing the translational worth of a compound before costly human trials are initiated. Animal model biomarker assessments can verify proof of concept for a candidate treatment. Furthermore, the identification of consistent biomarkers may shed light on core mechanisms responsible for the disorder, as well as interactions between several of the identified pathologies. Notably, the subsequent use of both human and animal biomarkers can form a bridge between animal and human studies to facilitate translational research. By using the same biomarkers in animals and humans, observations in the preclinical stage can be more easily extended to clinical trials. This forward translation can be complemented by a backward one, where observations in humans can be studied via animals.

An additional challenge is that the spectral bands associated with some biomarkers are also present in several other proteins, and so these changes cannot always solely be attributed to a particular molecule. Therefore, a broad panel of biomarkers should be used in such cases, essential to delivering a diagnosis with high accuracy and specificity. This, with further emerging novel hybrid Raman-AI techniques [195, 196], will in turn enable supporting large-scale triaging and screening for early signs of brain injury, particularly useful for identifying high-risk patients and implementing intervention measures, given both the increased incidence and the prevalence of TBIs. Indeed, considerable research in recent years has focused on potential biomarkers to improve

diagnosis and patient phenotyping to enable timely and targeted management. For instance, S100B has been implemented in Scandinavian countries and the ALERT-TBI study showed high sensitivity for the combination of GFAP and neuronal UCHL1 measured within 12 h of injury, forming the basis of the first FDA-approved TBI test for triaging the need for CT scanning [197].

One further issue that needs to be addressed for real-world adoption is a lack of standardisation in methods used within the current literature, from matters pertaining to biofluid collection, storage and pre-processing, to those concerning Raman measurement protocols and chemometric analyses and classification. Standardisation of protocols and conducting larger-scale clinical studies are vital for advancing the clinical translation of Raman spectroscopy biomarker profiling in TBI diagnostic and prognostic applications.

Finally, there has been an increase in the literature surrounding the development of Raman spectroscopy-based technologies for TBI detection, utilising surface-enhanced Raman spectroscopy (SERS), microfluidics, and Raman probes [32, 34, 35, 198, 199]. As such new spectroscopic technologies are being engineered and prototyped, it is essential to improve the understanding of brain injury biomarkers and their mechanism in various post-TBI phases, which will continue to grow alongside these, particularly when utilising human biofluids and TBI models.

3.6 Conclusions

A Raman spectroscopy fingerprint library has been generated for a large cohort of TBI-indicative biomarkers. The spectral fingerprint of each studied biomarker generates a unique signature and comparisons of certain values for determined frequencies and their raw and aqueous solution states are determined. These spectra provide the fundamental information necessary to track the biochemical changes induced by the neurological markers categorised according to the different stages post-brain injury, i.e., the acute, sub-acute and chronic phases. These can not only assist in understanding the TBI mechanism and check the presence, persistence or fading of characteristic biomolecules in brain tissue or biofluids following injuries but also establish Raman spectroscopy-aided diagnosis of TBI as a complementary point-of-need technique. The longer-term goal would be to identify biomarkers or distinctive patterns, which would help to rapidly detect, triage, and monitor TBIs by analysing the differences in Raman spectral signatures.

The most dominant peak ratios for each biomarker have been further identified, highlighting the various advantages amongst which, by using the ratio-metric approach over the absolute Raman intensity of individual bands, is elimination of the need to measure the amplitude of each peak, often necessary for ensuring consistency and reproducibility of the intensity and/or wavenumber position, which can be challenging between each measurement, especially when performed by a non-expert at the point of care.

Reliable point-of-care diagnostic tools, such as Raman spectroscopy, could improve the specificity of diagnosis and triage of TBI and would greatly aid resource availability in healthcare by reducing the number of unnecessary ED visits for mild TBI and increasing the proportion of patients with moderate/severe TBIs appropriately triaged to attend trauma facilities. With millions of ED visits every year and the high cost per visit without treatment or investigation, even a small reduction will result in massive cost savings. Furthermore, the pathophysiology of injury evolution is multi-faceted, and not understood well enough to provide effective pharmacological targeting to reduce burden or progression. An in-depth understanding of the biochemical injury evolution will allow interventions to be used more effectively and identify novel therapeutic targets to guide tactful treatments. The generated spectral library would further assist in the emerging developments of Raman spectroscopy-based technologies, for rapid acquisition of molecular fingerprints of TBI biochemistry to safely measure proxies for cerebral injury via the body fluids, which will soon provide a tangible path towards non-invasive point-of-care diagnostics for TBI.

3.7 References

[1] K. K. Wang *et al.*, "An update on diagnostic and prognostic biomarkers for traumatic brain injury," *Expert review of molecular diagnostics,* vol. 18, no. 2, pp. 165-180, 2018.

[2] H. Adrian, K. Mårten, N. Salla, and V. Lasse, "Biomarkers of traumatic brain injury: temporal changes in body fluids," *Eneuro,* vol. 3, no. 6, 2016.

[3] A. Ercole, E. Thelin, A. Holst, B. Bellander, and D. Nelson, "Kinetic modelling of serum S100b after traumatic brain injury," *BMC neurology,* vol. 16, pp. 1-8, 2016.

[4] S. M. Lippa, J. K. Werner, M. C. Miller, J. M. Gill, R. Diaz-Arrastia, and K. Kenney, "Recent advances in blood-based biomarkers of remote combat-related traumatic brain injury," *Current neurology and neuroscience reports,* vol. 20, pp. 1-11, 2020.

[5] F. H. Kobeissy *et al.*, "Neuroproteomics and systems biology-based discovery of protein biomarkers for traumatic brain injury and clinical validation," *PROTEOMICS–Clinical Applications,* vol. 2, no. 10-11, pp. 1467-1483, 2008.

[6] D. V. Agoston, A. Shutes-David, and E. R. Peskind, "Biofluid biomarkers of traumatic brain injury," *Brain injury,* vol. 31, no. 9, pp. 1195-1203, 2017.

[7] P. Shahim *et al.*, "Time course and diagnostic utility of NfL, tau, GFAP, and UCH-L1 in subacute and chronic TBI," *Neurology,* vol. 95, no. 6, pp. e623-e636, 2020.

[8] R. Rubenstein *et al.*, "Comparing plasma phospho tau, total tau, and phospho tau–total tau ratio as acute and chronic traumatic brain injury biomarkers," *JAMA neurology,* vol. 74, no. 9, pp. 1063-1072, 2017.

[9] J. Chitturi, Y. Li, V. Santhakumar, and S. S. Kannurpatti, "Consolidated biochemical profile of subacute stage traumatic brain injury in early development," *Frontiers in Neuroscience,* vol. 13, p. 431, 2019.

[10] M. C. Dewan *et al.*, "Estimating the global incidence of traumatic brain injury," *Journal of neurosurgery,* vol. 130, no. 4, pp. 1080-1097, 2018.

[11] A. Capizzi, J. Woo, and M. Verduzco-Gutierrez, "Traumatic brain injury: an overview of epidemiology, pathophysiology, and medical management," *Medical Clinics,* vol. 104, no. 2, pp. 213-238, 2020.

[12] G. Teasdale and B. Jennett, "Assessment of coma and impaired consciousness: a practical scale," *The Lancet,* vol. 304, no. 7872, pp. 81-84, 1974.

[13] J. R. Huie *et al.*, "Biomarkers for traumatic brain injury: data standards and statistical considerations," *Journal of neurotrauma,* vol. 38, no. 18, pp. 2514-2529, 2021.

[14] J. J. Bazarian, P. Veazie, S. Mookerjee, and E. B. Lerner, "Accuracy of mild traumatic brain injury case ascertainment using ICD-9 codes," *Academic emergency medicine,* vol. 13, no. 1, pp. 31-38, 2006.

[15] W. R. McBride, N. R. Eltman, and R. L. Swanson, "Blood-Based Biomarkers in Traumatic Brain Injury: A Narrative Review with Implications for the Legal System," *Cureus,* vol. 15, no. 6, 2023.

[16] I. Mavroudis, F. Petridis, I.-M. Balmus, A. Ciobica, D. L. Gorgan, and A. C. Luca, "Review on the role of salivary biomarkers in the diagnosis of mild traumatic brain injury and post-concussion syndrome," *Diagnostics,* vol. 13, no. 8, p. 1367, 2023.

[17] J. Mozafari, M. A. Fahimi, K. Mohammadi, H. Barzegari, M. G. Hanafi, and A. Saki-Malehi, "The diagnostic accuracy of serum and urinary S100B protein in children

and adolescents with mild traumatic brain injury," *New Zealand Journal of Medical Laboratory Science,* vol. 73, no. 3, pp. 88-91, 2019.

[18] H. Zetterberg and K. Blennow, "Fluid markers of traumatic brain injury," *Molecular and cellular neuroscience,* vol. 66, pp. 99-102, 2015.

[19] E. Cordero, I. Latka, C. Matthäus, I. W. Schie, and J. Popp, "In-vivo Raman spectroscopy: from basics to applications," *Journal of biomedical optics,* vol. 23, no. 7, pp. 071210-071210, 2018.

[20] E. Hanlon *et al.*, "Prospects for in vivo Raman spectroscopy," *Physics in Medicine & Biology,* vol. 45, no. 2, p. R1, 2000.

[21] S. Guo, T. Bocklitz, and J. Popp, "Optimization of Raman-spectrum baseline correction in biological application," *Analyst,* vol. 141, no. 8, pp. 2396-2404, 2016.

[22] Z. Birech, P. W. Mwangi, F. Bukachi, and K. M. Mandela, "Application of Raman spectroscopy in type 2 diabetes screening in blood using leucine and isoleucine amino-acids as biomarkers and in comparative anti-diabetic drugs efficacy studies," *PLoS One,* vol. 12, no. 9, p. e0185130, 2017.

[23] H. J. Koster, A. Guillen-Perez, J. S. Gomez-Diaz, M. Navas-Moreno, A. C. Birkeland, and R. P. Carney, "Fused Raman spectroscopic analysis of blood and saliva delivers high accuracy for head and neck cancer diagnostics," *Scientific reports,* vol. 12, no. 1, p. 18464, 2022.

[24] E. Ryzhikova *et al.*, "Raman spectroscopy and machine learning for biomedical applications: Alzheimer's disease diagnosis based on the analysis of cerebrospinal fluid," *Spectrochimica Acta Part A: Molecular and Biomolecular Spectroscopy,* vol. 248, p. 119188, 2021.

[25] R. Sathyavathi *et al.*, "Raman spectroscopy provides a powerful, rapid diagnostic tool for the detection of tuberculous meningitis in ex vivo cerebrospinal fluid samples," *Journal of biophotonics,* vol. 6, no. 8, pp. 567-572, 2013.

[26] C. Chen *et al.*, "Urine Raman spectroscopy for rapid and inexpensive diagnosis of chronic renal failure (CRF) using multiple classification algorithms," *Optik,* vol. 203, p. 164043, 2020.

[27] V. Kavuru, R. S. Senger, J. L. Robertson, and D. Choudhury, "Analysis of urine Raman spectra differences from patients with diabetes mellitus and renal pathologies," *PeerJ,* vol. 11, p. e14879, 2023.

[28] E. Buchan, M. Hardy, P. d. C. Gomes, L. Kelleher, H. O. M. Chu, and P. G. Oppenheimer, "Emerging Raman spectroscopy and saliva-based diagnostics: from challenges to applications," *Applied Spectroscopy Reviews,* vol. 59, no. 3, pp. 277-314, 2024.

[29] S. Kim *et al.*, "Label-free surface-enhanced Raman spectroscopy biosensor for on-site breast cancer detection using human tears," *ACS applied materials & interfaces,* vol. 12, no. 7, pp. 7897-7904, 2020.

[30] C. Camerlingo *et al.*, "Characterization of human tear fluid by means of surface-enhanced Raman spectroscopy," *Sensors,* vol. 19, no. 5, p. 1177, 2019.

[31] G. Cennamo *et al.*, "Surface-enhanced Raman spectroscopy of tears: toward a diagnostic tool for neurodegenerative disease identification," *Journal of biomedical optics,* vol. 25, no. 8, pp. 087002-087002, 2020.

[32] J. J. Rickard, V. Di-Pietro, D. J. Smith, D. J. Davies, A. Belli, and P. G. Oppenheimer, "Rapid optofluidic detection of biomarkers for traumatic brain injury via surface-enhanced Raman spectroscopy," *Nature biomedical engineering,* vol. 4, no. 6, pp. 610-623, 2020.

[33] C. Li, K. A. Shah, and R. K. Narayan, "Rapid detection of traumatic brain injury," *Nature biomedical engineering,* vol. 4, no. 6, pp. 579-580, 2020.

[34] M. Mowbray, C. Banbury, J. J. Rickard, D. J. Davies, and P. Goldberg Oppenheimer, "Development and Characterization of a Probe Device toward Intracranial Spectroscopy of Traumatic Brain Injury," *ACS biomaterials science & engineering,* vol. 7, no. 3, pp. 1252-1262, 2021.

[35] A. R. Stevens *et al.*, "Raman Spectroscopy as a Neuromonitoring Tool in Traumatic Brain Injury: A Systematic Review and Clinical Perspectives," *Cells,* vol. 11, no. 7, p. 1227, 2022.

[36] C. Feinberg *et al.*, "Association of pharmacological interventions with symptom burden reduction in patients with mild traumatic brain injury: a systematic review," *JAMA neurology,* vol. 78, no. 5, pp. 596-608, 2021.

[37] M. Marro *et al.*, "Dynamic molecular monitoring of retina inflammation by in vivo Raman spectroscopy coupled with multivariate analysis," vol. 7, ed: Wiley Online Library, 2014, pp. 724-734.

[38] G. Harris *et al.*, "Emerging Eye-Based Diagnostic Technologies for Traumatic Brain Injury," *IEEE reviews in biomedical engineering,* vol. 16, pp. 530-559, 2022.

[39] A. E. Böhmer *et al.*, "Neuron-specific enolase, S100B, and glial fibrillary acidic protein levels as outcome predictors in patients with severe traumatic brain injury," *Neurosurgery,* vol. 68, no. 6, pp. 1624-1631, 2011.

[40] M. U. Gutierre, J. P. M. Telles, L. C. Welling, N. N. Rabelo, M. J. Teixeira, and E. G. Figueiredo, "Biomarkers for traumatic brain injury: A short review," *Neurosurgical Review,* vol. 44, pp. 2091-2097, 2021.

[41] H. Zetterberg, D. H. Smith, and K. Blennow, "Biomarkers of mild traumatic brain injury in cerebrospinal fluid and blood," *Nature Reviews Neurology,* vol. 9, no. 4, pp. 201-210, 2013.

[42] D. Bouvier, C. Oris, M. Brailova, J. Durif, and V. Sapin, "Interest of blood biomarkers to predict lesions in medical imaging in the context of mild traumatic brain injury," *Clinical biochemistry,* vol. 85, pp. 5-11, 2020.

[43] A. S. Woods *et al.*, "Gangliosides and ceramides change in a mouse model of blast induced traumatic brain injury," *ACS chemical neuroscience,* vol. 4, no. 4, pp. 594-600, 2013.

[44] H. J. Kim, J. W. Tsao, and A. G. Stanfill, "The current state of biomarkers of mild traumatic brain injury," *JCI insight,* vol. 3, no. 1, 2018.

[45] E. J. Perez *et al.*, "Enhanced astrocytic d-serine underlies synaptic damage after traumatic brain injury," *The Journal of Clinical Investigation,* vol. 127, no. 8, pp. 3114-3125, 2017.

[46] S. H. Lee *et al.*, "Acid sphingomyelinase inhibitor, imipramine, reduces hippocampal neuronal death after traumatic brain injury," *International Journal of Molecular Sciences,* vol. 23, no. 23, p. 14749, 2022.

[47] L. J. Sparvero *et al.*, "Imaging mass spectrometry reveals loss of polyunsaturated cardiolipins in the cortical contusion, hippocampus, and thalamus after traumatic brain injury," *Journal of neurochemistry,* vol. 139, no. 4, pp. 659-675, 2016.

[48] H. Chao *et al.*, "Disentangling oxidation/hydrolysis reactions of brain mitochondrial cardiolipins in pathogenesis of traumatic injury," *JCI insight,* vol. 3, no. 21, 2018.

[49] C. Banbury *et al.*, "Spectroscopic detection of traumatic brain injury severity and biochemistry from the retina," *Biomedical optics express,* vol. 11, no. 11, pp. 6249-6261, 2020.

[50] A. A. Antunes, V. S. Sotomaior, K. S. Sakamoto, C. P. de Camargo Neto, C. Martins, and L. R. Aguiar, "Interleukin-6 plasmatic levels in patients with head trauma and intracerebral hemorrhage," *Asian journal of neurosurgery,* vol. 5, no. 1, p. 68, 2010.

[51] R. Kumar *et al.*, "Acute CSF interleukin-6 trajectories after TBI: associations with neuroinflammation, polytrauma, and outcome," *Brain, behavior, and immunity,* vol. 45, pp. 253-262, 2015.

[52] K. K. Wang, F. H. Kobeissy, Z. Shakkour, and J. A. Tyndall, "Thorough overview of ubiquitin C-terminal hydrolase-L1 and glial fibrillary acidic protein as tandem biomarkers recently cleared by US Food and Drug Administration for the evaluation of intracranial injuries among patients with traumatic brain injury," *Acute Medicine & Surgery,* vol. 8, no. 1, p. e622, 2021.

[53] J. Guan *et al.*, "Transplantation of human mesenchymal stem cells loaded on collagen scaffolds for the treatment of traumatic brain injury in rats," *Biomaterials,* vol. 34, no. 24, pp. 5937-5946, 2013.

[54] C. Krafft, L. Neudert, T. Simat, and R. Salzer, "Near infrared Raman spectra of human brain lipids," *Spectrochimica Acta Part A: Molecular and Biomolecular Spectroscopy,* vol. 61, no. 7, pp. 1529-1535, 2005.

[55] J. Shi *et al.*, "Traumatic brain injury and hyperglycemia, a potentially modifiable risk factor," *Oncotarget,* vol. 7, no. 43, p. 71052, 2016.

[56] A. S. Kierans *et al.*, "Myoinositol and glutamate complex neurometabolite abnormality after mild traumatic brain injury," *Neurology,* vol. 82, no. 6, pp. 521-528, 2014.

[57] A. Ciaramella *et al.*, "Increased levels of serum IL-18 are associated with the long-term outcome of severe traumatic brain injury," *Neuroimmunomodulation,* vol. 21, no. 1, pp. 8-12, 2013.

[58] A. Belli *et al.*, "Extracellular N-acetylaspartate depletion in traumatic brain injury," *Journal of neurochemistry,* vol. 96, no. 3, pp. 861-869, 2006.

[59] V. Rubovitch, Y. Zilberstein, J. Chapman, S. Schreiber, and C. G. Pick, "Restoring GM1 ganglioside expression ameliorates axonal outgrowth inhibition and cognitive impairments induced by blast traumatic brain injury," *Scientific reports,* vol. 7, no. 1, p. 41269, 2017.

[60] L. Koza and D. A. Linseman, "Glutathione precursors shield the brain from trauma," *Neural regeneration research,* vol. 14, no. 10, p. 1701, 2019.

[61] R. Smith, M. Chepisheva, T. Cronin, and B. M. Seemungal, "Diagnostic approaches techniques in concussion/mild traumatic brain injury: Where are we?," in *Neurosensory disorders in mild traumatic brain injury*: Elsevier, 2019, pp. 247-277.

[62] T. Mehta *et al.*, "Current trends in biomarkers for traumatic brain injury," *Open access journal of neurology & neurosurgery,* vol. 12, no. 4, p. 86, 2020.
[63] C. M. Cartagena *et al.*, "Cortical injury increases cholesterol 24S hydroxylase (Cyp46) levels in the rat brain," *Journal of neurotrauma,* vol. 25, no. 9, pp. 1087-1098, 2008.
[64] M. S. Bergholt, A. Serio, and M. B. Albro, "Raman spectroscopy: guiding light for the extracellular matrix," *Frontiers in bioengineering and biotechnology,* vol. 7, p. 303, 2019.
[65] A. H. Chau, J. T. Motz, J. A. Gardecki, S. Waxman, B. E. Bouma, and G. J. Tearney, "Fingerprint and high-wavenumber Raman spectroscopy in a human-swine coronary xenograft in vivo," *Journal of biomedical optics,* vol. 13, no. 4, pp. 040501-040501-3, 2008.
[66] J. R. Moffett, P. Arun, P. S. Ariyannur, and A. M. Namboodiri, "N-Acetylaspartate reductions in brain injury: impact on post-injury neuroenergetics, lipid synthesis, and protein acetylation," *Frontiers in neuroenergetics,* vol. 5, p. 11, 2013.
[67] R. J. Shannon *et al.*, "Extracellular N-acetylaspartate in human traumatic brain injury," *Journal of neurotrauma,* vol. 33, no. 4, pp. 319-329, 2016.
[68] S. Sipione, J. Monyror, D. Galleguillos, N. Steinberg, and V. Kadam, "Gangliosides in the brain: physiology, pathophysiology and therapeutic applications," *Frontiers in neuroscience,* vol. 14, p. 572965, 2020.
[69] N. Khatri, M. Thakur, V. Pareek, S. Kumar, S. Sharma, and A. K. Datusalia, "Oxidative stress: major threat in traumatic brain injury," *CNS & Neurological Disorders-Drug Targets (Formerly Current Drug Targets-CNS & Neurological Disorders),* vol. 17, no. 9, pp. 689-695, 2018.
[70] A. Haque, S. K. Ray, A. Cox, and N. L. Banik, "Neuron specific enolase: a promising therapeutic target in acute spinal cord injury," *Metabolic brain disease,* vol. 31, pp. 487-495, 2016.
[71] Z. Yang and K. K. Wang, "Glial fibrillary acidic protein: from intermediate filament assembly and gliosis to neurobiomarker," *Trends in neurosciences,* vol. 38, no. 6, pp. 364-374, 2015.
[72] M. V. Sofroniew, "Molecular dissection of reactive astrogliosis and glial scar formation," *Trends in neurosciences,* vol. 32, no. 12, pp. 638-647, 2009.
[73] S.-F. Tzeng, H.-Y. Hsiao, and O.-T. Mak, "Prostaglandins and cyclooxygenases in glial cells during brain inflammation," *Current Drug Targets-Inflammation & Allergy,* vol. 4, no. 3, pp. 335-340, 2005.
[74] H. Liu *et al.*, "Role of UCHL1 in axonal injury and functional recovery after cerebral ischemia," *Proceedings of the National Academy of Sciences,* vol. 116, no. 10, pp. 4643-4650, 2019.
[75] S. Shahjouei *et al.*, "The diagnostic values of UCH-L1 in traumatic brain injury: a meta-analysis," *Brain injury,* vol. 32, no. 1, pp. 1-17, 2018.
[76] N. Nathoo, R. Chetty, J. Van Dellen, and G. Barnett, "Genetic vulnerability following traumatic brain injury: the role of apolipoprotein E," *Molecular Pathology,* vol. 56, no. 3, p. 132, 2003.
[77] J. M. Surmacki, L. Ansel-Bollepalli, F. Pischiutta, E. R. Zanier, A. Ercole, and S. E. Bohndiek, "Label-free monitoring of tissue biochemistry following traumatic brain

injury using Raman spectroscopy," *Analyst,* 10.1039/C6AN02238C vol. 142, no. 1, pp. 132-139, 2017, doi: 10.1039/C6AN02238C.

[78] A. D. Kay, S. P. Day, M. Kerr, J. A. Nicoll, C. J. Packard, and M. J. Caslake, "Remodeling of cerebrospinal fluid lipoprotein particles after human traumatic brain injury," *Journal of neurotrauma,* vol. 20, no. 8, pp. 717-723, 2003.

[79] H. Xu *et al.*, "Brain-specific loss of Abcg1 disturbs cholesterol metabolism and aggravates pyroptosis and neurological deficits after traumatic brain injury," *Brain pathology,* vol. 33, no. 3, p. e13126, 2023.

[80] S. A. Tapanes *et al.*, "Inhibition of glial D-serine release rescues synaptic damage after brain injury," *Glia,* vol. 70, no. 6, pp. 1133-1152, 2022.

[81] A. V. Alessenko and E. Albi, "Exploring sphingolipid implications in neurodegeneration," *Frontiers in Neurology,* vol. 11, p. 437, 2020.

[82] N. Schneider *et al.*, "Sphingomyelin in brain and cognitive development: preliminary data," *Eneuro,* vol. 6, no. 4, 2019.

[83] J. O. Ojo *et al.*, "Converging and differential brain phospholipid dysregulation in the pathogenesis of repetitive mild traumatic brain injury and Alzheimer's disease," *Frontiers in Neuroscience,* vol. 13, p. 103, 2019.

[84] G. Wang and E. Bieberich, "Sphingolipids in neurodegeneration (with focus on ceramide and S1P)," *Advances in biological regulation,* vol. 70, pp. 51-64, 2018.

[85] K. Yang, W. C. Taft, C. E. Dixon, C. A. Todaro, R. K. YU, and R. L. HAYES, "Alterations of protein kinase C in rat hippocampus following traumatic brain injury," *Journal of neurotrauma,* vol. 10, no. 3, pp. 287-295, 1993.

[86] T. Takahashi and T. Suzuki, "Role of sulfatide in normal and pathological cells and tissues," *Journal of lipid research,* vol. 53, no. 8, pp. 1437-1450, 2012.

[87] G. Paradies, V. Paradies, F. M. Ruggiero, and G. Petrosillo, "Role of cardiolipin in mitochondrial function and dynamics in health and disease: molecular and pharmacological aspects," *Cells,* vol. 8, no. 7, p. 728, 2019.

[88] C. T. Chu *et al.*, "Cardiolipin externalization to the outer mitochondrial membrane acts as an elimination signal for mitophagy in neuronal cells," *Nature cell biology,* vol. 15, no. 10, pp. 1197-1205, 2013.

[89] H. Chao *et al.*, "Cardiolipin-dependent mitophagy guides outcome after traumatic brain injury," *Journal of Neuroscience,* vol. 39, no. 10, pp. 1930-1943, 2019.

[90] A. J. Williams, H. H. Wei, J. R. Dave, and F. C. Tortella, "Acute and delayed neuroinflammatory response following experimental penetrating ballistic brain injury in the rat," *Journal of Neuroinflammation,* vol. 4, no. 1, pp. 1-12, 2007.

[91] S. Z. Y. Ooi *et al.*, "Interleukin-6 as a prognostic biomarker of clinical outcomes after traumatic brain injury: a systematic review," *Neurosurgical Review,* vol. 45, no. 5, pp. 3035-3054, 2022.

[92] G. Schett, "Physiological effects of modulating the interleukin-6 axis," *Rheumatology,* vol. 57, no. suppl_2, pp. ii43-ii50, 2018.

[93] H. Nishiyama, T. Knöpfel, S. Endo, and S. Itohara, "Glial protein S100B modulates long-term neuronal synaptic plasticity," *Proceedings of the National Academy of Sciences,* vol. 99, no. 6, pp. 4037-4042, 2002.

[94] A. Goyal *et al.*, "S100b as a prognostic biomarker in outcome prediction for patients with severe traumatic brain injury," *Journal of neurotrauma,* vol. 30, no. 11, pp. 946-957, 2013.

[95] R.-M. Boustany, I. Al-Shareef, and S. El-Haddad, "Sphingolipid disorders and the neuronal Ceroid Lipofuscinoses or batten disease (Wolman disease, Cholesteryl Ester storage disease, and Cerebrotendinous Xanthomatosis)," in *Publication Name: Emery and Rimoin's Principles and Practice of Medical Genetics; Publication Year: 2013; Pages:(1-85);*: Elsevier Ltd;, 2013.

[96] J. Marcus and B. Popko, "Galactolipids are molecular determinants of myelin development and axo–glial organization," *Biochimica et Biophysica Acta (BBA)-General Subjects,* vol. 1573, no. 3, pp. 406-413, 2002.

[97] P. Mergenthaler, U. Lindauer, G. A. Dienel, and A. Meisel, "Sugar for the brain: the role of glucose in physiological and pathological brain function," *Trends in neurosciences,* vol. 36, no. 10, pp. 587-597, 2013.

[98] P. M. Vespa *et al.*, "Persistently low extracellular glucose correlates with poor outcome 6 months after human traumatic brain injury despite a lack of increased lactate: a microdialysis study," *Journal of Cerebral Blood Flow & Metabolism,* vol. 23, no. 7, pp. 865-877, 2003.

[99] I. Jalloh, K. L. Carpenter, A. Helmy, T. A. Carpenter, D. K. Menon, and P. J. Hutchinson, "Glucose metabolism following human traumatic brain injury: methods of assessment and pathophysiological findings," *Metabolic brain disease,* vol. 30, pp. 615-632, 2015.

[100] A. J. López-Gambero, C. Sanjuan, P. J. Serrano-Castro, J. Suárez, and F. Rodríguez de Fonseca, "The biomedical uses of inositols: A nutraceutical approach to metabolic dysfunction in aging and neurodegenerative diseases," *Biomedicines,* vol. 8, no. 9, p. 295, 2020.

[101] A. Brand, C. Richter-Landsberg, and D. Leibfritz, "Multinuclear NMR studies on the energy metabolism of glial and neuronal cells," *Developmental neuroscience,* vol. 15, no. 3-5, pp. 289-298, 1993.

[102] M. Haris, K. Cai, A. Singh, H. Hariharan, and R. Reddy, "In vivo mapping of brain myo-inositol," *Neuroimage,* vol. 54, no. 3, pp. 2079-2085, 2011.

[103] S. Ashwal *et al.*, "Proton spectroscopy detected myoinositol in children with traumatic brain injury," *Pediatric research,* vol. 56, no. 4, pp. 630-638, 2004.

[104] S. Alboni, D. Cervia, S. Sugama, and B. Conti, "Interleukin 18 in the CNS," *Journal of neuroinflammation,* vol. 7, no. 1, pp. 1-12, 2010.

[105] U. Felderhoff-Mueser, O. I. Schmidt, A. Oberholzer, C. Bührer, and P. F. Stahel, "IL-18: a key player in neuroinflammation and neurodegeneration?," *Trends in neurosciences,* vol. 28, no. 9, pp. 487-493, 2005.

[106] S. Narayanan, A. Shanker, T. Khera, and B. Subramaniam, "Neurofilament light: a narrative review on biomarker utility," *Faculty reviews,* vol. 10, 2021.

[107] M. Khalil *et al.*, "Neurofilaments as biomarkers in neurological disorders," *Nature Reviews Neurology,* vol. 14, no. 10, pp. 577-589, 2018.

[108] L. Gaetani, K. Blennow, P. Calabresi, M. Di Filippo, L. Parnetti, and H. Zetterberg, "Neurofilament light chain as a biomarker in neurological disorders," *Journal of Neurology, Neurosurgery & Psychiatry,* vol. 90, no. 8, pp. 870-881, 2019.

[109] A. I. Maas *et al.*, "Traumatic brain injury: integrated approaches to improve prevention, clinical care, and research," *The Lancet Neurology,* vol. 16, no. 12, pp. 987-1048, 2017.
[110] J. Zhang, V. Puvenna, and D. Janigro, "Biomarkers of traumatic brain injury and their relationship to pathology," 2015.
[111] G. Socrates, *Infrared and Raman characteristic group frequencies: tables and charts*. John Wiley & Sons, 2004.
[112] E. Staniszewska-Slezak, K. Malek, and M. Baranska, "Complementary analysis of tissue homogenates composition obtained by Vis and NIR laser excitations and Raman spectroscopy," *Spectrochimica Acta Part A: Molecular and Biomolecular Spectroscopy,* vol. 147, pp. 245-256, 2015.
[113] S. Qiu *et al.*, "Raman profile alterations of irradiated human nasopharyngeal cancer cells detected with laser tweezer Raman spectroscopy," *RSC advances,* vol. 10, no. 24, pp. 14368-14373, 2020.
[114] A. Pastore, G. Federici, E. Bertini, and F. Piemonte, "Analysis of glutathione: implication in redox and detoxification," *Clinica chimica acta,* vol. 333, no. 1, pp. 19-39, 2003.
[115] H. J. Shin, J. H. Lee, Y. D. Kim, I. Shin, T. Sim, and D.-K. Lim, "Raman-based in situ monitoring of changes in molecular signatures during mitochondrially mediated apoptosis," *ACS omega,* vol. 4, no. 5, pp. 8188-8195, 2019.
[116] S. Rolfe, M. Patel, I. Gilmour, K. Olsson-Francis, and T. Ringrose, "Defining multiple characteristic Raman bands of α-amino acids as biomarkers for planetary missions using a statistical method," *Origins of Life and Evolution of Biospheres,* vol. 46, pp. 323-346, 2016.
[117] R. Galli *et al.*, "Rapid label-free analysis of brain tumor biopsies by near infrared Raman and fluorescence spectroscopy—a study of 209 patients," *Frontiers in oncology,* vol. 9, p. 1165, 2019.
[118] G. Pezzotti, "Raman spectroscopy in cell biology and microbiology," *Journal of Raman Spectroscopy,* vol. 52, no. 12, pp. 2348-2443, 2021.
[119] Z. Huang, A. McWilliams, H. Lui, D. I. McLean, S. Lam, and H. Zeng, "Near-infrared Raman spectroscopy for optical diagnosis of lung cancer," *International journal of cancer,* vol. 107, no. 6, pp. 1047-1052, 2003.
[120] A. Mudalige and J. E. Pemberton, "Raman spectroscopy of glycerol/D2O solutions," *Vibrational Spectroscopy,* vol. 45, no. 1, pp. 27-35, 2007.
[121] E. P. Thelin *et al.*, "Utility of neuron-specific enolase in traumatic brain injury; relations to S100B levels, outcome, and extracranial injury severity," *Critical care,* vol. 20, pp. 1-15, 2016.
[122] Z. Movasaghi, S. Rehman, and I. U. Rehman, "Raman spectroscopy of biological tissues," *Applied Spectroscopy Reviews,* vol. 42, no. 5, pp. 493-541, 2007.
[123] S. Tfaili, C. Gobinet, G. Josse, J.-F. Angiboust, M. Manfait, and O. Piot, "Confocal Raman microspectroscopy for skin characterization: a comparative study between human skin and pig skin," *Analyst,* vol. 137, no. 16, pp. 3673-3682, 2012.
[124] C. Nims, B. Cron, M. Wetherington, J. Macalady, and J. Cosmidis, "Low frequency Raman Spectroscopy for micron-scale and in vivo characterization of elemental sulfur in microbial samples," *Scientific reports,* vol. 9, no. 1, p. 7971, 2019.

[125] N. Kourkoumelis, G. Gaitanis, A. Velegraki, and I. D. Bassukas, "Nail Raman spectroscopy: A promising method for the diagnosis of onychomycosis. An ex vivo pilot study," *Medical Mycology,* vol. 56, no. 5, pp. 551-558, 2018.

[126] E. Koglin, J.-M. Sequaris, and P. Valenta, "Surface enhanced raman spectroscopy of nucleic acid bases on Ag electrodes," *Journal of Molecular Structure,* vol. 79, pp. 185-189, 1982.

[127] Z. Luan *et al.*, "Identification of lesional tissues and nonlesional tissues in early gastric cancer endoscopic submucosal dissection specimens using a fiber optic raman system," *Gastroenterology Research and Practice,* vol. 2020, no. 1, p. 8015024, 2020.

[128] J. Depciuch *et al.*, "Spectroscopic evaluation of carcinogenesis in endometrial cancer," *Scientific Reports,* vol. 11, no. 1, p. 9079, 2021.

[129] C. Farber *et al.*, "Complementarity of raman and infrared spectroscopy for structural characterization of plant epicuticular waxes," *ACS Omega,* vol. 4, no. 2, pp. 3700-3707, 2019.

[130] F.-Q. Zhou, "Genetic study of axon regeneration with cultured adult dorsal root ganglion neurons," *JoVE (Journal of Visualized Experiments),* no. 66, p. e4141, 2012.

[131] J. Sacharz *et al.*, "Epileptic rat brain tissue analyzed by 2D correlation Raman spectroscopy," *Spectrochimica Acta Part A: Molecular and Biomolecular Spectroscopy,* vol. 188, pp. 581-588, 2018.

[132] J. Zhu *et al.*, "Surface-enhanced Raman spectroscopy investigation on human breast cancer cells," *Chemistry Central Journal,* vol. 7, pp. 1-5, 2013.

[133] M. Jahmani, M. Hammadeh, M. Al Smadi, and M. K. Baller, "Label-free evaluation of chromatin condensation in human normal morphology sperm using Raman spectroscopy," *Reproductive Sciences,* vol. 28, pp. 2527-2539, 2021.

[134] A. Synytsya, M. Judexova, D. Hoskovec, M. Miskovicova, and L. Petruzelka, "Raman spectroscopy at different excitation wavelengths (1064, 785 and 532 nm) as a tool for diagnosis of colon cancer," *Journal of Raman Spectroscopy,* vol. 45, no. 10, pp. 903-911, 2014.

[135] K. Katsara, K. Psatha, G. Kenanakis, M. Aivaliotis, and V. M. Papadakis, "Subtyping on live lymphoma cell lines by raman spectroscopy," *Materials,* vol. 15, no. 2, p. 546, 2022.

[136] L.-L. Tay, R. G. Tremblay, J. Hulse, B. Zurakowski, M. Thompson, and M. Bani-Yaghoub, "Detection of acute brain injury by Raman spectral signature," *Analyst,* vol. 136, no. 8, pp. 1620-1626, 2011.

[137] K. I. Hadjiivanov *et al.*, "Power of infrared and raman spectroscopies to characterize metal-organic frameworks and investigate their interaction with guest molecules," *Chemical Reviews,* vol. 121, no. 3, pp. 1286-1424, 2020.

[138] B. A. Marekha *et al.*, "Intermolecular interactions in mixtures of 1-n-butyl-3-methylimidazolium acetate and water: Insights from IR, Raman, NMR spectroscopy and quantum chemistry calculations," *Journal of Molecular Liquids,* vol. 210, pp. 227-237, 2015.

[139] P. Freire, F. M. Barboza, J. A. Lima, F. Melo, and J. Mendes Filho, "Raman spectroscopy of amino acid crystals," *Raman Spectroscopy and Applications,* vol. 201, p. 171, 2017.
[140] L. Papa *et al.*, "Serum levels of ubiquitin C-terminal hydrolase distinguish mild traumatic brain injury from trauma controls and are elevated in mild and moderate traumatic brain injury patients with intracranial lesions and neurosurgical intervention," *Journal of Trauma and Acute Care Surgery,* vol. 72, no. 5, pp. 1335-1344, 2012.
[141] E. Bik, A. Dorosz, L. Mateuszuk, M. Baranska, and K. Majzner, "Fixed versus live endothelial cells: The effect of glutaraldehyde fixation manifested by characteristic bands on the Raman spectra of cells," *Spectrochimica Acta Part A: Molecular and Biomolecular Spectroscopy,* vol. 240, p. 118460, 2020.
[142] A. Ricciardi *et al.*, "Raman spectroscopy characterization of the major classes of plasma lipoproteins," *Vibrational Spectroscopy,* vol. 109, p. 103073, 2020.
[143] K. Czamara, K. Majzner, M. Z. Pacia, K. Kochan, A. Kaczor, and M. Baranska, "Raman spectroscopy of lipids: a review," *Journal of Raman spectroscopy,* vol. 46, no. 1, pp. 4-20, 2015.
[144] T. Huff, B. Boyd, and I. Jialal, "Physiology, cholesterol," 2017.
[145] T. Ito *et al.*, "D-Serine metabolism and its importance in development of Dictyostelium discoideum," *Frontiers in Microbiology,* vol. 9, p. 784, 2018.
[146] J. P. Slotte, "Biological functions of sphingomyelins," *Progress in lipid research,* vol. 52, no. 4, pp. 424-437, 2013.
[147] K. Kurek, B. Łukaszuk, D. M. Piotrowska, P. Wiesiołek, A. M. Chabowska, and M. Żendzian-Piotrowska, "Metabolism, physiological role, and clinical implications of sphingolipids in gastrointestinal tract," *BioMed research international,* vol. 2013, 2013.
[148] S. A. Novgorodov *et al.*, "Essential roles of neutral ceramidase and sphingosine in mitochondrial dysfunction due to traumatic brain injury," *Journal of Biological Chemistry,* vol. 289, no. 19, pp. 13142-13154, 2014.
[149] N. Buzgar, A. Buzatu, and I. V. Sanislav, "The Raman study on certain sulfates," *An. Stiint. U. Al. I-Mat,* vol. 55, no. 1, pp. 5-23, 2009.
[150] A. Uphoff, M. Hermansson, P. Haimi, and P. Somerharju, "Analysis of complex lipidomes," in *Medical Applications of Mass Spectrometry*: Elsevier, 2008, pp. 223-249.
[151] J. Freeman, B. Wopenka, M. Silva, and J. Pasteris, "Raman spectroscopic detection of changes in bioapatite in mouse femora as a function of age and in vitro fluoride treatment," *Calcified tissue international,* vol. 68, no. 3, 2001.
[152] Y. Cao, D. Shen, Y. Lu, and Y. Huang, "A Raman-scattering study on the net orientation of biomacromolecules in the outer epidermal walls of mature wheat stems (Triticum aestivum)," *Annals of Botany,* vol. 97, no. 6, pp. 1091-1094, 2006.
[153] C. Farber, M. Shires, K. Ong, D. Byrne, and D. Kurouski, "Raman spectroscopy as an early detection tool for rose rosette infection," *Planta,* vol. 250, pp. 1247-1254, 2019.

[154] E. Timchenko, L. Zherdeva, P. Timchenko, L. Volova, and U. Ponomareva, "Detailed analysis of the structural changes of bone matrix during the demineralization process using Raman spectroscopy," *Physics Procedia,* vol. 73, pp. 221-227, 2015.
[155] O. Calcagnile, A. Anell, and J. Undén, "The addition of S100B to guidelines for management of mild head injury is potentially cost saving," *BMC neurology,* vol. 16, pp. 1-7, 2016.
[156] Y. Li *et al.*, "Micro-Raman spectroscopy study of cancerous and normal nasopharyngeal tissues," *Journal of biomedical optics,* vol. 18, no. 2, pp. 027003-027003, 2013.
[157] A. Girard *et al.*, "Raman spectroscopic analysis of skin as a diagnostic tool for Human African Trypanosomiasis," *PLoS Pathogens,* vol. 17, no. 11, p. e1010060, 2021.
[158] T. Menge, P. H. Lalive, H.-C. von Büdingen, B. Cree, S. L. Hauser, and C. P. Genain, "Antibody responses against galactocerebroside are potential stage-specific biomarkers in multiple sclerosis," *Journal of allergy and clinical immunology,* vol. 116, no. 2, pp. 453-459, 2005.
[159] M. Podbielska, S. B. Levery, and E. L. Hogan, "The structural and functional role of myelin fast-migrating cerebrosides: pathological importance in multiple sclerosis," *Clinical lipidology,* vol. 6, no. 2, p. 159, 2011.
[160] I. Thomas *et al.*, "Serum metabolome associated with severity of acute traumatic brain injury," *Nature communications,* vol. 13, no. 1, p. 2545, 2022.
[161] O. D. Ayala *et al.*, "Raman microspectroscopy differentiates perinatal pathogens on ex vivo infected human fetal membrane tissues," *Journal of biophotonics,* vol. 12, no. 9, p. e201800449, 2019.
[162] I. Palings, J. A. Pardoen, E. Van den Berg, C. Winkel, J. Lugtenburg, and R. A. Mathies, "Assignment of fingerprint vibrations in the resonance Raman spectra of rhodopsin, isorhodopsin, and bathorhodopsin: implications for chromophore structure and environment," *Biochemistry,* vol. 26, no. 9, pp. 2544-2556, 1987.
[163] T. Dhanani, T. Dou, K. Biradar, J. Jifon, D. Kurouski, and B. S. Patil, "Raman spectroscopy detects changes in carotenoids on the surface of watermelon fruits during maturation," *Frontiers in plant science,* vol. 13, p. 832522, 2022.
[164] F. Liu, H. Gu, X. Yuan, Y. Lin, and X. Dong, "Chloride ion-dependent surface-enhanced Raman scattering study of biotin on the silver surface," in *Journal of Physics: Conference Series*, 2011, vol. 277, no. 1: IOP Publishing, p. 012025.
[165] X. Zhang, Q. Zhou, Y. Huang, Z. Li, and Z. Zhang, "Contrastive analysis of the Raman spectra of polychlorinated benzene: hexachlorobenzene and benzene," *Sensors,* vol. 11, no. 12, pp. 11510-11515, 2011.
[166] K. A. Khnykina, V. V. Kireev, N. V. Krunina, N. D. Kundikova, and E. V. Verina, "Influence of Environment on Raman Spectra of Glycine and Prospect of Their Use for Functional Diagnostics of Human Beings," in *2018 Global Smart Industry Conference (GloSIC)*, 2018: IEEE, pp. 1-7.
[167] F. Quiles and A. Burneau, "Infrared and Raman spectra of alkaline-earth and copper (II) acetates in aqueous solutions," *Vibrational Spectroscopy,* vol. 16, no. 2, pp. 105-117, 1998.

[168] I. M. Asher, K. J. Rothschild, E. Anastassakis, and H. E. Stanley, "Raman spectroscopy of uncomplexed valinomycin. I. The solid state," *Journal of the American Chemical Society,* vol. 99, no. 7, pp. 2024-2032, 1977.

[169] S. Duraipandian, D. Traynor, P. Kearney, C. Martin, J. J. O'Leary, and F. M. Lyng, "Raman spectroscopic detection of high-grade cervical cytology: Using morphologically normal appearing cells," *Scientific reports,* vol. 8, no. 1, p. 15048, 2018.

[170] A. Guimarães *et al.*, "Near Infrared Raman Spectroscopy (NIRS): A technique for doping control," *Spectroscopy,* vol. 20, no. 4, pp. 185-194, 2006.

[171] H. Liu, S. Lin, and N. Yu, "Resonance Raman enhancement of phenyl ring vibrational modes in phenyl iron complex of myoglobin," *Biophysical journal,* vol. 57, no. 4, pp. 851-856, 1990.

[172] V. Nava, M. L. Frezzotti, and B. Leoni, "Raman spectroscopy for the analysis of microplastics in aquatic systems," *Applied Spectroscopy,* vol. 75, no. 11, pp. 1341-1357, 2021.

[173] P. Bock and N. Gierlinger, "Infrared and Raman spectra of lignin substructures: Coniferyl alcohol, abietin, and coniferyl aldehyde," *Journal of Raman Spectroscopy,* vol. 50, no. 6, pp. 778-792, 2019.

[174] J. C. Ramirez-Perez and D. Durigo, "Surface-enhanced raman spectroscopy (SERS) for characterization SARS-CoV-2," *Journal of Saudi Chemical Society,* vol. 26, no. 5, p. 101531, 2022.

[175] L. F. Maia, R. F. Fernandes, M. R. Almeida, and L. F. d. Oliveira, "Rapid assessment of chemical compounds from Phyllogorgia dilatata using Raman spectroscopy," *Revista Brasileira de Farmacognosia,* vol. 25, no. 6, pp. 619-626, 2015.

[176] D. Tong *et al.*, "Application of Raman spectroscopy in the detection of hepatitis B virus infection," *Photodiagnosis and photodynamic therapy,* vol. 28, pp. 248-252, 2019.

[177] A. Rygula, K. Majzner, K. M. Marzec, A. Kaczor, M. Pilarczyk, and M. Baranska, "Raman spectroscopy of proteins: a review," *Journal of Raman Spectroscopy,* vol. 44, no. 8, pp. 1061-1076, 2013.

[178] A. Bankapur, E. Zachariah, S. Chidangil, M. Valiathan, and D. Mathur, "Raman tweezers spectroscopy of live, single red and white blood cells," *PLoS one,* vol. 5, no. 4, p. e10427, 2010.

[179] M. V. Cañamares, F. Pozzi, and J. R. Lombardi, "Raman, SERS, and DFT Analysis of the main alkaloids Contained in Syrian rue," *The Journal of Physical Chemistry C,* vol. 123, no. 14, pp. 9262-9271, 2019.

[180] O. Anjos, R. P. Guiné, A. J. Santos, V. B. Paula, H. Pereira, and L. M. Estevinho, "Evaluation of FT-Raman and FTIR-ATR spectroscopy for the quality evaluation of Lavandula spp. Honey," *Open Agriculture,* vol. 6, no. 1, pp. 47-56, 2021.

[181] S. M. Moosavinejad, M. Madhoushi, M. Vakili, and D. Rasouli, "Evaluation of degradation in chemical compounds of wood in historical buildings using FT-IR and FT-Raman vibrational spectroscopy," *Maderas. Ciencia y tecnología,* vol. 21, no. 3, pp. 381-392, 2019.

[182] A. Fiedler, M. Baranska, and H. Schulz, "FT-Raman spectroscopy—a rapid and reliable quantification protocol for the determination of natural indigo dye in

Polygonum tinctorium," *Journal of Raman Spectroscopy,* vol. 42, no. 3, pp. 551-557, 2011.

[183] J. Gao, H. Gu, and X. Dong, "The determination of captopril in Solution by Raman spectroscopy," in *Journal of Physics: Conference Series*, 2011, vol. 277, no. 1: IOP Publishing, p. 012009.

[184] L.-Q. Zheng, M. Servalli, A. D. Schlüter, and R. Zenobi, "Tip-enhanced Raman spectroscopy for structural analysis of two-dimensional covalent monolayers synthesized on water and on Au (111)," *Chemical science,* vol. 10, no. 42, pp. 9673-9678, 2019.

[185] N. Tsutsumi *et al.*, "The structural basis for receptor recognition of human interleukin-18," *Nature communications,* vol. 5, no. 1, p. 5340, 2014.

[186] S. J. Choquette, E. S. Etz, W. S. Hurst, D. H. Blackburn, and S. D. Leigh, "Relative intensity correction of Raman spectrometers: NIST SRMs 2241 through 2243 for 785 nm, 532 nm, and 488 nm/514.5 nm excitation," *Applied spectroscopy,* vol. 61, no. 2, pp. 117-129, 2007.

[187] R. R. Jones, D. C. Hooper, L. Zhang, D. Wolverson, and V. K. Valev, "Raman techniques: fundamentals and frontiers," *Nanoscale research letters,* vol. 14, pp. 1-34, 2019.

[188] P. M. Iannaccone and H. J. Jacob, "Rats!," vol. 2, ed: The Company of Biologists Limited, 2009, pp. 206-210.

[189] B. Weber *et al.*, "Modeling trauma in rats: similarities to humans and potential pitfalls to consider," *Journal of translational medicine,* vol. 17, pp. 1-19, 2019.

[190] S. Basu, A. M. Schultz, M. Basu, and S. Roseman, "Enzymatic synthesis of galactocerebroside by a galactosyltransferase from embryonic chicken brain," *Journal of Biological Chemistry,* vol. 246, no. 13, pp. 4272-4279, 1971.

[191] Z. Kaabia *et al.*, "Plasma lipidomic analysis reveals strong similarities between lipid fingerprints in human, hamster and mouse compared to other animal species," *Scientific reports,* vol. 8, no. 1, p. 15893, 2018.

[192] F. Huang *et al.*, "Analysis and comparison of mouse and human brain gangliosides via two-stage matching of MS/MS spectra," *ACS omega,* vol. 7, no. 7, pp. 6403-6411, 2022.

[193] Z. Jiang, T. Shen, H. Huynh, X. Fang, Z. Han, and K. Ouyang, "Cardiolipin regulates mitochondrial ultrastructure and function in mammalian cells," *Genes,* vol. 13, no. 10, p. 1889, 2022.

[194] J. J. Sabbagh, J. W. Kinney, and J. L. Cummings, "Alzheimer's disease biomarkers in animal models: closing the translational gap," *American journal of neurodegenerative disease,* vol. 2, no. 2, p. 108, 2013.

[195] C. Banbury *et al.*, "Development of the self optimising Kohonen index network (SKiNET) for Raman spectroscopy based detection of anatomical eye tissue," *Scientific reports,* vol. 9, no. 1, p. 10812, 2019.

[196] F. Lussier, V. Thibault, B. Charron, G. Q. Wallace, and J.-F. Masson, "Deep learning and artificial intelligence methods for Raman and surface-enhanced Raman scattering," *TrAC Trends in Analytical Chemistry,* vol. 124, p. 115796, 2020.

[197] M. D. Ward, A. Weber, V. D. Merrill, R. D. Welch, J. J. Bazarian, and R. H. Christenson, "Predictive performance of traumatic brain injury biomarkers in high-

risk elderly patients," *The journal of applied laboratory medicine,* vol. 5, no. 1, pp. 91-100, 2020.

[198] O. Terrones, J. Olazar-Intxausti, I. Anso, M. Lorizate, J. A. Nieto-Garai, and F.-X. Contreras, "Raman spectroscopy as a tool to study the pathophysiology of brain diseases," *International Journal of Molecular Sciences,* vol. 24, no. 3, p. 2384, 2023.

[199] M. Ge *et al.*, "Serum-based Raman spectroscopic diagnosis of blast-induced brain injury in a rat model," *Biomedical Optics Express,* vol. 14, no. 7, pp. 3622-3634, 2023.

Chapter 4: Validation of Optimised Intracranial Spectroscopic Probe for Instantaneous In-Situ Monitoring and Classification of Traumatic Brain Injury

This chapter was submitted to and published by Experimental Neurology as a research article. Raman spectroscopy results from this chapter have been entirely collected and analysed by **Miss C. A. Stickland**. The 3D modelling of the cranial bolt was carried out by **Miss C. A. Stickland**. Finite element analysis was performed and analysed by Dr Z. Sztranyovszky. The investigation was conceptualized by **Miss C. A. Stickland**, Dr Z. Sztranyovszky, Dr J. J. Rickard and Prof. P. Goldberg Oppenheimer. Animal tissue samples were provided by Mr A. Stevens, Mr D. Davies and Prof. Z. Ahmed. Surgical procedures performed on animal models were performed by Mr A. Stevens and Prof. Z. Ahmed. Biomarker spiking of the animal brain tissue was performed by **Miss C. A. Stickland**.

4.1 Abstract

The development of an optical interface to directly distinguish the brain tissue's biochemistry is the next step in understanding TBI pathophysiology and the best and most appropriate treatment in cases where in-hospital intracranial access is required. Despite TBI being a globally leading cause of morbidity and mortality in patients under 40, there is still a lack of objective diagnostical tools. Further, given its pathophysiological complexity the majority of treatments provided are purely symptomatic without standardized therapeutic targets. Our tailor-engineered prototype of the intracranial Raman spectroscopy probe (Intra-RSP) is designed to bridge the gap and provide real-time spectroscopic insights to monitor TBI and its evolution as well as identify patient-specific molecular targets for timely intervention. Raman spectroscopy being rapid, label-free and

non-destructive, renders it an ideal portable diagnostics tool. In combination with our in-house developed software, using machine learning algorithms for multivariate analysis, the Intra-RSP is shown to accurately differentiate simulated TBI conditions in rat brains from the healthy controls, directly from the brain surface as well as through the rat's skull. Using clinically pre-established methods of cranial entry, the Intra-RSP can be inserted into a 2-piece optimized cranial bolt with integrated focussing and correctly identify a sample in real-life conditions with an accuracy >80%. To further validate the Intra-RSP's efficiency as a TBI monitoring device, rat brains mildly damaged from inflicted spinal cord injury were found to be correctly classified with 94.5% accuracy. Through optimization and rigorous *in-vivo* validation, the Intra-RSP prototype is envisioned to seamlessly integrate into existing standards of neurological care, serving as a minimally invasive*, in-situ* neuromonitoring tool. This transformative approach has the potential to revolutionize the landscape of neurological care by providing clinicians with unprecedented insights into the nature of brain injuries and fostering targeted, timely and effective therapeutic interventions.

4.2 Introduction

Development of applicable, timely, and cost-effective *in-vivo* and point-of-need triaging and monitoring tools is of a vital importance to address the current unmet needs around TBI [1]. Due to the complex pathophysiology of the traumatic brain injuries and various degrees of severity, there is a potential for a large array of therapeutic targets. For instance, in sTBI, the entire brain can be affected by a life-threatening widespread

swelling and major changes in biochemical state. Currently, the clinical standard of care revolves heavily around regulating the intracranial conditions to prevent further secondary injuries [2], and hence, monitoring the ICP is vital for the neuroprotection and regulation of metabolic requirements in the brain.

In cases of sTBI, increases in ICP are moderated through insertion of a catheter directly into brain parenchyma [3]. The intracranial environment consists of approximately 83% brain tissue, 11% CSF, and 6% blood enclosed in a non-expandable area by the skull [2]. Increase in any of these components post TBI triggers a corresponding decrease in another to maintain the ICP, with the CSF being the most typical since its excess can be relocated to the spinal theca to maintain the correct distribution of oxygen and glucose. Disruption to the autoregulatory mechanisms can lead to devastating secondary injuries requiring therapeutic procedures, such as the decompressive craniectomy [3].

More effective diagnostics monitoring, as well as interventions and treatments of TBI primary injuries, could be enabled *via* timely detection of TBI-induced biochemical changes, pinpointing the extent of damage which for different stages and severity of injury have been shown to be present in serum, CSF or brain parenchyma as indicators for vascular, metabolic and axonal disruptions as well as tissue inflammation [4-15].

Herein, building upon a self-tapping cranial bolt, the Intra-RSP is engineered, which is tailor designed to be easily integrated into existing surgical procedures, such as an ICP catheter insertion or a decompressive craniectomy (Figure 4-1), and subsequently employed to validate the detection and tracking of a panel of TBI indicative biomarkers, providing live feedback on the pathophysiology of TBI in the brain during surgery. The Intra-RSP device internally consists of two single co-axially aligned fibres (Figure 4-1**A**) with a

100 µm excitation fibre and a 200 µm collection fibre, filtering and steering micro-optics and a design to filter laser lines and quartz spectral contributions from both the input and output fibres, all encased in a cylindrical stainless-steel head [16]. The probe is coupled to a 785 nm laser and a portable spectrometer (Figure 4-1**C**). A model skull with a representative operative configuration ICP catheter insertion, featuring the probe head and 3D printed self-tapping cranial bolt and was validated for clinical applications, inserting the probe into the site of interest, and acquiring *in-situ* measurements.

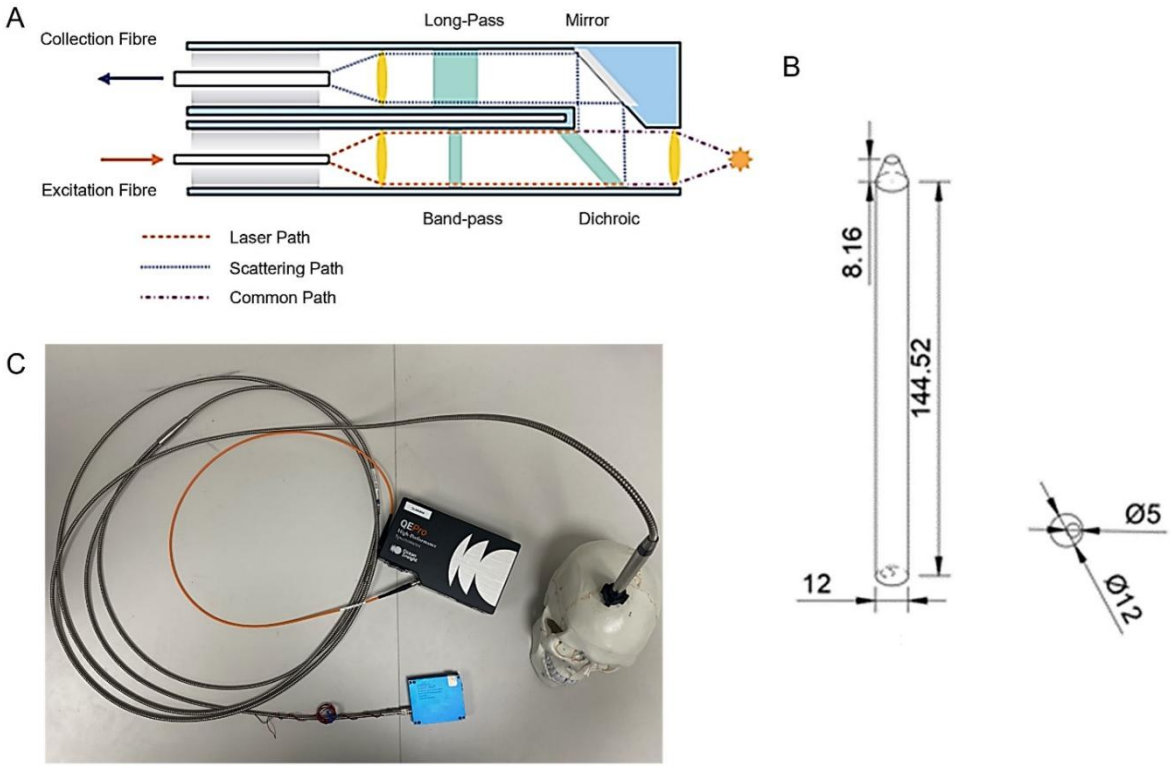

Figure 4-1– Portable Intracranial Raman Spectroscopy Probe Overview. A) Internal structure of the probe, consisting of permanently aligned combination of two single fibres (100 µm excitation fibre, 200 µm collection fibre) with filtering and steering micro-optics, N.A. 0.22, with stainless-steel cabled fibre with a design to filter laser line and quartz spectral contributions from both input and output fibres (O.D.>8 at laser line) [16]. B) Characteristic dimensions (mm) of the probe head, corresponding with the cranial device dimensions, mandated by standard cranial access during larger craniotomies [17]. C) Aerial view of the engineered Intra-RSP handheld setup, including probe, Raman spectrometer and 785 nm laser.

To simulate biochemical changes in the brain following TBI, seven neurological prospective biomarkers of TBI including glucose, myo-inositol, serine, GSH, GFAP, S100B and UCHL1, (Table 4-1) selected due to their biocompatibility, generate a representative panel and are inserted into dead rat brains. The corresponding changes in the brain's environment post-TBI have been studied in rat brain models, detected *in-situ via* the engineered Intra-RSP. Further to validation in spiked rodent brains, we have acquired and analysed a cohort of complementary spinal cord injured (SCI) rats brains, hypothesising that due the proximity of the central nervous system, a traumatic event occurring on the spine will also be reflected in the brain, as a milder injury [18-20]. The acquired Raman spectral signatures, collected *via* the Intra-RSP, are subsequently classified using our artificial neural networks algorithm as a decision support tool, the self-optimizing Kohonen index network (SKiNET). SKiNET acts as a framework for multivariate analysis, simultaneously providing i) dimensionality reduction, ii) feature extraction and iii) multiclass classification [21, 22] by performing a visual separation to identify the underlying biochemical differences between classes. The outputs yield a rapid and accurate classification, even for low laser powers and short acquisition times, representative of real-world conditions. SKiNET's supervised learning, in conjunction with sensing techniques, enables its exploitation for rapid and accurate diagnostic and prognostic applications *via* the inherent self-organised maps (SOM). This results in visually intuitive 2D clustering based on injury state. Additionally, the self-organizing map discriminant index (SOMDI) efficiently identifies the specific spectral features of importance, representing biochemical changes which most contribute to the observed clustering in SOMs [22-24]. Herein, the integrated SKiNET with the Intra-RSP successfully

and rapidly distinguishes between TBI-simulated and SCI rodent brains from healthy control cohorts and correctly identifies and classifies brains from a simulated *in-situ* model. These collectively lay the platform for translation of the developed technology to *real-world* clinical point-of-need neurological diagnostic, monitoring, and prognostic applications along with developments of new therapeutic interventions.

Table 4-1 – Prospective TBI biomarkers and their physiological effect following trauma

Biomarker	**TBI Effect**
β-D-Glucose	Low levels demonstrate increased requirement of energy, which with low lactate/glucose ratio correlated with poor outcomes [4, 5].
Myo-Inositol	Myo-Inositol build-up relates to glial proliferation, astrogliosis, dysregulation of cellular osmotic functions, membrane turnover and myelin sheet damage [6-8].
D-Serine	Reactive glial cells synthesise serine when prompted by inflammatory signals. Serine overproduction results in hyperactivation of NMDA receptors and synaptic damage in the hippocampus [9].
Glutathione (GSH)	GSH converted to oxidised form to regulate free radicals in the brain thus, depleting GSH resources. In extreme neuroinflammation, more free radicals are formed and the lack of GSH further damages the brains and neurons [10, 11].
Glial Fibrillary Acidic Protein (GFAP)	Astrogliosis increases GFAP expression, potentially leading to glial scarring and delayed axon regeneration [13, 14].
S100B	S100B overexpression results in calcium homeostatic dysregulation, indicating structural damage and cellular death [15].
Ubiquitin C-terminal Hydrolase L1 (UCHL1)	Increased following axonal damage to aid in removal of damaged and defective axonal proteins [12].

4.3 Methods and Materials

4.3.1 Materials and Biomarkers

Glucose (Cambridge Biosciences, CAY23733-50), Myo-Inositol (VWR International, A13586.22), D-Serine (VWR International, 312-84-5), GSH (Merck Life Science Limited, Y0000517), GFAP (Generon, C227-10ug), S100B (Cambridge Bioscience, HY-P70659), UCHL1 (Generon, 6B9379) were purchased and used without purification.

4.3.2 Spiked Brain Tissue Sample Preparation

Healthy Sprague-Dawley rat samples were sacrificed and stored at -80^{O}C, licensed by the UK Home Office and approved by the University of Birmingham Animal and Ethical Review Board. Nine brains were removed from the skull, while six were kept in the skull with the back removed allowing visibility to the brain. Two 1 mM biomarker solutions (BS1 and BS2) were prepared with BS1 including, Glucose, Myo-Inositol, Serine and GSH and BS2 consisting of glucose, myo-inositol, serine, GSH, GFAP, S100B and UCHL1. The solutions were injected in two locations at a 1.5 mm depth into the brain for both the exposed and unexposed brains, through the back of both cortical hemispheres, yielding a phantom TBI [25]. Reference TBI biomarkers were dissolved in distilled water (18.2 MΩ) generating a solution of 1 mM according to the data sheets supplied by the manufacturers. These were

dissolved for 20 mins and subsequently 3 µL was pipetted onto an aluminium slide and dried at room temperature, as described in **Chapter 3** [26].

4.3.3 SCI Rat Brains

Surgical procedures were carried out by collaborators (Mr A. Stevens and Prof Z. Ahmed) as described in Stevens *et* al. [27]. Briefly, SCI was inflicted on eight anesthetized (inhalation, 5% isoflurane, 1.8 L/min O_2) Sprague-Dawley (190-250 g, n = 12, male: female 1:1) rats through a dorsal column crush injury on thoracic level 8 (T8). The animals were sacrificed through exposure to rising CO_2 concentrations. Whole brains were removed three days post injury and stored at -80^{O}C. Four healthy controls were subjected to all the above, save the dorsal column crush. This procedure was licensed by the UK Home Office and approved by the University of Birmingham Animal and Ethical Review Board.

4.3.4 Raman Spectra Acquisition and Analysis

The optimised prototype 3D prints of the Intra-RSP were manufactured *via* Ultimaker2+ 3D printer, employing 2.88 mm poly-lactic acid (PLA) filament. Brain spectra were acquired using the Intra-RSP consisting of an InPhotonics probe II coupled to Ocean Insight's QE Pro-Raman spectrometer and a LuxxMaster Raman Boxx (PD-LD) 785 nm laser (Figure 4-1**C**). The applied laser power was set to 40 mW, with 30 s acquisition time and 5 accumulations for the full spectral range (100-3000 cm^{-1}). Training samples for SOMs were acquired with the probe attached to a clamp stand to optimize parameters.

To validate the SOM, test spectra were acquired using BS1-spiked rat brains in a simulated craniotomy setting, using a model skull and a cranial bolt prototype (Figure 4-1**B-C**). Reference TBI biomarker fingerprints were acquired, as described in details in Ref. [26]. Briefly, *via* using 785 nm excitation laser (InVia confocal Renishaw) at the corresponding measuring conditions, three extended scans with an acquisition time of 10 s and 5 accumulations under a x50 objective lens.

4.3.5 Multivariate Data Analysis and AI Classification

The raw data has been truncated to 250-2000 cm^{-1}, baseline subtracted, corrected for cosmic rays, and is presented as an average spectrum. A detailed multivariate analysis was performed *via* SKiNET [21]. For each cohort, a total of 100 spectra were input and randomly split as 80% training spectra and 20% test spectra to ascertain the accuracy of the maps. SOM grid size was decided according to Lek and Park, 2008 [28], as number of spectra input equal to the number of neurons, and ran with 10000 iterations at a learning rate of 0.1 with learning vector quantization (LVQ) enabled. To determine the efficacy of the probe, a separate map was generated using three BS1-spiked test samples from the model skull input as additional test spectra into a SOM containing 100% training data consisting of control, BS1-spiked and BS2-spiked spectra. Each SOM was cross-validated 10 times to determine accuracy, which was calculated using the number of correctly identified test spectra from a confusion matrix.

4.3.6 Finite Element Analysis

Computational modelling and finite element analysis was conducted using Autodesk Fusion 360 to assess the safety and robustness of the bolt design. The simulation "Static Stress" option was employed to conduct the study and calculate the safety factor and stresses [1]. For the 5 mm thread length, the weak point of the structure was found at the joint between the thread and the main body of the bolt. Therefore, a simplified version was designed, omitting the model of the skull while constraining the lower half of the thread to be fixed and the rest of the bolt free to deform under load. A stress was then applied to the four baffles, shared equally amongst them, to model the torque exerted by the tightening clip. The model overall was meshed with the default settings, while the thin plate between the main body and the thread was meshed with the option "local mesh control" set to "fine", giving mesh elements with a size of 0.049 mm.

4.4 Results and Discussion

4.4.1 Intra-RSP Bolt Design for ICP Catheter Insertion

The cranial bolt has been designed *via* Autodesk Fusion 360 and is represented in Figure 4-2. Iterative testing and refinement of the 3D printed components were conducted using a model of a human skull, featuring a hole replicated with the same drill employed by

neurosurgeons during a craniotomy to ensure accuracy. During surgery, a burr hole is typically created using a disposable clutched perforator drill, which to prevent the surgeon from drilling into the tissue, allows for an internal ledge, providing a change in geometry throughout the site.

The cranial bolt is a key part of the development of the Intra-RSP's function for use during the ICP catheter insertion. The bolt is hand-placed and self-tapping using a tapping tool, providing stability and allowing for the probe sleeve to be inserted at a user defined distance for the purpose of focussing it onto the brain surface according to the brain distance from the skull, depending on potential neuroinflammation.

Rigorous testing and adjustments were made to guarantee the precision and functionality of the cranial bolt in simulating the real-world conditions. Simulations were performed for titanium 6Al-4V and nylon 6, based on their biocompatibility and availability as feasibly reproducible materials. The figures of merit are summarised in Table 4-2, where titanium shows a minor maximum displacement and a large safety factor even at high torques

For a torque of 0.8 Nm, building upon our initial bolt prototype [1], the safety factor has been reduced by 8% from 11.58 to 10.69, due to the thinner connection between the thread and the main body of the bolt, where the stress is highest (Figure 4-2**C**). The thinner section is essential in this design to reduce the working distance of the device. The safety factor is the margin between the minimum required performance desired from the device and the actual performance [29]. The maximum displacement describes the total movement from the original coordinates to displaced position when a load is applied [30]. The 10.69 safety factor is well above 3 (considered safe) or >1 (considered as a breaking point) [31].

For nylon, the fracture point reduced significantly from a torque of 0.96 to 0.684 Nm. To achieve a minimum safety factor of 3, the maximum supported torque is only 0.228 Nm. This indicates that for the optimised bolt design, nylon does not constitute an appropriate option, and titanium is chosen as the most suitable, safe material.

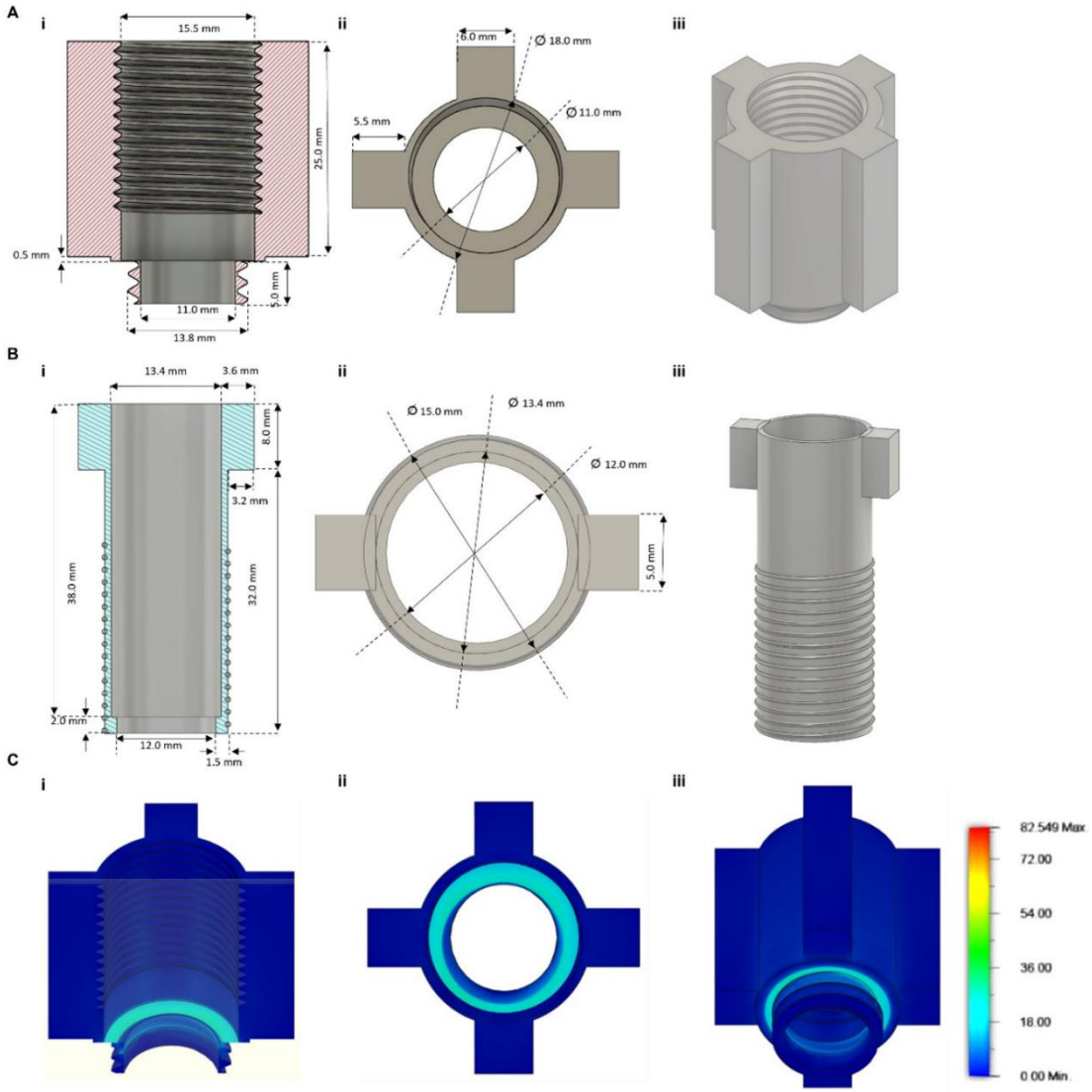

Figure 4-2 Schematic of A) cranial bolt with a i) side view cross-section, ii) top view, iii) top-angled side view and the corresponding B) focusable probe sleeve with its i) side view cross-section, ii) top view and iii) top-angled side view. C). Top/side i) intersection, ii) top and iii) bottom/side view of the bolt, with stress indicated in the model. The higher stress occurs in an extremely narrow region where the outer thread meets the narrow plate connecting to the body and is not visible.

Table 4-2 Outputs from finite element analysis including torque and the corresponding safety factors for titanium and nylon.

Material	Torque at Fracture (Nm)	Maximum Displacement (mm)	Stress (MPa)	Safety Factor (A.U.)
Titanium 6Al-4V	0.8	0.002	82.55	10.69
	1.6	0.004	165.1	5.35
Nylon 6	0.228	0.025	23.5	3.00
	0.684	0.075	70.5	1

4.4.2 Biomarker Spiked Brain Tissue

To validate the ability of the handheld Intra-RSP to distinguish between TBI brains and healthy control cohorts, two solutions consisting of TBI biomarkers were formulated and integrated into rat brain tissue. Biomarker solution 1 (BS1) contained glucose, myo-inositol, serine and GSH, and biomarker solution 2 (BS2) contained glucose, myo-inositol, serine, GSH, GFAP, S100B and UCHL1. Both solutions contained four identical biomarkers, to further enable the evaluation of the probe's specificity. Representative mean spectra of each biomarker, obtained from **Chapter 2** [26], in solutions BS1 and BS2 presented in Figure 4-3**A** yield the fingerprints of the candidate signature spectral bands for further identification within the spectra of the spiked brain tissue.

Notable spectral differences emerge among the three conditions shown in Figure 4-3**B**, particularly in the 650-800 cm^{-1}, 1100-1250 cm^{-1} and the 1500-1675 cm^{-1} regions. The distinctions between the TBI biomarker-spiked and the control cohorts are validated in the ensuing SOM clustering in Figure 4-3**D**. The SOM clearly defines distinct clusters for each cohort. When only inputting the benchtop recorded healthy control and spiked brains, the SOM clusters the groups to an accuracy of 92% ±0.04 from randomly selected test spectra (n = 60), validating the potential to pick out biochemical changes in the immersed environment. Following the validation of the differentiating spiked brains, spectra were subsequently recorded through a model human skull using the optimised cranial bolt as a validation of the device performance. The BS1-spiked brain tissue was placed under the bolt in the model skull and tested on the SOM, exhibiting a correct classification on the SOM to an accuracy of 80% ±0.21.

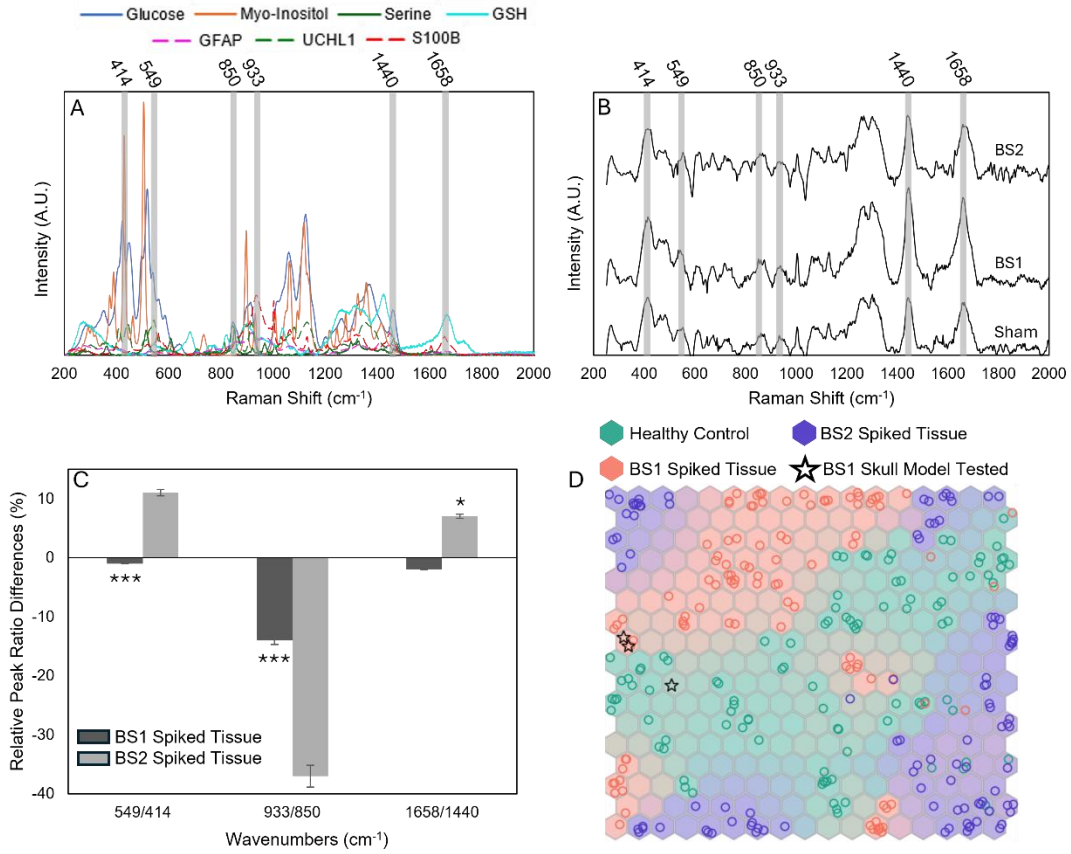

Figure 4-3 – Representative average superimposed spectra of A) individual TBI biomarkers present in BS1 and BS2 solutions including Glucose (dark blue), Myo-Inositol (orange), Serine (dark green), Glutathione (GSH, light blue), Glial Fibrillary Acidic Protein (GFAP, dashed pink), Ubiquitin C-terminal Hydrolase L1 (UCHL1, dashed green) and saS100B (dashed red). Solid line spectra represent biomarkers present both in BS1 and BS2, dashed line spectra are indicative of biomarkers exclusively present in BS2. B) Averaged Raman spectra of control (green), BS1-spiked (red) and BS2-spiked (blue) brains with the highlighted Raman peaks at 414, 549, 850, 933, 1440 and 1658 cm^{-1} of key markers in the evaluation of C) the relative differences in intensity ratios between the 549 and 414 cm^{-1}, the 933 and 850 cm^{-1} and the 1658 and 1440 cm^{-1} peaks for the BS1 (red) and the BS2 (blue) *versus* controls. D) SOM clustering the characteristic features of each cohort for BS1, BS2 spiked brains and controls including the training data (circles) and the three BS1 test spectra (black stars). The SOM classifies healthy controls, BS1, and BS2 brain spectra correctly to an accuracy of 92% ±0.04, and the BS1 brain spectra recorded through the model skull with an accuracy of 80% ±0.21 (*p <0.05 and ***p <0.0001, student's t-test).

Further insights through SOMDI scoring in Table 4-3 quantify pivotal peaks responsible for differentiating between the spectra in Figure 4-3**B**. The scoring assigns a value to each

Raman shift according to its influence in characterising the acquired spectra. Identifying characteristic features of a group enables further comparison of the differences in relative intensity of dominant peak ratios, represented in Figure 4-3**C**.

Relative intensity ratio differences between spiked tissue and healthy controls are used to identify changes within samples using Raman spectral intensities. A significant increase of 11% in the relative intensity ratios for the 414 and 549 cm^{-1} wavenumbers shown in Figure 4-3**C** is observed between the BS2-spiked and the control brain spectra, indicative of a greater presence of skeletal C=C lipid bonds and C-S bonds from cysteine residues, respectively [32]. Cysteine levels are found to be increased in the BS2 spiked brains due to the amino acid's presence in the GSH, GFAP, S100B and UCHL–1 neuromarkers, all of which are biomarkers included in BS2 [33-36].

Within BS1, only GSH contains C-S bonds related to the 549 cm^{-1} Raman shift observed in Table 4-3. Both the 549 and 414 cm^{-1} wavenumbers are more prevalently being picked up by Intra-RSP in the healthy control brains than the BS1-spiked tissue, as demonstrated by the 1% decrease in ratio intensity from the BS1-spiked brain spectra from the control, as well as by the lower SOMDI scores in Table 4-3 for both 414 and 549 cm^{-1} (0.77 and 0.40 for BS1, respectively) in contrast to the control (0.84 and 0.47, respectively) cohort.

The relative difference in intensity ratios for the 1658 and 1440 cm^{-1} between the BS2-spiked and the control spectra further show a significant 7% increase (p <0.05). This is consistent with the addition of amide I bonds to the brain tissue, stemming from the secondary protein structures of the BS2 biomarkers [37, 38], as well as the CH_2 bending associated with the 1440 cm^{-1} peak, also associated with glucose. The 1440 cm^{-1} shift is also commonly indicative of lipids through the twisting of CH_2 bonds. Despite the

absence of lipids in both biomarker solutions, (deliberately omitted due to the need to exclude sample-damaging or Raman active solvents), SOMDI scores reported in Table indicate that the bands both play a significant role in distinguishing the spiked spectra from controls, in correspondence with our previous studies where these were established as TBI-indicative candidates [1, 39]. In addition to the added biomarker solutions, the equally high SOMDI score of 0.90 for the 1440 cm^{-1} band in both the BS1 and BS2 spiked brains could therefore also be due to the ability of Raman spectroscopy to more readily detect lipids compared to proteins and nucleic acids due the abundance of polarizable C-H and C-C bonds.

Furthermore, both the CH_2 rocking, detected in Table 4-3 *via* the 850 cm^{-1} band and the C-C stretching of amino acids, detected *via* the 933 cm^{-1} band [40] are identified by SOMDI as characteristic in differentiating the BS2-spiked brain spectra from the BS1-spiked and control brain tissue with scores of 0.50 and 0.44, respectively. In contrast to the healthy control tissue, those spiked with BS1 and BS2 exhibited a lower relative intensity 850:933 cm^{-1} ratio by 14% and 37%, respectively (Figure 4-3**C**).

Table 4-3 - SOMDI scores for control, BS1 and BS2 brain tissue with the corresponding assignments of the identified characteristic peaks. *ν = stretching; δ = bending; τ = twisting; ρ = rocking; s = symmetric; arom = aromatic; skel = skeletal;* Δ = ring breathing vibration.

Raman Band (cm^{-1})	SOMDI Scores			Assignment	Reference
	Control	BS1	BS2		
267	0.46	0.38	0.46	*Ring mode vibrations*	[41]
414	0.84	0.77	0.78	ν_{skel}(C=C)	[32]
482	0.66	0.58	0.58	ν_{skel}(C=C)	[32]
549	0.47	0.40	0.48	δ(C–S)	[32]
612	0.44	0.31	0.48	ν(–C=CH)	[32]
673	0.39	0.32	0.50	τ(C=C)	[32]
716	0.34	0.33	0.49	ν_s(C–N)	[42]
805	0.32	0.24	0.45	ν_s(O–P–O), ν_s(C–N–C)	[32, 42]
850	0.38	0.37	0.50	$\rho(CH_2)$	[40]
857	0.38	0.34	0.52	ν_s(C–N–C)	[32]
933	0.36	0.29	0.44	ν(C–C)	[40]
1004	0.45	0.39	0.50	$\delta(CH_2)$, Δ_{arom}(C–C)	[43]
1064	0.48	0.38	0.54	ν(C–O), ν(C–C), $\tau(NH_2)$	[42, 44, 45]
1129	0.51	0.39	0.55	ν(C–N), ν(C–C), ν_{skel}(C-C)	[39, 46, 47]
1191	0.46	0.34	0.47	δ (CH), $\omega(CH_2)$	[48]
1267	0.80	0.77	0.87	ν(C–O), δ (CH), *Amide III*	[49-51]
1302	0.83	0.81	0.88	$\tau(CH_2)$	[52]
1440	0.79	0.90	0.90	$\delta(CH_2)$, $\tau(CH_2)$	[53, 54]
1554	0.38	0.33	0.43	$\delta(NH_3^+)$	[32]
1580	0.37	0.29	0.41	Δ_{arom}(C–C), ν(C=O)	[32, 55]
1658	0.74	0.84	0.81	ν(C=O), ν(C=C)	[37, 38]

Similarities between the TBI biomarker spectra in Figure 4-3**A** and the biomarker-spiked brain tissue in Figure 4-3**B** are identified at the 805, 850, 933, 1004, 1130 and 1658 cm^{-1} shifts. Symmetrical C-N-C stretching at 805 cm^{-1} is mainly a contributing factor of the BS2 spiked tissue, with a SOMDI score of 0.45, directly linked to the higher protein content [32], characteristic to UCHL1, D-Serine and GSH biomarkers. The increase in the 850 cm^{-1} SOMDI weight in BS2 samples relative to the control and BS1 spectra is attributed to the rocking of CH_2 bonds in proteins from leucine, which Figure 4-3**B** shows is determinative of UCHL1 [40]. This biomarker is present only in the BS2 solution, rendering the 850 cm^{-1}

shift as a potential predicative band of axonal damage observed through the presence of UCHL1 post-TBI.

S100B, a biomarker only present in BS2, exhibits a characteristic feature peak in Figure 4-3**A** at 933 cm^{-1} [26] for which the BS2-spiked brain spectra are found to exhibit the highest SOMDI scores compared to the control and BS1. The combination of the greater SOMDI score for the 850 and 933 cm^{-1} peaks in BS2-spiked brain tissue and these Raman shifts relating to biomarkers exclusively present in BS2 demonstrate the probe's ability to detect simulated change in a complex biochemical environment.

Further bands at 1004 and 1658 cm^{-1}, common to proteins, are attributed to the aromatic stretching of C-C bonds in the phenylalanine R group and the stretching of C=O bonds in the amide I group, respectively [37, 38, 43]. A lower SOMDI score at 1004 cm^{-1} for BS1-spiked tissue compared to both control and BS2 spiked brain tissue could be a result of the introduction of biomarkers not containing phenylalanine in BS1, consequently overshadowing the significance of this particular protein peak as a characterising feature of the BS1-spiked brain tissue spectrum. This is further shown in Figure 4-3**A**, in which the most intense peak at 1004 cm^{-1} is produced by S100B.

4.4.3 Transcranial Brain Spectra Acquisition

The Intra-RSP probe was further validated on unexposed rat brains through the examination of the brain directly through the skull. The skull itself was found to exhibit a sharp Raman spike at 960 cm^{-1} visible in Figure 4-4**A** due to the high density of PO_4 in

bones [56, 57]. A complete separation in the SOM is detected in Figure 4-4**B** between the rat skull and the transcranial brain (TB), with each test spectrum correctly identified to an accuracy of 99% ±0.03, indicating the unprecedented capacity for transcranial

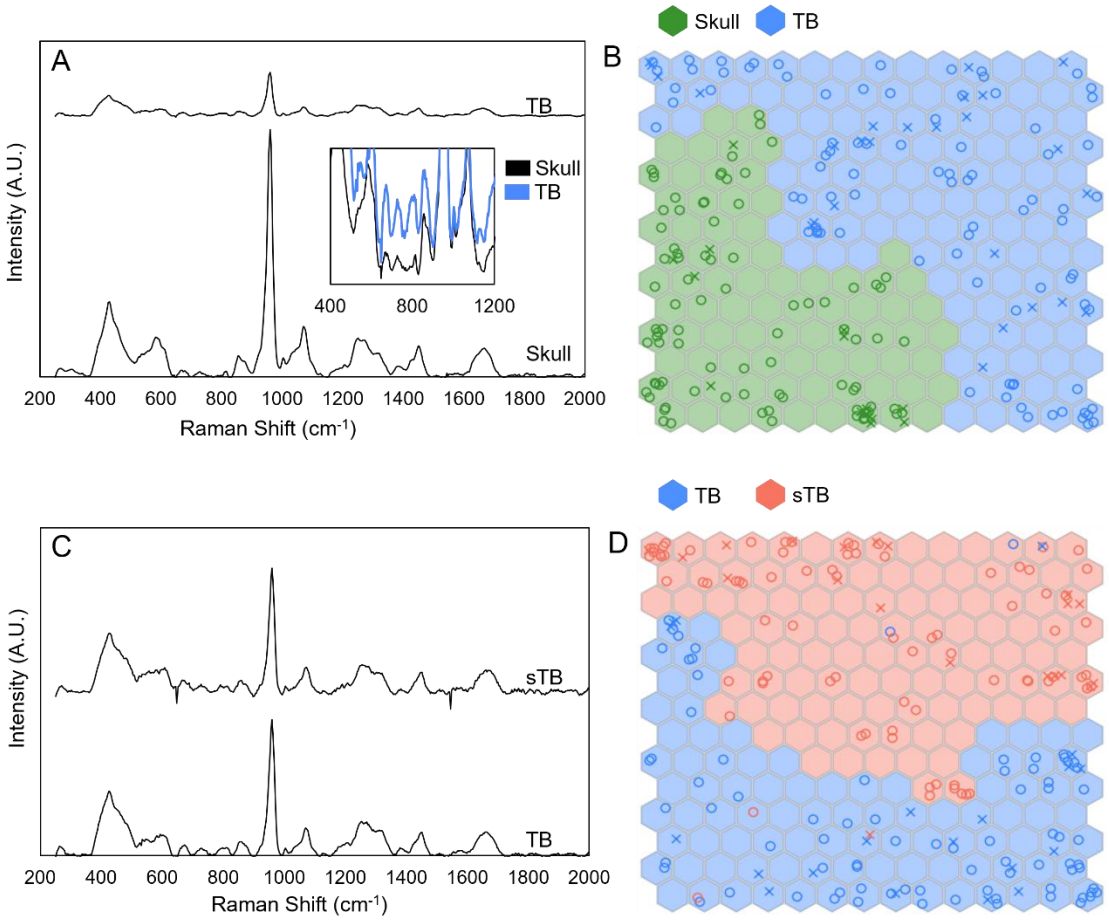

Figure 4-4 - Spectral Analysis of Transcranial Brains. A). Analysis of the average spectra (*n* = 100) of raw skull *versus* brain tissue without removal of the skull *i.e.,* transcranial brain (TB). An extract of the normalised data is included to demonstrate key differences in spectral features, identifying brain tissue related peaks. B). Corresponding SOM, including the training spectra (circles) and test spectra (crosses) within a set of spectra to ascertain the differentiation of skull and skull covering rat brains with an accuracy of 99% ±0.03. (C). Average spectra of spiked transcranial brains (sTB) spiked with BS2 solution *versus* TB with the corresponding D) SOM, accurate to 92.8% ±0.06.

spectroscopy. Whilst the baseline subtracted spectra in Figure 4-4**A** appear to show similar peaks at vastly different intensities, the focussed normalized spectral data extract reveals brain tissue representative Raman shifts primarily in the 600-800 cm^{-1} region for the TB absent in the skull's spectra, visually confirming recorded spectral differences.

Brain tissue was subsequently spiked under the skull and spectra were acquired for comparison, demonstrated in Figure 4-4**C**. To ensure a uniform coverage, these were spiked with BS2 in two locations, once into the left cerebral hemisphere and once into the right. Although a general spectral homology is observed, SKiNET successfully extracts characteristic features distinguishing the transcranial brains from spiked transcranial brains (sTB) in a SOM in Figure 4-4**D** with a classification accuracy of 92.8% ±0.06. Ultimately, the probe in conjunction with SKiNET demonstrates the device's capability to detect subtle changes in sample conditions without direct exposure, which may be used as a crucial stepping stone into less invasive animal testing, paediatric TBI studies and technological developments.

4.4.4 Classification of brain tissue extracted from spinal cord injured animals

To further assess the probe's ability to distinguish biochemical changes, a comparative analysis between brains extracted from SCI and healthy rats was performed. A traumatic injury to the spine can cause neuroinflammation and neurodegeneration in the brain,

observable through axonal degeneration and cellular shrinkage, effectively simulating a mild TBI [18-20].

Figure 4-5 establishes the probe's capacity to differentiate between the left cerebral hemispheres of rat brains with injured spines *versus* healthy controls. Whilst the average spectra (n = 100) for each cohort (Figure 4-5**A**) show a homology between control and SCI injured samples, the relative intensity ratios (Figure 4-5**B**) exhibit certain differences.

Firstly, the lipid to protein ratio detected *via* the 1444 and 1661 cm^{-1} bands [1, 39, 51] are found to be significantly increased (p <0.05) in the SCI in contrast to the healthy rat brains. This is in accordance with the previously observed increased presence in lipids following damage to spinal cord tissue [20]. Furthermore, the relative intensity ratio between the 533 and 409 cm^{-1} peaks is found to be decreased by 44% in SCI compared to the uninjured brains, indicating an alteration of the disulfide bond concentration, possibly due to the changing levels of protein in the SCI brains [32]. There is a further 50% relative ratio decrease in the 1004:864 cm^{-1} peak ratio between the control and the SCI brains, attributed to the phenylalanine residues and backbone peptide bonds [42, 43]. Collectively, these detected changes not only cement the Intra-RSP's ability to detect subtle biochemical post injury variations but also establish the detection of the potential damage and dysregulation occurring in the brain as a result of SCI. The identified changes are found to be consistent throughout the analysed samples (n = 100) (Figure 4-5**C**).

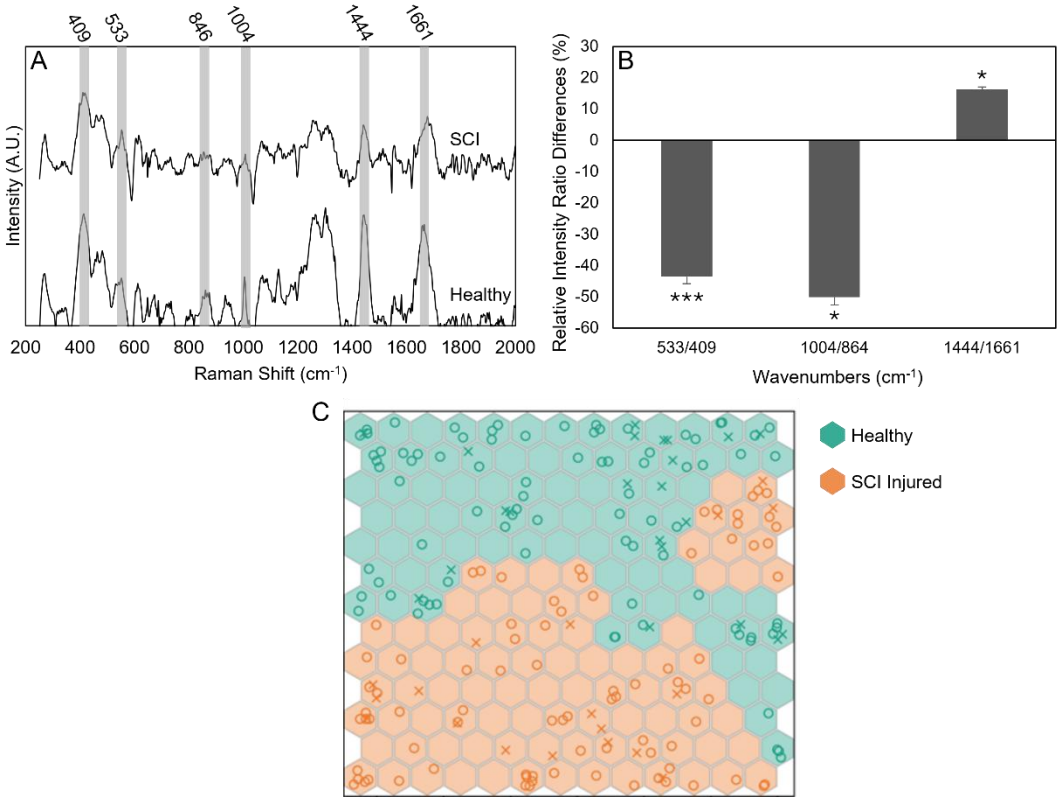

Figure 4-5 - Spectral Brain Analysis of SCI Injured Rodents. A) Representative average Raman spectra of SCI injured (orange) rat brains *versus* the uninjured control cohort (green), with highlighted peaks used to investigate B) the difference in relative intensity ratios between injured and uninjured rats using 533/409, 1004/864 and 1444/1661 cm^{-1} ratios. Error bars present the standard error. C) SOM classification of healthy control brain spectra (green) *vs*. SCI injured (orange), with training (circles) and test (crosses) data with an accuracy of 94.5% ±0.03. (*p <0.05 and ***p<0.0001, student's t-test).

Additionally detected Raman shifts at 1213 and 1553 cm^{-1} in Table 4-4 are attributed to Haem groups in deoxygenated cells and the lipid C=C stretching and protein NH_3^+ bending, respectively [32, 58, 59]. The corresponding SOMDI scores exhibit a greater importance in SCI rat brains relative to controls, at 0.60 for 1213 cm^{-1} and 0.63 for 1553 cm^{-1}, and 0.53 for 1213 cm^{-1} and 0.39 for 1553 cm^{-1}, respectively. These are indicative of a higher level of hypoxia from the injured rats; however, some hypoxia is expected in both conditions from the sacrifice [59, 60].

Table 4-4 - SOMDI scores for SCI injured rat brains and the corresponding spectral assignments. *v = stretching; δ = bending; τ = twisting; ρ = rocking; s = symmetric; arom = aromatic; skel = skeletal;* Δ = ring breathing vibration.

Raman Band (cm^{-1})	SOMDI Scores		Assignment	References
	Control	Injured		
269	0.47	0.64	*Ring mode vibrations*	[41]
409	0.83	0.95	v_{skel}(C=C*)*	[32]
484	0.63	0.78	*v*(S–S)	[32]
533	0.46	0.60	*v*(S–S)	[32]
549	0.48	0.65	*δ*(C–S)	[32]
619	0.42	0.65	*v*(–C=CH)	[32]
688	0.35	0.44	*v*(C–S)	[32, 42]
864	0.38	0.54	v_s(C–N–C)	[32]
938	0.34	0.52	*v*(C–C)	[40]
1004	0.47	0.52	*δ*(CH_2), Δ_{arom}(C–C)	[42, 43]
1066	0.48	0.64	v(C–O), v(C–C), τ(NH_2)	[32, 44, 45]
1128	0.52	0.62	*v*(C–N), *v*(C–C)*,* v_{skel}(C–C)	[39, 46, 47]
1200	0.40	0.41	δ (CH), ω(CH_2)	[48]
1213	0.53	0.60	*v*(C=C)*, Deoxygenated cells*	[58, 59]
1258	0.67	0.69	*Amide III*	[51, 61]
1300	0.80	0.70	*τ*(CH_2)	[52]
1314	0.73	0.68	δ(CH), *v*(NH) Amide I Couplet	[32, 62, 63]
1377	0.27	0.44	v_s(COO^-)	[64]
1444	0.79	0.74	*δ*(CH_2), *τ*(CH_2)	[53, 54]
1513	0.29	0.60	*v*(NH)	[32]
1553	0.39	0.63	δ(NH_3^+), *Deoxygenated cells*	[32, 59]
1661	0.71	0.71	*v*(C=O), *v*(C=C)	[37, 38]

Characteristic peaks at 688 and 1377 cm^{-1}, attributed to the stretching of C-S bonds in cysteine and carboxylic acid from amino acids, respectively [32, 42, 64], are found to significantly contribute to the SOM classification of SCI samples exhibiting an increase in protein content, in accordance with the study by Wu *et* al. as a response to spinal cord trauma [20]. This further validates the probe's ability to rapidly detect, and *in-situ* differentiate the biochemical changes within the brain's environment, with an accuracy of 94.5% ±0.03. In addition to the 688 and 1377 cm^{-1} peaks, the 484 and 533 cm^{-1} shifts

arising from the disulfide bonds, the 1004 cm^{-1}, attributed phenylalanine, the 1661 cm^{-1} amide I and the 1258 cm^{-1} amide III group shifts are all observed to be scored less by the SOMDI in the control relative to the injured cohort (Table 4-4), collectively pointing to the occurrence of protein accumulation [20, 32, 37, 38, 42, 43, 61] post brain trauma.

Finally, the correlation between the SCI brains (Figure 4-5**A**) and the TBI indicative biomarkers from Table 4-1 can be established. The acute phase response and neuroinflammation are identified through the detection of IL-6, exhibiting characteristic Raman shifts at 549, 1128, and 1066 cm^{-1} [26, 65]. IL-6, typically undetectable in healthy brain tissue, is upregulated in response to trauma for neuron salvation [66].

An increased S100B presence indicates mitochondrial structural damage as well as cellular death. S100B indicative Raman shifts present in the SCI brains at 938, 1066, and 1128 cm^{-1} are all depicted in Table 4-4 as exhibiting higher SOMDI scores for the injured (0.52, 0.64 and 0.62, respectively) compared to the controls (0.38, 0.48 and 0.52, respectively) [67].

Raman shifts at 1066, 1128 and 1300 cm^{-1} are common to both the SCI brains and sphingomyelin, with roles in cellular regulation and brain myelination [68], gangliosides, which if disrupted, causes neurodegeneration [69], and sulfatides, which affect membrane functional properties [26, 70]. The 1066 cm^{-1} band is particularly indicative of GFAP, which if overexpressed leads to glial scars and delayed axonal regeneration [14, 71].

An increase in UCHL1 following axonal damage as an aid in the removal of damaged axonal proteins, exhibits a characteristic Raman band in common with the SCI brains at

1128 cm^{-1} [12, 26]. IL-18 shares a characteristic peak with the brain tissue spectra at 1258 cm^{-1} [26]. IL-18 is an inflammatory cytokine inducer, which in response to trauma causes a release of neurotoxic enzymes [72]. Table 4-4 indicates a slightly higher influence from this peak in the characterisation of damaged tissue than control.

Cardiolipin plays key roles in mitochondrial metabolism and acts as a signal for mitophagy [73, 74]. The shift present at 1300 cm^{-1} can therefore be targeted to monitor mitochondrial damage in the SCI brains. Finally, a Raman shift common to both the tissue and NAA at 1377 cm^{-1} is indicative in an inversely proportional manner to the degree of injury, where the damaged tissue is significantly more influential with a score of 0.44 compared to the 0.27 in the healthy controls [75, 76].

Overall, the probe's ability to detect signature peak changes representative of a multiplex of TBI biomarkers is a promising technological development. The long-term potential for the device to enable real-time monitoring of evolving injuries post-TBI is an important step towards the identification of therapeutic targets.

4.5 Conclusions

Herein, we design, engineer, optimise and establish Raman spectroscopy-based measurements utilising the specificity of inelastic scattering of light for TBI assessment. Through standard clinically established cranial access techniques, undertaken in admissions to secondary care, the Intra-RSP exhibits potential to track the pathology and injury evolution. This study demonstrates the efficacity of our developed and optimised

biologically safe handheld Intra-RSP to distinguish changes in the brain's biochemical environment within TBI simulated samples. The development of a self-tapping three-dimensionally printed cranial bolt with mechanical stress test simulations for auto-tapping thread, when combined with the Intra-RSP, is established, and validated to be efficiently functional under conditions mimicking the real-world scenarios.

The developed probe-device is further validated in a rat model presenting mild TBI, as a result of SCI, differentiating between the CNS injured animals and the healthy controls, thus rapidly classifying injuries *via* SKiNET. Finite element analysis confirms that titanium is the most compatible and safe material, ensuring the bolts integrity even under high torques. The Intra-RSP accurately and rapidly detects and differentiates brains spiked with indicative biomarkers of sTBI from both direct and indirect brain surface exposure. Spectral signatures associated with these biomarkers are identified through an AI developed algorithm and its corresponding feature extraction discriminant index, SOMDI, provides further insights into characteristic spectral features. By quantitatively attributing changes to the underlying biochemistry, it characterises the spiked brain tissue by highlighting the dominant wavenumbers distinguishing TBI samples from controls. Similarly, brains from SCI injured rats are differentiated from the healthy controls to an accuracy of 94.5% ±0.03. This not only solidifies the ability of the probe to separate representative TBI brains from non-TBI, but also supports existing evidence of potential brain damage accompanying SCI.

Further work is needed to include varying concentrations of the biomarker solutions to establish limits of detection as well as trials for *in-vivo* TBI models. With optimisation and *in-vivo* validation, the Intra-RSP will be translatable for integration into currently available

standards of neurological care as an *in-situ* neuromonitoring modality. Real-time spectroscopy of TBI pathology *via* the developed Intra-RSP 'brain-optical' interface to track injury evolution will, in the long-term, improve target-management and understanding of injury heterogeneity, evolution, penetrance of pharmacological agents, identify novel targets for intervention and will lay the platform as a modality for disease modifying therapies in TBIs.

4.6 References

[1] M. Mowbray, C. Banbury, J. J. Rickard, D. J. Davies, and P. Goldberg Oppenheimer, "Development and Characterization of a Probe Device toward Intracranial Spectroscopy of Traumatic Brain Injury," *ACS biomaterials science & engineering,* vol. 7, no. 3, pp. 1252-1262, 2021.

[2] M. Galgano, G. Toshkezi, X. Qiu, T. Russell, L. Chin, and L.-R. Zhao, "Traumatic brain injury: current treatment strategies and future endeavors," *Cell transplantation,* vol. 26, no. 7, pp. 1118-1130, 2017.

[3] M. Smith, "Monitoring intracranial pressure in traumatic brain injury," *Anesthesia & Analgesia,* vol. 106, no. 1, pp. 240-248, 2008.

[4] I. Jalloh, K. L. Carpenter, A. Helmy, T. A. Carpenter, D. K. Menon, and P. J. Hutchinson, "Glucose metabolism following human traumatic brain injury: methods of assessment and pathophysiological findings," *Metabolic brain disease,* vol. 30, pp. 615-632, 2015.

[5] P. M. Vespa *et al.*, "Persistently low extracellular glucose correlates with poor outcome 6 months after human traumatic brain injury despite a lack of increased lactate: a microdialysis study," *Journal of Cerebral Blood Flow & Metabolism,* vol. 23, no. 7, pp. 865-877, 2003.

[6] M. Haris, K. Cai, A. Singh, H. Hariharan, and R. Reddy, "In vivo mapping of brain myo-inositol," *Neuroimage,* vol. 54, no. 3, pp. 2079-2085, 2011.

[7] S. Ashwal *et al.*, "Proton spectroscopy detected myoinositol in children with traumatic brain injury," *Pediatric research,* vol. 56, no. 4, pp. 630-638, 2004.

[8] A. J. López-Gambero, C. Sanjuan, P. J. Serrano-Castro, J. Suárez, and F. Rodríguez de Fonseca, "The biomedical uses of inositols: A nutraceutical approach to metabolic dysfunction in aging and neurodegenerative diseases," *Biomedicines,* vol. 8, no. 9, p. 295, 2020.

[9] S. A. Tapanes *et al.*, "Inhibition of glial D-serine release rescues synaptic damage after brain injury," *Glia,* vol. 70, no. 6, pp. 1133-1152, 2022.

[10] L. Koza and D. A. Linseman, "Glutathione precursors shield the brain from trauma," *Neural regeneration research,* vol. 14, no. 10, p. 1701, 2019.

[11] N. Khatri, M. Thakur, V. Pareek, S. Kumar, S. Sharma, and A. K. Datusalia, "Oxidative stress: major threat in traumatic brain injury," *CNS & Neurological Disorders-Drug Targets (Formerly Current Drug Targets-CNS & Neurological Disorders),* vol. 17, no. 9, pp. 689-695, 2018.

[12] S. Shahjouei *et al.*, "The diagnostic values of UCH-L1 in traumatic brain injury: a meta-analysis," *Brain injury,* vol. 32, no. 1, pp. 1-17, 2018.

[13] Z. Yang and K. K. Wang, "Glial fibrillary acidic protein: from intermediate filament assembly and gliosis to neurobiomarker," *Trends in neurosciences,* vol. 38, no. 6, pp. 364-374, 2015.

[14] S.-F. Tzeng, H.-Y. Hsiao, and O.-T. Mak, "Prostaglandins and cyclooxygenases in glial cells during brain inflammation," *Current Drug Targets-Inflammation & Allergy,* vol. 4, no. 3, pp. 335-340, 2005.

[15] A. Goyal *et al.*, "S100b as a prognostic biomarker in outcome prediction for patients with severe traumatic brain injury," *Journal of neurotrauma,* vol. 30, no. 11, pp. 946-957, 2013.

[16] I. Inc. "RamanProbe TM II." http://www.inphotonics.com/probeii.htm (accessed 28/04/22, 2022).
[17] *General Catalogue*, 2023, p. 270. [Online]. Available: https://karnasch.tools/en/all-products/sinking-tools/stub-subland-drills/hss-xe-subland-drill-401020080/. Accessed: 27/08/2024.
[18] B. C. Hains, J. A. Black, and S. G. Waxman, "Primary cortical motor neurons undergo apoptosis after axotomizing spinal cord injury," *Journal of Comparative Neurology,* vol. 462, no. 3, pp. 328-341, 2003.
[19] N. Klapka *et al.*, "Suppression of fibrous scarring in spinal cord injury of rat promotes long-distance regeneration of corticospinal tract axons, rescue of primary motoneurons in somatosensory cortex and significant functional recovery," *European Journal of Neuroscience,* vol. 22, no. 12, pp. 3047-3058, 2005.
[20] J. Wu *et al.*, "Spinal cord injury causes brain inflammation associated with cognitive and affective changes: role of cell cycle pathways," *Journal of Neuroscience,* vol. 34, no. 33, pp. 10989-11006, 2014.
[21] C. Banbury *et al.*, "Development of the self optimising Kohonen index network (SKiNET) for Raman spectroscopy based detection of anatomical eye tissue," *Scientific reports,* vol. 9, no. 1, p. 10812, 2019.
[22] T. Kohonen, "Self-organized formation of topologically correct feature maps," *Biological cybernetics,* vol. 43, no. 1, pp. 59-69, 1982.
[23] G. R. Lloyd, K. Wongravee, C. J. Silwood, M. Grootveld, and R. G. Brereton, "Self Organising Maps for variable selection: Application to human saliva analysed by nuclear magnetic resonance spectroscopy to investigate the effect of an oral healthcare product," *Chemometrics and Intelligent Laboratory Systems,* vol. 98, no. 2, pp. 149-161, 2009.
[24] K. Wongravee, G. R. Lloyd, C. J. Silwood, M. Grootveld, and R. G. Brereton, "Supervised self organizing maps for classification and determination of potentially discriminatory variables: illustrated by application to nuclear magnetic resonance metabolomic profiling," *Analytical chemistry,* vol. 82, no. 2, pp. 628-638, 2010.
[25] M. Dong *et al.*, "Standardized methods to generate mock (spiked) clinical specimens by spiking blood or plasma with cultured pathogens," *Journal of applied microbiology,* vol. 120, no. 4, pp. 1119-1129, 2016.
[26] G. Harris, C. A. Stickland, M. Lim, and P. Goldberg Oppenheimer, "Raman Spectroscopy Spectral Fingerprints of Biomarkers of Traumatic Brain Injury," *Cells,* vol. 12, no. 22, p. 2589, 2023.
[27] A. R. Stevens *et al.*, "Implantable and transcutaneous photobiomodulation promote neuroregeneration and recovery of lost function after spinal cord injury," *Bioengineering & Translational Medicine,* p. e10674, 2024.
[28] S. Lek and Y. Park, "Artificial neural networks," in *Encyclopedia of Ecology, Five-Volume Set*: Elsevier Inc., 2008, pp. 237-245.
[29] J. Ward, J. Clarkson, D. Bishop, and S. Fox, "Good Design Practice for Medical Devices and Equipment–Design Verification," *Institute for Manufacturing,* 2002.
[30] N.-H. Kim, B. V. Sankar, and A. V. Kumar, *Introduction to finite element analysis and design*. John Wiley & Sons, 2018.

[31] "Safety factor result." Autodesk. https://help.autodesk.com/view/fusion360/ENU/?guid=GUID-8D0B2980-6B54-4006-A89E-53C0C2E202B4 (accessed 08/02/2024.
[32] G. Socrates, *Infrared and Raman characteristic group frequencies: tables and charts*. John Wiley & Sons, 2004.
[33] A. Meister and M. E. Anderson, "Glutathione," *Annual review of biochemistry,* vol. 52, no. 1, pp. 711-760, 1983.
[34] R. Jensen, D. R. Marshak, C. Anderson, T. J. Lukas, and D. M. Watterson, "Characterization of human brain S100 protein fraction: amino acid sequence of S100β," *Journal of neurochemistry,* vol. 45, no. 3, pp. 700-705, 1985.
[35] Y. Kajimoto, T. Hashimoto, Y. Shirai, N. Nishino, T. Kuno, and C. Tanaka, "cDNA cloning and tissue distribution of a rat ubiquitin carboxyl-terminal hydrolase PGP9. 5," *The Journal of Biochemistry,* vol. 112, no. 1, pp. 28-32, 1992.
[36] S. A. Reeves, L. J. Helman, A. Allison, and M. A. Israel, "Molecular cloning and primary structure of human glial fibrillary acidic protein," *Proceedings of the National Academy of Sciences,* vol. 86, no. 13, pp. 5178-5182, 1989.
[37] R. Galli *et al.*, "Rapid label-free analysis of brain tumor biopsies by near infrared Raman and fluorescence spectroscopy—a study of 209 patients," *Frontiers in oncology,* vol. 9, p. 1165, 2019.
[38] E. Timchenko, L. Zherdeva, P. Timchenko, L. Volova, and U. Ponomareva, "Detailed analysis of the structural changes of bone matrix during the demineralization process using Raman spectroscopy," *Physics Procedia,* vol. 73, pp. 221-227, 2015.
[39] J. M. Surmacki, L. Ansel-Bollepalli, F. Pischiutta, E. R. Zanier, A. Ercole, and S. E. Bohndiek, "Label-free monitoring of tissue biochemistry following traumatic brain injury using Raman spectroscopy," *Analyst,* 10.1039/C6AN02238C vol. 142, no. 1, pp. 132-139, 2017, doi: 10.1039/C6AN02238C.
[40] P. Freire, F. M. Barboza, J. A. Lima, F. Melo, and J. Mendes Filho, "Raman spectroscopy of amino acid crystals," *Raman Spectroscopy and Applications,* vol. 201, p. 171, 2017.
[41] P. Bock *et al.*, "Infrared and Raman spectra of lignin substructures: Dibenzodioxocin," *Journal of Raman Spectroscopy,* vol. 51, no. 3, pp. 422-431, 2020.
[42] G. Pezzotti, "Raman spectroscopy in cell biology and microbiology," *Journal of Raman Spectroscopy,* vol. 52, no. 12, pp. 2348-2443, 2021.
[43] A. Guimarães *et al.*, "Near Infrared Raman Spectroscopy (NIRS): A technique for doping control," *Spectroscopy,* vol. 20, no. 4, pp. 185-194, 2006.
[44] M. Jahmani, M. Hammadeh, M. Al Smadi, and M. K. Baller, "Label-free evaluation of chromatin condensation in human normal morphology sperm using Raman spectroscopy," *Reproductive Sciences,* vol. 28, pp. 2527-2539, 2021.
[45] S. Tfaili, C. Gobinet, G. Josse, J.-F. Angiboust, M. Manfait, and O. Piot, "Confocal Raman microspectroscopy for skin characterization: a comparative study between human skin and pig skin," *Analyst,* vol. 137, no. 16, pp. 3673-3682, 2012.
[46] A. Synytsya, M. Judexova, D. Hoskovec, M. Miskovicova, and L. Petruzelka, "Raman spectroscopy at different excitation wavelengths (1064, 785 and 532 nm) as a tool

for diagnosis of colon cancer," *Journal of Raman Spectroscopy,* vol. 45, no. 10, pp. 903-911, 2014.

[47] K. Katsara, K. Psatha, G. Kenanakis, M. Aivaliotis, and V. M. Papadakis, "Subtyping on live lymphoma cell lines by raman spectroscopy," *Materials,* vol. 15, no. 2, p. 546, 2022.

[48] P. C. Babu, N. Sundaraganesan, S. Sudha, V. Aroulmoji, and E. Murano, "Molecular structure and vibrational spectra of Irinotecan: A density functional theoretical study," *Spectrochimica Acta Part A: Molecular and Biomolecular Spectroscopy,* vol. 98, pp. 1-6, 2012.

[49] Y. Cao, D. Shen, Y. Lu, and Y. Huang, "A Raman-scattering study on the net orientation of biomacromolecules in the outer epidermal walls of mature wheat stems (Triticum aestivum)," *Annals of Botany,* vol. 97, no. 6, pp. 1091-1094, 2006.

[50] C. Banbury *et al.*, "Spectroscopic detection of traumatic brain injury severity and biochemistry from the retina," *Biomedical optics express,* vol. 11, no. 11, pp. 6249-6261, 2020.

[51] Z. Movasaghi, S. Rehman, and I. U. Rehman, "Raman spectroscopy of biological tissues," *Applied Spectroscopy Reviews,* vol. 42, no. 5, pp. 493-541, 2007.

[52] A. Ricciardi *et al.*, "Raman spectroscopy characterization of the major classes of plasma lipoproteins," *Vibrational Spectroscopy,* vol. 109, p. 103073, 2020.

[53] E. Staniszewska-Slezak, K. Malek, and M. Baranska, "Complementary analysis of tissue homogenates composition obtained by Vis and NIR laser excitations and Raman spectroscopy," *Spectrochimica Acta Part A: Molecular and Biomolecular Spectroscopy,* vol. 147, pp. 245-256, 2015.

[54] C. Farber, M. Shires, K. Ong, D. Byrne, and D. Kurouski, "Raman spectroscopy as an early detection tool for rose rosette infection," *Planta,* vol. 250, pp. 1247-1254, 2019.

[55] L.-L. Tay, R. G. Tremblay, J. Hulse, B. Zurakowski, M. Thompson, and M. Bani-Yaghoub, "Detection of acute brain injury by Raman spectral signature," *Analyst,* vol. 136, no. 8, pp. 1620-1626, 2011.

[56] Y. Ishimaru *et al.*, "Raman spectroscopic analysis to detect reduced bone quality after sciatic neurectomy in mice," *Molecules,* vol. 23, no. 12, p. 3081, 2018.

[57] J. S. Nyman *et al.*, "Measuring differences in compositional properties of bone tissue by confocal Raman spectroscopy," *Calcified tissue international,* vol. 89, pp. 111-122, 2011.

[58] I. Palings, J. A. Pardoen, E. Van den Berg, C. Winkel, J. Lugtenburg, and R. A. Mathies, "Assignment of fingerprint vibrations in the resonance Raman spectra of rhodopsin, isorhodopsin, and bathorhodopsin: implications for chromophore structure and environment," *Biochemistry,* vol. 26, no. 9, pp. 2544-2556, 1987.

[59] B. R. Wood, P. Caspers, G. J. Puppels, S. Pandiancherri, and D. McNaughton, "Resonance Raman spectroscopy of red blood cells using near-infrared laser excitation," *Analytical and bioanalytical chemistry,* vol. 387, pp. 1691-1703, 2007.

[60] H. Doshi *et al.*, "Cerebral hemodynamic changes of mild traumatic brain injury at the acute stage," *PloS one,* vol. 10, no. 2, p. e0118061, 2015.

[61] D. Tong *et al.*, "Application of Raman spectroscopy in the detection of hepatitis B virus infection," *Photodiagnosis and photodynamic therapy,* vol. 28, pp. 248-252, 2019.
[62] Z. Wen, L. Hecht, and L. Barron, "β-Sheet and associated turn signatures in vibrational Raman optical activity spectra of proteins," *Protein Science,* vol. 3, no. 3, pp. 435-439, 1994.
[63] K. I. Hadjiivanov *et al.*, "Power of infrared and raman spectroscopies to characterize metal-organic frameworks and investigate their interaction with guest molecules," *Chemical Reviews,* vol. 121, no. 3, pp. 1286-1424, 2020.
[64] B. A. Marekha *et al.*, "Intermolecular interactions in mixtures of 1-n-butyl-3-methylimidazolium acetate and water: Insights from IR, Raman, NMR spectroscopy and quantum chemistry calculations," *Journal of Molecular Liquids,* vol. 210, pp. 227-237, 2015.
[65] R. Kumar *et al.*, "Acute CSF interleukin-6 trajectories after TBI: associations with neuroinflammation, polytrauma, and outcome," *Brain, behavior, and immunity,* vol. 45, pp. 253-262, 2015.
[66] G. Schett, "Physiological effects of modulating the interleukin-6 axis," *Rheumatology,* vol. 57, no. suppl_2, pp. ii43-ii50, 2018.
[67] H. Nishiyama, T. Knöpfel, S. Endo, and S. Itohara, "Glial protein S100B modulates long-term neuronal synaptic plasticity," *Proceedings of the National Academy of Sciences,* vol. 99, no. 6, pp. 4037-4042, 2002.
[68] A. V. Alessenko and E. Albi, "Exploring sphingolipid implications in neurodegeneration," *Frontiers in Neurology,* vol. 11, p. 437, 2020.
[69] S. Sipione, J. Monyror, D. Galleguillos, N. Steinberg, and V. Kadam, "Gangliosides in the brain: physiology, pathophysiology and therapeutic applications," *Frontiers in neuroscience,* vol. 14, p. 572965, 2020.
[70] T. Takahashi and T. Suzuki, "Role of sulfatide in normal and pathological cells and tissues," *Journal of lipid research,* vol. 53, no. 8, pp. 1437-1450, 2012.
[71] M. V. Sofroniew, "Molecular dissection of reactive astrogliosis and glial scar formation," *Trends in neurosciences,* vol. 32, no. 12, pp. 638-647, 2009.
[72] S. Alboni, D. Cervia, S. Sugama, and B. Conti, "Interleukin 18 in the CNS," *Journal of neuroinflammation,* vol. 7, no. 1, pp. 1-12, 2010.
[73] G. Paradies, V. Paradies, F. M. Ruggiero, and G. Petrosillo, "Role of cardiolipin in mitochondrial function and dynamics in health and disease: molecular and pharmacological aspects," *Cells,* vol. 8, no. 7, p. 728, 2019.
[74] C. T. Chu *et al.*, "Cardiolipin externalization to the outer mitochondrial membrane acts as an elimination signal for mitophagy in neuronal cells," *Nature cell biology,* vol. 15, no. 10, pp. 1197-1205, 2013.
[75] J. L. Harris *et al.*, "Altered neurochemical profile after traumatic brain injury: 1H-MRS biomarkers of pathological mechanisms," *Journal of Cerebral Blood Flow & Metabolism,* vol. 32, no. 12, pp. 2122-2134, 2012.
[76] R. J. Shannon *et al.*, "Extracellular N-acetylaspartate in human traumatic brain injury," *Journal of neurotrauma,* vol. 33, no. 4, pp. 319-329, 2016.

Chapter 5: Efficacy of Raman Spectroscopy as a Neuromonitoring Tool for the Treatment of SCI Using Photobiomodulation

Results from this chapter have been entirely collected and analysed by **Miss C. A. Stickland**. The investigation was conceptualized by Mr A. Stevens, Mr D. Davies, Prof. Z. Ahmed, **Miss C. A. Stickland** and Prof. P. Goldberg Oppenheimer. Animal tissue samples were provided by Mr A. Stevens, Mr D. Davies and Prof. Z. Ahmed. Procedures performed on animal models were performed by Mr A. Stevens and Prof. Z. Ahmed.

5.1 Abstract

Spinal cord injury (SCI) causes a major stress on healthcare institutions and providers, in both the long and short term, and the current situation provides no feasible SCI therapy for improved functional outcomes. Photobiomodulation (PBM) has been proposed as a novel therapy for SCI, however the exact mechanism of action has remained unclear. Here, Raman spectroscopy is employed to monitor the biochemical changes in spinal cord, dorsal root ganglia (DRG) and brain tissue following PGM on SCI injured animals. Rat models inflicted with experimental SCI were treated with 660 nm light for 1 min per day for 3 days on the spinal cord. While the spinal cord tissue itself exhibited a modest therapeutic response, DRG tissue showed positive responses to PBM and a tendency for the spectra to revert to a healthy baseline, consistent with the DRG's critical role in dendrite growth and axonal regeneration. A more comprehensive investigation involving larger sample sizes and varied time points would be beneficial to acquire definitive results and a more thorough understanding of PBM's mechanism of action. Although there is indication of damage in the brain tissue, there is inconclusive evidence of PBM efficacy throughout the central nervous system as the responses were inconsistent. Among three

hypothetically target monitoring biomarkers, Raman spectroscopy identified fibronectin as the sole candidate to exhibit statistically significant changes in treated and injured tissue with respect to the healthy, suggesting its potential as a therapeutic monitoring target to determine a specific clinical outcome. Glial fibrillary acidic protein and laminin, both tested alongside fibronectin, showed no significant changes, indicating these specific biomarkers may be less suitable for the evaluation of PBM outcomes through Raman spectroscopy. Overall, these findings support the use of Raman spectroscopy as a monitoring tool of PBM for SCI therapy.

5.2 Introduction

SCI victims can be physically affected through motor, sensory and autonomic functions, as well as negatively impacted through emotional and psychological wellbeing. Currently, the standard of care for SCI patients revolves around surgical interventions and rehabilitation in order to alleviate symptoms as well as any secondary complications, but the CNS remains unable to regenerate itself, making any damage to the spinal cord permanent [1, 2]. Research into regenerative treatments for SCI is therefore not only potentially life-changing for patients but would be a massive relief on costs to healthcare systems and patients. Photobiomodulation (PBM) is proposed as a novel approach to SCI treatment, promising due to its non-invasive application as well as its potential anti-inflammatory and neuro-regenerative effects, despite its exact mechanism of action remaining unclear [3].

Cellular chromophores mostly exist within the mitochondria, determining that PBM should effectively influence mitochondrial functions [4]. Upon SCI, mitochondria have shown to have decisive roles throughout different stages of the injury: i) mitochondrial dysfunction, combined with excitotoxicity and free radical formation, causes important neuronal and glial death [5, 6], ii) immune cell expression and inflammation signals are regulated through cellular metabolism [7, 8], iii) axonal regeneration is dependent on mitochondria number and localisation [9, 10], and iv) neural stem progenitor cell proliferation, differentiation and neurogenesis is regulated through mitochondrial abundance [2, 11]. If PBM is capable of influencing the pathophysiology of mitochondria, the aforementioned functions could therefore be regulated towards a positive outcome. Despite definite positive outcomes having been recorded in literature, including anti-inflammatory effects, neural growth, improved neurological function, neuroprotective effects, wound healing acceleration to name but a few, the lack of clear understanding of the underlying biochemical pathways relating PBM to the mitochondria prevents therapeutic targeting of specific functions [4, 12].

The mammalian peripheral nervous system (PNS) has more regenerative properties than the CNS, prompting the examination of the role dorsal root ganglia (DRG) may have in PBM's effectiveness as a treatment [2]. Previous research has indicated that direct application of PBM to DRG has a positive effect on chronic back pain [13]. PBM is expected to influence the hyperexcitability of peripheral neurons which occurs as a result of inflammation and damage. The light influences Na^+, K^+, and Ca^{2+} current flux and ion channels, as well as Ca^{2+} pump function and expression, resulting in increased

intracellular Ca^{2+} that prompt degranulation and endocytic release of ATP, suggesting a possible mechanistic basis for PBM in the PNS [13, 14].

Biomarkers such as fibronectin, laminin, and GFAP are reported to be used in the evaluation of SCI and any therapeutic interventions [15-17]. Fibronectin, an extracellular matrix protein, is typically growth-permissive to axons, and supports cell adhesion and migration. Following SCI, however, fibronectin is deposited and constitutes a core component of the fibrotic scar. This scar initially serves neuroprotective purposes by containing the extent of injury, however provides an axonal growth-inhibitive environment [15]. Laminins are a group of glycoproteins present in the extracellular matrix, also involved in the induction of axonal growth [18, 19]. Endogenous laminin will increase following injury, a phenomenon caused by the axonal regeneration process [20]. GFAP is an intermediate filament-III protein found in the CNS in astrocytes and in the PNS in non-myelinating Schwann cells [21]. The induction of GFAP following injury is thought to be associated with reactive gliosis for the purpose of nerve regeneration [21, 22]. GFAP provides a beneficial marker given its cellular source. It's specificity to indicate neuronal cytoskeletal damage, as opposed to inflammatory markers, increases its appeal as an indicator of damage. Changes in any of these concentrations would be a positive indicator of the effectiveness of PBM as a treatment.

Through the use of Raman spectroscopy, we aim to identify key markers in the therapeutic effects of PBM in the spinal cord, DRG and brain tissue following inflicted SCI in a rat model.

5.3 Methods

5.3.1 Surgical Procedures

Surgical procedures were carried out as described in Stevens *et* al. [23]. Briefly, SCI was inflicted on eight anesthetized (inhalation, 5% isoflurane, 1.8 $Lmin^{-1}$ O_2) Sprague-Dawley (190-250 g, n = 12, male: female 1:1) rats through a dorsal column crush injury on thoracic level 8 (T8). Four of the injured animals were given an implant included in the wound closure. The implant was immobilised directly over the T8 injury site and left in contact with skin. Pre- and post-operative intraperitoneal buprenorphine analgesia was administered in accordance with ethical standard. At 3 days post injury, the animals were sacrificed through exposure to rising CO_2 concentrations. Spinal cord, DRG and whole brain tissue were removed following sacrifice. Spinal cord tissue was transported directly for Raman spectroscopic evaluation, DRG and brain tissue were frozen. Four healthy controls were subjected to all the above, save the dorsal column crush and the device implant. These procedures are all licensed by the UK Home Office and approved by the University of Birmingham Animal and Ethical Review Board.

5.3.2 Photobiomodulation

Delivery of PBM was carried out as described in Stevens *et* al. [23]. Animals implanted with the PBM device received 24.42 $mWcm^{-2}$ of 660 nm light for 1 min per day in the direct orientation to the injury site. Treatment was first administered 15 min post-injury, then every 20-24 hrs for 3 days.

5.3.3 Raman Spectroscopy

Spinal cord tissue was evaluated by Raman spectroscopy within 30 minutes of the animal's death. DRG and brain tissue were thawed at room temperature before placement under the Raman spectrometer. Raman spectra were acquired on Renishaw's Qontor *InVia* confocal Raman spectrometer coupled to a 785 nm laser. Optical measurements were taken through a 50× objective on an adapted microscope (Leica DM 2700M), allowing up to 2.0 µm depth resolution. Spectra were taken using the Renishaw InVia's LiveTrack map scan feature. 25 static scans were taken per animal tissue at two ranges, centred at 690 and 1610 cm^{-1}, at 30 mW laser power (50% on WiRE 5.2), 1 s acquisition time for 10 accumulations, cosmic ray correction enabled.

5.3.4 Data Processing

Raw spectra have been spliced together at 1204 cm^{-1}, baseline subtracted using WiRE 5.2's intelligent polynomial fitting tool with a polynomial order of 11 and is presented as an average spectrum of the 100 spectra per condition. Multivariate analysis was performed using the self-optimizing Kohonen index network (SKiNET) [24], a supervised machine learning method that projects high-dimensional data onto a 2D map for spatial clustering and classification. Self-organising maps (SOM) with a 14 x 14 grid size, as established according to Lek and Park [25], were produced with 10000 iterations and learning vector quantization enabled. The healthy and injured spectra were randomly split 10 times as 80% training data and 20% test data to determine the accuracy of the maps. Separate maps were then constructed using 100% of the healthy and injured spectra as training data in order to test the treated spectra. PBM treated spectra were introduced onto the map and are placed according to the features they share most closely with the trained data on the SOM.

5.4 Results and Discussion

5.4.1 Raman Spectroscopy on SCI Tissue

The aim of this research was to investigate the capacity for Raman spectroscopy to evaluate the potential of PBM as a therapeutic technique for SCI. Table 5-1 assigns Raman

detected peaks to specific bonds and determines their origins. These assignments are referred to throughout the entirety of this section.

Table 5-1 - Associated Raman bands and their assignments. *v* = stretching; δ = bending; τ = twisting; ρ = rocking; s = symmetric; skel = skeletal.

Wavenumber (cm^{-1})	Assignment	Origin	Reference
420	C−(CO)−C	Protein	[26, 27]
547	*?*		
606	δ(*Amide VI;* CO)	Protein	[26]
629	δ(*Amide VI;* O═C−N)	Protein	[26]
700	*Sterol ring*	Cholesterol	[26]
720	v_s(C-N), δ(*Amide V;* C−N)	Phospholipids	[26, 28]
744	*Pyranose breathing*	Heam	[29, 30]
852	*Anomeric pyranose ring v*(CH)	Glucopyranose	[26]
1003	*Ring breathing vibration*	Phenylalanine	[31, 32]
1064	*v*(C−C)	Lipids	[30]
1088	*v*(PO_2^-)	Lipid Head	[26]
1124	*v*(C−N), v_{skel}(C−C)	Lipids	[33, 34]
1293	τ(CH_2)	Lipids	[35]
1345	*v*(CH)	Lipids	[26]
1440	*v*(CH_2/CH_3)	Lipids, Protein	[36]
1613	*v*(*Amide I*; C═O)	Protein	[26]
1661	*v*(*Amide II*; C═O, NH)	Protein	[26]

Given the spinal cord's role as the primary injury location, distinct spectral differences were expected between healthy, injured and treated samples. Figure 5-1**A** depicts the average Raman spectra for healthy, injured and treated rat spinal cords, with prominent spectral peaks highlighted to reflect key markers for each condition.

The Raman shift at 420 cm^{-1}, associated with ring bending in C–OH bonds [26], is present throughout all three conditions, appearing sharpest in the healthy spinal cords and broader in the injured and treated. The broadening suggests increased molecular

interaction or disorder in the injured and treated tissues, evidencing trauma-induced alterations.

The Raman shifts in the notable 700/720 cm^{-1} doublet can be attributed to cholesterol's B-ring deformation [37] and phospholipids [38], respectively. In the injured and treated samples, the 700 cm^{-1} peak intensity qualitatively decreases in relation to the 720 cm^{-1} peak in comparison to the healthy tissue samples, potentially relating to a trauma-related reduction in cholesterol content and organisation. Since the spectra were acquired directly from the white matter of the spinal cord, which is abundant in cholesterol and lipids, this doublet is particularly significant to observe.

The 744 cm^{-1} Raman shift, assigned to pyranose differentiation [26], is present as a broad feature in the healthy tissue, sharpens in the injured, and returns to a broader shape in the treated spinal cords. This pattern links to an increase in polysaccharide interaction [26] with the Raman laser in the injured spinal cords, suggestive of an elevation in polysaccharides levels post-injury which are rectified following PBM treatment. The 1003 cm^{-1} shift, linked to phenylalanine's aromatic side group, commonly serves as an indicator of protein content and appears more prominently in injured tissue at the site of injury, consistent with literature on protein changes following trauma [38, 39]. Protein levels in the treated tissue spectra approximate those in healthy spectra, suggesting a restoration of pre-injury protein content.

A shoulder peak at 1613 cm^{-1} attributed to C═O amino acid amide stretching [26], appears prominently in both the injured and treated tissue. This peak is superimposed on the Amide I 1661 cm^{-1} Raman shift [26], possibly indicating a persistence of injury-

induced amide interactions even post-PBM treatment, highlighting potential residual effects of SCI on protein conformations in the spinal cord.

Multivariate analysis was performed using SKiNET. The SOM, as shown in Figure 5-1**B**, successfully differentiates the healthy spinal cord spectra from the injured to an accuracy of 97% ±0.03, affirming Raman spectrometry's capability of extracting key features specific to each condition. Treated spectra were introduced on the map, tested for similarity, and classified according to their resemblance to either the healthy or the injured data clusters.

Approximately 37.2% of the PBM treated spinal cords were classified as most similar to healthy tissue, indicating treatment partially reverted tissue towards a state similar to pre-injury spectral characteristics. Figure 5-1**C** and Table 5-2 demonstrate that amongst the four treated subjects, the percentage of independent spectral classification of the treated tissue ranged from 96% to 0% classified as most similar to healthy tissue, indicating different responses to the treatment between the subjects. Specifically, sample **1** has the highest response to PBM treatment, and establishes the treatment was consistently effective in this sample, whereas samples **3** and **4** show no spectral difference at this time point. Moreover, treated samples exhibited a tendency to cluster within similar neurons of the SOM, indicating that specific spectral features, which could be associated to specific biomarkers, are contributing to the healing process.

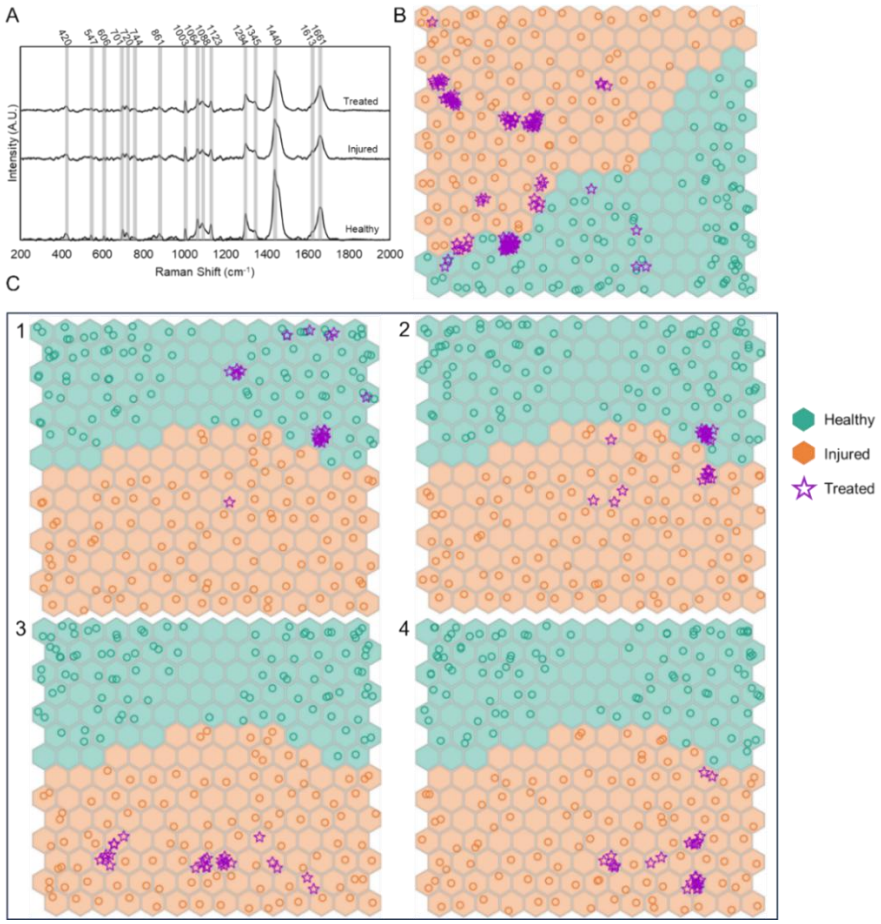

Figure 5-1 – Spinal cord tissue spectral analysis. A) Mean spectra from the healthy, injured and treated rat spinal cords. Spectra are calibrated for x-axis and intensity, and the injured and treated animal spectra are manually moved up for visual clarity. B) Healthy (green) and injured (orange) spinal cords are separated in the SOM, showing that the spectra are capable of being fully separated. The map is used to place treated spectra (purple stars) to identify which features are most similar. C) SOM for the four individual rat spinal cord samples. The animal samples are referred to numerically, **1-4**. The map dimensions are established by Lek and Park [25]. The cross-validation values are tabulated in Table 5-2. The separation of the healthy and injured spectra is accurate to 97% ±0.03.

Table 5-2 – 10-fold cross validation scores for identification of number of PBM treated spinal cord spectra classified as healthy. A total of 25 spectra were taken per animal.

Spinal Cord Sample	1	2	3	4	5	6	7	8	9	10	X-Val Score (%)
1	24/25	24/25	24/25	24/25	24/25	24/25	24/25	24/25	24/25	24/25	**96.0**
2	13/25	14/25	13/25	13/25	14/25	13/25	13/25	13/25	13/25	13/25	**52.8**
3	0/25	0/25	0/25	0/25	0/25	0/25	0/25	0/25	0/25	0/25	**0.0**
4	0/25	0/25	0/25	0/25	0/25	0/25	0/25	0/25	0/25	0/25	**0.0**

DRG, located adjacent to the spinal cord, and are recognised for their axonal regenerative properties [40]. Relevant Raman shifts are highlighted in Figure 5-2**A**. Overall, the average injured spectra display a higher count intensity than those of treated and healthy samples. The average treated spectrum, however, displays less defined peaks than either of the other conditions, suggesting structural or compositional changes. Qualitatively, the first observation is the decreased presence in the treated spectra of the 1061:1088:1124 cm^{-1} triplet, corresponding to the stretching of C–O [30], PO_2^- [26], and skeletal C–C lipid bonds [33, 34], respectively. Secondly, the treated 700:720 cm^{-1} doublet shift exhibits a decreased ratio, in which the cholesterol peak is less prominent than the phospholipids peak.

Elevated ketone levels are expected in SCI, denoted by the increased 420 cm^{-1} peak in the injured spectra, potentially supporting a neuroprotective purpose in their metabolism through macrophage polarisation [27]. Macrophages in nerves and DRG contribute to debris clearing for axonal regeneration, and numbers of DRG macrophages are elevated following nerve damage [40-42]. PBM has previously been shown to activate undifferentiated macrophages, promote and regulate macrophage polarisation, ultimately improving neuronal survival [43-45]; the decrease experienced in the treated spectra from the injured could indicate an accelerated regeneration, thus returning the number of macrophages to a healthy standard.

The overall SOM (Figure 5-2**B**) distinguishes the injured DRG from the healthy to an accuracy of 98.5% ±0.02, indicating effective feature extraction from the spectral data. The clustering in the SOMs appears different here, as each neuron may be activated more

randomly due to fewer distinguishing features in the DRG spectra compared to the spinal cord. As a result, neighbouring neurons are less likely to be assigned weight vectors representing the same class, leading to less coherent clustering. The average classification of 78.2% of the treated spectra into the healthy cluster suggests PBM has a pronounced effect on the DRG compared to spinal cord tissue. When examining the samples individually, they consistently maintained a high percentage efficiency, ranging from 87.2% to 72.0% treated spectra classified as healthy, indicating that the treatment is having a positive effect on all four samples, demonstrated in Figure 5-2**C** and Table 5-3. The clustering of treated spectra with injury characteristics within two neurons indicates specific features of the injured DRG that are determinative in the characterisation of injury of the treated spectra, although there is no present method of recognising which features these are attributed to. Overall, the SOM shows a more even spatial distribution of the healthy classified treated spectra in the healthy cluster, showing a more prominent effect of the PBM treatment in the DRG than in the spinal cord, with a majority considered as a return to healthy baselines.

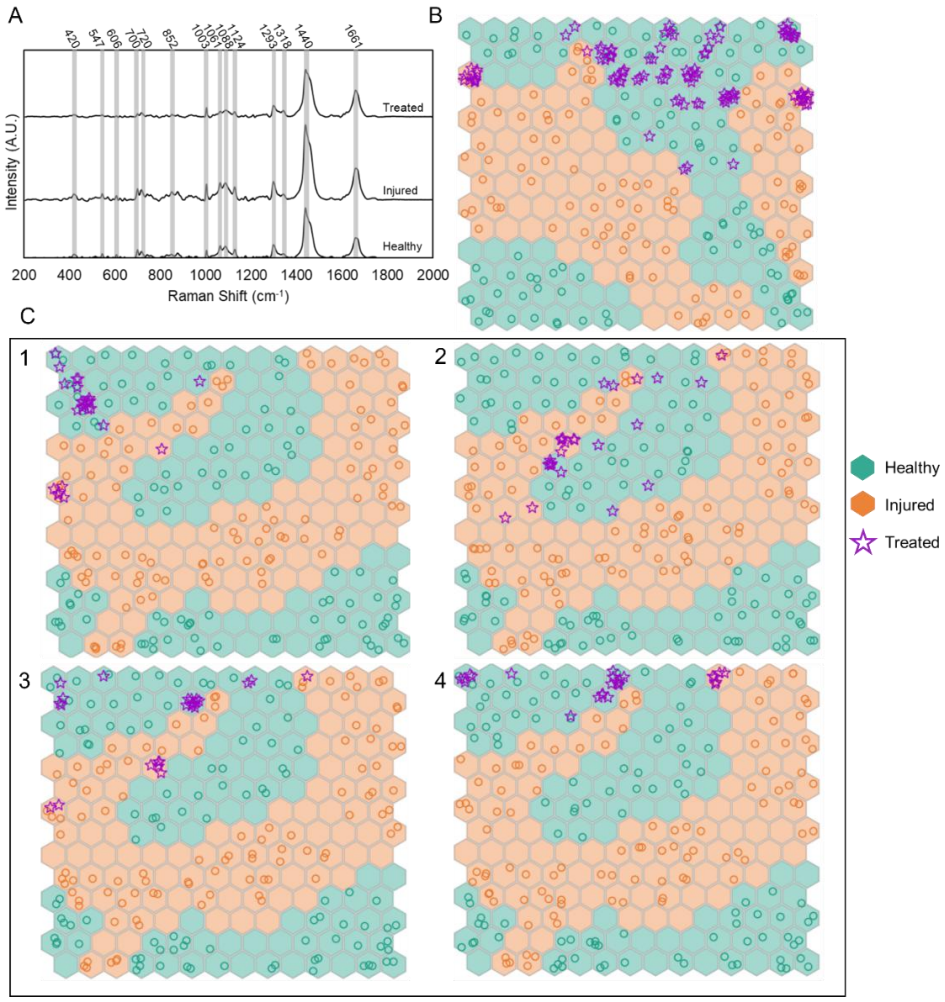

Figure 5-2 – DRG tissue spectral analysis. A) Mean DRG spectra from the healthy, injured and treated animals. B) Healthy (green) and injured (orange) DRG spectra are separated in the SOM, showing that the spectra are capable of being fully separated to an accuracy of 98.5% ±0.02. The map dimensions are established by Lek and Park [25]. The map is used to place treated spectra (purple stars) to identify which features are most similar. C) SOM for the four individual rat DRG samples. The animal samples are referred to numerically, **1-4**. The cross-validation values of each SOM are tabulated in Table 5-3.

Table 5-3 - 10-fold cross validation scores for identification of number of DRG spectra from PBM treated samples classified as healthy. A total of 25 spectra were taken per animal.

DRG Sample	1	2	3	4	5	6	7	8	9	10	X Val Score (%)
1	20/25	24/25	19/25	21/25	21/25	22/25	19/25	24/25	24/25	24/25	**87.2**
2	18/25	19/25	17/25	17/25	19/25	21/25	20/25	21/25	21/25	21/25	**77.6**
3	17/25	17/25	20/25	15/25	20/25	22/25	17/25	17/25	18/25	17/25	**72.6**
4	19/25	19/25	19/25	18/25	20/25	19/25	19/25	19/25	20/25	18/25	**76.0**

Brain samples were considered for their proximity within the CNS, and for their use in assessing the spread of the PBM treatment effect within the CNS. Spectrally, brains from all three cohorts in Figure 5-3**A** resemble each other with few changes in peak geometry. The differences in the 200-330 cm^{-1} region having not been recognised by the peak picking function can be attributed to defects from the background subtraction and are therefore considered as noise. Primarily the 1441 and 1662 cm^{-1} peaks are more intense in the treated spectra than both the injured and healthy, which will be further discussed later with reference to Figure 5-4.

The SOM has a considerably low accuracy of 61.25%, corroborating the similarities between the features. The treated spectra tested on the SOM in Figure 5-3**B** are relatively spread out in the healthy cluster, however those classified as injured are grouped into 3 main neurons, once again indicating a specificity of a feature used in the classification. Examining the animals individually, **1**, **3** and **4** show distinct improvement in the brain as a result of PBM treatment, however given the low accuracy of the SOM and the inconsistencies in their classification as recorded in Table 5-4, these alone cannot be considered as conclusive evidence of PBM efficacy throughout the CNS.

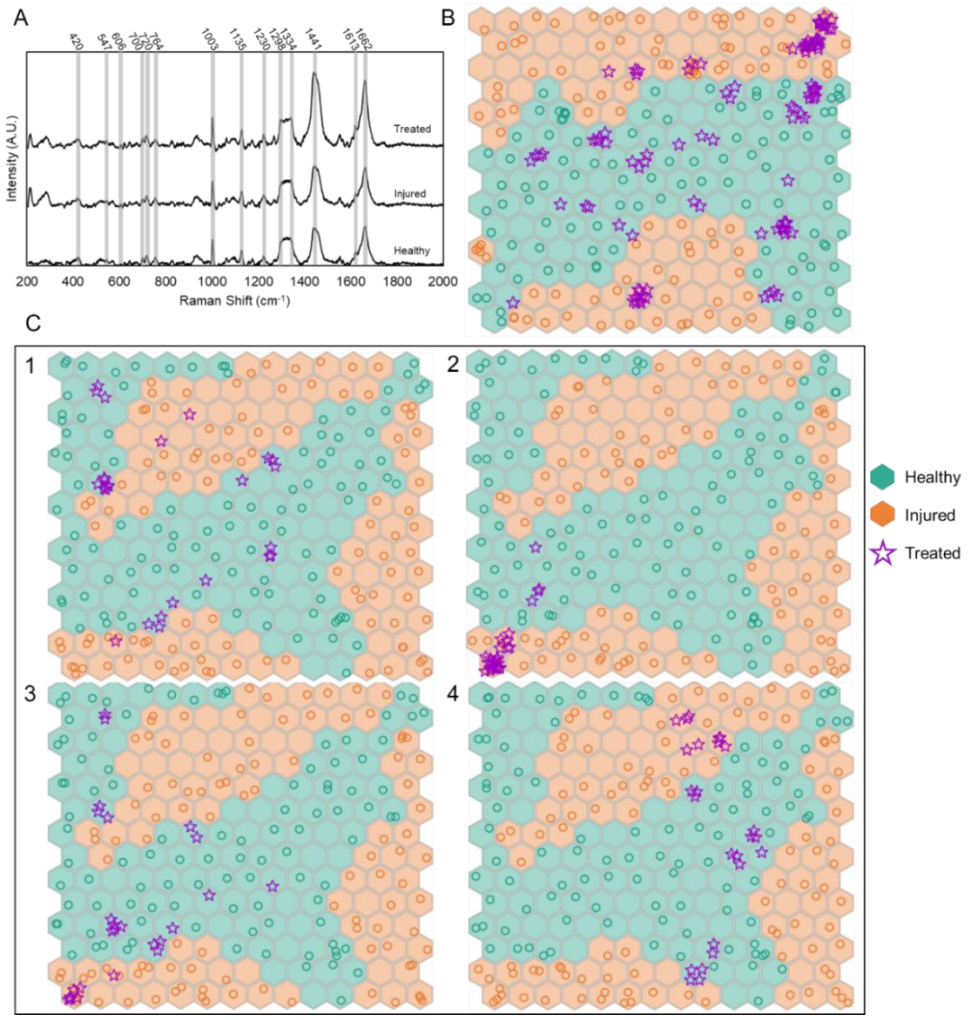

Figure 5-3 – Brain tissue spectral analysis. A) Mean whole brain spectra from the healthy, injured and PBM treated animals. B) Healthy (green) and injured (orange) brain spectra are separated in the SOM, showing separation to an accuracy of 61.25%. The map dimensions are established by Lek and Park [25]. The map is used to classify PBM treated spectra (purple stars) to according to the most similar features. C) Individual SOMs for each PBM treated animal, labelled and referred to in-text as **1-4**. 10-fold cross-validations for these SOMs are tabulated in Table 5-4.

Table 5-4 - 10-fold cross validation scores for identification of number of brain spectra from PBM treated samples classified as healthy. A total of 25 spectra were taken per animal.

Brain Sample	1	2	3	4	5	6	7	8	9	10	X-Val Score (%)
1	21/25	17/25	17/25	17/25	23/25	21/25	17/25	23/25	17/25	24/25	**78.8**
2	6/25	2/25	4/25	10/25	10/25	1/25	6/25	6/25	1/25	1/25	**18.8**
3	17/25	19/25	16/25	16/25	19/25	15/25	17/25	16/25	16/25	16/25	**66.8**
4	18/25	24/25	17/25	19/25	19/25	17/25	16/25	16/25	16/25	15/25	**70.4**

Overall, the values in Table 5-2, Table 5-3, and Table 5-4 consistently show sample **1** as being the most positively affected by PBM treatment, with the highest cross validation of classification in the spinal cord, DRG and brain tissue. Interestingly, despite samples **3** and **4** indicating no meaningful therapeutic effect of PBM on the spinal cord, 72.6% of the DRG spectra from **3** and 76% of the DRG spectra from **4** are classified as healthy, and 66.8% of the brain spectra from **3** and 70.4% of the brain spectra from **4** are classified as healthy. This further indicates that PBM has a positive effect on the CNS, however the animals may not have been given enough time for there to be a spectrally observable improvement in the spinal cord. Furthermore, the improvement in the DRG spectra corroborate their involvement in the regeneration of the spinal cord, and indicate they are a good target for potential therapeutics.

Differences in spectral intensities represented in Figure 5-4 allow for the identification of key changes between conditions. In Figure 5-4**A,** an expected general decrease of intensity is observed in the spinal cord following injury, with notable reductions in intensity from the cholesterol (700 cm^{-1}) peak and the CH_2/CH_3 stretching at 1440 cm^{-1}. Both of these reductions serve as hallmarks of SCI, as they correlate with axonal demyelination, membrane disorganisation and cell death [46, 47]. Small increases in the injured spectra from the healthy in the 950-1000 cm^{-1} region are in accordance with the upregulation and aggregation of glycosaminoglycans (GAGs) and chondroitin sulphate proteoglycans (CSPGs) that commonly follow SCI [48]. GAGs and CSPGs play a dual role following injury; whilst they help to stabilise the injury site by forming the glial scar, they are also growth inhibitory towards axons through the generation of a biochemically hostile environment. In particular, CSPGs interact with neuronal receptors to inhibit axonal

outgrowth, marking an inhibitory response that limits regeneration [49]. Thus, an increased intensity in this region can reflect the biochemical shift towards an injury state with high inhibitory signalling and can therefore be considered a marker for axonal regeneration.

Figure 5-4**C**, also supported by Figure 5-4**B**, reveals minimal spectral differences between injured and treated spinal cords, indicating that the PBM treatment may not be immediately detectable via spectral analysis. The greatest variation in spectral intensity in Figure 5-4**C** stems from the 1440 cm^{-1} peak, linking this variation as an influencing factor in the classification in the SOM in Figure 5-1**B**, and therefore indicates lipids as a potential PBM target. This lack of detectable change could reflect fundamental differences in regenerative potential between spinal cord tissue and DRG, where a more pronounced response to PBM was observed.

Figure 5-4**D** indicates a consistently greater average spectral intensity count in the injured DRG than in the healthy. In Figure 5-4**E**, the treated DRG spectra demonstrate a shift closer to those of healthy DRG tissue, indicating a return to a healthy standard, with the most prominent spectral differences at the 1440 and 1661 cm^{-1} peaks. The recurrence of the 1440 cm^{-1} peak as a differentiator further suggests lipid-related changes in cellular membranes or lipid composition is targeted by PBM treatment. The 1661 cm^{-1} peak difference reflects changes in protein folding and stability exerted by PBM. The treatment may promote protective structural stability post-injury, thus reducing denaturation. Figure 5-4**E** also exhibits a slight decrease in the 1061:1088:1124 cm^{-1} triplet, linked to lipids through the stretching of C–C backbone bonds and PO_2^- bonds in the headgroups,

respectively, as well as the cholesterol sterol ring 700 cm^{-1} shift. Together, these shifts correspond to PBM treatment supporting lipid and protein stabilisation, potentially in the aid of cellular integrity and enhancement of regenerative environment of DRG. Figure 5-4**F** confirms the efficacy of PBM treatment on injured DRG spectral characteristics, as demonstrated by the increased intensity difference.

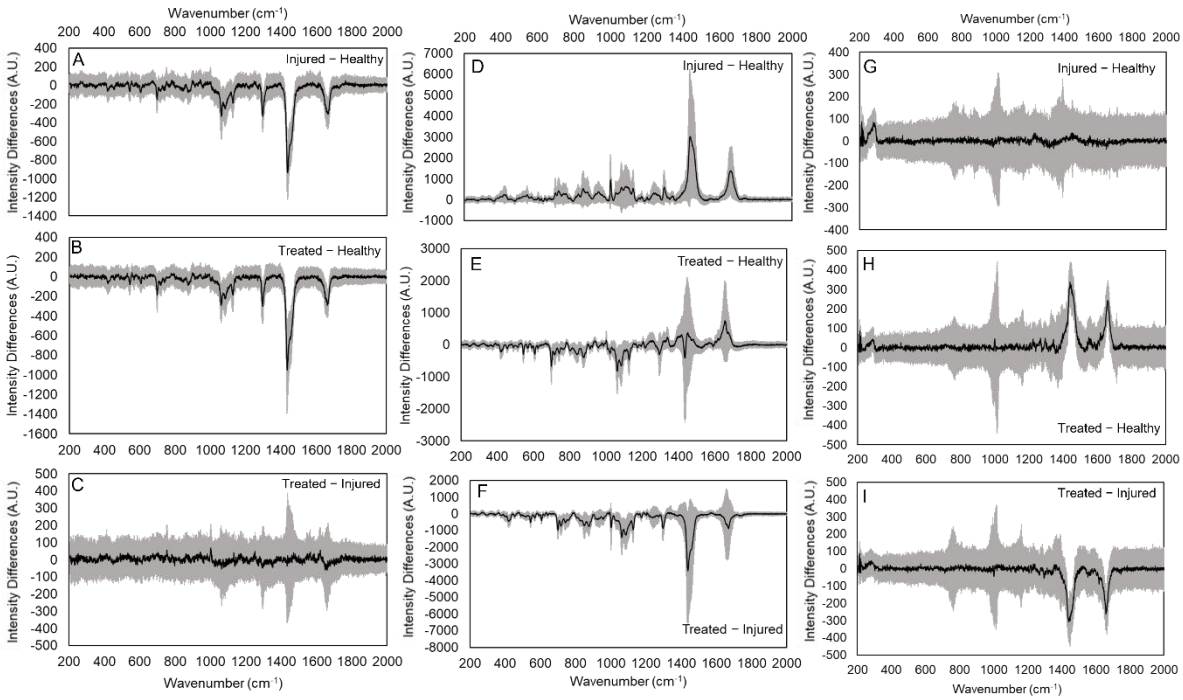

Figure 5-4 – Differences in spectral intensities in the A) spinal cord between injured and healthy spectra, B) treated and healthy, and C) treated and injured. Differences in DRG tissue spectra between D) injured and healthy, E) treated and healthy and F) treated and injured. Standard deviations of differences are highlighted in dark gray.

Examination of brain tissue (Figure 5-4**G-I**) illustrates PBM's systemic impact on CNS recovery. Figure 5-4**G** shows that while minimal spectral differences exist between healthy and injured brain tissue, tissue from treated samples exhibit cohesive change through the 1440 and 1661 cm^{-1} shifts in which they increase in comparison to healthy, and decrease in comparison to the injured tissue, demonstrated in Figure 5-4**H** and Figure

5-4**I**, respectively. In all three comparisons (Figure 5-4**G-I**), there are variances in protein content and phospholipids indicated via the intensity differences observed at 1003 and 720 cm^{-1} shifts. These shifts suggest PBM may facilitate subtle biochemical adjustments throughout the CNS, including areas that were not directly injured or treated. The consistent presence of lipid and protein related shift differences further corroborates these biomolecules as PBM's therapeutic target.

Although four animals per class are sufficient for a preliminary study, including additional animals in future experiments would strengthen the dataset and improve statistical robustness. Extending the study to incorporate 3-, 7-, and 10-day post-injury timepoints would also provide deeper insight into the mechanism of action of PBM. Given the positive results observed in the DRG, and the critical role the DRG play in axon regeneration, a focused study examining the effects of varying numbers of days PBM treatment has been employed on the spinal cord could help determine the minimum number of time and treatments required to achieve a therapeutic effect at the injury site. Raman spectroscopy could then be employed to identify spectral peaks that show the most significant changes occurring in the tissue.

5.4.2 SCI Biomarkers

Figure 5-5 depicts the spectral features of fibronectin, laminin and GFAP, highlighting key Raman characterising shifts that will be used to spectrally track injury. Linking the shifts in the biomarkers observed in Figure 5-5 to the spectra of the spinal cords, DRG and brain

tissue allowed the identification of common features to assess and can be used as an indicator of treatment efficiency. Relative intensity ratios of these common shifts are presented in Figure 5-6. Ratios were calculated using the common shift against a peak only present in the biomarker assessed to determine the biomarkers behaviour and to standardise the ratios. Fibronectin ratios are measured against the 1408 cm^{-1} peak, laminin against 1247 cm^{-1}, and GFAP against 914 cm^{-1}.

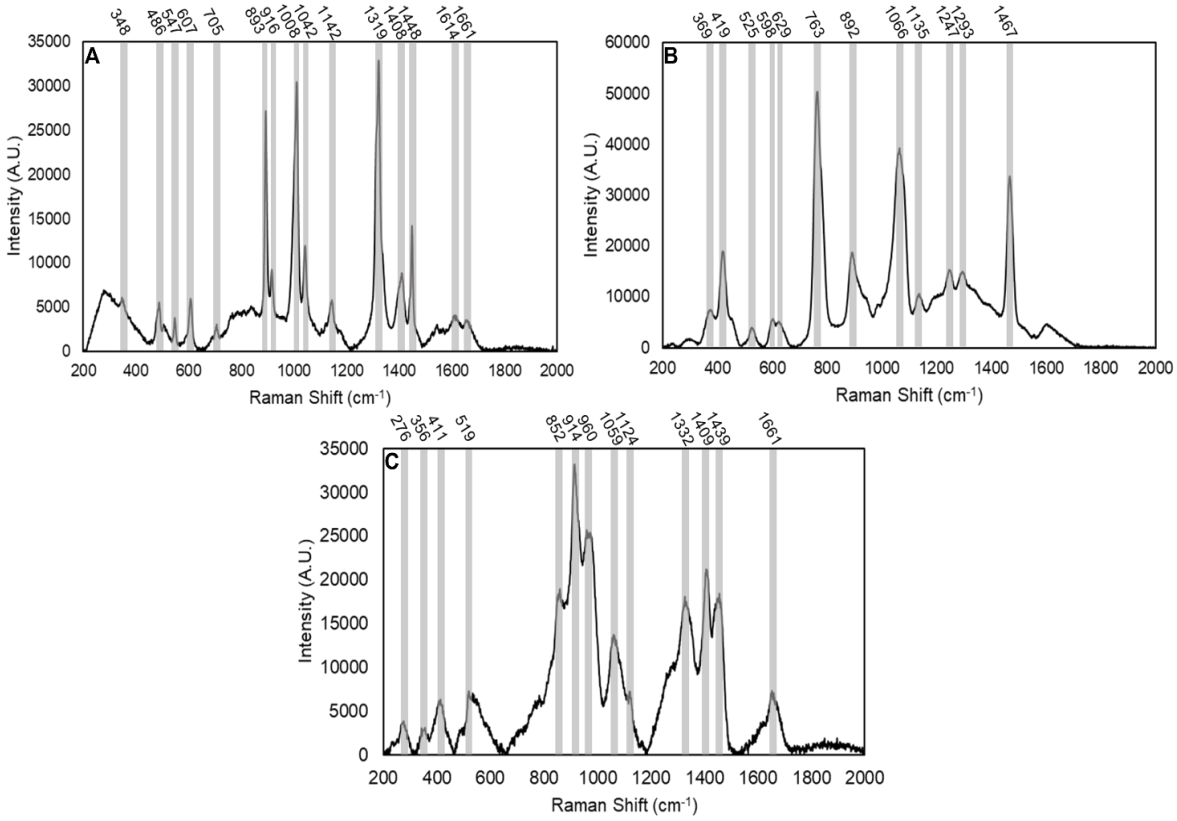

Figure 5-5 – SCI biomarker spectra. Spectral features of A) fibronectin, B) laminin and C) GFAP. Characteristic shifts are highlighted in grey.

Differences in relative intensity ratios for biomarker related peaks in the spinal cords, DRG and brains are observed in Figure 5-6. Overall, there are no statistically significant observations for the ratio differences specifically relating to laminin and GFAP between

injured and treated samples compared to healthy controls (Figure 5-6 **B-C, E-F, H-I**). Fibronectin has previously been shown to be further induced following PBM [50]. Fibronectin in the glial scar mediates the necessary interaction between reactive astrocytes and microglia for tissue homeostasis restoration [51, 52].

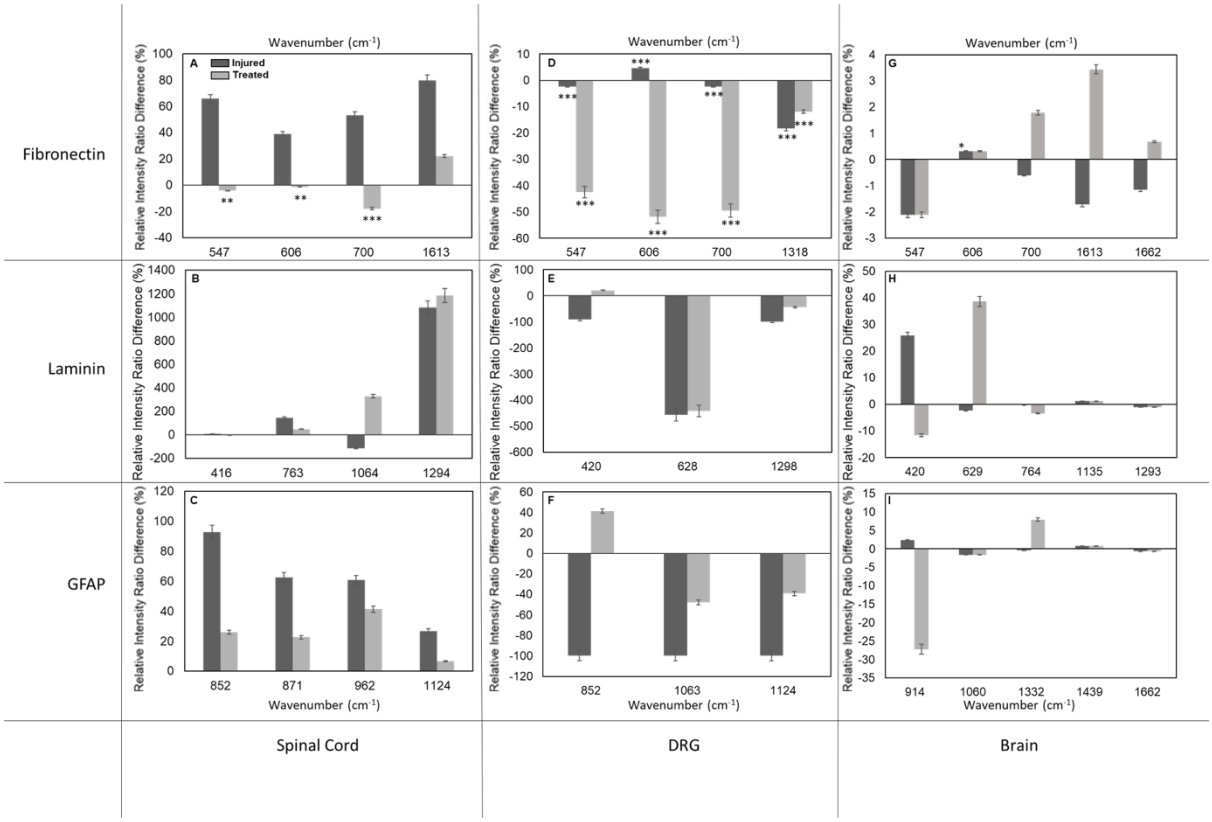

Figure 5-6 – Percentage differences in relative intensity ratios of injured and treated spinal cord intensities against healthy, using wavenumbers specific to A) fibronectin, B) laminin and C) GFAP. Differences in relative intensity ratios of injured and treated DRG intensities against healthy, using wavenumbers specific to D) fibronectin, E) laminin and F) GFAP. Differences in relative intensity ratios of injured and treated brain spectra intensities against healthy, using wavenumbers specific to G) fibronectin, H) laminin and I) GFAP. * $p < 0.05$, ** $p < 0.01$, *** $p < 0.001$.

Increased levels of fibronectin improves the rate at which the interaction occurs, thus restoring homeostasis earlier [51]. PBM spinal cord ratio differences are all closer in value to the healthy than the injured (Figure 5-6**A**), reflecting the restoration of tissue

biochemistry encouraged by fibronectin. Interestingly, the DRG demonstrate more prominent changes in fibronectin intensity ratios (Figure 5-6**D**). This observation correlates with the earlier findings indicating greater responsiveness of the DRG tissue to PBM. This finding also aligns with the conclusion that the DRG's regenerative capacity may be the contributing factor to the tissue's sensitivity to PBM. Changes in fibronectin levels in the DRG would indicate extracellular matrix remodelling and axonal repair facilitation. Through the monitoring of known biomarkers, clinicians can evaluate tissue condition following PBM based on the biochemical response. Future studies could explore the specific PBM induced upregulation of DRG fibronectin effects on axonal sprouting, neural apoptosis, and other functional outcomes.

5.5 Conclusion

Raman spectroscopy can be used as a therapeutic monitoring tool. Although PBM applied directly on the spinal cord following SCI does confirm some indication of therapeutic effects, a more comprehensive study, with a greater cohort of animals and varying time points, is needed to properly assess any benefits. DRG display more beneficial effects from PBM treatment, as expected due to their involvement in axonal regeneration and dendritic growth. Rats having undergone experimental SCI show some evidence of damage in the brain, however, there is no strong indication of the effectiveness of PBM working throughout the CNS as the rat brains are inconsistent in the reporting of positive effects. Spectral differences are comparatively visible and show the

spectra for treated DRG to tend back towards healthy DRG spectra, whereas the differences in the spinal cord support the observation that there is a low positive effect on the tissue as a result of PBM. Fibronectin is the only recorded biomarker to show statistically significant evidence of concentration changes following treatment. This is an indication that GFAP and laminin may not be optimum monitoring targets for PBM using Raman spectroscopy.

5.6 References

[1] M. Schiller and R. Mobbs, "The historical evolution of the management of spinal cord injury," *Journal of Clinical Neuroscience,* vol. 19, no. 10, pp. 1348-1353, 2012.

[2] P. G. Slater, M. E. Domínguez-Romero, M. Villarreal, V. Eisner, and J. Larraín, "Mitochondrial function in spinal cord injury and regeneration," *Cellular and Molecular Life Sciences,* vol. 79, no. 5, p. 239, 2022.

[3] F. Ramezani *et al.*, "Photobiomodulation for spinal cord injury: a systematic review and meta-analysis," *Physiology & Behavior,* vol. 224, p. 112977, 2020.

[4] S. Passarella and T. Karu, "Absorption of monochromatic and narrow band radiation in the visible and near IR by both mitochondrial and non-mitochondrial photoacceptors results in photobiomodulation," *Journal of Photochemistry and Photobiology B: Biology,* vol. 140, pp. 344-358, 2014.

[5] E. Park, A. A. Velumian, and M. G. Fehlings, "The role of excitotoxicity in secondary mechanisms of spinal cord injury: a review with an emphasis on the implications for white matter degeneration," *Journal of neurotrauma,* vol. 21, no. 6, pp. 754-774, 2004.

[6] D. Liu, X. Ling, J. Wen, and J. Liu, "The role of reactive nitrogen species in secondary spinal cord injury: formation of nitric oxide, peroxynitrite, and nitrated protein," *Journal of neurochemistry,* vol. 75, no. 5, pp. 2144-2154, 2000.

[7] R. Afridi, J.-H. Kim, M. H. Rahman, and K. Suk, "Metabolic regulation of glial phenotypes: implications in neuron–glia interactions and neurological disorders," *Frontiers in cellular neuroscience,* vol. 14, p. 20, 2020.

[8] K. A. Kigerl, J. C. Gensel, D. P. Ankeny, J. K. Alexander, D. J. Donnelly, and P. G. Popovich, "Identification of two distinct macrophage subsets with divergent effects causing either neurotoxicity or regeneration in the injured mouse spinal cord," *Journal of Neuroscience,* vol. 29, no. 43, pp. 13435-13444, 2009.

[9] S. Kiryu-Seo and H. Kiyama, "Mitochondrial behavior during axon regeneration/degeneration in vivo," *Neuroscience research,* vol. 139, pp. 42-47, 2019.

[10] L. A. Patrón and K. E. Zinsmaier, "Mitochondria on the road to power axonal regeneration," *Neuron,* vol. 92, no. 6, pp. 1152-1154, 2016.

[11] M. Khacho *et al.*, "Mitochondrial dynamics impacts stem cell identity and fate decisions by regulating a nuclear transcriptional program," *Cell stem cell,* vol. 19, no. 2, pp. 232-247, 2016.

[12] N. J. Prindeze, L. T. Moffatt, and J. W. Shupp, "Mechanisms of action for light therapy: a review of molecular interactions," *Experimental biology and medicine,* vol. 237, no. 11, pp. 1241-1248, 2012.

[13] V. M. Holanda *et al.*, "Photobiomodulation of the dorsal root ganglion for the treatment of low back pain: A pilot study," *Lasers in Surgery and Medicine,* vol. 48, no. 7, pp. 653-659, 2016.

[14] E. S. Krames, "The dorsal root ganglion in chronic pain and as a target for neuromodulation: a review," *Neuromodulation: Technology at the Neural Interface,* vol. 18, no. 1, pp. 24-32, 2015.

[15] Y. Zhu, C. Soderblom, M. Trojanowsky, D.-H. Lee, and J. K. Lee, "Fibronectin matrix assembly after spinal cord injury," *Journal of neurotrauma,* vol. 32, no. 15, pp. 1158-1167, 2015.

[16] A. A. Albayar *et al.*, "Biomarkers in spinal cord injury: prognostic insights and future potentials," *Frontiers in Neurology,* vol. 10, p. 27, 2019.

[17] H. Abou-El-Hassan *et al.*, "Protein degradome of spinal cord injury: Biomarkers and potential therapeutic targets," *Molecular Neurobiology,* vol. 57, pp. 2702-2726, 2020.

[18] K. Menezes, J. R. L. De Menezes, M. A. Nascimento, R. d. S. Santos, and T. Coelho-Sampaio, "Polylaminin, a polymeric form of laminin, promotes regeneration after spinal cord injury," *The FASEB Journal,* vol. 24, no. 11, pp. 4513-4522, 2010.

[19] K. Menezes *et al.*, "Human mesenchymal cells from adipose tissue deposit laminin and promote regeneration of injured spinal cord in rats," *PloS one,* vol. 9, no. 5, p. e96020, 2014.

[20] P. Liesi, "Laminin-immunoreactive glia distinguish regenerative adult CNS systems from non-regenerative ones," *The EMBO journal,* vol. 4, no. 10, pp. 2505-2511, 1985.

[21] Z. Yang and K. K. Wang, "Glial fibrillary acidic protein: from intermediate filament assembly and gliosis to neurobiomarker," *Trends in neurosciences,* vol. 38, no. 6, pp. 364-374, 2015.

[22] D. Triolo *et al.*, "Loss of glial fibrillary acidic protein (GFAP) impairs Schwann cell proliferation and delays nerve regeneration after damage," *Journal of cell science,* vol. 119, no. 19, pp. 3981-3993, 2006.

[23] A. R. Stevens *et al.*, "Implantable and transcutaneous photobiomodulation promote neuroregeneration and recovery of lost function after spinal cord injury," *Bioengineering & Translational Medicine,* p. e10674, 2024.

[24] C. Banbury *et al.*, "Development of the self optimising Kohonen index network (SKiNET) for Raman spectroscopy based detection of anatomical eye tissue," *Scientific reports,* vol. 9, no. 1, p. 10812, 2019.

[25] S. Lek and Y. Park, "Artificial neural networks," in *Encyclopedia of Ecology, Five-Volume Set*: Elsevier Inc., 2008, pp. 237-245.

[26] G. Socrates, *Infrared and Raman characteristic group frequencies: tables and charts*. John Wiley & Sons, 2004.

[27] J. Lin *et al.*, "Neuroprotective effect of ketone metabolism on inhibiting inflammatory response by regulating macrophage polarization after acute cervical spinal cord injury in rats," *Frontiers in Neuroscience,* vol. 14, p. 583611, 2020.

[28] G. Pezzotti, "Raman spectroscopy in cell biology and microbiology," *Journal of Raman Spectroscopy,* vol. 52, no. 12, pp. 2348-2443, 2021.

[29] K. Kochan *et al.*, "Pathological changes in the biochemical profile of the liver in atherosclerosis and diabetes assessed by Raman spectroscopy," *Analyst,* vol. 138, no. 14, pp. 3885-3890, 2013.

[30] Y. Gong *et al.*, "Interpreting the biochemical specificity of mouse spinal cord by confocal raman microspectral imaging," *Journal of Innovative Optical Health Sciences,* vol. 10, no. 05, p. 1743007, 2017.

[31] A. Guimarães *et al.*, "Near Infrared Raman Spectroscopy (NIRS): A technique for doping control," *Spectroscopy,* vol. 20, no. 4, pp. 185-194, 2006.
[32] A. Girard *et al.*, "Raman spectroscopic analysis of skin as a diagnostic tool for Human African Trypanosomiasis," *PLoS Pathogens,* vol. 17, no. 11, p. e1010060, 2021.
[33] K. Katsara, K. Psatha, G. Kenanakis, M. Aivaliotis, and V. M. Papadakis, "Subtyping on live lymphoma cell lines by raman spectroscopy," *Materials,* vol. 15, no. 2, p. 546, 2022.
[34] A. Synytsya, M. Judexova, D. Hoskovec, M. Miskovicova, and L. Petruzelka, "Raman spectroscopy at different excitation wavelengths (1064, 785 and 532 nm) as a tool for diagnosis of colon cancer," *Journal of Raman Spectroscopy,* vol. 45, no. 10, pp. 903-911, 2014.
[35] S. Qiu *et al.*, "Raman profile alterations of irradiated human nasopharyngeal cancer cells detected with laser tweezer Raman spectroscopy," *RSC advances,* vol. 10, no. 24, pp. 14368-14373, 2020.
[36] C. Farber *et al.*, "Complementarity of raman and infrared spectroscopy for structural characterization of plant epicuticular waxes," *ACS Omega,* vol. 4, no. 2, pp. 3700-3707, 2019.
[37] A. Ricciardi *et al.*, "Raman spectroscopy characterization of the major classes of plasma lipoproteins," *Vibrational Spectroscopy,* vol. 109, p. 103073, 2020.
[38] J. M. Surmacki, L. Ansel-Bollepalli, F. Pischiutta, E. R. Zanier, A. Ercole, and S. E. Bohndiek, "Label-free monitoring of tissue biochemistry following traumatic brain injury using Raman spectroscopy," *Analyst,* 10.1039/C6AN02238C vol. 142, no. 1, pp. 132-139, 2017, doi: 10.1039/C6AN02238C.
[39] M. Mowbray, C. Banbury, J. J. Rickard, D. J. Davies, and P. Goldberg Oppenheimer, "Development and Characterization of a Probe Device toward Intracranial Spectroscopy of Traumatic Brain Injury," *ACS biomaterials science & engineering,* vol. 7, no. 3, pp. 1252-1262, 2021.
[40] F.-Q. Zhou, "Genetic study of axon regeneration with cultured adult dorsal root ganglion neurons," *JoVE (Journal of Visualized Experiments),* no. 66, p. e4141, 2012.
[41] M. J. Kwon *et al.*, "Contribution of macrophages to enhanced regenerative capacity of dorsal root ganglia sensory neurons by conditioning injury," *Journal of Neuroscience,* vol. 33, no. 38, pp. 15095-15108, 2013.
[42] R. Feng, V. Muraleedharan Saraswathy, M. H. Mokalled, and V. Cavalli, "Self-renewing macrophages in dorsal root ganglia contribute to promote nerve regeneration," *Proceedings of the National Academy of Sciences,* vol. 120, no. 7, p. e2215906120, 2023.
[43] T. Tian, Z. Wang, L. Chen, W. Xu, and B. Wu, "Photobiomodulation activates undifferentiated macrophages and promotes M1/M2 macrophage polarization via PI3K/AKT/mTOR signaling pathway," *Lasers in Medical Science,* vol. 38, no. 1, p. 86, 2023.
[44] J. W. Song *et al.*, "Low-level laser facilitates alternatively activated macrophage/microglia polarization and promotes functional recovery after crush spinal cord injury in rats," *Scientific reports,* vol. 7, no. 1, p. 620, 2017.

[45] B. Svobodova *et al.*, "The effect of 808 nm and 905 nm wavelength light on recovery after spinal cord injury," *Scientific reports,* vol. 9, no. 1, p. 7660, 2019.
[46] S. M. Ruberto, "Raman spectroscopic investigation of chondroitinase ABC treatment after spinal cord injury in an organotypic model," Syracuse University, 2013.
[47] F. Zhang, Z. Liang, D. Song, Z. Wang, K. Wang, and S. Wang, "Raman spectroscopic investigation on the biomedical evolution of spinal cord injury and the therapeutic outcomes of its low-level laser therapy," *Vibrational Spectroscopy,* vol. 118, p. 103337, 2022.
[48] R. Bansil, I. Yannas, and H. Stanley, "Raman spectroscopy: a structural probe of glycosaminoglycans," *Biochimica et Biophysica Acta (BBA)-General Subjects,* vol. 541, no. 4, pp. 535-542, 1978.
[49] T. Saxena, B. Deng, D. Stelzner, J. Hasenwinkel, and J. Chaiken, "Raman spectroscopic investigation of spinal cord injury in a rat model," *Journal of biomedical optics,* vol. 16, no. 2, pp. 027003-027003-14, 2011.
[50] P. Garrido *et al.*, "Effects of photobiomodulation therapy on the extracellular matrix of human dental pulp cell sheets," *Journal of Photochemistry and Photobiology B: Biology,* vol. 194, pp. 149-157, 2019.
[51] S. Yoshizaki *et al.*, "Microglial inflammation after chronic spinal cord injury is enhanced by reactive astrocytes via the fibronectin/β1 integrin pathway," *Journal of neuroinflammation,* vol. 18, pp. 1-15, 2021.
[52] X. Hu *et al.*, "Spinal cord injury: molecular mechanisms and therapeutic interventions," *Signal transduction and targeted therapy,* vol. 8, no. 1, p. 245, 2023.

Chapter 6: Conclusions and Future Outlook

6.1 Summary

This thesis has compiled a Raman library of TBI biomarkers, explored the potential for a portable Raman probe for TBI detection, and assessed the therapeutic efficacy of PBM for SCI treatment. The potential for Raman spectroscopy applications in the field of CNS trauma is significant. By gaining an understanding of the exact biochemical makeup of post-injury tissue, novel therapeutic pathways can be investigated to address the primary injuries directly, thus minimising the risk of secondary damage, rather than relying on the symptomatic relief of secondary injuries, which remains the current standard of care. Whilst there is still progress to be made before this can be achieved, this thesis initiates the process of improving the understanding the biochemical pathways that are the result of CNS trauma. The growing interest in Raman diagnostic devices will eventually lead to a standardisation of the technique, alongside the development of improved software analysis tools for noise filtrations and peak analysis, ultimately making future devices easier to integrate into diagnostic research.

Chapter 3 creates a meaningful tool and data bank for future Raman based TBI research. The molecular profiling of each biomarker will facilitate identification of concentration changes within TBI tissue or biofluids, eventually contributing to novel therapeutic targets and improved diagnostic accuracy. The biomarkers have been split and classified into time-dependent TBI phases for the ease for any future user of the library, to easily identify relevant markers for a particular study. Considerations of the study must be taken into account, however, in that several TBI biomarkers relevant to literature were not able to be included due to their Raman active buffers or additives, so as not to impact the results. In

addition, this meant the biomarkers were procured from synthetic, animal, and human sources, which must be taken into account in further use of the library. Finally, the biomarkers were recorded with the sole purpose of characterising fingerprints, and do not take into consideration TBI or healthy levels when in solution. However, this is, to-date, the largest spectral library of TBI biomarkers available online, rendering this chapter an important addition to the relatively recent application of Raman spectroscopy for medical devices.

Chapter 4 describes a portable Raman spectroscopy probe for TBI identification in animal brain tissue. The device is practical, handheld and portable, and will not require specialised Raman training. The concept is to integrate this probe into clinically established procedures in which part of the skull will be removed, namely an ICP catheter insertion and a decompressive craniectomy. SKiNET is employed to confirm results and assess the viability of the device. In the absence of TBI inflicted models (for financial reasons and as part of the 3 R's), representative samples were designed as a validation though the spiking of brain tissue with TBI-representative biomarkers as well as through damage incurred from SCI models. Although not the preferred method of validation, both studies support the useability of the probe in its current setup and provide a foundation for an *in vivo* protocol. The ability to detect environmental changes in the brain through the skull opens a wide range of pathways for the probe, extending even beyond neurological uses. Of course, alongside upcoming animal *in vivo* TBI studies, there is more groundwork for the probe being carried out to determine safety and the extent of its capacity. More prospects for the probe are described below in the Future Outlooks section. An interesting addition to the study would have been the addition of a non-Raman

based technique to support the results, however the opportunity did not arise for various reasons.

Finally, **Chapter 5** provides evidence of Raman spectroscopy's capability as a neuromonitoring tool for the testing of therapeutic interventions in the CNS. Specifically, SCI animal models are treated with PBM on the site of injury, and records of the effects are taken from three tissues associated to the spinal cord: the spinal cord itself, DRG, and brain tissue. Again, in accordance with the 3 R's, sample numbers were low, although preliminary results were encouraging. Identifying changes in the spectra not only solidifies the performance of Raman spectroscopy on neurological tissue, but also helps to elucidate some understanding of the processes targeted by PBM. Before this work is considered for publication, further confirmation of the results will be required from alternative techniques.

6.2 Future Outlook

Currently, a pathway is being set up for the use of the probe in a more relevant setting. Whilst *in vivo* tests are still not available to us, we are investigating the potential for 3D printing brain organoids from human derived pluripotent stem cells to mimic specific injury pathways over time, such as neuroinflammation. A study to establish the probe's limit of detection in complex samples will determine to what extent biomarkers can be observed in brain tissue and the overall capacity for the probe. Additionally, the transcranial approach opens the door to paediatric TBI in infants where the skull is not yet

fully developed, and the light will be able to pass through the skin. A further application could include the study of CSF from patients with a drain to develop a monitoring tool for recovery. Beyond CNS trauma, the research in this thesis surrounding a probe device can be extended to other neurological conditions, including Parkinson's during a deep brain stimulation implant procedure, awake craniectomies, and with patients who might receive a drain or catheter for reasons unrelated to increased ICP.

In terms of Raman spectroscopy efficacy for therapeutic monitoring, the study in **Chapter 5** provided a solid groundwork for future investigations. A more comprehensive study with more animals and larger variety of time references would be beneficial, as well as cell staining to confirm the observed activities in tissue.

Beyond CNS trauma, the research in this thesis surrounding a probe device can be extended to other neurological conditions, including Parkinson's, Alzheimer's, awake craniectomies, and with patients who might receive a drain for reasons unrelated to increased ICP. In all, Raman spectroscopy has the potential to be a game changer in the field of diagnostic devices, however in terms of accessibility and useability it is still a relatively new concept, as opposed to established techniques such as mass spectroscopy or enzyme-linked immunosorbent assays (or ELISA). Raman band assignment is still a manual procedure, and the collection of Raman spectra is yet to be standardised, all of which are bridges which need to be crossed before the full potential of Raman spectroscopy can be achieved, but conversely the only way to address these issues are through the continued use and research around Raman spectroscopy.

Appendices

Appendix A: Raman Spectroscopy Spectral Fingerprints of Biomarkers of Traumatic Brain Injury

cells

MDPI

Article

Raman Spectroscopy Spectral Fingerprints of Biomarkers of Traumatic Brain Injury

Georgia Harris [1], Clarissa A. Stickland [1], Matthias Lim [1] and Pola Goldberg Oppenheimer [1,2,*]

[1] Advanced Nanomaterials Structures and Applications Laboratories, School of Chemical Engineering, College of Engineering and Physical Sciences, University of Birmingham, Edgbaston, Birmingham B15 2TT, UK
[2] Institute of Healthcare Technologies, Mindelsohn Way, Birmingham B15 2TH, UK
* Correspondence: goldberp@bham.ac.uk

Abstract: Traumatic brain injury (TBI) affects millions of people of all ages around the globe. TBI is notoriously hard to diagnose at the point of care, resulting in incorrect patient management, avoidable death and disability, long-term neurodegenerative complications, and increased costs. It is vital to develop timely, alternative diagnostics for TBI to assist triage and clinical decision-making, complementary to current techniques such as neuroimaging and cognitive assessment. These could deliver rapid, quantitative TBI detection, by obtaining information on biochemical changes from patient's biofluids. If available, this would reduce mis-triage, save healthcare providers costs (both over- and under-triage are expensive) and improve outcomes by guiding early management. Herein, we utilize Raman spectroscopy-based detection to profile a panel of 18 raw (human, animal, and synthetically derived) TBI-indicative biomarkers (N-acetyl-aspartic acid (NAA), Ganglioside, Glutathione (GSH), Neuron Specific Enolase (NSE), Glial Fibrillary Acidic Protein (GFAP), Ubiquitin C-terminal Hydrolase L1 (UCHL1), Cholesterol, D-Serine, Sphingomyelin, Sulfatides, Cardiolipin, Interleukin-6 (IL-6), S100B, Galactocerebroside, Beta-D-(+)-Glucose, Myo-Inositol, Interleukin-18 (IL-18), Neurofilament Light Chain (NFL)) and their aqueous solution. The subsequently derived unique spectral reference library, exploiting four excitation lasers of 514, 633, 785, and 830 nm, will aid the development of rapid, non-destructive, and label-free spectroscopy-based neuro-diagnostic technologies. These biomolecules, released during cellular damage, provide additional means of diagnosing TBI and assessing the severity of injury. The spectroscopic temporal profiles of the studied biofluid neuro-markers are classed according to their acute, sub-acute, and chronic temporal injury phases and we have further generated detailed peak assignment tables for each brain-specific biomolecule within each injury phase. The intensity ratios of significant peaks, yielding the combined unique spectroscopic barcode for each brain-injury marker, are compared to assess variance between lasers, with the smallest variance found for UCHL1 (σ^2 = 0.000164) and the highest for sulfatide (σ^2 = 0.158). Overall, this work paves the way for defining and setting the most appropriate diagnostic time window for detection following brain injury. Further rapid and specific detection of these biomarkers, from easily accessible biofluids, would not only enable the triage of TBI, predict outcomes, indicate the progress of recovery, and save healthcare providers costs, but also cement the potential of Raman-based spectroscopy as a powerful tool for neurodiagnostics.

Keywords: traumatic brain injury; TBI biomarkers; acute, sub-acute and chronic phases; Raman spectroscopy; neurodiagnostics

Citation: Harris, G.; Stickland, C.A.; Lim, M.; Goldberg Oppenheimer, P. Raman Spectroscopy Spectral Fingerprints of Biomarkers of Traumatic Brain Injury. *Cells* **2023**, *12*, 2589. https://doi.org/10.3390/cells12222589

Academic Editor: Xiang Gao

Received: 11 October 2023
Revised: 2 November 2023
Accepted: 6 November 2023
Published: 8 November 2023

1. Introduction

Traumatic brain injury (TBI) is the leading cause of death under the age of 40, presenting a major burden on healthcare services worldwide [1]. The severity of TBIs ranges from mild/moderate concussion to severe and chronic loss of cognitive and motor function, resulting from sudden impact to the head, often following road accidents, falls, assaults,

and in contact sports [2]. The physiological symptoms of TBI vary from fatigue and headaches in mild injuries, to temporary (and occasionally permanent) loss of memory or consciousness, short and long-term disability, neurological disorders and death, in the more severe scenarios [3,4]. Importantly, recent research [3–8] has been focusing on establishing the temporal profile of TBIs and the associated biomarkers including their emergence (i.e., acute phase), crucial for early-stage diagnostics, persistence, and decline (sub-acute and chronic phases)—indicative of the longer-term effects and prognosis as well as development of new therapeutics. TBI biomarkers have been shown to have a characteristic timeframe of acute (<24 h), sub-acute (1 day–3 weeks) and chronic (3 weeks–6 months), as the initial insult causes acute damage to the brain, is typically followed by a biochemical cascade leading to secondary injuries over the following month [9–11]. This indicates that identifying TBI in the acute phase and intervening before further damage occurs is vital for long-term neurological recovery. However, despite the important time window alongside an estimate of 69 million people suffering from TBI each year worldwide, the development of point-of-care, timely TBI diagnostic technologies remains an unmet need and there is no definite triaging and therapeutic patient pathway [12].

Current TBI diagnostic techniques include the Glasgow Coma Scale (GCS), a cognitive assessment method, and neuroimaging such as Computerised Tomography (CT) and Magnetic Resonance Imaging (MRI) scans [2]. The GCS uses the patient's eye, verbal, and motor responses to enumerate the injury and categorise it as either severe (3–8), moderate (9–12), or mild (13–15) [13]. Whilst neuroimaging will identify skull fractures, hematoma, and haemorrhage to determine if neurosurgery is necessary [2]. The main challenge lies in the fact that pre-hospital and emergency department (ED) assessment is predominantly based on insensitive GCS and history acquisition with guidance on CT being often vague and costly. Mild TBI (mTBI) is often underdiagnosed if not identified rapidly at the point of injury, with 90% of acute cases undetected and not admitted to ED [2,14,15]. Therefore, development of successful TBI biomarker diagnostics from blood [16], or other biofluids, i.e., cerebrospinal fluid (CSF) [8], saliva [17], urine [18], and tears [19], would lead to improved triage of severe and high-risk injuries and improve outcomes, whilst appropriate classification of low-risk and mTBI patients would allow for the focusing of resources on those who need it the most. Furthermore, reduced resource demand would mitigate the relatively low costs of the investigation in comparison to ED assessment, CT imaging and hospital admission, and have distinct yet complementary use cases. In the pre-hospital space, improved triage of TBI as mild will support decision-making by pre-hospital healthcare providers to reduce referral to hospital care, reducing the number of ED visits.

Concurrently, Raman spectroscopy, a rapid, label-free technique has been increasingly used in medical and diagnostic applications for producing non-destructive chemical information [20]. This sensitive vibrational spectroscopy excites molecular bonds within a sample, providing a unique biomolecular spectral fingerprint of target biomarkers in a rapid analytical response [21,22]. These spectroscopic barcodes have been shown to identify the various diseases from which the biofluid has been collected, such as blood [23,24], CSF [25,26], urine [27,28], saliva [24,29], and tears [30,31]. In contrast to the in vitro bioassays, the availability of inexpensive, portable Raman devices makes this technique particularly attractive for point-of-care testing, analysis, and screening of biofluids. There is limited yet growing research in the development of Raman spectroscopy for biofluid-based neurodiagnostics [32–36]. Whilst research continues to unravel new technologies for rapid point-of-care technologies for TBI diagnostics from biofluids and tissue, it is imperative to establish fingerprints of the inherent characteristics of TBI biomarkers in various injury phases, where the detected changes via Raman spectroscopy could, in the long-term, be attributed to underpinning the variations in TBIs with various severity and as a function of temporal evolution.

Herein, we consistently study a broad panel of TBI biomarkers via Raman spectroscopy profiling and establish a spectral reference library for the interpretation of the Raman finger-

prints of TBI-indicative biomarkers via biologically applicable laser excitation wavelengths in different post-injury phases. A carefully selected cohort of TBI-indicative biomarkers are classed into three main injury phases with spectra in the raw and reconstituted (mimicking the biomarker biofluid) state forms acquired via a range of Raman-applicable laser excitation wavelengths of 514, 633, 785, and 830 nm. Subsequently, for each post-TBI phase, Raman spectroscopy temporal-phase biomarker-profiling establishes an important baseline library in the form of a "multi-biochemical barcode", yielding a characteristic tool for ongoing and future spectroscopic studies for diagnostic applications. Awareness of the spectroscopic temporal profiles of TBI biomarkers provides an essential pathway for defining and setting the most appropriate diagnostic time window for sampling after injury. The derived Raman fingerprints, combined with the identified biochemical peaks, closely matching notable biomarker characteristics, equip us with the knowledge of the molecule's physiological role. This could not only improve the treatment of TBI through specific targeting of the damage in contrast to current methods, which mostly rely on symptomatic relief [37], but could also provide a further panel of candidate first-line screening TBI-indicative biomarkers. This lays the platform for defining their functionality in the complex TBI aetiology and, in the longer term, cements Raman spectroscopy as a powerful technique for future biomarker discovery in both neurodiagnostics as well as for other detrimental diseases with many ramifications.

2. Materials and Methods

2.1. TBI Biomarkers

The selected raw biomarkers were purchased without purification and tested in both solid and solution states. These were divided into three main groups of acute, sub-acute, and chronic phases (Figure 1). The TBI cohort selection was based on an extensive literature overview of recent research on TBI biomarkers (animal and human) and temporal courses studied in a range of biofluids including blood, plasma, CSF, urine, and the key biomarkers of neuroinflammation [3,38–45]. Biomarkers included in the panel were obtained in the purest form without any active additives, to avoid impacting spectral signatures. This yielded a cohort of 18 biomarkers including the N-Acetyl-L-aspartic acid (NAA), ganglioside, Glutathione (GSH), Neuron-Specific Enolase (NSE), Glial fibrillary acidic protein (GFAP), Ubiquitin carboxyl-terminal hydrolase isozyme L1 (UCHL1), cholesterol, D-serine, sphingomyelin, sulfatide, cardiolipin, Interleukin-6 (IL-6), S100B, galactocerebroside, glucose, myo-inositol, Interleukin-18 (IL-18), and Neurofilament light chain (NFL). Subsequently, reconstituted biomarker samples were prepared following the technical details provided in the individual data sheets. Typically, this included centrifugation at 8 G for 2 min prior to adding the solvent of distilled H_2O (18.2 MΩ) or chloroform/ethanol, yielding 1:1 v/v solutions. After 20 min, to allow full dissolvement, 3 µL samples of each biomarker were deposited onto an aluminium slide and dried in an ambient environment for Raman measurement.

2.2. Reference Chemicals

Human derived biomarkers included the S100B (HY-P70659, Cambridge Bioscience, Cambridge, UK), IL-6 (H7416-10UG, Merck, Darmstadt, Germany), NSE (13219-H08E-SIB-50 ug, Stratech, Ely, UK), GFAP (C227-10 ug, Generon, Slough, UK), IL-18 (CSB-YP614514HU, Antibodies.com, Cambridge, UK), NFL (pro-2584-10 ug, Generon), and UCHL1 (UC1-H5140-50 ug, Generon). Animal derived biomarkers included the galactocerebroside (C4905-10MG, Merck), sphingomyelin (1051-25 mg, Cambridge Bioscience), ganglioside (860053P-10MG, Scientific Laboratory Supplies, Nottingham, UK), sulfatide (56-1085-7-LAO-25 mg, Stratech), and cardiolipin (C0563-10MG, Merck). Synthetically produced biomarkers included the NAA (00920-5G, Merck), cholesterol (C8667-1G, Generon), glucose (CAY23733-50, Cambridge Bioscience), D-serine (A11353.06, VWR International, Lutterworth, UK), myo-inositol (A13586.22, VWR International), and GSH (G4251-300MG, Merck).

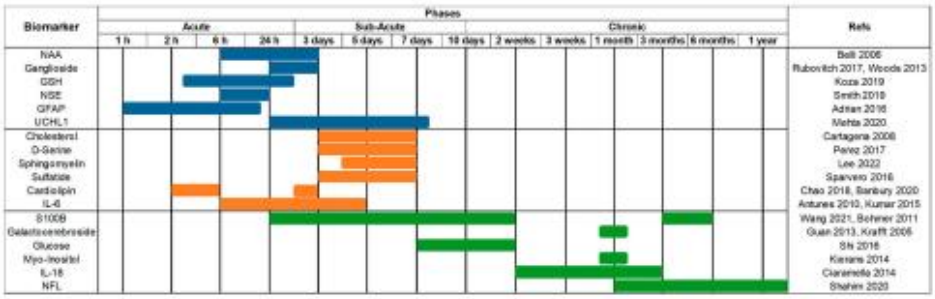

Figure 1. Schematic timeline overview of the TBI biomarkers and their phases, acute (blue), sub-acute (orange), and chronic (green), during which each biomarker has been reported to either increase, persist, or decline post-injury [4,9,40,44,46–64]. Biomarkers: N-Acetyl-L-aspartic acid (NAA), Glutathione (GSH), Neuron-Specific Enolase (NSE), Glial fibrillary acidic protein (GFAP), Ubiquitin carboxyl-terminal hydrolase isozyme L1 (UCHL1), Interleukin-6 (IL-6), Interleukin-18 (IL-18), and Neurofilament light chain (NFL).

2.3. *Raman Spectroscopy*

Raman measurements were carried out using the InVia Qontor confocal Raman system (Renishaw) equipped with four excitation lasers, which were adjusted for optimal throughput, fluorescence control, and sensitivity. Optical measurements were carried out with a specially adapted research-grade microscope (Leica [Wetzlar, Germany] DM 2700M) equipped with an incoherent white light source, allowing confocal measurements with a 2.0 µm depth resolution. Four excitation wavelengths of 514, 633, 785, and 830 nm were employed in this study to enable a breadth of spectral profiles. To avoid photochemical effects in the spectra, sample damage or degradation, extended spectral Raman scans were acquired over a range of 200–3200 cm^{-1}, 50× objective lens, and an acquisition time of 10 s with 5 accumulations. All Raman spectra were collected at the ambient temperature.

2.4. *Data Analysis*

The acquired Raman spectra were collected using Renishaw WiRE 5.2 (Renishaw Plc, Wotton-under-Edge, UK) and cosmic rays were removed during baseline subtraction with a polynomial order of 11 and a 1.5 noise tolerance. Extended spectra were subsequently averaged per biomarker, taking into account the laser excitation wavelength as well as the raw and reconstituted states. The Peak Pick tool (WiRE 5.2) was utilised across the x-axis range to select the six characteristic bands for each assignment, while the slope detection method was utilised with 15 smooth points and a peak threshold height of 500 counts.

3. Results and Discussion

The Raman spectrum is commonly referred to in terms of discrete regions, the low wavenumber region (100–200 cm^{-1}), the fingerprint region (500–2000 cm^{-1}), and the high wavenumber region (2000–4000 cm^{-1}) [65,66]. In this study, Raman spectra were collected in the extended spectral regions of 200–3200 cm^{-1}, however, only the fingerprint region from 200 to 1800 cm^{-1} was used where the main bands of interest were identified.

The biomarkers studied, based on references to TBIs in the literature, were classified within three main injury phases as acute, sub-acute, and chronic (Figure 1), the corresponding detailed information for each biomarker, including the accessible biofluid source, physiological function, post-TBI response, and the role they play in head injuries along with the associated phase behaviour are summarised in Table 1.

Spectral profiles for each biomarker were acquired for both solids as well as of the solute forms, with the former inherently yielding better resolved, sharper Raman peaks. It is well-established that Raman band frequencies are more complex and shifted in the

liquid phase, relative to the solid, due to the higher variability of the intermolecular forces and molecular collisions in the liquid phase, which shift the frequencies of intra-molecular vibrations and broaden the bands, relative to the highly regular and stable solid structures. Since the behaviour of biomarkers in aqueous solutions is of particular importance, given that an aqueous medium is a natural environment for biological molecules, we have identified the spectral signatures of the reconstituted solutions of TBI biomarkers classified by injury state (Figures 2–4). Further studied variation, due to the excitation wavelengths along with the comparison between the raw and reconstituted biomarkers' form, are shown in 'Supporting Information', Figures S1–S3.

Table 1. Overview of the studied TBI biomarker cohort with the corresponding physiological significance. Source refers to the biofluid in which the biomarker has been analysed in the literature. N-Acetyl-L-aspartic acid (NAA); Glutathione (GSH); Neuron-Specific Enolase (NSE); Glial fibrillary acidic protein (GFAP); Ubiquitin carboxyl-terminal hydrolase isozyme L1 (UCHL1); Inter-leukin-6 (IL-6); Interleukin-18 (IL-18); and Neurofilament light chain (NFL). Increase in concentration (↑), decrease in concentration (↓).

Biomarker	Source	Physiological Function	TBI Role	TBI Response	Reference
NAA	Blood CSF	Synthesised in neurons, specific to the nervous system. Has roles in maintaining myelin lipid synthesis and in promoting neuronal mitochondria ATP production.	Marks injury type. Depletion in grey matter and white matter represent neuronal loss and axonal damage, respectively. Rate of replenishment is inversely proportional to injury severity.	↓	[33,67,68]
Ganglioside	Serum CSF Brain	Cellular signalling, protein, and ion channel modulator. Main carrier of sialic acid in the nervous system, improving intercellular communications.	Functional disruption causes neurodegeneration, cellular dysfunctions and promotes disease pathogenesis.	↑	[69]
GSH	Blood CSF	Essential antioxidant, converted from its reduced state (GSH) to its oxidised form to regulate free radicals from the brain.	GSH depletion coupled with neuroinflammation leads to build-up of free radicals, further damaging the brain and neurons.	↓	[61,70]
NSE	CSF	Tissue-specific cytosol-based enzymes, upon stimulation they translocate to the cell surface to act as a plasminogen receptors.	The degree of damage is directly correlated to the amount of NSE expressed.	↑	[71]
GFAP	Blood CSF	Intermediate filament III protein. Maintains glial cytoskeleton structure, neighbouring neurons, and blood-brain barrier (BBB).	Post-trauma, astroglial cells undergo astrogliosis, causing cellular hypertrophy and increased GFAP expression. Excess GFAP can cause glial scars in brain tissue which delays axon regeneration.	↑	[72–74]

Table 1. *Cont.*

Biomarker	Source	Physiological Function	TBI Role	TBI Response	Reference
UCHL1	Blood CSF	A brain-specific enzyme features in the ubiquitin-proteasome pathway to maintain axonal protein integrity. Regulates axonal transport, structure, and synapsis.	Selectively increases upon axonal damage, utilised to remove damaged and defective proteins from axons.	↑	[75,76]
Cholesterol	CSF Brain Serum	Key component of the cellular membrane, maintaining structure and fluidity. Cholesterol and phospholipids are transported to nerve cells for repair, upkeep and to promote neurite proliferation.	Increased cholesterol is in proportion to cellular damage. Removing excess cholesterol has an anti-inflammatory effect. Dysregulation of brain cholesterol negatively affects neuronal and glial function. Cholesterol builds up from dysregulation causes cellular toxicity.	↑	[64,77–80]
D-Serine	Brain CSF Blood	α-amino acid, abundant in the brain. Binds to N-methyl-d-aspartate (NMDA) and δ_2 glutamate receptors to contribute to learning and memory function.	Reactive glial cells become D-Serine synthesisers under inflammatory conditions, causing NMDA receptor hyperactivation, and leading to hippocampal synaptic damage.	↑	[81]
Sphingomyelin	CSF Blood	Vital in regulation of cellular growth rate, differentiation, and death in the central nervous system. Supports myelination in the brain, and aids in cognitive maturation and regulation of inflammatory responses.	Increased levels are reported in the hippocampus over 12 months after TBI, contributing to neurological disease pathogenesis. Breakdown products regulate the sphingomyelin cycle which inhibits protein kinase c, regulating neuronal signal transduction and function.	↑	[82–86]
Sulfatides	Brain CSF Serum	Abundant in myelin sheath and myelinating cells. Negatively regulates and improves oligodendrocyte differentiation and survival. Maintains myelin and axonal-glial signalling.	Effects functional properties of the membrane, and dysregulation of sulfatides can lead to seizures.	↓	[87]
Cardiolipin	Inner Mitochondrial Membrane	Involved in regulating mitochondrial metabolism. The structural component of mitochondrial membranes regulates protein and enzyme activity central to mitochondrial function.	Damaged mitochondria trigger neuronal death when oxidised. Cardiolipin acts as an elimination signal for damaged mitochondria, thus limiting neuronal damage and preserving cognitive functions.	↑	[88–90]

Table 1. *Cont.*

Biomarker	Source	Physiological Function	TBI Role	TBI Response	Reference
IL-6	CSF Serum Blood	Pleiotropic cytokine with operations in immunity regulation, regeneration processes, neural functions, and cardiovascular protective mechanisms.	Usually undetectable in healthy brain parenchyma but present within an hour following TBI. Upregulated production following trauma from inflammatory cascades to salvage neurons. Sustained inflammation is ultimately damaging.	↑	[52,91–93]
S100B	Blood CSF Brain	Calcium-binding protein involved in long-term synaptic plasticity modulation, cellular growth and structure, calcium concentration maintenance, and energy metabolism. Mitigates mitochondrial failure through calcium modulation.	Overexpression leads to disrupted calcium homeostasis. Increased levels indicate structural damage and cellular death.	↑	[94,95]
Galactocerebroside	CSF Brain	Major lipid component in the brain, which maintains myelin sheath structure and stability. Important for development of normal myelin in the central nervous system.	Galactosylcerimidase dysfunction prevents Galactocerebroside from degrading, instead it accumulates in globoid cells in the brain, leading to white matter diseases.	↑	[55,96,97]
Glucose	Blood	Main energy source to the brain, used for action potential and postsynaptic potential generation. Synthesises BBB-regulated neuroactive compounds and sustains brain homeostasis.	Early low glucose levels and low lactate/glucose ratio post-TBI are associated with poor outcomes. Not associated with ischemia.	↓	[98–100]
Myo-Inositol	CSF Blood	Regulates glial and neuronal activity and participates in intracellular signalling pathways. Regulates intracellular [Ca^{2+}] and membrane permeability.	Increased levels are correlated to glial proliferation, increased rate of membrane turnover, and myelin sheath damage. Correlated to astrogliosis and dysregulation of cellular osmotic functions.	↑	[101–104]
IL-18	CSF	Inducer of inflammatory cytokines; synthesised as an inactive precursor in microglia and activated by caspase-1 in a forward loop.	Has roles in neuroinflammation and neurodegeneration. Induces respiratory burst and degranulation of polymorphonuclear leukocytes resulting in a release of neurotoxic enzymes.	↑	[105,106]

Table 1. *Cont.*

Biomarker	Source	Physiological Function	TBI Role	TBI Response	Reference
NFL	CSF Blood	Integral in maintaining axonal cytoskeleton through radial growth. Larger myelinated axons result in more NFL, leading to faster conduction speed.	NFL levels rapidly increase following trauma to account for damaged axons and NFL is released into the interstitial space and integrated into CSF. Indicates significant axonal damage and progression rate of disease.	↑	[107–109]

3.1. Acute Phase

Acute TBI biomarkers have been shown to be applicable in triaging, diagnosing, and eliminating the presence of TBI at the earliest stages (i.e., golden-hour biomarkers) and are thus particularly important for the development of diagnostic point-of-care modalities as well as intervention for TBI [110,111]. Therefore, biochemical changes and concentration variations in biomarkers are reflected through the spectral information when comparing healthy control cohorts to acute, sub-acute, and chronic phases, which are vital for PoC diagnostics and injury monitoring. Representative average spectra of acute TBI biomarkers are presented in Figure 2 alongside peak assignment provided in Table 2. Each biomarker produced unique and distinctive spectral features.

Strong characteristic peaks of NAA are found in the 949–957 cm^{-1} and 987–992 cm^{-1} regions for the four-excitation laser used (Figure 2a), with the main peaks being associated with the C-N stretching as well as CH_2-CH wagging [112]. NAA is an amino acid derivative located in neurons where the decreasing levels are proportional to neuronal loss and axonal damage [68] and, thus, a decrease in characteristic Raman peak intensity can be an important indicator following brain trauma.

The most intense peaks of ganglioside, a sialic acid-bearing glycosphingolipid [60], are detected at 1297–1298 cm^{-1} and 1437–1442 cm^{-1} (Figure 2b). The bands at 1297 and 1440 cm^{-1} are assigned to bending and twisting of CH_2 bonds [113], which optimally could be employed relative to other characteristic peaks of ganglioside post-TBI [114]. These peak intensities have been reported to decrease in counts in tandem with cell loss [114], in contrast to the other characteristic peaks of ganglioside (Table 2), which are typically shown to increase in response to neurodegeneration and cellular dysfunction (Table 1) [69].

GSH, a non-enzymatic antioxidant tripeptide present in cells to protect membranes from oxidative damage [115], exhibits the most intense peaks located at 1420–1424 cm^{-1} and 1660–1662 cm^{-1} (Figure 2c), attributed to the -CH_2 bending mode of proteins [116], and symmetrical stretching of the carboxylic acid COO^- [117], and the Amide I region, indicative of amino acids [118], respectively. Post-TBI apoptosis could lead to GSH depletion and thus a reduction in characteristic peak intensity which, when coupled with neuroinflammation, results in TBI secondary injury due to free radicals build-up further damaging neurons and the brain (Table 1) [70].

NSE is a glycolytic tissue-specific enzyme associated with neuronal damage and post-traumatic inflammation [41,63], increasing in expression with injury severity [71]. The strongest peak for NSE (Figure 2d) at 875–877 cm^{-1} at all four employed excitation wavelengths is assigned to the stretching of C-C bonds and the asymmetric stretching of C-N bonds [55,119] associated with phenylalanine. A secondary peak of interest at 1077–1082 cm^{-1} is attributed to the stretching of C-O and C-C bonds [120] along with the twisting of CH_2 bonds [121]. NSE is plausible for monitoring post-TBI changes since it is only expressed in a direct correlation to the degree of damage and translocated from the cytosol to cell surface upon stimulation, acting as a plasminogen receptor [62,71,122].

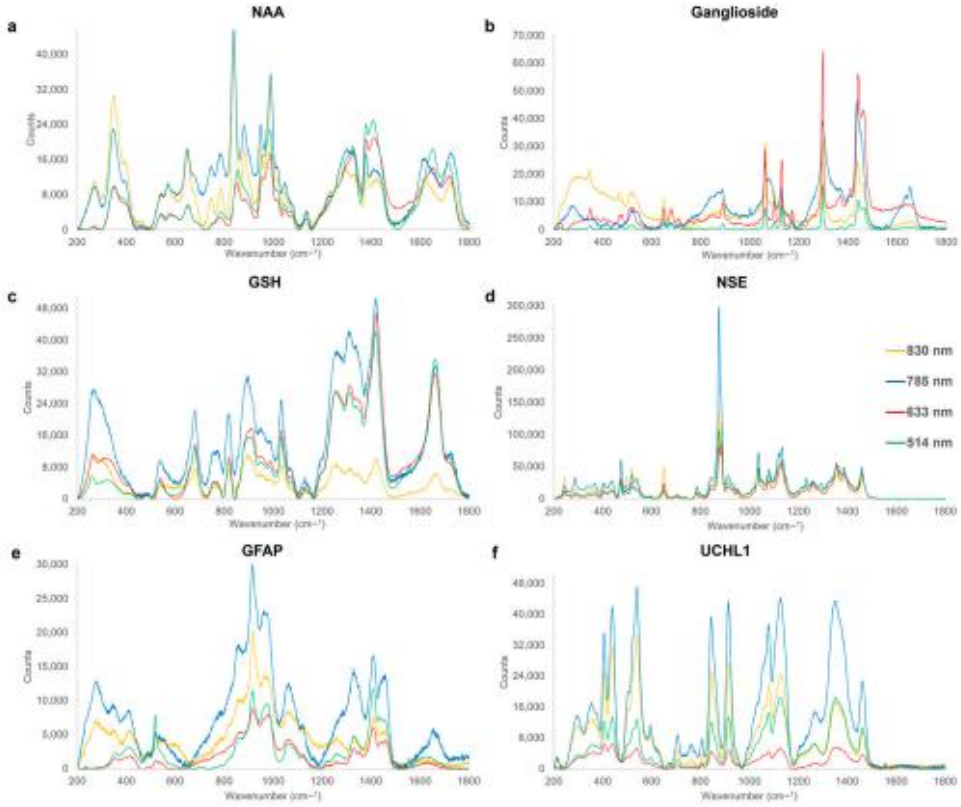

Figure 2. Characteristic Raman spectra fingerprints of acute-phase TBI biomarkers, acquired at excitation wavelengths of 514 nm (green), 633 nm (red), 785 nm (blue), and 830 nm (yellow). Significant Raman peak assignments for each are summarized in Table 2. N-Acetyl-L-aspartic acid (NAA); Glutathione (GSH); Neuron-Specific Enolase (NSE); Glial fibrillary acidic protein (GFAP); and Ubiquitin carboxyl-terminal hydrolase isozyme L1 (UCHL1).

GFAP is a structural filament protein of astrocytes [15], with its levels known to increase in response to astrogliosis post-trauma, as discussed in Table 1. The most intense detected spectral bands are found in the region of 914–918 cm^{-1} (Figure 2e), assigned to C-N stretching [119], and asymmetric vibration of the pyranose ring [112], also present in the UCHL1 spectrum (Figure 2f), increasing in response to TBI, and thus might collectively be an important candidate peak of interest for TBI Raman-based diagnostics.

A further sharp peak present in the 1408–1410 cm^{-1} region is assigned to the bending of C-H bonds and symmetrical stretching of COO^- bonds [119,123], along with a wider band at 1060–1068 cm^{-1}, assigned to the skeletal stretching of C-C bonds and indicative of changes in protein levels [124]. GFAP has been shown to increase after brain trauma because of reactive astrogliosis. Its overexpression, causing scarring of the brain, can be used to distinguish between the healthy and damaged tissue, giving an indication of the amount of damage, and delaying the axonal regeneration [73].

Table 2. Acute TBI phase associated Raman bands and their assignments. υ = stretching; δ = bending; τ = twisting; ρ = rocking; ω = wagging; s = symmetric; a = anti-symmetric; *arom* = aromatic; *skel* = skeletal.

Wavenumber (cm^{-1})	Assignment	Origin	Reference
347–353	υ_{skel}(C-C)	NAA	[112]
473–475	υ(S-S)	NSE	[125]
518–521	C(OH), *Ring deformation*	GFAP	[112,119]
647–651	υ(C-S), τ(C-C), *Ring breathing mode*	NAA, NSE, Ganglioside	[119,126,127]
679–682	υ(C-S)	GSH	[119]
705–708	*Ring deformation*	UCHL1	[119]
806	υ_s(C-N-C)	UCHL1	[112]
819–821	CH *deformation*	GSH	[112]
843–845	δ(H(C-O-H)), ρ(H(C-O-H))	UCHL1	[119]
875–877	υ(C-C), υ_a(C-N)	NSE	[55,119]
889–891	υ_{arom}(C-O), υ(C-C), ω(CH_2)	Ganglioside	[128–130]
914–918	υ(C-N), *Pyranose ring asymmetric vibration*	GFAP, UCHL1	[112,119]
949–957	υ(C-N)	NAA	[112]
974–980	υ_a(C-C), ρ(CH_2)	GFAP	[119,131]
987–992	υ(C-N), ω(CH_2- CH)	NAA	[112]
1031–1037	δ(C-H), υ(C-C), υ_a(C-C-N^+)	GSH, NSE	[132,133]
1060–1068	υ(C-O), υ_{skel}(C-C), τ(NH_2)	Ganglioside, GFAP	[119,124,134]
1077–1082	υ(C-O), υ(C-C), τ(CH_2)	NSE, UCHL1	[120,121]
1127–1130	υ(C-N), υ(C-C)	Ganglioside, UCHL1	[135,136]
1131–1138	υ(C-C)	NAA	[137]
1297–1298	τ(CH_2)	Ganglioside	[114]
1311–1315	δ(C-H)	GSH	[138]
1328–1336	ω(CH_2), τ(CH_2)	GFAP	[119]
1352–1354	τ(CH_2)	UCHL1	[121]
1378–1383	υ_s(COO^-)	NAA	[139]
1408–1410	δ(C-H), υ_s(COO^-)	GFAP	[119,123]
1420–1424	δ(CH_2), υ_s(COO^-), υ_s(CO_2)	GSH	[116,117,138]
1437–1442	δ(CH_2), τ(CH_2)	Ganglioside	[113]
1458–1460	δ(CH_2)	NSE	[140]
1660–1662	υ(C-N(H)-C=O), υ(C=C)	GSH	[112]

UCHL1, a cytoplasmic enzyme found in neurons, is selectively increased following axonal trauma to remove damaged and defective proteins from axons [75,141]. Unfortunately, the glycerol-environment buffer of this protein dominates the spectral fingerprint with aliphatic chains [121,142] and, therefore, only smaller peaks in the 600–800 cm^{-1} region are identified to be unique to the UCHL1 marker (Figure 2f) with the 705–708 cm^{-1} band assigned to ring deformation [119], and the 806 cm^{-1} peak assigned to the symmetrical stretching of C-N-C bonds present in amino acids [112].

3.2. Sub-Acute Phase

Detection of sub-acute TBI biomarkers is vital for multiple-level diagnostics when the patient is admitted to hospital and a complementary rapid diagnostic technique is required alongside structural neuroimaging. This lays the platform for not only enabling timely TBI management at ED, A&E, etc. for early neuroprotective measures but also for the correct transfer to the most appropriate neurological facility. Rapid diagnosis in the early clinical phase will lay a platform for a range of improvements in personalised medicine and management, reduce strain on the healthcare system, and enable better-quality post-neurotraumatic care. Similarly, in the military context, where neurosurgical support is not routinely deployed and TBI management often requires evacuation, the ability to diagnose and assess TBI severity pre-hospital would avoid unnecessary strategic evacuation and maintain operational effectiveness. Representative average spectra of sub-acute TBI solute-form biomarkers are shown in Figure 3 with the corresponding peak assignments summarised in Table 3.

Cholesterol's sterol-centred structure presents a unique and large number of intense peaks (Figure 3a), including the 700 cm^{-1} band of the in-plane deformation of its B ring [143], as well as a sharp peak at 1673 cm^{-1}, assigned to the B ring C=C stretching [144]. Cholesterol is structurally important in the cellular membrane with its increases following TBI proportionally related to the cellular damage [145]. As a response to neuroinflammation, apolipoprotein E transports cholesterol and phospholipids by forming a protein–lipid complex to damaged nerve cells to assist the cellular damage as well as to increase neurite proliferation [77,78]; whilst cholesterol removal is associated with the anti-inflammatory response [64,79]. If left unchecked, the dysregulation of cholesterol in the brain can negatively affect neuronal and glial functions and in due course, leading to cellular toxicity [80].

D-Serine is a non-essential polar amino acid, which serves as a precursor to purines and pyrimidines, and is an important neurotransmitter [146]. The characteristic fingerprint of D-Serine (Figure 3b) exhibits strong peaks in the range of 917–923 cm^{-1}, attributed to its C-C backbone stretching [140], as well as at 1327–1336 cm^{-1} from the twisting of its CH_2 groups [119]. Serine is a co-ligand activator of NMDA receptors and of δ_2 glutamate receptors, which have regulatory roles in synaptic plasticity and long-term potentiation [81]. Increases in serine following TBI is caused by reactive glial cells, which under inflammatory conditions turn into D-serine synthesisers. An increase in D-serine leads to hyperactivation of NMDA receptors, which damages hippocampal synapsis and is known to disrupt learning and memory formation [46,81]. Blocking D-serine production under inflammatory conditions has been related to improved outcome following brain trauma [81].

Sphingomyelin can be spectrally identified by a characteristic set of peaks in the range of 717–720 cm^{-1} and 1295–1299 cm^{-1}, due to the symmetric stretching of C-N and the twisting of CH_2, respectively [114,119] (Figure 4c). Sphingomyelin is a prominent sphingolipid, found in the plasma membrane with a distribution ratio correlating specifically with cholesterol for suitable membrane function [147]. This lipid plays vital roles within the CNS in terms of cellular growth, differentiation, and death [82]. In the brain, sphingomyelin is also associated with improved cognitive maturation, brain myelination, and regulation of inflammatory responses [83,148]. Levels of sphingomyelin have been shown to increase following TBIs for over 12 months, rendering it a neuro-marker for both sub-acute as well as chronic phases [84]. Disruption of sphingomyelin metabolism is known to dysregulate the mitochondrial energy pathways, slowing the healing process and increasing the risk of secondary injuries, contributing to the overall TBI pathogenesis [149].

Sulfatides are a class of sulfo-lipids, abundantly present in brain tissue and are a main feature in myelin sheath and within myelinating cells [87]. Spectral characteristic fingerprints of sulfatides are shown in Figure 4d. These representative peaks include the stretching of the C-OH from the sulphated pyranose ring and C-C backbone along with the CH_2 wagging in the range of 888–893 cm^{-1} [128–130], with the anti-symmetric stretching of the SO_4 group identified at 1107–1111 cm^{-1} [150]. Sulfatides, directly derived from galactocerebrosides, constitute promising candidate TBI biomarkers due to their roles in protein trafficking, neuronal transduction, and negative regulation in oligodendrocyte differentiation [151]. Following TBI, sulfatide levels decrease in the brain subsequently, allowing the oligodendrocyte production to occur at a higher rate, thus providing axonal myelin wrapping with improved action potential and transmission. However, due to the functional role of sulfatides within the membrane, the dysregulation can lead to physiological responses such as seizures [87].

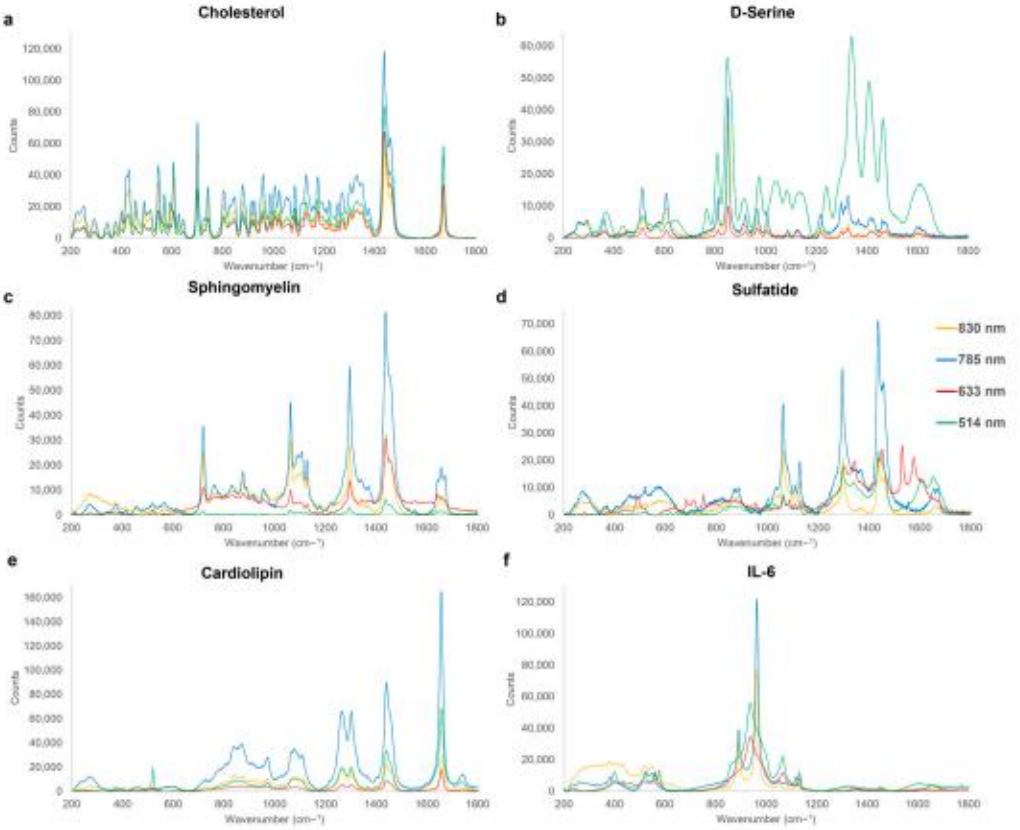

Figure 3. Characteristic Raman spectra fingerprints of sub-acute-phase TBI biomarkers, acquired at excitation wavelengths of 514 nm (green), 633 nm (red), 785 nm (blue), and 830 nm (yellow). Significant Raman peak assignments for each are summarised in Table 3.

Cardiolipin, a mitochondrial-specific phospholipid, which signals damaged mitochondria [88] (Figure 4e), is found to exhibit dominant PO_4 vibrations at 959–964 cm^{-1} and C-O stretching from the linoleic acid groups in the range of 1266–1268 cm^{-1} [152,153]. Cardiolipin is known to be central to mitochondrial function, with roles in both regulation of metabolism and membrane structure maintenance [88], with damaged and dysregulated mitochondria triggering neuronal death [89,90]. Cardiolipin is externalised from the inner mitochondrial membrane to signal damaged mitochondria and promote mitophagy, ultimately limiting further neuronal damage and retaining cognitive functions [90], resulting in increases in its concentration linked to the extent of mitochondrial damage [89,90].

IL-6, an inflammatory cytokine, yields a distinctive spectral signature (Figure 4f) with peptide bonds bending within the protein detected in the 520–525 cm^{-1} region [112], and a sharp peak at 959–964 cm^{-1}, associated with the symmetric stretching of the C-N-C bonds of proteins [112]. The pleiotropic IL-6 is involved in immunity, regeneration, and neural functions [93]. Whilst in healthy brain tissue it is not typically detectable, it has been found to be present within an hour of brain injury, making it a reliable marker of TBI-induced damage [91,92]. IL-6 is further upregulated during inflammatory cascades to help healing including the salvation of neurons; however, a prolonged detection of this biomarker is indicative of sustained inflammation, resulting in more damage over healing [90].

Table 3. Peak assignments of significant peaks present in the sub-acute TBI biomarker phase. υ = stretching, δ = bending, τ = twisting, ρ = rocking, ω = wagging, *s* = symmetric, *a* = anti-symmetric, *arom* = aromatic, *skel* = skeletal.

Wavenumber (cm^{-1})	Assignment	Origin	References
512–516	$\rho(COO^-)$	D-Serine	[140]
520–525	δ(N-C=O)	IL-6	[112]
549	δ(N-C-S)	IL-6	[112]
561	-OH *out of plane deformation*	IL-6	[112]
700–702	*In-plane deformation of B ring*	Cholesterol	[143]
717–720	υ_s(C-N)	Sphingomyelin	[119]
809–815	υ(C-C)	D-Serine	[112]
850–854	$\rho(CH_2)$	D-Serine	[140]
888–893	$\upsilon_{arom}(C\text{-}O)_4$, υ(C-C), $\omega(CH_2)$	Sulfatide	[128–130]
917–923	υ(C-C)	D-Serine	[140]
959–964	PO_4 *vibration*, υ_s(C-N-C), δ(C-H)	Cholesterol, IL-6, Cardiolipin	[112,152]
970–974	υ(C-N)	D-Serine	[140]
1062–1067	υ(C-O), υ(C-C), $\tau(NH_2)$	Sphingomyelin, Sulfatide, IL-6	[119,124,134]
1107–1111	$\upsilon_a(SO_4)$, υ(C-N), υ(C-C), υ(C-OH),	Sulfatide, Cardiolipin	[23,150]
1127–1130	υ(C-N), υ(C-C), υ_{skel}(C-C)	Sphingomyelin, Sulfatide, IL-6	[135,136]
1176–1179	υ_{skel}(C-C)	Cholesterol	[144]
1266–1268	υ(C –O)	Cardiolipin	[153]
1295–1299	$\tau(CH_2)$	Sphingomyelin, Sulfatide	[114]
1302–1304	$\tau(CH_2)$	Cardiolipin	[143]
1327–1336	$\omega(CH_2)$, $\tau(CH_2)$	Cholesterol, D-Serine	[119]
1436–1441	$\delta(CH_2)$, $\tau(CH_2)$, $\upsilon(CH_2/CH_3)$	Cholesterol, Sphingomyelin, Sulfatide, Cardiolipin	[113,154]
1656–1660	υ(C=O), υ(C=C)	Sphingomyelin, Cardiolipin	[118,155]
1672–1674	υ(C=C)	Cholesterol	[144]

3.3. Chronic Phase

Chronic TBI biomarkers span a larger timeframe and are particularly important in cases of undiagnosed mTBI, frequently causing patients long-term effects. Certain chronic biomarkers are expressed in the early phase, during the acute phase, and continue to be expressed in the longer-term [40,53,56]. The chosen representative chronic biomarkers (Figure 1) provide important underpinning spectral fingerprints, contributing towards ongoing investigations on chronic biomarkers and their post-TBI mechanisms and, once confirmed, the emerging findings would enable the detected biomarker levels at late time points to be used to identify TBI survivors who are at high risk of progressive neurological damage, triggered by their initial TBI. Rapid detection and an in-depth understanding of chronic TBI biomarkers would aid the development of TBI therapeutics and enable in situ tracking of TBI pathology and injury evolution at hospital. Real-time spectroscopy for TBI monitoring would further improve target management and understanding of injury heterogeneity, evolution, penetrance of pharmacological agents, identify novel targets for intervention, and could lead to the development of modalities for tactful therapeutic modifying therapies in TBIs. Representative average spectra of chronic, TBI, solute form biomarkers are shown in Figure 4 with the corresponding peak assignments summarised in Table 4.

S100B is a calcium-binding protein expressed in astrocytes and is the first brain biomarker to be recognised and utilised within clinical practice guidelines [15,156]. S100B, known to be neuroprotective and neurotrophic, is regarded as a suitable marker due to its involvement in the modulation of long-term synaptic plasticity and energy metabolism by maintaining calcium concentration and ensuring correct mitochondrial function [94,95]. Characteristic dominant spectral peaks are identified for S100B throughout the entire 200–1800 cm^{-1} region (Figure 4a and Table 4). The most intense bands are at 936–937 cm^{-1}, assigned to stretching of the C-C bond of proline and valine [157], and at 1002–1004 cm^{-1}, due to aromatic phenyl breathing of the C-C bond of the phenylalanine [119,158]. Post TBI,

increased S100B levels accompany structural damage and cellular death [95]. This would result in higher intensity of identified Raman peaks, posing it as a promising marker for Raman-based neuro-diagnostics. Physiologically, the implication of increased S100B levels disrupts the correct calcium homeostasis, leading to mitochondrial failures and damaging long-term hippocampal potentiation [94,95].

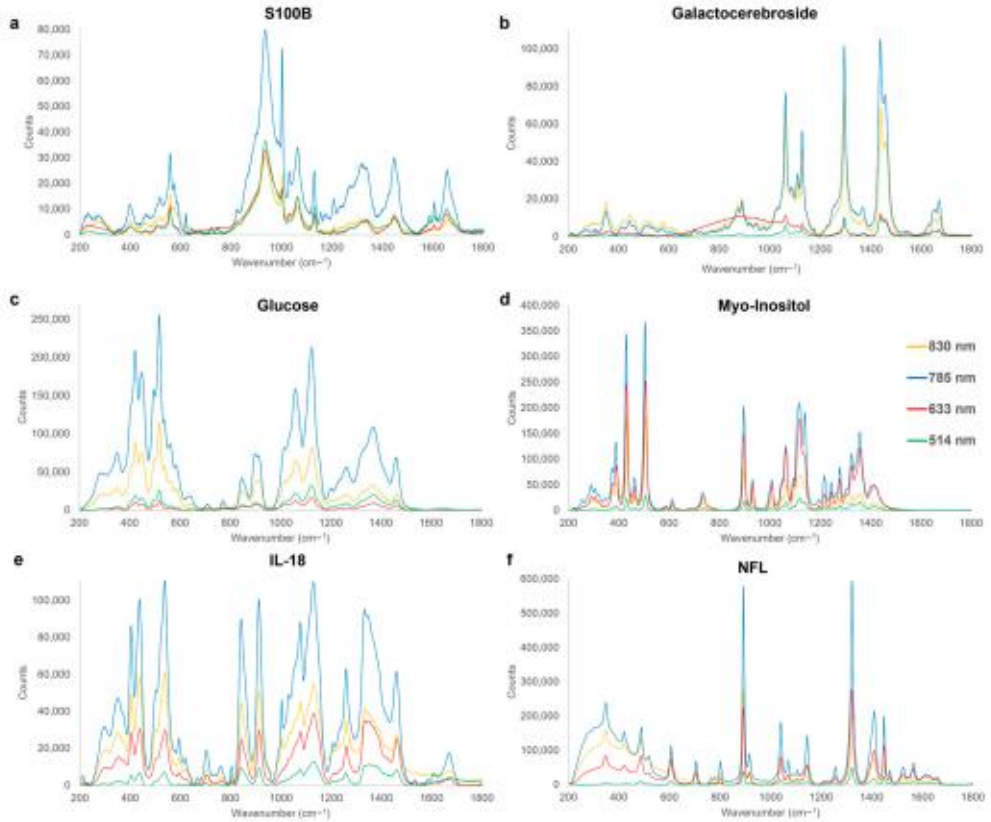

Figure 4. Characteristic Raman spectra fingerprints of chronic-phase TBI biomarkers, acquired at excitation wavelengths of 514 nm (green), 633 nm (red), 785 nm (blue), and 830 nm (yellow). Significant Raman peak assignments for each are summarised in Table 4.

Galactocerebrosides are a major glycolipid of the myelin within the CNS and the most abundant glycolipid component of myelin [159,160]. Figure 4b exhibits dominant spectral peaks in the fingerprint spectrum, particularly, above the 1000 cm^{-1} region. A characteristic peak in the 1128–1133 cm^{-1} range is assigned to the C-N stretching of the amine bond in the acyl chain [119], and the C-C bond skeletal stretching of the acyl backbone common to lipids [136], and further in the 1295–1298 cm^{-1} region, assigned to the twisting of CH_2 bonds of lipids [114]. This biomarker accumulates in the brain in globoid cells when there is galactosylcerimidase dysfunction, preventing galactocerebroside from degrading, potentially leading to a long-term white matter disease (Table 1).

Overall, peaks in the range of 1295–1299 cm^{-1} are also present in the spectra of sphingomyelin, sulfatide and ganglioside, creating a potential band of interest for the detection of chronic TBI biomarkers via Raman spectroscopy as well as to assess post-TBI recovery and response to interventions.

Glucose is the predominant and preferred energy source of the mammalian brain, with levels present indicating metabolism in astrocytes [56,100]. Overall, biomarkers in the chronic phase had a larger number of characteristic peaks identified in the lower wavenumber and fingerprint regions 200–800 cm^{-1} than the earlier phases with two intense bands determined from the glucose spectrum (Figure 4c) in the 422–424 and 517–520 cm^{-1} regions, with the former attributed to the in-plane aromatic bending of the C-OH bond [112] and the latter assigned to C-OH bond deformation (Table 4) [112]. Decreases in glucose levels post-TBI have been shown to be associated with poor outcomes due to the indication of an increased need for energy for tissue repair. Glucose metabolism post-trauma has also been shown to lead to an increase in anaerobic glycolysis; however, this has been specifically proven to be a result of ischemia. Furthermore, glucose levels can be compared to other metabolites downstream in the glycolytic pathway such as the ratio of pyruvate (aerobic product) to lactate (anaerobic product). A larger ratio typically correlates to more glycolytic than mitochondrial activity and is associated with worse outcomes, due to an indication that neurons might be too damaged to take up lactate for the TCA cycle [100].

Myo-inositol, a sugar derivative, has been reported to increase in proportion with TBI severity [161], and in correlation with glial proliferation, membrane turnover, and myelin sheath damage (Table 1). Spectral peaks of myo-inositol are highly consistent across the four excitation wavelengths used (Figure 4d) with the most intense bands at 504–506 cm^{-1}, assigned to out-of-plane deformation of -OH bonds and further in 1116–1121 cm^{-1} and 1217–1218 cm^{-1} regions, attributed to stretching of the C-C bonds [162–164]. Further intense peaks at 896–899 cm^{-1} and 1357–1359 cm^{-1} arise from CH bending within the aliphatic structure of myo-inositol [112]. Increases in myo-inositol levels post TBI provide a good marker of proliferation of glial cells, membrane turnover, myelin sheath damage as well as astrogliosis and cellular osmotic dysregulation [101–104].

Table 4. Peak assignments of significant peaks present in the chronic TBI biomarkers phase. υ = stretching, δ = bending, τ = twisting, ρ = rocking, ω = wagging, s = symmetric, a = anti-symmetric, *arom* = aromatic, *skel* = skeletal, Δ = ring breathing vibration.

Wavenumber (cm^{-1})	Assignment	Origin	Reference
422–424	*In-plane* δ_{arom}(C-OH)	Glucose	[112]
504–506	OH *out-of-plane deformation*	Myo-Inositol	[112]
517–520	C-OH *deformation*	Glucose	[112]
559–560	OH *out-of-plane deformation*	S100B	[165]
606–607	CCC *in-plane deformation*	NFL	[166]
804–807	υ_s (C-N-C)	IL-18	[112]
842–844	*Out-of-plane* δ_{arom}(CH), ρ (H(C-O-H))	IL-18	[119,142]
891–893	$\upsilon_s(COO^-)$, υ(C-C)	NFL	[167,168]
896–899	$\upsilon_{aliphatic}$(C-H)	Myo-Inositol	[112]
912–914	$\upsilon(C\text{-}CH_3)$	IL-18	[169]
936–937	υ(C-C)	S100B	[157,170]
1002–1004	Δ_{arom}(C-C)	S100B	[119,171]
1008–1010	Δ_{arom}(C-C)	Myo-Inositol	[172]
1040–1041	$\upsilon(C\text{-}CH_3)$, υ(C-C), δ(CH)	NFL	[158,173]
1058–1066	υ(C-O), υ_{skel}(C-C), $\tau(NH_2)$	S100B, Galactocerebroside, Glucose	[124,134]
1077–1080	υ(C-C), υ(C-O)	IL-18	[119,120]
1116–1121	δ(CH), υ(C-C),	Myo-Inositol	[162,174]

Table 4. *Cont.*

Wavenumber (cm^{-1})	Assignment	Origin	Reference
1124–1127	υ(C-C)	Glucose	[135]
1128–1133	υ_{alef}(C-C), υ(C-N)	S100B, Galactocerebroside, IL-18	[119,135,136]
1143–1146	υ(C-N), δ(CH)	NFL	[138,175,176]
1217–1218	υ(C-C)	Myo-Inositol	[163]
1259–1261	Amide III (υ(CN) δ(NH)	IL-18	[177,178]
1295–1298	$\tau(CH_2)$	Galactocerebroside	[114]
1321–1323	δ(CH), $\tau(CH_2)$,	NFL (glycine)	[179,180]
1357–1359	$\upsilon_{aliphatic}$(CH)	Myo-Inositol	[112]
1368–1371	$\delta(CH_2)$	Glucose	[181]
1409–1411	υ(C-C), δ(C-H)	NFL	[119]
1439–1441	$\upsilon(CH_2/CH_3)$	Galactocerebroside	[154]
1458–1464	ω(C-H), $\delta(CH_3)$, τ(C=O), υ_{arom}(C=C)	Galactocerebroside, Glucose, IL-18	[182–184]
1603–1608	$\upsilon_a(COO^-)$, υ(C=C), υ(C=O)	S100B	[119,138,185]
1672–1676	υ(C=C)	Galactocerebroside	[144]

IL-18 is a pro-inflammatory cytokine, produced by microglia and stored in the cytosol as an inactive precursor (Figure 4e) [105]. The most representative fingerprint peaks of IL-18 are identified at 1259–1261 cm^{-1}, from the amide III stretching of C-N and bending of N-H, specific to proteins [177,178], and a sharp peak at 806 cm^{-1}, assigned to the protein specific symmetrical stretch of C-N-C bonds [112]. Following TBI, IL-18 is known to externalise and bind to the plasma membrane. Uncontrolled or dysregulated IL-18 can lead to releases of neurotoxic enzymes as well as cause chronic inflammatory diseases, whilst IL-18 inhibition has been shown to prevent further damage [106,186].

Finally, the NFL marker has been shown to play a role in maintaining the axonal cytoskeleton [107], and although not necessarily specific to TBI, its rapid increase in CSF is indicative of a considerable axonal injury with change in its concentration correlating the severity of damage [108]. It has been therefore suggested that monitoring the NFL levels is useful for determining the extent of trauma as well as the response to any therapeutic interventions [109]. This marker exhibits a characteristic spectral fingerprint consisting of sharp peaks (Figure 4f), with the most prominent at 891–893 cm^{-1}, due to symmetrical stretching of carboxylic acids and C-C bonds [167,168], and the 1321–1323 cm^{-1}, attributed to CH bending and CH_2 twisting modes [179,180].

Further to the spectral assignments of brain-specific molecular species, it is of importance to consider the identified and selected group of correlative changes in Raman peak ratios with key features of these representing quantifiable biochemical changes. The use of characteristic Raman peak ratios allows for the important information to be easily extracted from spectra (particularly, for multiplex mixtures in complex biological environments such as the body fluid or brain tissue) to gain more information and in conjunction with multivariate analysis methods, the ratio-metric inspection and assignment of Raman spectra can be used to identify spectral changes informed by chemical and spectroscopic knowledge, showing clear systematic trends with identifiable features of biomolecules. With these key Raman peak ratios correlating with structural and quantitative biomarker information, analysis of fingerprint spectra could be performed more accurately than the individual peak changes, which could be often masked in complex biofluids. We have thus utilised dominant peak ratios of the solute state TBI biomarkers, which also allows comparison of their variation across the four excitation wavelength lasers (Figure 5).

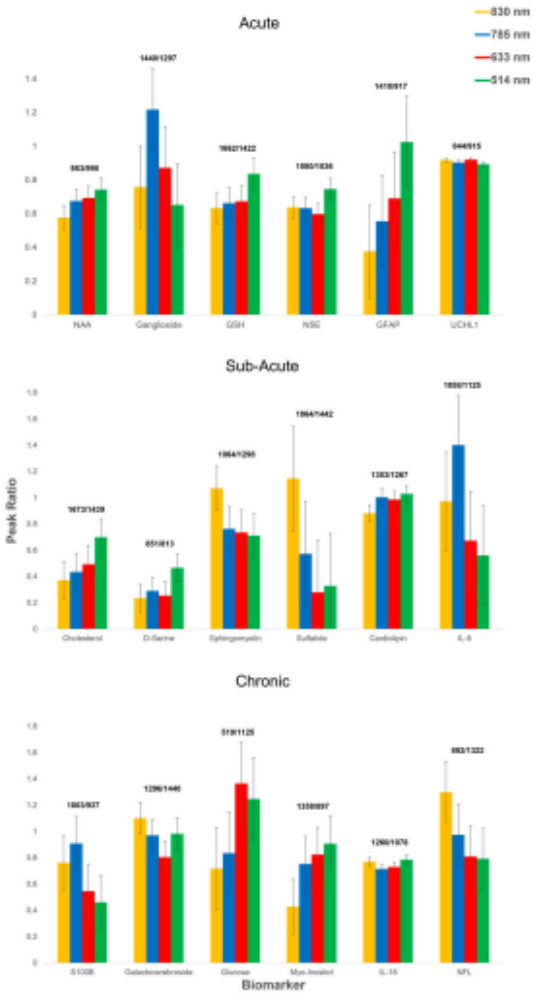

Figure 5. Characteristic peak ratios identified from spectral fingerprints per each studied TBI-indicative biomarker at four excitation wavelengths of 514 nm (green), 633 nm (red), 785 nm (blue), and 830 nm (yellow). ($p < 0.0001$, one-way ANOVA). N-Acetyl-L-aspartic acid (NAA); Glutathione (GSH); Neuron-Specific Enolase (NSE); Glial fibrillary acidic protein (GFAP); Ubiquitin carboxyl-terminal hydrolase isozyme L1 (UCHL1); Interleukin-6 (IL-6); Interleukin-18 (IL-18); and Neurofilament light chain (NFL).

Characteristic peaks were selected without bias from the six assigned bands identified via the peak pick method for each studied biomarker in acute, sub-acute and chronic phases, generating the unique intensity ratios barcode in the fingerprint region. The use of the relative peak ratio intensity provides more accurate and reproducible information over the absolute Raman intensity, which differs among different Raman devices and changing conditions, and is of further importance for multivariate analysis methods often employed in conjunction with Raman spectroscopy detection and analysis [187,188]. These peak ratios yield the combined unique spectroscopic barcode for each brain-injury marker, which could be used as a reference for rapid and accurate diagnostics of TBI in easily accessible

biofluids as well as allow to easier quantify the performance of emerging spectroscopic techniques via the standard variation of the ratios between the amplitudes of two Raman bands from a given biomarker over repeated measurements (Figure 5). For the majority of the biomarkers, within the experimental error, there was no significant difference in the identified peak ratios when varying the excitation laser except for GFAP, sulfatide and glucose (p *** < 0.0001, one-way ANOVA), which had the largest variance per phase group, with sulfatide having the highest variance of the entire cohort ($\sigma^2 = 0.158$). This suggests that greater consideration should be given to the choice of the Raman excitation laser to detect this biomarker, since the molecular bonds of interest are excited at varied intensity strengths depending on the laser wavelength. Conversely, UCHL1, cardiolipin, and IL-18 exhibited the lowest variance within their corresponding phase group, with the lowest overall cohort variance found to be for UCHL1 ($\sigma^2 = 0.000164$) with the highest peak agreement amongst the four excitation lasers.

4. Current Challenges and Future Outlook

Overall, Raman based diagnosis of TBI pathologies via biofluid detection is emerging as a promising tool for rapid point-of-care diagnostics, and with the addition of the identified molecular profiles, a simple process of a 'spectroscopic barcode' will ensure variation due to the presence and/or change in the level of a particular TBI-indicative biomarker and, further, therapeutic treatments and various underlying conditions will be taken into account and reduce the error in the data interpretation of the associated changes, leading towards improved diagnostic accuracy.

It is worth noting, however, that whilst important progress has been accomplished herein via Raman spectroscopy spectral fingerprints of biomarkers of TBI, several limitations and challenges remain. Firstly, in terms of study design, biomarkers were sourced with the intention to avoid Raman-active additives such as buffers, which would impact the accuracy of the characters' fingerprint. This has, therefore, removed several candidate biomarkers identified in the literature since pure forms were not available. Furthermore, we used a varied source of human/animal TBI biomarkers, with five out of the overall eighteen investigated biomarkers derived from animals, due to limitations in availability. Whilst animal model systems frequently share similarities of specific aspects of TBIs, providing the opportunity to target specific biomarkers, animal neuromarker models, however, can occasionally recapitulate only parts of the pathology observed in human TBI [189–194]. Recognising the opportunities and limitations of translational biomarkers is therefore critical to advancing human TBI therapies. Importantly, this study aims to bridge the gap between preclinical and clinical research as well as to better demonstrate interactions between central expression of TBI pathological markers and peripheral examinations, which could subsequently be used for diagnosis and evaluation of treatment efficacy. Nevertheless, it is important to note, that we did not carry out spectroscopic detection and classification of TBI vs. healthy biomarkers but rather established the characteristic fingerprints for each chosen biomarker, which is a standalone spectroscopic barcode for either human- or animal-derived neuromarkers. In each case, there is a value and significance to having the 'baseline' fingerprint data, as in the case of a rapidly evolving and multifaceted pathology such as TBI, they may provide integrative and complementary clinically useful information, or may be useful for different investigations, time points, or settings. For instance, animal biomarker models provide a major advantage for investigating preclinical measures of therapeutic efficacy [189,190]. Faster and less expensive results can be garnered from these allowing only the most promising candidates to advance to more costly clinical trials (e.g., Sabbagh et al. [195]) and represent an important approach to exploring the translational utility of a novel compound. In preclinical systems, animal biomarkers could also be effective for valuing the translational worth of a compound before costly human trials are initiated. Animal model biomarker assessments can verify proof of concept for a candidate treatment. Furthermore, the identification of consistent biomarkers may shed light on core mechanisms responsible for the disorder, as well as interactions between several of the

identified pathologies. Notably, the subsequent use of both human and animal biomarkers can form a bridge between animal and human studies to facilitate translational research. By using the same biomarkers in animals and humans, observations in the preclinical stage can be more easily extended to clinical trials. This forward translation can be complemented by a backward one, where observations in humans can be studied via animals.

An additional challenge is that the spectral bands associated with some biomarkers are also present in several other proteins, and so these changes cannot always solely be attributed to a particular molecule. Therefore, a broad panel of biomarkers should be used in such cases, essential to delivering a diagnosis with high accuracy and specificity. This, with further emerging novel hybrid Raman-AI techniques, refs. [196,197], will in turn enable supporting large-scale triaging and screening for early signs of brain injury, particularly useful for identifying high-risk patients and implementing intervention measures, given both the increased incidence and the prevalence of TBIs. Indeed, considerable research in recent years has focused on potential biomarkers to improve diagnosis and patient phenotyping to enable timely and targeted management. For instance, S100B has been implemented in Scandinavian countries and the ALERT-TBI study showed high sensitivity for the combination of GFAP and neuronal UCHL1 measured within 12 h of injury, forming the basis of the first FDA-approved TBI test for triaging the need for CT scanning [198].

One further issue that needs to be addressed for real-world adoption is a lack of standardisation in methods used within the current literature, from matters pertaining to biofluid collection, storage and pre-processing, to those concerning Raman measurement protocols and chemometric analyses and classification. Standardisation of protocols and conducting larger-scale clinical studies are vital for advancing the clinical translation of Raman spectroscopy biomarker profiling in TBI diagnostic and prognostic applications.

Finally, there has been an increase in the literature surrounding the development of Raman spectroscopy-based technologies for TBI detection, utilising surface-enhanced Raman spectroscopy (SERS), microfluidics, and Raman probes [33,35,36,199,200]. As such new spectroscopic technologies are being engineered and prototyped, it is essential to improve the understanding of brain injury biomarkers and their mechanism in various post-TBI phases, which will continue to grow alongside these, particularly when utilising human biofluids and TBI models.

5. Conclusions

A Raman spectroscopy fingerprint library has been generated for a large cohort of TBI-indicative biomarkers. The spectral fingerprint of each studied biomarker generates a unique signature and comparisons of certain values for determined frequencies and their raw and aqueous solution states are determined. These spectra provide the fundamental information necessary to track the biochemical changes induced by the neurological markers categorised according to the different stages post-brain injury, i.e., the acute, sub-acute and chronic phases. These can not only assist in understanding the TBI mechanism and check the presence, persistence or fading of characteristic biomolecules in brain tissue or biofluids following injuries but also establish Raman spectroscopy-aided diagnosis of TBI as a complementary point-of-need technique. The longer-term goal would be to identify biomarkers or distinctive patterns, which would help to rapidly detect, triage, and monitor TBIs by analysing the differences in Raman spectral signatures.

The most dominant peak ratios for each biomarker have been further identified, highlighting the various advantages amongst which, by using the ratio-metric approach over the absolute Raman intensity of individual bands, is elimination of the need to measure the amplitude of each peak, often necessary for ensuring consistency and reproducibility of the intensity and/or wavenumber position, which can be challenging between each measurement, especially when performed by a non-expert at the point of care.

Reliable point-of-care diagnostic tools, such as Raman spectroscopy, could improve the specificity of diagnosis and triage of TBI and would greatly aid resource availability in healthcare by reducing the number of unnecessary ED visits for mild TBI and increasing the

proportion of patients with moderate/severe TBIs appropriately triaged to attend trauma facilities. With millions of ED visits every year and the high cost per visit without treatment or investigation, even a small reduction will result in massive cost savings. Furthermore, the pathophysiology of injury evolution is multi-faceted, and not understood well enough to provide effective pharmacological targeting to reduce burden or progression. An in-depth understanding of the biochemical injury evolution will allow interventions to be used more effectively and identify novel therapeutic targets to guide tactful treatments. The generated spectral library would further assist in the emerging developments of Raman spectroscopy-based technologies, for rapid acquisition of molecular fingerprints of TBI biochemistry to safely measure proxies for cerebral injury via the body fluids, which will soon provide a tangible path towards non-invasive point-of-care diagnostics for TBI.

Supplementary Materials: The following supporting information can be downloaded at: https://www.mdpi.com/article/10.3390/cells12222589/s1, Figure S1: Spectra of raw and reconstituted acute TBI biomarkers.; Figure S2: Spectra of raw and reconstituted sub-acute TBI biomarkers.; Figure S3: Spectra of raw and reconstituted Chronic TBI biomarkers.

Author Contributions: Conceptualization, P.G.O. and G.H.; Methodology, G.H., C.A.S., M.L. and P.G.O.; Formal analysis, G.H., C.A.S. and P.G.O.; Investigation, G.H., C.A.S. and M.L.; Resources, P.G.O.; Data curation, G.H., C.A.S. and P.G.O.; Writing—original draft preparation, G.H. and C.A.S. and P.G.O.; Writing—review and editing, G.H. and C.A.S. and P.G.O.; Supervision, project administration and funding acquisition, P.G.O. All authors have read and agreed to the published version of the manuscript.

Funding: This research was funded by the Wellcome Trust (174ISSFPP) and the EPSRC (EP/V029983/1). We also acknowledge the funding from UK Research and Innovation (UKRI) under the UK Government's Horizon Europe Funding Guarantee (ERC Consolidator Grant, EP/Y030206/1). The APC was funded by the UKRI.

Data Availability Statement: Data supporting reported results can be provided by the authors upon reasonable request.

Conflicts of Interest: The authors declare no conflict of interest.

References

1. Khellaf, A.; Khan, D.Z.; Helmy, A. Recent advances in traumatic brain injury. *J. Neurol.* **2019**, *266*, 2878–2889. [CrossRef] [PubMed]
2. Capizzi, A.; Woo, J.; Verduzco-Gutierrez, M. Traumatic Brain Injury: An Overview of Epidemiology, Pathophysiology, and Medical Management. *Med. Clin. N. Am.* **2020**, *104*, 213–238. [CrossRef] [PubMed]
3. Wang, K.K.; Yang, Z.; Zhu, T.; Shi, Y.; Rubenstein, R.; Tyndall, J.A.; Manley, G.T. An update on diagnostic and prognostic biomarkers for traumatic brain injury. *Expert Rev. Mol. Diagn.* **2018**, *18*, 165–180. [CrossRef]
4. Adrian, H.; Mårten, K.; Salla, N.; Lasse, V. Biomarkers of traumatic brain injury: Temporal changes in body fluids. *eNeuro* **2016**, *3*, e0294-16. [CrossRef]
5. Ercole, A.; Thelin, E.P.; Holst, A.; Bellander, B.M.; Nelson, D.W. Kinetic modelling of serum S100b after traumatic brain injury. *BMC Neurol.* **2016**, *16*, 93. [CrossRef]
6. Lippa, S.M.; Werner, J.K.; Miller, M.C.; Gill, J.M.; Diaz-Arrastia, R.; Kenney, K. Recent Advances in Blood-Based Biomarkers of Remote Combat-Related Traumatic Brain Injury. *Curr. Neurol. Neurosci. Rep.* **2020**, *20*, 54. [CrossRef] [PubMed]
7. Kobeissy, F.H.; Sadasivan, S.; Oli, M.W.; Robinson, G.; Larner, S.F.; Zhang, Z.; Hayes, R.L.; Wang, K.K.W. Neuroproteomics and systems biology-based discovery of protein biomarkers for traumatic brain injury and clinical validation. *Proteom.—Clin. Appl.* **2008**, *2*, 1467–1483. [CrossRef] [PubMed]
8. Agoston, D.V.; Shutes-David, A.; Peskind, E.R. Biofluid biomarkers of traumatic brain injury. *Brain Inj.* **2017**, *31*, 1195–1203. [CrossRef]
9. Shahim, P.; Politis, A.; van der Merwe, A.; Moore, B.; Ekanayake, V.; Lippa, S.M.; Chou, Y.Y.; Pham, D.L.; Butman, J.A.; Diaz-Arrastia, R.; et al. Time course and diagnostic utility of NfL, tau, GFAP, and UCH-L1 in subacute and chronic TBI. *Neurology* **2020**, *95*, e623–e636. [CrossRef]
10. Rubenstein, R.; Chang, B.; Yue, J.K.; Chiu, A.; Winkler, E.A.; Puccio, A.M.; Diaz-Arrastia, R.; Yuh, E.L.; Mukherjee, P.; Valadka, A.B.; et al. Comparing plasma phospho tau, total tau, and phospho tau–total tau ratio as acute and chronic traumatic brain injury biomarkers. *JAMA Neurol.* **2017**, *74*, 1063–1072. [CrossRef]
11. Chitturi, J.; Li, Y.; Santhakumar, V.; Kannurpatti, S.S. Consolidated biochemical profile of subacute stage traumatic brain injury in early development. *Front. Neurosci.* **2019**, *13*, 431. [CrossRef]

12. Dewan, M.C.; Rattani, A.; Gupta, S.; Baticulon, R.E.; Hung, Y.C.; Punchak, M.; Agrawal, A.; Adeleye, A.O.; Shrime, M.G.; Rubiano, A.M.; et al. Estimating the global incidence of traumatic brain injury. *J. Neurosurg.* **2019**, *130*, 1080–1097. [CrossRef]
13. Teasdale, G.; Maas, A.; Lecky, F.; Manley, G.; Stocchetti, N.; Murray, G. The Glasgow Coma Scale at 40 years: Standing the test of time. *Lancet Neurol.* **2014**, *13*, 844–854. [CrossRef] [PubMed]
14. Bazarian, J.J.; Veazie, P.; Mookerjee, S.; Lerner, E.B. Accuracy of mild traumatic brain injury case ascertainment using ICD-9 codes. *Acad. Emerg. Med.* **2006**, *13*, 31–38. [CrossRef]
15. Huie, J.R.; Mondello, S.; Lindsell, C.J.; Antiga, L.; Yuh, E.L.; Zanier, E.R.; Masson, S.; Rosario, B.L.; Ferguson, A.R.; Adeoye, O.; et al. Biomarkers for Traumatic Brain Injury: Data Standards and Statistical Considerations. *J. Neurotrauma* **2021**, *38*, 2514–2529. [CrossRef]
16. McBride, W.R.; Eltman, N.R.; Swanson, R.L. Blood-Based Biomarkers in Traumatic Brain Injury: A Narrative Review with Implications for the Legal System. *Cureus* **2023**, *15*, e40417. [CrossRef]
17. Mavroudis, I.; Petridis, F.; Balmus, I.M.; Ciobica, A.; Gorgan, D.L.; Luca, A.C. Review on the Role of Salivary Biomarkers in the Diagnosis of Mild Traumatic Brain Injury and Post-Concussion Syndrome. *Diagnostics* **2023**, *13*, 1367. [CrossRef]
18. Mozafari, J.; Fahimi, M.A.; Mohammadi, K.; Barzegari, H.; Hanafi, M.G.; Saki-Malehi, A. The diagnostic accuracy of serum and urinary S100B protein in children and adolescents with mild traumatic brain injury. *N. Z. J. Med. Lab. Sci.* **2019**, *73*, 88–91.
19. Zetterberg, H.; Blennow, K. Fluid markers of traumatic brain injury. *Mol. Cell. Neurosci.* **2015**, *66*, 99–102. [CrossRef] [PubMed]
20. Cordero, E.; Latka, I.; Matthäus, C.; Schie, I.; Popp, J. In-vivo Raman spectroscopy: From basics to applications. *J. Biomed. Opt.* **2018**, *23*, 071210. [CrossRef]
21. Hanlon, E.B.; Manoharan, R.; Koo, T.W.; Shafer, K.E.; Motz, J.T.; Fitzmaurice, M.; Kramer, J.R.; Itzkan, I.; Dasari, R.R.; Feld, M.S. Prospects for in vivo Raman spectroscopy. *Phys. Med. Biol.* **2000**, *45*, R1. [CrossRef]
22. Guo, S.; Bocklitz, T.; Popp, J. Optimization of Raman-spectrum baseline correction in biological application. *Analyst* **2016**, *141*, 2396–2404. [CrossRef]
23. Birech, Z.; Mwangi, P.W.; Bukachi, F.; Mandela, K.M. Application of Raman spectroscopy in type 2 diabetes screening in blood using leucine and isoleucine amino-acids as biomarkers and in comparative anti-diabetic drugs efficacy studies. *PLoS ONE* **2017**, *12*, e0185130. [CrossRef]
24. Koster, H.J.; Guillen-Perez, A.; Gomez-Diaz, J.S.; Navas-Moreno, M.; Birkeland, A.C.; Carney, R.P. Fused Raman spectroscopic analysis of blood and saliva delivers high accuracy for head and neck cancer diagnostics. *Sci. Rep.* **2022**, *12*, 18464. [CrossRef] [PubMed]
25. Ryzhikova, E.; Ralbovsky, N.M.; Sikirzhytski, V.; Kazakov, O.; Halamkova, L.; Quinn, J.; Zimmerman, E.A.; Lednev, I.K. Raman spectroscopy and machine learning for biomedical applications: Alzheimer's disease diagnosis based on the analysis of cerebrospinal fluid. *Spectrochim. Acta A Mol. Biomol. Spectrosc.* **2021**, *248*, 119188. [CrossRef]
26. Sathyavathi, R.; Dingari, N.C.; Barman, I.; Prasad, P.S.R.; Prabhakar, S.; Narayana Rao, D.; Dasari, R.R.; Undamatla, J. Raman spectroscopy provides a powerful, rapid diagnostic tool for the detection of tuberculous meningitis in ex vivo cerebrospinal fluid samples. *J. Biophotonics* **2013**, *6*, 567. [CrossRef] [PubMed]
27. Chen, C.; Yang, L.; Zhao, J.; Yuan, Y.; Chen, C.; Tang, J.; Yang, H.; Yan, Z.; Wang, H.; Lv, X. Urine Raman spectroscopy for rapid and inexpensive diagnosis of chronic renal failure (CRF) using multiple classification algorithms. *Optik* **2020**, *203*, 164043. [CrossRef]
28. Kavuru, V.; Senger, R.S.; Robertson, J.L.; Choudhury, D. Analysis of urine Raman spectra differences from patients with diabetes mellitus and renal pathologies. *PeerJ* **2023**, *11*, e14879. [CrossRef]
29. Buchan, E.; Hardy, M.; de Carvalho Gomes, P.; Kelleher, L.; Chu, H.O.M.; Oppenheimer, P.G. Emerging Raman spectroscopy and saliva-based diagnostics: From challenges to applications. *Appl. Spectrosc. Rev.* **2022**. [CrossRef]
30. Kim, S.; Kim, T.G.; Lee, S.H.; Kim, W.; Bang, A.; Moon, S.W.; Song, J.; Shin, J.H.; Yu, J.S.; Choi, S. Label-Free Surface-Enhanced Raman Spectroscopy Biosensor for On-Site Breast Cancer Detection Using Human Tears. *ACS Appl. Mater. Interfaces* **2020**, *12*, 7897–7904. [CrossRef]
31. Camerlingo, C.; Lisitskiy, M.; Lepore, M.; Portaccio, M.; Montorio, D.; Del Prete, S.; Cennamo, G. Characterization of human tear fluid by means of surface-enhanced raman spectroscopy. *Sensors* **2019**, *19*, 1177. [CrossRef] [PubMed]
32. Cennamo, G.; Montorio, D.; Morra, V.B.; Criscuolo, C.; Lanzillo, R.; Salvatore, E.; Camerlingo, C.; Lisitskiy, M.; Delfino, I.; Portaccio, M.; et al. Surface-enhanced Raman spectroscopy of tears: Toward a diagnostic tool for neurodegenerative disease identification. *J. Biomed. Opt.* **2020**, *25*, 1. [CrossRef] [PubMed]
33. Rickard, J.J.S.; Di-Pietro, V.; Smith, D.J.; Davies, D.J.; Belli, A.; Oppenheimer, P.G. Rapid optofluidic detection of biomarkers for traumatic brain injury via surface-enhanced Raman spectroscopy. *Nat. Biomed. Eng.* **2020**, *4*, 610–623. [CrossRef] [PubMed]
34. Li, C.; Shah, K.A.; Narayan, R.K. Rapid detection of traumatic brain injury. *Nat. Biomed. Eng.* **2020**, *4*, 579–580. [CrossRef]
35. Mowbray, M.; Banbury, C.; Rickard, J.J.S.; Davies, D.J.; Goldberg Oppenheimer, P. Development and Characterization of a Probe Device toward Intracranial Spectroscopy of Traumatic Brain Injury. *ACS Biomater. Sci. Eng.* **2021**, *7*, 1252–1262. [CrossRef]
36. Stevens, A.R.; Stickland, C.A.; Harris, G.; Ahmed, Z.; Oppenheimer, P.G.; Belli, A.; Davies, D.J. Raman Spectroscopy as a Neuromonitoring Tool in Traumatic Brain Injury: A Systematic Review and Clinical Perspectives. *Cells* **2022**, *11*, 1227. [CrossRef]
37. Feinberg, C.; Carr, C.; Zemek, R.; Yeates, K.O.; Master, C.; Schneider, K.; Bell, M.J.; Wisniewski, S.; Mannix, R. Association of Pharmacological Interventions With Symptom Burden Reduction in Patients With Mild Traumatic Brain Injury: A Systematic Review. *JAMA Neurol.* **2021**, *78*, 596–608. [CrossRef]

38. Marro, M.; Taubes, A.; Abernathy, A.; Balint, S.; Moreno, B.; Sanchez-Dalmau, B.; Martínez-Lapiscina, E.H.; Amat-Roldan, I.; Petrov, D.; Villoslada, P. Dynamic molecular monitoring of retina inflammation by in vivo Raman spectroscopy coupled with multivariate analysis. *J. Biophotonics* **2014**, *7*, 724–734. [CrossRef]
39. Harris, G.; Rickard, J.J.S.; Butt, G.; Kelleher, L.; Blanch, R.J.; Cooper, J.; Oppenheimer, P.G. Review: Emerging Eye-Based Diagnostic Technologies for Traumatic Brain Injury. *IEEE Rev. Biomed. Eng.* **2023**, *16*, 530–559. [CrossRef]
40. Böhmer, A.E.; Oses, J.P.; Schmidt, A.P.; Perón, C.S.; Krebs, C.L.; Oppitz, P.P.; D'Avila, T.T.; Souza, D.O.; Portela, L.V.; Stefani, M.A. Neuron-specific enolase, S100B, and glial fibrillary acidic protein levels as outcome predictors in patients with severe traumatic brain injury. *Neurosurgery* **2011**, *68*, 1624–1630. [CrossRef]
41. Gutierre, M.U.; Telles, J.P.M.; Welling, L.C.; Rabelo, N.N.; Teixeira, M.J.; Figueiredo, E.G. Biomarkers for traumatic brain injury: A short review. *Neurosurg. Rev.* **2021**, *44*, 2091–2097. [CrossRef] [PubMed]
42. Zetterberg, H.; Smith, D.H.; Blennow, K. Biomarkers of mild traumatic brain injury in cerebrospinal fluid and blood. *Nat. Rev. Neurol.* **2013**, *9*, 201. [CrossRef] [PubMed]
43. Damien, B.; Charlotte, O.; Marina, B.; Julie, D.; Vincent, S. Interest of blood biomarkers to predict lesions in medical imaging in the context of mild traumatic brain injury. *Clin. Biochem.* **2020**, *85*, 5–11. [CrossRef]
44. Woods, A.S.; Colsch, B.; Jackson, S.N.; Post, J.; Baldwin, K.; Roux, A.; Hoffer, B.; Cox, B.M.; Hoffer, M.; Rubovitch, V.; et al. Gangliosides and CeramidesChange in a Mouse Model of Blast Induced Traumatic Brain Injury. *ACS Chem. Neurosci.* **2013**, *4*, 594. [CrossRef]
45. Kim, H.J.; Tsao, J.W.; Stanfill, A.G. The current state of biomarkers of mild traumatic brain injury. *JCI Insight* **2018**, *3*, e97105. [CrossRef]
46. Perez, E.J.; Tapanes, S.A.; Loris, Z.B.; Balu, D.T.; Sick, T.J.; Coyle, J.T.; Liebl, D.J. Enhanced astrocytic d-serine underlies synaptic damage after traumatic brain injury. *J. Clin. Investig.* **2017**, *127*, 3114–3125. [CrossRef]
47. Lee, S.H.; Kho, A.R.; Lee, S.H.; Hong, D.K.; Kang, B.S.; Park, M.K.; Lee, C.J.; Yang, H.W.; Woo, S.Y.; Park, S.W.; et al. Acid Sphingomyelinase Inhibitor, Imipramine, Reduces Hippocampal Neuronal Death after Traumatic Brain Injury. *Int. J. Mol. Sci.* **2022**, *23*, 14749. [CrossRef]
48. Sparvero, L.J.; Amoscato, A.A.; Fink, A.B.; Anthonymuthu, T.; New, L.A.; Kochanek, P.M.; Watkins, S.; Kagan, V.E.; Bayır, H. Imaging mass spectrometry reveals loss of polyunsaturated cardiolipins in the cortical contusion, hippocampus, and thalamus after traumatic brain injury. *J. Neurochem.* **2016**, *139*, 659–675. [CrossRef]
49. Chao, H.; Anthonymuthu, T.S.; Kenny, E.M.; Amoscato, A.A.; Cole, L.K.; Hatch, G.M.; Ji, J.; Kagan, V.E.; Bayır, H. Disentangling oxidation/hydrolysis reactions of brain mitochondrial cardiolipins in pathogenesis of traumatic injury. *JCI Insight* **2018**, *3*, e97677. [CrossRef]
50. Banbury, C.; Styles, I.; Eisenstein, N.; Zanier, E.R.; Vegliante, G.; Belli, A.; Logan, A.; Goldberg Oppenheimer, P. Spectroscopic detection of traumatic brain injury severity and biochemistry from the retina. *Biomed. Opt. Express* **2020**, *11*, 6249–6261. [CrossRef]
51. Antunes, A.A.; Sotomaior, V.S.; Sakamoto, K.S.; de Camargo Neto, C.P.; Martins, C.; Aguiar, L.R. Interleukin-6 Plasmatic Levels in Patients with Head Trauma and Intracerebral Hemorrhage. *Asian J. Neurosurg.* **2010**, *5*, 68–77.
52. Kumar, R.G.; Diamond, M.L.; Boles, J.A.; Berger, R.P.; Tisherman, S.A.; Kochanek, P.M.; Wagner, A.K. Acute CSF interleukin-6 trajectories after TBI: Associations with neuroinflammation, polytrauma, and outcome. *Brain. Behav. Immun.* **2015**, *45*, 253–262. [CrossRef] [PubMed]
53. Wang, K.K.W.; Kobeissy, F.H.; Shakkour, Z.; Tyndall, J.A. Thorough overview of ubiquitin C-terminal hydrolase-L1 and glial fibrillary acidic protein as tandem biomarkers recently cleared by US Food and Drug Administration for the evaluation of intracranial injuries among patients with traumatic brain injury. *Acute Med. Surg.* **2021**, *8*, e622. [CrossRef] [PubMed]
54. Guan, J.; Zhu, Z.; Zhao, R.C.; Xiao, Z.; Wu, C.; Han, Q.; Chen, L.; Tong, W.; Zhang, J.; Han, Q.; et al. Transplantation of human mesenchymal stem cells loaded on collagen scaffolds for the treatment of traumatic brain injury in rats. *Biomaterials* **2013**, *34*, 5937–5946. [CrossRef]
55. Krafft, C.; Neudert, L.; Simat, T.; Salzer, R. Near infrared Raman spectra of human brain lipids. *Spectrochim. Acta—Part A Mol. Biomol. Spectrosc.* **2005**, *61*, 1529–1535. [CrossRef] [PubMed]
56. Shi, J.; Dong, B.; Mao, Y.; Guan, W.; Cao, J.; Zhu, R.; Wang, S. Review: Traumatic brain injury and hyperglycemia, a potentially modifiable risk factor. *Oncotarget* **2016**, *7*, 71052. [CrossRef]
57. Kierans, A.S.; Kirov, I.I.; Gonen, O.; Haemer, G.; Nisenbaum, E.; Babb, J.S.; Grossman, R.I.; Lui, Y.W. Myoinositol and glutamate complex neurometabolite abnormality after mild traumatic brain injury. *Neurology* **2014**, *82*, 521. [CrossRef]
58. Ciaramella, A.; Della Vedova, C.; Salani, F.; Viganotti, M.; D'Ippolito, M.; Caltagirone, C.; Formisano, R.; Sabatini, U.; Bossù, P. Increased Levels of Serum IL-18 Are Associated with the Long-Term Outcome of Severe Traumatic Brain Injury. *Neuroimmunomodulation* **2014**, *21*, 8–12. [CrossRef]
59. Belli, A.; Sen, J.; Petzold, A.; Russo, S.; Kitchen, N.; Smith, M.; Tavazzi, B.; Vagnozzi, R.; Signoretti, S.; Amorini, A.M.; et al. Extracellular N-acetylaspartate depletion in traumatic brain injury. *J. Neurochem.* **2006**, *96*, 861–869. [CrossRef]
60. Rubovitch, V.; Zilberstein, Y.; Chapman, J.; Schreiber, S.; Pick, C.G. Restoring GM1 ganglioside expression ameliorates axonal outgrowth inhibition and cognitive impairments induced by blast traumatic brain injury. *Sci. Rep.* **2017**, *7*, 41269. [CrossRef]
61. Koza, L.; Linseman, D. Glutathione precursors shield the brain from trauma. *Neural Regen. Res.* **2019**, *14*, 1701. [CrossRef]

62. Smith, R.; Chepisheva, M.; Cronin, T.; Seemungal, B.M. Diagnostic Approaches Techniques in Concussion/Mild Traumatic Brain Injury: Where are we? In *Neurosensory Disorders in Mild Traumatic Brain Injury*; Academic Press: Cambridge, MA, USA, 2019; pp. 247–277. [CrossRef]
63. Mehta, T.; Fayyaz, M.; Giler, G.E.; Kaur, H.; Raikwar, S.P.; Kempuraj, D.; Selvakumar, G.P.; Ahmed, M.E.; Thangavel, R.; Zaheer, S.; et al. Current Trends in Biomarkers for Traumatic Brain Injury. *Open Access J. Neurol. Neurosurg.* **2020**, *12*, 86–94. [CrossRef]
64. Cartagena, C.M.; Ahmed, F.; Burns, M.P.; Pajoohesh-Ganji, A.; Pak, D.T.; Faden, A.I.; Rebeck, G.W. Cortical Injury Increases Cholesterol 24S Hydroxylase (Cyp46) Levels in the Rat Brain. *J. Neurotrauma* **2008**, *25*, 1087. [CrossRef]
65. Bergholt, M.S.; Serio, A.; Albro, M.B. Raman Spectroscopy: Guiding Light for the Extracellular Matrix. *Front. Bioeng. Biotechnol.* **2019**, *7*, 491962. [CrossRef] [PubMed]
66. Chau, A.H.; Motz, J.T.; Gardecki, J.A.; Waxman, S.; Bouma, B.E.; Tearney, G.J. Fingerprint and high-wavenumber Raman spectroscopy in a human-swine coronary xenograft in vivo. *J. Biomed. Opt.* **2008**, *13*, 040501. [CrossRef] [PubMed]
67. Moffett, J.R.; Arun, P.; Ariyannur, P.S.; Namboodiri, A.M.A. N-Acetylaspartate reductions in brain injury: Impact on post-injury neuroenergetics, lipid synthesis, and protein acetylation. *Front. Neuroenergetics* **2013**, *5*, 69505. [CrossRef]
68. Shannon, R.J.; van der Heide, S.; Carter, E.L.; Jalloh, I.; Menon, D.K.; Hutchinson, P.J.; Carpenter, K.L.H. Extracellular *N*-Acetylaspartate in Human Traumatic Brain Injury. *J. Neurotrauma* **2016**, *33*, 319–329. [CrossRef]
69. Sipione, S.; Monyror, J.; Galleguillos, D.; Steinberg, N.; Kadam, V. Gangliosides in the Brain: Physiology, Pathophysiology and Therapeutic Applications. *Front. Neurosci.* **2020**, *14*, 1004. [CrossRef]
70. Khatri, N.; Thakur, M.; Pareek, V.; Kumar, S.; Sharma, S.; Datusalia, A.K. Oxidative Stress: Major Threat in Traumatic Brain Injury. *CNS Neurol. Disord. Drug Targets* **2018**, *17*, 689–695. [CrossRef]
71. Haque, A.; Ray, S.K.; Cox, A.; Banik, N.L. Neuron specific enolase: A promising therapeutic target in acute spinal cord injury. *Metab. Brain Dis.* **2016**, *31*, 487–495. [CrossRef] [PubMed]
72. Yang, Z.; Wang, K.K.W. Glial fibrillary acidic protein: From intermediate filament assembly and gliosis to neurobiomarker. *Trends Neurosci.* **2015**, *38*, 364–374. [CrossRef] [PubMed]
73. Sofroniew, M.V. Molecular dissection of reactive astrogliosis and glial scar formation. *Trends Neurosci.* **2009**, *32*, 638–647. [CrossRef]
74. Tzeng, S.F.; Hsiao, H.Y.; Mak, O.T. Prostaglandins and cyclooxygenases in glial cells during brain inflammation. *Curr. Drug Targets Inflamm. Allergy* **2005**, *4*, 335–340. [CrossRef] [PubMed]
75. Liu, H.; Povysheva, N.; Rose, M.E.; Mi, Z.; Banton, J.S.; Li, W.; Chen, F.; Reay, D.P.; Barrionuevo, G.; Zhang, F.; et al. Role of UCHL1 in axonal injury and functional recovery after cerebral ischemia. *Proc. Natl. Acad. Sci. USA* **2019**, *116*, 4643–4650. [CrossRef]
76. Shahjouei, S.; Sadeghi-Naini, M.; Yang, Z.; Kobeissy, F.; Rathore, D.; Shokraneh, F.; Blackburn, S.; Manley, G.T.; Wang, K.K.W. The diagnostic values of UCH-L1 in traumatic brain injury: A meta-analysis. *Brain Inj.* **2017**, *32*, 1–17. [CrossRef] [PubMed]
77. Nathoo, N.; Chetty, R.; Van Dellen, J.R.; Barnett, G.H. Genetic vulnerability following traumatic brain injury: The role of apolipoprotein E. *Mol. Pathol.* **2003**, *56*, 132–136. [CrossRef]
78. Surmacki, J.M.; Ansel-Bollepalli, L.; Pischiutta, F.; Zanier, E.R.; Ercole, A.; Bohndiek, S.E. Label-free monitoring of tissue biochemistry following traumatic brain injury using Raman spectroscopy. *Analyst* **2017**, *142*, 132–139. [CrossRef]
79. Kay, A.D.; Day, S.P.; Kerr, M.; Nicoll, J.A.R.; Packard, C.J.; Caslake, M.J. Remodeling of Cerebrospinal Fluid Lipoprotein Particles after Human Traumatic Brain Injury. *J. Neurotrauma* **2004**, *20*, 717–723. [CrossRef]
80. Xu, H.; Zheng, L.X.; Chen, X.S.; Pang, Q.Y.; Yan, Y.N.; Liu, R.; Guo, H.M.; Ren, Z.Y.; Yang, Y.; Gu, Z.Y.; et al. Brain-specific loss of Abcg1 disturbs cholesterol metabolism and aggravates pyroptosis and neurological deficits after traumatic brain injury. *Brain Pathol.* **2023**, *33*, e13126. [CrossRef]
81. Tapanes, S.A.; Arizanovska, D.; Díaz, M.M.; Folorunso, O.O.; Harvey, T.; Brown, S.E.; Radzishevsky, I.; Close, L.N.; Jagid, J.R.; Graciolli Cordeiro, J.; et al. Inhibition of glial D-serine release rescues synaptic damage after brain injury. *Glia* **2022**, *70*, 1133. [CrossRef]
82. Alessenko, A.V.; Albi, E. Exploring Sphingolipid Implications in Neurodegeneration. *Front. Neurol.* **2020**, *11*, 513554. [CrossRef] [PubMed]
83. Schneider, N.; Hauser, J.; Oliveira, M.; Cazaubon, E.; Mottaz, S.C.; O'Neill, B.V.; Steiner, P.; Deoni, S.C.L. Sphingomyelin in Brain and Cognitive Development: Preliminary Data. *eNeuro* **2019**, *6*, e0421-18. [CrossRef] [PubMed]
84. Ojo, J.O.; Algamal, M.; Leary, P.; Abdullah, L.; Mouzon, B.; Evans, J.E.; Mullan, M.; Crawford, F. Converging and differential brain phospholipid dysregulation in the pathogenesis of repetitive mild traumatic brain injury and Alzheimer's disease. *Front. Neurosci.* **2019**, *13*, 416109. [CrossRef]
85. Wang, G.; Bieberich, E. Sphingolipids in neurodegeneration (with focus on ceramide and S1P). *Adv. Biol. Regul.* **2018**, *70*, 51–64. [CrossRef]
86. Yang, K.; Taft, W.C.; Dixon, C.E.; Todaro, C.A.; Yu, R.K.; Hayes, R.L. Alterations of protein kinase C in rat hippocampus following traumatic brain injury. *J. Neurotrauma* **1993**, *10*, 287–295. [CrossRef] [PubMed]
87. Takahashi, T.; Suzuki, T. Role of sulfatide in normal and pathological cells and tissues. *J. Lipid Res.* **2012**, *53*, 1437–1450. [CrossRef]
88. Paradies, G.; Paradies, V.; Ruggiero, F.M.; Petrosillo, G. Role of Cardiolipin in Mitochondrial Function and Dynamics in Health and Disease: Molecular and Pharmacological Aspects. *Cells* **2019**, *8*, 728. [CrossRef]
89. Chu, C.T.; Ji, J.; Dagda, R.K.; Jiang, J.F.; Tyurina, Y.Y.; Kapralov, A.A.; Tyurin, V.A.; Yanamala, N.; Shrivastava, I.H.; Mohammadyani, D.; et al. Cardiolipin externalization to the outer mitochondrial membrane acts as an elimination signal for mitophagy in neuronal cells. *Nat. Cell Biol.* **2013**, *15*, 1197–1205. [CrossRef]

90. Chao, H.; Lin, C.; Zuo, Q.; Liu, Y.; Xiao, M.; Xu, X.; Li, Z.; Bao, Z.; Chen, H.; You, Y.; et al. Cardiolipin-Dependent Mitophagy Guides Outcome after Traumatic Brain Injury. *J. Neurosci.* **2019**, *39*, 1930–1943. [CrossRef]
91. Williams, A.J.; Wei, H.H.; Dave, J.R.; Tortella, F.C. Acute and delayed neuroinflammatory response following experimental penetrating ballistic brain injury in the rat. *J. Neuroinflamm.* **2007**, *4*, 17. [CrossRef]
92. Ooi, S.Z.Y.; Spencer, R.J.; Hodgson, M.; Mehta, S.; Phillips, N.L.; Preest, G.; Manivannan, S.; Wise, M.P.; Galea, J.; Zaben, M. Interleukin-6 as a prognostic biomarker of clinical outcomes after traumatic brain injury: A systematic review. *Neurosurg. Rev.* **2022**, *45*, 3035–3054. [CrossRef]
93. Schett, G. Physiological effects of modulating the interleukin-6 axis. *Rheumatology* **2018**, *57*, ii43–ii50. [CrossRef]
94. Nishiyama, H.; Knöpfel, T.; Endo, S.; Itohara, S. Glial protein S100B modulates long-term neuronal synaptic plasticity. *Proc. Natl. Acad. Sci. USA* **2002**, *99*, 4037–4042. [CrossRef]
95. Goyal, A.; Failla, M.D.; Niyonkuru, C.; Amin, K.; Fabio, A.; Berger, R.P.; Wagner, A.K. S100b as a Prognostic Biomarker in Outcome Prediction for Patients with Severe Traumatic Brain Injury. *J. Neurotrauma* **2013**, *30*, 946. [CrossRef]
96. Boustany, R.M.N. Lysosomal storage diseases—The horizon expands. *Nat. Rev. Neurol.* **2013**, *9*, 583–598. [CrossRef] [PubMed]
97. Marcus, J.; Popko, B. Galactolipids are molecular determinants of myelin development and axo–glial organization. *Biochim. Biophys. Acta—Gen. Subj.* **2002**, *1573*, 406–413. [CrossRef] [PubMed]
98. Mergenthaler, P.; Lindauer, U.; Dienel, G.A.; Meisel, A. Sugar for the brain: The role of glucose in physiological and pathological brain function. *Trends Neurosci.* **2013**, *36*, 587. [CrossRef]
99. Vespa, P.M.; McArthur, D.; O'Phelan, K.; Glenn, T.; Etchepare, M.; Kelly, D.; Bergsneider, M.; Martin, N.A.; Hovda, D.A. Persistently low extracellular glucose correlates with poor outcome 6 months after human traumatic brain injury despite a lack of increased lactate: A microdialysis study. *J. Cereb. Blood Flow Metab.* **2003**, *23*, 865–877. [CrossRef] [PubMed]
100. Jalloh, I.; Carpenter, K.L.H.; Helmy, A.; Carpenter, T.A.; Menon, D.K.; Hutchinson, P.J. Glucose metabolism following human traumatic brain injury: Methods of assessment and pathophysiological findings. *Metab. Brain Dis.* **2015**, *30*, 615–632. [CrossRef] [PubMed]
101. López-Gambero, A.J.; Sanjuan, C.; Serrano-Castro, P.J.; Suárez, J.; Fonseca, F.R. De The Biomedical Uses of Inositols: A Nutraceutical Approach to Metabolic Dysfunction in Aging and Neurodegenerative Diseases. *Biomedicines* **2020**, *8*, 295. [CrossRef]
102. Brand, A.; Richter-Landsberg, C.; Leibfritz, D. Multinuclear NMR studies on the energy metabolism of glial and neuronal cells. *Dev. Neurosci.* **1993**, *15*, 289–298. [CrossRef] [PubMed]
103. Haris, M.; Cai, K.; Singh, A.; Hariharan, H.; Reddy, R. In vivo mapping of brain myo-inositol. *Neuroimage* **2011**, *54*, 2079–2085. [CrossRef]
104. Ashwal, S.; Holshouser, B.; Tong, K.; Serna, T.; Osterdock, R.; Gross, M.; Kido, D. Proton Spectroscopy Detected Myoinositol in Children with Traumatic Brain Injury. *Pediatr. Res.* **2004**, *56*, 630–638. [CrossRef]
105. Alboni, S.; Cervia, D.; Sugama, S.; Conti, B. Interleukin 18 in the CNS. *J. Neuroinflamm.* **2010**, *7*, 9. [CrossRef]
106. Felderhoff-Mueser, U.; Schmidt, O.I.; Oberholzer, A.; Bührer, C.; Stahel, P.F. IL-18: A key player in neuroinflammation and neurodegeneration? *Trends Neurosci.* **2005**, *28*, 487–493. [CrossRef]
107. Narayanan, S.; Shanker, A.; Khera, T.; Subramaniam, B. Neurofilament light: A narrative review on biomarker utility. *Fac. Rev.* **2021**, *10*, 46. [CrossRef]
108. Khalil, M.; Teunissen, C.E.; Otto, M.; Piehl, F.; Sormani, M.P.; Gattringer, T.; Barro, C.; Kappos, L.; Comabella, M.; Fazekas, F.; et al. Neurofilaments as biomarkers in neurological disorders. *Nat. Rev. Neurol.* **2018**, *14*, 577–589. [CrossRef] [PubMed]
109. Gaetani, L.; Blennow, K.; Calabresi, P.; Di Filippo, M.; Parnetti, L.; Zetterberg, H. Neurofilament light chain as a biomarker in neurological disorders. *J. Neurol. Neurosurg. Psychiatry* **2019**, *90*, 870–881. [CrossRef]
110. Maas, A.I.R.; Menon, D.K.; Adelson, P.D.; Andelic, N.; Bell, M.J.; Belli, A.; Bragge, P.; Brazinova, A.; Büki, A.; Chesnut, R.M.; et al. Traumatic brain injury: Integrated approaches to improve prevention, clinical care, and research. *Lancet Neurol.* **2017**, *16*, 987–1048. [CrossRef]
111. Zhang, J.; Puvenna, V.; Janigro, D. Biomarkers of Traumatic Brain Injury and Their Relationship to Pathology. In *Translational Research in Traumatic Brain Injury*; CRC Press/Taylor and Francis Group: Boca Raton, FL, USA, 2016; pp. 263–276. ISBN 9781466584921.
112. Socrates, G. *Infrared and Raman Characteristic Group Frequencies: Tables and Charts*, 3rd ed.; John Wiley & Sons, Ltd.: Hoboken, NJ, USA, 2004.
113. Staniszewska-Slezak, E.; Malek, K.; Baranska, M. Complementary analysis of tissue homogenates composition obtained by Vis and NIR laser excitations and Raman spectroscopy. *Spectrochim. Acta—Part A Mol. Biomol. Spectrosc.* **2015**, *147*, 245–256. [CrossRef] [PubMed]
114. Qiu, S.; Weng, Y.; Li, Y.; Chen, Y.; Pan, Y.; Liu, J.; Lin, W.; Chen, X.; Li, M.; Lin, T.; et al. Raman profile alterations of irradiated human nasopharyngeal cancer cells detected with laser tweezer Raman spectroscopy. *RSC Adv.* **2020**, *10*, 14368–14373. [CrossRef] [PubMed]
115. Pastore, A.; Federici, G.; Bertini, E.; Piemonte, F. Analysis of glutathione: Implication in redox and detoxification. *Clin. Chim. Acta* **2003**, *333*, 19–39. [CrossRef] [PubMed]
116. Shin, H.J.; Lee, J.H.; Kim, Y.D.; Shin, I.; Sim, T.; Lim, D.K. Raman-Based in Situ Monitoring of Changes in Molecular Signatures during Mitochondrially Mediated Apoptosis. *ACS Omega* **2019**, *4*, 8188–8195. [CrossRef]

117. Rolfe, S.M.; Patel, M.R.; Gilmour, I.; Olsson-Francis, K.; Ringrose, T.J. Defining Multiple Characteristic Raman Bands of α-Amino Acids as Biomarkers for Planetary Missions Using a Statistical Method. *Orig. Life Evol. Biosph.* **2016**, *46*, 323–346. [CrossRef]
118. Galli, R.; Meinhardt, M.; Koch, E.; Schackert, G.; Steiner, G.; Kirsch, M.; Uckermann, O. Rapid Label-Free Analysis of Brain Tumor Biopsies by Near Infrared Raman and Fluorescence Spectroscopy—A Study of 209 Patients. *Front. Oncol.* **2019**, *9*, 1165. [CrossRef] [PubMed]
119. Pezzotti, G. Raman spectroscopy in cell biology and microbiology. *J. Raman Spectrosc.* **2021**, *52*, 2348–2443. [CrossRef]
120. Huang, Z.; McWilliams, A.; Lui, H.; McLean, D.I.; Lam, S.; Zeng, H. Near-infrared Raman spectroscopy for optical diagnosis of lung cancer. *Int. J. Cancer* **2003**, *107*, 1047–1052. [CrossRef]
121. Mudalige, A.; Pemberton, J.E. Raman spectroscopy of glycerol/D2O solutions. *Vib. Spectrosc.* **2007**, *45*, 27–35. [CrossRef]
122. Thelin, E.P.; Jeppsson, E.; Frostell, A.; Svensson, M.; Mondello, S.; Bellander, B.M.; Nelson, D.W. Utility of neuron-specific enolase in traumatic brain injury; relations to S100B levels, outcome, and extracranial injury severity. *Crit. Care* **2016**, *20*, 285. [CrossRef]
123. Movasaghi, Z.; Rehman, S.; Rehman, I.U. Raman Spectroscopy of Biological Tissues. *Appl. Spectrosc. Rev.* **2007**, *42*, 493–541. [CrossRef]
124. Tfaili, S.; Gobinet, C.; Josse, G.; Angiboust, J.F.; Manfait, M.; Piot, O. Confocal Raman microspectroscopy for skin characterization: A comparative study between human skin and pig skin. *Analyst* **2012**, *137*, 3673–3682. [CrossRef] [PubMed]
125. Nims, C.; Cron, B.; Wetherington, M.; Macalady, J.; Cosmidis, J. Low frequency Raman Spectroscopy for micron-scale and in vivo characterization of elemental sulfur in microbial samples. *Sci. Rep.* **2019**, *9*, 7971. [CrossRef]
126. Kourkoumelis, N.; Gaitanis, G.; Velegraki, A.; Bassukas, I.D. Nail Raman spectroscopy: A promising method for the diagnosis of onychomycosis. An ex vivo pilot study. *Med. Mycol.* **2018**, *56*, 551–558. [CrossRef] [PubMed]
127. Koglin, E.; Séquaris, J.M.; Valenta, P. Surface enhanced raman spectroscopy of nucleic acid bases on Ag electrodes. *J. Mol. Struct.* **1982**, *79*, 185–189. [CrossRef]
128. Luan, Z.; Qin, Y.; Dai, J.; Wu, H.; Chen, Y.; Feng, X.; Peng, G. Identification of lesional tissues and nonlesional tissues in early gastric cancer endoscopic submucosal dissection specimens using a fiber optic raman system. *Gastroenterol. Res. Pract.* **2020**, *2020*, 8015024. [CrossRef]
129. Depciuch, J.; Barnaś, E.; Skręt-Magierło, J.; Skręt, A.; Kaznowska, E.; Łach, K.; Jakubczyk, P.; Cebulski, J. Spectroscopic evaluation of carcinogenesis in endometrial cancer. *Sci. Rep.* **2021**, *11*, 9079. [CrossRef]
130. Farber, C.; Li, J.; Hager, E.; Chemelewski, R.; Mullet, J.; Rogachev, A.Y.; Kurouski, D. Complementarity of Raman and Infrared Spectroscopy for Structural Characterization of Plant Epicuticular Waxes. *ACS Omega* **2019**, *4*, 3700–3707. [CrossRef]
131. Zhou, Y.; Liu, C.; Sun, Y.; Pu, Y.; Boydston-White, S.; Liu, Y.; Alfano, R.R. Human brain cancer studied by resonance Raman spectroscopy. *J. Biomed. Opt.* **2012**, *17*, 116021. [CrossRef]
132. Sacharz, J.; Wesełucha-Birczyńska, A.; Zięba-Palus, J.; Lewandowski, M.H.; Kowalski, R.; Palus, K.; Chrobok, Ł.; Moskal, P.; Birczyńska, M.; Sozańska, A. Epileptic rat brain tissue analyzed by 2D correlation Raman spectroscopy. *Spectrochim. Acta—Part A Mol. Biomol. Spectrosc.* **2018**, *188*, 581–588. [CrossRef]
133. Zhu, J.; Zhou, J.; Guo, J.; Cai, W.; Liu, B.; Wang, Z.; Sun, Z. Surface-enhanced Raman spectroscopy investigation on human breast cancer cells. *Chem. Cent. J.* **2013**, *7*, 37. [CrossRef]
134. Jahmani, M.Y.; Hammadeh, M.E.; Al Smadi, M.A.; Baller, M.K. Label-Free Evaluation of Chromatin Condensation in Human Normal Morphology Sperm Using Raman Spectroscopy. *Reprod. Sci.* **2021**, *28*, 2527–2539. [CrossRef] [PubMed]
135. Synytsya, A.; Judexova, M.; Hoskovec, D.; Miskovicova, M.; Petruzelka, L. Raman spectroscopy at different excitation wavelengths (1064, 785 and 532 nm) as a tool for diagnosis of colon cancer. *J. Raman Spectrosc.* **2014**, *45*, 903–911. [CrossRef]
136. Katsara, K.; Psatha, K.; Kenanakis, G.; Aivaliotis, M.; Papadakis, V.M. Subtyping on Live Lymphoma Cell Lines by Raman Spectroscopy. *Materials* **2022**, *15*, 546. [CrossRef]
137. Tay, L.L.; Tremblay, R.G.; Hulse, J.; Zurakowski, B.; Thompson, M.; Bani-Yaghoub, M. Detection of acute brain injury by Raman spectral signature. *Analyst* **2011**, *136*, 1620–1626. [CrossRef] [PubMed]
138. Hadjiivanov, K.I.; Panayotov, D.A.; Mihaylov, M.Y.; Ivanova, E.Z.; Chakarova, K.K.; Andonova, S.M.; Drenchev, N.L. Power of Infrared and Raman Spectroscopies to Characterize Metal-Organic Frameworks and Investigate Their Interaction with Guest Molecules. *Chem. Rev.* **2021**, *121*, 1286–1424. [CrossRef]
139. Marekha, B.A.; Bria, M.; Moreau, M.; De Waele, I.; Miannay, F.A.; Smortsova, Y.; Takamuku, T.; Kalugin, O.N.; Kiselev, M.; Idrissi, A. Intermolecular interactions in mixtures of 1-n-butyl-3-methylimidazolium acetate and water: Insights from IR, Raman, NMR spectroscopy and quantum chemistry calculations. *J. Mol. Liq.* **2015**, *210*, 227–237. [CrossRef]
140. Freire, P.T.C.; Barboza, F.M.; Lima, J.A.; Melo, F.E.A.; Filho, J.M. Raman Spectroscopy of Amino Acid Crystals. *Raman Spectrosc. Appl.* **2017**, *201*, 171. [CrossRef]
141. Papa, L.; Lewis, L.M.; Silvestri, S.; Falk, J.L.; Giordano, P.; Brophy, G.M.; Demery, J.A.; Liu, M.C.; Mo, J.; Akinyi, L.; et al. Serum levels of ubiquitin C-terminal hydrolase distinguish mild traumatic brain injury from trauma controls and are elevated in mild and moderate traumatic brain injury patients with intracranial lesions and neurosurgical intervention. *J. Trauma Acute Care Surg.* **2012**, *72*, 1335–1344. [CrossRef]
142. Bik, E.; Dorosz, A.; Mateuszuk, L.; Baranska, M.; Majzner, K. Fixed versus live endothelial cells: The effect of glutaraldehyde fixation manifested by characteristic bands on the Raman spectra of cells. *Spectrochim. Acta Part A Mol. Biomol. Spectrosc.* **2020**, *240*, 118460. [CrossRef]

143. Ricciardi, A.; Piuri, G.; Della Porta, M.; Mazzucchelli, S.; Bonizzi, A.; Truffi, M.; Sevieri, M.; Allevi, R.; Corsi, F.; Cazzola, R.; et al. Raman spectroscopy characterization of the major classes of plasma lipoproteins. *Vib. Spectrosc.* **2020**, *109*, 103073. [CrossRef]
144. Czamara, K.; Majzner, K.; Pacia, M.Z.; Kochan, K.; Kaczor, A.; Baranska, M. Raman spectroscopy of lipids: A review. *J. Raman Spectrosc.* **2015**, *46*, 4–20. [CrossRef]
145. Huff, T.; Boyd, B.; Jialal, I. Physiology, Cholesterol. In *StatPearls*; StatPearls Publishing: Treasure Island, FL, USA, 2017.
146. Ito, T.; Hamauchi, N.; Hagi, T.; Morohashi, N.; Hemmi, H.; Sato, Y.G.; Saito, T.; Yoshimura, T. D-serine metabolism and its importance in development of Dictyostelium discoideum. *Front. Microbiol.* **2018**, *9*, 334767. [CrossRef]
147. Slotte, J.P. Biological functions of sphingomyelins. *Prog. Lipid Res.* **2013**, *52*, 424–437. [CrossRef]
148. Kurek, K.; Łukaszuk, B.; Piotrowska, D.M.; Wiesiołek, P.; Chabowska, A.M.; Zendzian-Piotrowska, M. Metabolism, physiological role, and clinical implications of sphingolipids in gastrointestinal tract. *BioMed Res. Int.* **2013**, *2013*, 908907. [CrossRef] [PubMed]
149. Novgorodov, S.A.; Riley, C.L.; Yu, J.; Borg, K.T.; Hannun, Y.A.; Proia, R.L.; Kindy, M.S.; Gudz, T.I. Essential roles of neutral ceramidase and sphingosine in mitochondrial dysfunction due to traumatic brain injury. *J. Biol. Chem.* **2014**, *289*, 13142–13154. [CrossRef] [PubMed]
150. Buzgar, N.; Buzatu, A.; Sanislav, I. The Raman study on certain sulfates. *Analele Stiintifice Univ. Al. I. Cuza* **2009**, *55*, 5–23.
151. Uphoff, A.; Hermansson, M.; Haimi, P.; Somerharju, P. Analysis of complex lipidomes. In *Medical Applications of Mass Spectrometry*; Elsevier: Amsterdam, The Netherlands, 2008; pp. 223–249. [CrossRef]
152. Freeman, J.J.; Wopenka, B.; Silva, M.J.; Pasteris, J.D. Raman spectroscopic detection of changes in bioapatite in mouse femora as a function of age and in vitro fluoride treatment. *Calcif. Tissue Int.* **2001**, *68*, 156–162. [CrossRef] [PubMed]
153. Cao, Y.; Shen, D.; Lu, Y.; Huang, Y. A Raman-scattering Study on the Net Orientation of Biomacromolecules in the Outer Epidermal Walls of Mature Wheat Stems (*Triticum aestivum*). *Ann. Bot.* **2006**, *97*, 1091–1094. [CrossRef]
154. Farber, C.; Shires, M.; Ong, K.; Byrne, D.; Kurouski, D. Raman spectroscopy as an early detection tool for rose rosette infection. *Planta* **2019**, *250*, 1247–1254. [CrossRef] [PubMed]
155. Timchenko, E.V.; Zherdeva, L.A.; Timchenko, P.E.; Volova, L.T.; Ponomareva, U.V. Detailed Analysis of the Structural Changes of Bone Matrix during the Demineralization Process Using Raman Spectroscopy. *Phys. Procedia* **2015**, *73*, 221–227. [CrossRef]
156. Calcagnile, O.; Anell, A.; Undén, J. The addition of S100B to guidelines for management of mild head injury is potentially cost saving. *BMC Neurol.* **2016**, *16*, 200. [CrossRef] [PubMed]
157. Li, Y.; Pan, J.; Chen, G.; Li, C.; Lin, S.; Shao, Y.; Feng, S.; Huang, Z.; Xie, S.; Zeng, H.; et al. Micro-Raman spectroscopy study of cancerous and normal nasopharyngeal tissues. *J. Biomed. Opt.* **2013**, *18*, 027003. [CrossRef] [PubMed]
158. Girard, A.; Cooper, A.; Mabbott, S.; Bradley, B.; Asiala, S.; Jamieson, L.; Clucas, C.; Capewell, P.; Marchesi, F.; Gibbins, M.P.; et al. Raman spectroscopic analysis of skin as a diagnostic tool for Human African Trypanosomiasis. *PLoS Pathog.* **2021**, *17*, e1010060. [CrossRef]
159. Menge, T.; Lalive, P.H.; Von Büdingen, H.C.; Cree, B.; Hauser, S.L.; Genain, C.P. Antibody responses against galactocerebroside are potential stage-specific biomarkers in multiple sclerosis. *J. Allergy Clin. Immunol.* **2005**, *116*, 453–459. [CrossRef]
160. Podbielska, M.; Levery, S.B.; Hogan, E.L. The structural and functional role of myelin fast-migrating cerebrosides: Pathological importance in multiple sclerosis. *Clin. Lipidol.* **2011**, *6*, 159. [CrossRef] [PubMed]
161. Thomas, I.; Dickens, A.M.; Posti, J.P.; Czeiter, E.; Duberg, D.; Sinioja, T.; Kråkström, M.; Retel Helmrich, I.R.A.; Wang, K.K.W.; Maas, A.I.R.; et al. Serum metabolome associated with severity of acute traumatic brain injury. *Nat. Commun.* **2022**, *13*, 2545. [CrossRef] [PubMed]
162. Ayala, O.D.; Doster, R.S.; Manning, S.D.; O'Brien, C.M.; Aronoff, D.M.; Gaddy, J.A.; Mahadevan-Jansen, A. Raman microspectroscopy differentiates perinatal pathogens on ex vivo infected human fetal membrane tissues. *J. Biophotonics* **2019**, *12*, e201800449. [CrossRef] [PubMed]
163. Palings, I.; Van den Berg, E.; Mathies, R.A.; Pardoen, J.A.; Winkel, C.; Lugtenburg, J. Assignment of Fingerprint Vibrations in the Resonance Raman Spectra of Rhodopsin, Isorhodopsin, and Bathorhodopsin: Implications for Chromophore Structure and Environment. *Biochemistry* **1987**, *26*, 2544–2556. [CrossRef]
164. Dhanani, T.; Dou, T.; Biradar, K.; Jifon, J.; Kurouski, D.; Patil, B.S. Raman Spectroscopy Detects Changes in Carotenoids on the Surface of Watermelon Fruits during Maturation. *Front. Plant Sci.* **2022**, *13*, 832522. [CrossRef]
165. Liu, F.; Gu, H.; Yuan, X.; Lin, Y.; Dong, X. Chloride ion-dependent surface-enhanced Raman scattering study of biotin on the silver surface. *J. Phys. Conf. Ser.* **2011**, *277*, 012025. [CrossRef]
166. Zhang, X.; Zhou, Q.; Huang, Y.; Li, Z.; Zhang, Z. Contrastive Analysis of the Raman Spectra of Polychlorinated Benzene: Hexachlorobenzene and Benzene. *Sensors* **2011**, *11*, 11510–11515. [CrossRef] [PubMed]
167. Khnykina, K.A.; Kireev, V.V.; Krunina, N.V.; Kundikova, N.D.; Verina, E.V. Influence of Environment on Raman Spectra of Glycine and Prospect of Their Use for Functional Diagnostics of Human Beings. In Proceedings of the 2018 Global Smart Industry Conference (GloSIC), Chelyabinsk, Russia, 13–15 November 2018. [CrossRef]
168. Quilès, F.; Burneau, A. Infrared and Raman spectra of alkaline-earth and copper(II) acetates in aqueous solutions. *Vib. Spectrosc.* **1998**, *16*, 105–117. [CrossRef]
169. Asher, I.M.; Rothschild, K.J.; Anastassakis, E.; Stanley, H.E. Raman Spectroscopy of Uncomplexed Valinomycin. 1. The Solid State. *J. Am. Chem. Soc.* **1977**, *99*, 2024–2032. [CrossRef] [PubMed]
170. Duraipandian, S.; Traynor, D.; Kearney, P.; Martin, C.; O'Leary, J.J.; Lyng, F.M. Raman spectroscopic detection of high-grade cervical cytology: Using morphologically normal appearing cells. *Sci. Rep.* **2018**, *8*, 15048. [CrossRef]

171. Guimarães, A.E.; Pacheco, M.T.T.; Silveira, L.; Barsottini, D.; Duarte, J.; Villaverde, A.B.; Zângaro, R.A. Near Infrared Raman Spectroscopy (NIRS): A technique for doping control. *J. Spectrosc.* **2006**, *20*, 185–194. [CrossRef]
172. Liu, H.-H.; Lin, S.-H.; Yu, N.-T. Resonance Raman enhancement of phenyl ring vibrational modes in phenyl iron complex of myoglobin. *Biophys. J.* **1990**, *57*, 851–856. [CrossRef]
173. Nava, V.; Frezzotti, M.L.; Leoni, B. Raman Spectroscopy for the Analysis of Microplastics in Aquatic Systems. *Appl. Spectrosc.* **2021**, *75*, 1341–1357. [CrossRef]
174. Bock, P.; Gierlinger, N. Infrared and Raman spectra of lignin substructures: Coniferyl alcohol, abietin, and coniferyl aldehyde. *J. Raman Spectrosc.* **2019**, *50*, 778–792. [CrossRef]
175. Ramirez-Perez, J.C.; Durigo, D. Surface-Enhanced Raman Spectroscopy (SERS) for characterization SARS-CoV-2. *J. Saudi Chem. Soc.* **2022**, *26*, 101531. [CrossRef]
176. Maia, L.F.; Fernandes, R.F.; Almeida, M.R.; de Oliveira, L.F.C. Rapid assessment of chemical compounds from Phyllogorgia dilatata using Raman spectroscopy. *Rev. Bras. Farmacogn.* **2015**, *25*, 619–626. [CrossRef]
177. Tong, D.; Chen, C.; Zhang, J.J.; Lv, G.D.; Zheng, X.; Zhang, Z.; Lv, X. Application of Raman spectroscopy in the detection of hepatitis B virus infection. *Photodiagnosis Photodyn. Ther.* **2019**, *28*, 248–252. [CrossRef]
178. Rygula, A.; Majzner, K.; Marzec, K.M.; Kaczor, A.; Pilarczyk, M.; Baranska, M. Raman spectroscopy of proteins: A review. *J. Raman Spectrosc.* **2013**, *44*, 1061–1076. [CrossRef]
179. Bankapur, A.; Zachariah, E.; Chidangil, S.; Valiathan, M.; Mathur, D. Raman Tweezers Spectroscopy of Live, Single Red and White Blood Cells. *PLoS ONE* **2010**, *5*, e10427. [CrossRef] [PubMed]
180. Cañamares, M.V.; Pozzi, F.; Lombardi, J.R. Raman, SERS, and DFT Analysis of the Main Alkaloids Contained in Syrian Rue. *J. Phys. Chem. C* **2019**, *123*, 9262–9271. [CrossRef]
181. Anjos, O.; Guiné, R.P.F.; Santos, A.J.A.; Paula, V.B.; Pereira, H.; Estevinho, L.M. Evaluation of FT-Raman and FTIR-ATR spectroscopy for the quality evaluation of *Lavandula* spp. Honey. *Open Agric.* **2021**, *6*, 47–56. [CrossRef]
182. Moosavinejad, S.M.; Madhoushi, M.; Vakili, M.; Rasouli, D.; Moosavinejad, S.M.; Madhoushi, M.; Vakili, M.; Rasouli, D. Evaluation of degradation in chemical compounds of wood in historical buildings using FT-IR and FT-Raman vibrational spectroscopy. *Maderas. Cienc. Tecnol.* **2019**, *21*, 381–392. [CrossRef]
183. Fiedler, A.; Baranska, M.; Schulz, H. FT-Raman spectroscopy—A rapid and reliable quantification protocol for the determination of natural indigo dye in Polygonum tinctorium. *J. Raman Spectrosc.* **2011**, *42*, 551–557. [CrossRef]
184. Gao, J.; Gu, H.; Dong, X.; Liu, F. The determination of captopril in Solution by Raman spectroscopy. *J. Phys. Conf. Ser.* **2011**, *277*, 012009. [CrossRef]
185. Zheng, L.Q.; Servalli, M.; Schlüter, A.D.; Zenobi, R. Tip-enhanced Raman spectroscopy for structural analysis of two-dimensional covalent monolayers synthesized on water and on Au (111). *Chem. Sci.* **2019**, *10*, 9673–9678. [CrossRef]
186. Tsutsumi, N.; Kimura, T.; Arita, K.; Ariyoshi, M.; Ohnishi, H.; Yamamoto, T.; Zuo, X.; Maenaka, K.; Park, E.Y.; Kondo, N.; et al. The structural basis for receptor recognition of human interleukin-18. *Nat. Commun.* **2014**, *5*, 5340. [CrossRef] [PubMed]
187. Choquette, S.J.; Etz, E.S.; Hurst, W.S.; Blackburn, D.H.; Leigh, S.D. Relative Intensity Correction of Raman Spectrometers: NIST SRMs 2241 Through 2243 for 785 nm, 532 nm, and 488 nm. *Appl. Spectrosc.* **2007**, *61*, 117–129. [CrossRef] [PubMed]
188. Jones, R.R.; Hooper, D.C.; Zhang, L.; Wolverson, D.; Valev, V.K. Raman Techniques: Fundamentals and Frontiers. *Nanoscale Res. Lett.* **2019**, *14*, 231. [CrossRef] [PubMed]
189. Iannaccone, P.M.; Jacob, H.J. Rats! *Dis. Model. Mech.* **2009**, *2*, 206–210. [CrossRef]
190. Weber, B.; Lackner, I.; Haffner-Luntzer, M.; Palmer, A.; Pressmar, J.; Scharffetter-Kochanek, K.; Knöll, B.; Schrezenemeier, H.; Relja, B.; Kalbitz, M. Modeling trauma in rats: Similarities to humans and potential pitfalls to consider. *J. Transl. Med.* **2019**, *17*, 305. [CrossRef] [PubMed]
191. Basu, S.; Schtjltz, A.M.; Manju, B.; Roseman, S. Enzymatic Synthesis of Galactocerebroside by a Galactosyltransferase from Embryonic Chicken Brain. *J. Biol. Chem.* **1971**, *246*, 4272–4279. [CrossRef] [PubMed]
192. Kaabia, Z.; Poirier, J.; Moughaizel, M.; Aguesse, A.; Billon-Crossouard, S.; Fall, F.; Durand, M.; Dagher, E.; Krempf, M.; Croyal, M. Plasma lipidomic analysis reveals strong similarities between lipid fingerprints in human, hamster and mouse compared to other animal species. *Sci. Rep.* **2018**, *8*, 15893. [CrossRef]
193. Huang, F.; Bailey, L.S.; Gao, T.; Jiang, W.; Yu, L.; Bennett, D.A.; Zhao, J.; Basso, K.B.; Guo, Z. Analysis and Comparison of Mouse and Human Brain Gangliosides via Two-Stage Matching of MS/MS Spectra. *ACS Omega* **2022**, *7*, 6403–6411. [CrossRef]
194. Jiang, Z.; Shen, T.; Huynh, H.; Fang, X.; Han, Z.; Ouyang, K. Cardiolipin Regulates Mitochondrial Ultrastructure and Function in Mammalian Cells. *Genes* **2022**, *13*, 1889. [CrossRef]
195. Sabbagh, J.J.; Kinney, J.W.; Cummings, J.L. Alzheimer's disease biomarkers in animal models: Closing the translational gap. *Am. J. Neurodegener. Dis.* **2013**, *2*, 108.
196. Banbury, C.; Mason, R.; Styles, I.; Eisenstein, N.; Clancy, M.; Belli, A.; Logan, A.; Goldberg Oppenheimer, P. Development of the Self Optimising Kohonen Index Network (SKiNET) for Raman Spectroscopy Based Detection of Anatomical Eye Tissue. *Sci. Rep.* **2019**, *9*, 10812. [CrossRef]
197. Lussier, F.; Thibault, V.; Charron, B.; Wallace, G.Q.; Masson, J.F. Deep learning and artificial intelligence methods for Raman and surface-enhanced Raman scattering. *TrAC Trends Anal. Chem.* **2020**, *124*, 115796. [CrossRef]
198. Ward, M.D.; Weber, A.; Merrill, V.D.; Welch, R.D.; Bazarian, J.J.; Christenson, R.H. Predictive Performance of Traumatic Brain Injury Biomarkers in High-Risk Elderly Patients. *J. Appl. Lab. Med.* **2020**, *5*, 91–100. [CrossRef]

199. Terrones, O.; Olazar-Intxausti, J.; Anso, I.; Lorizate, M.; Nieto-Garai, J.A.; Contreras, F.X. Raman Spectroscopy as a Tool to Study the Pathophysiology of Brain Diseases. *Int. J. Mol. Sci.* **2023**, *24*, 2384. [CrossRef] [PubMed]
200. Ge, M.; Ge, M.; Wang, Y.; Wang, Y.; Wu, T.; Li, H.; Li, H.; Yang, C.; Chen, T.; Feng, H.; et al. Serum-based Raman spectroscopic diagnosis of blast-induced brain injury in a rat model. *Biomed. Opt. Express* **2023**, *14*, 3622–3634. [CrossRef] [PubMed]

Appendix B: Validation of optimised intracranial spectroscopic probe for instantaneous in-situ monitoring and classification of traumatic brain injury

An update to this article is included at the end

Experimental Neurology 382 (2024) 114960

Contents lists available at ScienceDirect

Experimental Neurology

journal homepage: www.elsevier.com/locate/yexnr

Research paper

Validation of optimised intracranial spectroscopic probe for instantaneous *in-situ* monitoring and classification of traumatic brain injury

Clarissa A. Stickland [a], Zoltan Sztranyovszky [a], Jonathan J.S. Rickard [a,b], Pola Goldberg Oppenheimer [a,c,*]

[a] School of Chemical Engineering, College of Engineering and Physical Science, University of Birmingham, B15 2TT, UK
[b] Department of Physics, Cavendish Laboratory, University of Cambridge, JJ Thomson Avenue, Cambridge CB3 0HE, UK
[c] Institute of Healthcare Technologies, Mindelsohn Way, Birmingham B15 2TH, UK

ARTICLE INFO

Keywords:
Traumatic brain injury
Neuromonitoring
Raman spectroscopy
Intracranial Raman spectroscopy probe
SKiNET
Portable diagnostic device

ABSTRACT

The development of an optical interface to directly distinguish the brain tissue's biochemistry is the next step in understanding traumatic brain injury (TBI) pathophysiology and the best and most appropriate treatment in cases where in-hospital intracranial access is required. Despite TBI being a globally leading cause of morbidity and mortality in patients under 40, there is still a lack of objective diagnostical tools. Further, given its pathophysiological complexity the majority of treatments provided are purely symptomatic without standardized therapeutic targets. Our tailor-engineered prototype of the intracranial Raman spectroscopy probe (Intra-RSP) is designed to bridge the gap and provide real-time spectroscopic insights to monitor TBI and its evolution as well as identify patient-specific molecular targets for timely intervention. Raman spectroscopy being rapid, label-free and non-destructive, renders it an ideal portable diagnostics tool. In combination with our in-house developed software, using machine learning algorithms for multivariate analysis, the Intra-RSP is shown to accurately differentiate simulated TBI conditions in rat brains from the healthy controls, directly from the brain surface as well as through the rat's skull. Using clinically pre-established methods of cranial entry, the Intra-RSP can be inserted into a 2-piece optimised cranial bolt with integrated focussing and correctly identify a sample in real-life conditions with an accuracy >80 %. To further validate the Intra-RSP's efficiency as a TBI monitoring device, rat brains mildly damaged from inflicted spinal cord injury were found to be correctly classified with 94.5 % accuracy. Through optimization and rigorous *in-vivo* validation, the Intra-RSP prototype is envisioned to seamlessly integrate into existing standards of neurological care, serving as a minimally invasive, *in-situ* neuromonitoring tool. This transformative approach has the potential to revolutionize the landscape of neurological care by providing clinicians with unprecedented insights into the nature of brain injuries and fostering targeted, timely and effective therapeutic interventions.

1. Introduction

Traumatic brain injury (TBI) is a global health issue affecting at least half of the world's population during their lifetime and is one of the most common causes of death in those under the age of 40 (Maas et al., 2017). The non-conformity of TBI symptoms and the current diagnostic tools render the precise diagnosis and monitoring of the extent of brain damage untimely and highly subjective to the healthcare professional's opinion. Without understanding the precise degree of TBI severity and with no standardized therapeutic targets, the interventions and treatments are predominantly focussed on symptomatic patients (Galgano et al., 2017; Mowbray et al., 2021). Considering the long term risks of developing further permanent neurological disorders, TBI has not only been resulting in life changing complications, but also in a significant socio-economic burden (Chung and Khan, 2013).

Development of applicable, timely, and cost-effective *in-vivo* and point-of-need triaging and monitoring tools is, therefore, of a vital importance to address the current unmet need with TBIs (Mowbray et al., 2021). Due to the complex pathophysiology of the traumatic brain injuries and various degrees of severity, there is a potential for a large array of therapeutic targets. For instance, in severe TBIs (sTBI), the entire brain can be affected by a life-threatening widespread swelling

* Corresponding author at: School of Chemical Engineering, College of Engineering and Physical Science, University of Birmingham, B15 2TT, UK.
E-mail address: goldberp@bham.ac.uk (P. Goldberg Oppenheimer).

https://doi.org/10.1016/j.expneurol.2024.114960
Received 20 May 2024; Received in revised form 2 September 2024; Accepted 13 September 2024
Available online 18 September 2024

and major changes in biochemical state. Currently, the clinical standard of care revolves heavily around regulating the intracranial conditions to prevent further secondary injuries (Galgano et al., 2017), and hence, monitoring the intracranial pressure (ICP) is vital for the neuroprotection and regulation of metabolic requirements in the brain. In cases of sTBI, increases in ICP are moderated through insertion of a catheter directly into brain parenchyma (Smith, 2008). The intracranial environment consists of approximately 83 % brain tissue, 11 % cerebrospinal fluid (CSF), and 6 % blood enclosed in a non-expandable area by the skull (Galgano et al., 2017). Increase in any of these components post TBI triggers a corresponding decrease in another to accommodate the ICP, with the CSF being the most typical since its excess can be relocated to the spinal theca to maintain the correct distribution of oxygen and glucose. Disruption to the autoregulatory mechanisms can lead to devastating secondary injuries, requiring external aid from caregivers such as, the decompressive craniectomy (Smith, 2008). More effective diagnostics monitoring, as well as interventions and treatments of TBI primary injuries, could be enabled *via* timely detection of TBI-induced biochemical changes, pinpointing the extent of damage which for different stages and severity of injury have been shown to be present in serum, CSF or brain parenchyma as indicators for vascular, metabolic and axonal disruptions as well as tissue inflammation (Jalloh et al., 2015; Vespa et al., 2003; Haris et al., 2011; Ashwal et al., 2004; López-Gambero et al., 2020; Tapanes et al., 2022; Koza and Linseman, 2019; Khatri et al., 2018; Shahjouei et al., 2018; Yang and Wang, 2015; Tzeng et al., 2005; Goyal et al., 2013).

Concurrently, Raman spectroscopy (RS) has been emerging as a sensitive, non-destructive and label-free vibrational analytical detection technique, recently gaining a surge in popularity for its potential *in-vivo* disease diagnostics due to the ability to detect trace levels of target molecules of interest within minutes (Mowbray et al., 2021; Harris et al., 2023; Cordero et al., 2018; Banbury et al., 2020; Banbury et al., 2023). In this inelastic scattering spectroscopy, the excited photons yield a highly specific shift in energy following the molecular interactions (Long and Long, 2002; Koningstein, 2012), generating a unique fingerprint barcode consisting of Raman peaks. Decoding the highly specific peaks, representative of the unique molecular changes, to the established spectral barcodes of TBI biomarkers can, therefore, provide important insights into the TBI mechanisms as well as an accurate indication of the extent of damage and progression induced *via* brain trauma.

Herein, building upon a self-tapping cranial bolt, an Intracranial Raman Spectroscopy Probe (Intra-RSP) is engineered, which is tailor designed to be easily integrated into the existing surgical procedures (Fig. 1), and subsequently employed to validate the detection and tracking of a panel of TBI indicative biomarkers, providing live feedback on the pathophysiology of TBI in the brain during surgery. To simulate biochemical changes in the brain following TBI, seven neurological prospective biomarkers of TBI including Glucose, Myo-Inositol, Serine, Glutathione (GSH), Glial Fibrillary Acidic Protein (GFAP), S100B and Ubiquitin C-terminal Hydrolase L1 (UCHL-1), (Table 1) selected due to their biocompatibility, generate a representative panel and are inserted into dead rat brains. The corresponding changes in the brain's environment post-TBI have been studied in rat brain models, detected *in-situ via* the engineered Intra-RSP. Further to validation in spiked rodent brains, we have acquired and analysed a cohort of complementary spinal cord injured (SCI) rats brains, hypothesising that due the proximity of the central nervous system, a traumatic event occurring on the spine will also be reflected in the brain, as a milder injury (Hains et al., 2003; Klapka et al., 2005; Wu et al., 2014). The acquired Raman spectral signatures, collected *via* the Intra-RSP, are subsequently classified using our artificial neural networks algorithm as a decision support tool, the self-optimizing Kohonen index network (SKiNET). SKiNET acts as a

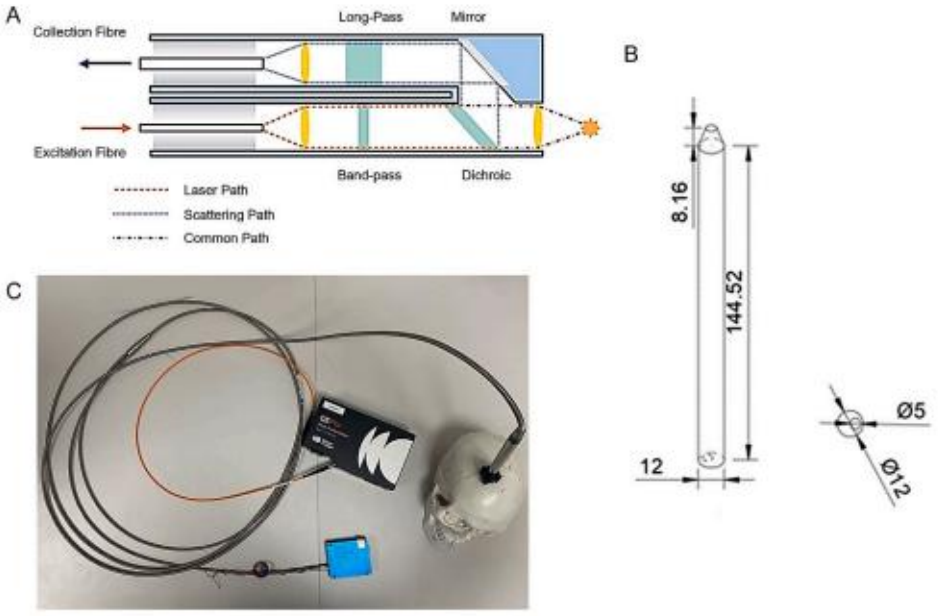

Fig. 1. Portable Intracranial Raman Spectroscopy Probe Overview. (A). Internal structure of the probe, consisting of permanently aligned combination of two single fibres (100 μm excitation fibre, 200 μm collection fibre) with filtering and steering micro-optics, N.A. 0.22, with stainless-steel cabled fibre with a design to filter laser line and quartz spectral contributions from both input and output fibres (O.D. > 8 at laser line) (Inc and RamanProbe II, 2022). (B). Characteristic dimensions (mm) of the probe head, corresponding with the cranial device dimensions, mandated by standard cranial access during larger craniotomies (Tools, 2023). (C). Aerial view of the engineered Intra-RSP handheld setup, including probe, Raman spectrometer and 785 nm laser.

Table 1
Prospective TBI biomarkers and their physiological effect following trauma.

Biomarker	TBI Effect
β-D-Glucose	Low levels demonstrate increased requirement of energy, which with low lactate/glucose ratio correlated with poor outcomes (Jalloh et al., 2015; Vespa et al., 2003).
Myo-Inositol	Myo-Inositol build-up relates to glial proliferation, astrogliosis, dysregulation of cellular osmotic functions, membrane turnover and myelin sheet damage (Haris et al., 2011; Ashwal et al., 2004; López-Gambero et al., 2020).
D-Serine	Reactive glial cells synthesise serine when prompted by inflammatory signals. Serine overproduction results in hyperactivation of NMDA receptors and synaptic damage in the hippocampus (Tapanes et al., 2022).
Glutathione (GSH)	GSH converted to oxidised form to regulate free radicals in the brain thus, depleting GSH resources. In extreme neuroinflammation, more free radicals are formed and the lack of GSH further damages the brains and neurons (Koza and Linseman, 2019; Khatri et al., 2018).
Glial Fibrillary Acidic Protein (GFAP)	Astrogliosis increases GFAP expression, potentially leading to glial scarring and delayed axon regeneration (Yang and Wang, 2015; Tzeng et al., 2005).
S100B	S100B overexpression results in calcium homeostatic dysregulation, indicating structural damage and cellular death (Goyal et al., 2013).
Ubiquitin C-terminal Hydrolase L1 (UCHL-1)	Increased following axonal damage to aid in removal of damaged and defective axonal proteins (Shahjouei et al., 2018).

framework for multivariate analysis, simultaneously providing i) dimensionality reduction, ii) feature extraction and iii) multiclass classification (Banbury et al., 2019; Kohonen, 1982) by performing a visual separation to identify the underlying biochemical differences between classes. The outputs yield a rapid and accurate classification, even for low laser powers and short acquisition times, representative of real-world conditions. SKiNET's supervised learning, in conjunction with sensing techniques, enables its exploitation for rapid and accurate diagnostic and prognostic applications *via* the inherent self-organised maps (SOM). This results in visually intuitive 2D clustering based on injury state. Additionally, the self-organizing map discriminant index (SOMDI) efficiently identifies the specific spectral features of importance, representing biochemical changes which most contribute to the observed clustering in SOMs (Kohonen, 1982; Lloyd et al., 2009; Wongravee et al., 2010). Herein, the integrated SKiNET with the Intra-RSP successfully and rapidly distinguishes between TBI-simulated and SCI rodent brains from healthy control cohorts and correctly identifies and classifies brains from a simulated *in-situ* model. These collectively lay the platform for translation of the developed technology to *real-world* clinical point-of-need neurological diagnostic, monitoring, and prognostic applications along with developments of new therapeutic interventions.

2. Methods and materials

2.1. Materials and biomarkers

Glucose (Cambridge Biosciences, CAY23733–50), Myo-Inositol (VWR International, A13586.22), D-Serine (VWR International, 312–84-5), GSH (Merck Life Science Limited, Y0000517), GFAP (Generon, C227-10μg), S100B (Cambridge Bioscience, HY-P70659), UCHL-1 (Generon, 6B9379) were purchased and used without purification.

2.2. Spiked brains sample preparation

Healthy Sprague-Dawley rat samples were sacrificed and stored at -80 °C, licensed by the UK Home Office and approved by the University of Birmingham Animal and Ethical Review Board (Ethics Ref PP3851114). Nine brains were removed from the skull, while six were kept in the skull with the back removed allowing visibility to the brain. Two 1 mM biomarker solutions (BS1 and BS2) were prepared with BS1 including, Glucose, Myo-Inositol, Serine and GSH and BS2 consisting of Glucose, Myo-Inositol, Serine, GSH, GFAP, S100B and UCHL-1. The solutions were injected in two locations at a 1.5 mm depth into the brain for both the exposed and unexposed brains, through the back of both cortical hemispheres, yielding a phantom TBI (Dong et al., 2016). Reference TBI biomarkers were dissolved in distilled water (18.2 MΩ) generating a solution of 1 mM according to the data sheets supplied by the manufacturers. These were dissolved for 20 mins and subsequently 3 μL was pipetted onto an aluminium slide and dried at room temperature, as described in Ref. (Harris et al., 2023).

2.3. SCI rat brains

SCI was inflicted by collaborators on four Sprague-Dawley rats through surgical intervention in which a partial laminectomy at thoracic level 8 was performed before the bilateral crushing of the dorsal column using watchmakers forceps, as described in Stevens et al. (Stevens et al., 2024). The brains were removed three days post injury and stored at -80 °C. These were licensed by the UK Home Office and approved by the University of Birmingham Animal and Ethical Review Board (Ref. PP3851114).

2.4. Raman spectra acquisition and analysis

The optimised prototype 3D prints of the Intra-RSP were manufactured *via* Ultimaker2+ 3D printer, employing 2.88 mm poly-lactic acid (PLA) filament. Brain spectra were acquired using the Intra-RSP consisting of an InPhotonics probe II coupled to Ocean Insight's QE Pro-Raman spectrometer and a LuxxMaster Raman Boxx (PD-LD) 785 nm laser (Fig. 1C). The applied laser power was set to 40 mW, with 30s acquisition time and 5 accumulations for the full spectral range (100–3000 cm^{-1}). Training samples for SOMs were acquired with the probe attached to a clamp stand to optimize parameters. To validate the SOM, test spectra were acquired using BS1-spiked rat brains in a simulated craniotomy setting, using a model skull and a cranial bolt prototype (Fig. 1B-C). Reference TBI biomarker fingerprints were acquired, as described in details in Ref. (Harris et al., 2023). Briefly, *via* using 785 nm excitation laser (InVia confocal Renishaw) at the corresponding measuring conditions, three extended scans with an acquisition time of 10s and 5 accumulations under a x50 objective lens.

2.5. Multivariate data analysis and AI classification

The raw data has been truncated to 250–2000 cm^{-1}, baseline subtracted, corrected for cosmic rays, and is presented as an average spectrum. A detailed multivariate analysis was performed *via* SKiNET (Banbury et al., 2019). For each cohort, a total of 100 spectra were input and randomly split as 80 % training spectra and 20 % test spectra to ascertain the accuracy of the maps. SOM grid size was decided according to Lek and Park, 2008 (Lek and Park, 2008), as number of spectra input equal to the number of neurons, and ran with 10,000 iterations at a learning rate of 0.1 with learning vector quantization (LVQ) enabled. To determine the efficacy of the probe, a separate map was generated using three BS1-spiked test samples from the model skull input as additional test spectra into a SOM containing 100 % training data consisting of control, BS1-spiked and BS2-spiked spectra. Each SOM was cross-validated 10 times to determine accuracy, which was calculated using the number of correctly identified test spectra from a confusion matrix.

2.6. Finite element analysis

Computational modelling and finite element analysis was conducted

using Autodesk Fusion 360 to assess the safety and robustness of the bolt design. The Simulation, Static Stress option was employed to conduct the study and calculate the safety factor and stresses (Mowbray et al., 2021). For the 5 mm thread length, the weak point of the structure was found at the joint between the thread and the main body of the bolt. Therefore, a simplified version was designed, omitting the model of the skull while constraining the lower half of the thread to be fixed and the rest of the bolt free to deform under load. A stress was then applied to the four baffles, shared equally among them, to model the torque exerted by the tightening clip. The model overall was meshed with the default settings, while the thin plate between the main body and the thread was meshed with the option "local mesh control" set to "fine", giving mesh elements with a size of 0.049 mm.

3. Results and discussion

The Intra-RSP device internally consists of two single co-axially aligned fibres (Fig. 1A) with a 100 μm excitation fibre and a 200 μm collection fibre, filtering and steering micro-optics, N.A. 0.22 and a design to filter laser lines and quartz spectral contributions from both the input and output fibres, all encased in a cylindrical stainless-steel head (Inc and RamanProbe II, 2022). The probe is coupled to a 785 nm laser and a portable spectrometer (Fig. 1C). A model skull with a representative operative configuration, featuring the probe head and 3D printed self-tapping cranial bolt and was validated for clinical applications, inserting the probe into the site of interest, and acquiring *in-situ* measurements. The cranial bolt has been initially designed *via* Autodesk Fusion 360. Iterative testing and refinement of the 3D printed components were conducted using a model of a human skull, which featured a hole replicated with the same drill employed by neurosurgeons during a

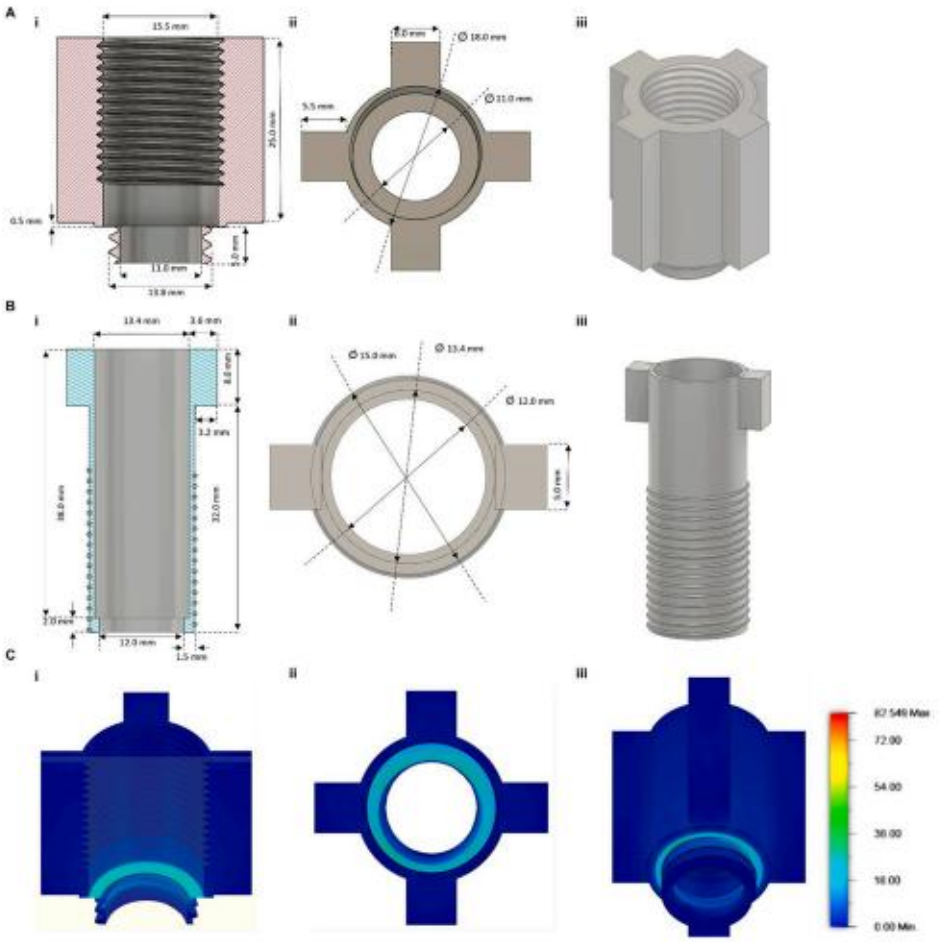

Fig. 2. Schematic of (A) cranial bolt with a (i) side view cross-section, (ii) top view, (iii) top-angled side view and the corresponding (B) focusable probe sleeve with its (i) side view cross-section, (ii) top view and (iii) top-angled side view. (C). Top/side (i) intersection, (ii) top and (iii) bottom/side view of the bolt, with stress indicated in the model. The higher stress occurs in an extremely narrow region where the outer thread meets the narrow plate connecting to the body and is not visible.

craniotomy to ensure accuracy (Fig. 1B-C). During post-TBI surgery, a craniotomy site is typically created *via* a disposable clutched perforator drill, which to prevent the surgeon from drilling into the tissue, allows for an internal ledge, providing a change in geometry throughout the site.

The cranial bolt is a key part of the development of the Intra-RSP's function. The bolt is hand-placed and self-tapping using the tapping tool (Fig. 2A), providing stability and allowing for the probe sleeve to be inserted at a user defined distance for the purpose of focussing it onto the brain surface according to its distance from the skull, depending on potential neuroinflammation. Rigorous testing and adjustments were made to guarantee the precision and functionality of the cranial bolt in simulating the *real-world* conditions. Simulations were performed for titanium 6Al-4 *V* and nylon 6, based on their biocompatibility and availability as feasibly reproducible materials. The figures of merit are summarised in Table 2, where titanium shows a minor maximum displacement and a large safety factor even at high torques.

For a torque of 0.8 Nm, building upon our initial bolt prototype (Mowbray et al., 2021), the safety factor has been reduced by 8 % from 11.58 to 10.69, due to the thinner connection between the thread and the main body of the bolt, where the stress is highest (Fig. 2C). The thinner section is essential in this design to reduce the working distance of the device. The safety factor is the margin between the minimum required performance desired from the device and the actual performance (Ward et al., 2002). The maximum displacement describes the total movement from the original coordinates to displaced position when a load is applied (Kim et al., 2018). The 10.69 safety factor is well above 3 (considered safe) or > 1 (considered as a breaking point) (*Safety factor result: Autodesk*, 2024). For nylon, the fracture point reduced significantly from a torque of 0.96 Nm to 0.684 Nm. To achieve a minimum safety factor of 3, the maximum supported torque is only 0.228 Nm. This indicates that for the optimised bolt design, nylon does not constitute an appropriate option and titanium is chosen as the most suitable, safe material.

To test the ability of the handheld Intra-RSP to distinguish between TBI brains and control cohorts, two biomarker solutions were formulated, the BS1 solution containing Glucose, Myo-Inositol, Serine and GSH and the BS2 containing Glucose, Myo-Inositol, Serine, GSH, GFAP, S100B and UCHL-1. Both solutions contained four identical biomarkers, to further enable the evaluation of the probe's specificity. Representative mean spectra of each biomarker in solutions BS1 and BS2 (Fig. 3A), yield the fingerprints of the candidate signature spectral bands for further identification within the spiked samples (Fig. 3B) (Harris et al., 2023).

Notable spectral differences emerge among the three rat brain conditions (Fig. 3B), particularly in the 650–800 cm^{-1}, 1100–1250 cm^{-1} and the 1500–1675 cm^{-1} regions. The distinctions between the TBI biomarker spiked and the control cohorts are validated *via* the subsequent SOM clustering (Fig. 3D). The SOM clearly defines distinct areas for each cohort. When only inputting the benchtop recorded healthy control and spiked brains, the SOM clusters the groups to an accuracy of 92 % ±0.04 from randomly selected test spectra ($n = 60$), validating the potential to pick out biochemical changes in the immersed environment. Following the validation of differentiating spiked brains, spectra were subsequently recorded through a model skull using the optimised cranial bolt as a validation of the device performance. The tested BS1-spiked samples SOM exhibit a correct classification with an accuracy of 80 % ±0.21 (Fig. 3D). Further insights through SOMDI scores (Table 3 and **Supporting Information S1**) quantify pivotal peaks responsible for differentiating between the spectra in Fig. 3B. The scoring assigns a value to each Raman shift according to its influence in the acquired spectra. Identifying characteristic features of a group enables further comparison of the differences in relative intensity of dominant peak ratios (Fig. 3C).

Relative intensity ratios between Raman shifts are used to identify changes within samples using Raman spectra. A significant increase of 11 % in the relative intensity ratios for the 414 and 549 cm^{-1} wavenumbers (Fig. 3C) is observed between the BS2-spiked and the control brain spectra, (Fig. 3C) indicative of a greater presence of skeletal *C*=*C* lipid bonds and *C*—*S* bonds from cysteine residues, which are represented by these peaks, respectively (Socrates, 2004). Cysteine levels are found to be increased in the BS2 spiked brains due to the amino acid's presence in the GSH, GFAP, S100B and UCHL–1 neuromarkers, all of which are biomarkers included in BS2 (Meister and Anderson, 1983; Jensen et al., 1985; Kajimoto et al., 1992; Reeves et al., 1989). Within BS1, only GSH contains C—S bonds related to the 549 cm^{-1} Raman shift (Table 2). Both the 549 and 414 cm^{-1} wavenumbers are more prevalently being picked up by Intra-RSP in the healthy control brains than the BS1-spiked brains, as demonstrated by the 1 % decrease in ratio intensity in the BS1-spiked brain spectra from the control (Fig. 2C) as well as by the lower SOMDI scores for both 414 and 549 cm^{-1} (0.77 and 0.40, respectively) in contrast to control (0.84 and 0.47, respectively) cohorts (Table 2).

The relative difference in intensity ratios for the 1658 and 1440 cm^{-1} (Fig. 3C) between the BS2-spiked and the control brain spectra further shows a significant 7 % increase ($p < 0.05$). This is consistent with the addition of Amide *I* bonds to the brain, stemming from the secondary protein structures of the BS2 biomarkers (Galli et al., 2019; Timchenko et al., 2015). Despite the absence of lipids in both biomarker solutions, (deliberately omitted due to the need to exclude sample-damaging or Raman active solvents), SOMDI scores (Table 3) indicate that these bands both play a significant role in distinguishing the spiked spectra from controls, in correspondence with our previous studies where these were established as TBI-indicative candidates (Mowbray et al., 2021; Surmacki et al., 2017). The equally high SOMDI score of 0.90 for the 1440 cm^{-1} band in both the BS1 and BS2 spiked brains (Table 3) could be due to the RS ability to more readily detect lipids compared to proteins and nucleic acids due the abundance of polarizable *C*—*H* and *C*—*C* bonds.

Furthermore, both the CH_2 rocking, detected *via* the 850 cm^{-1} band and the C—C stretching of amino acids, detected *via* the 933 cm^{-1} band (Freire et al., 2017) are identified by SOMDI as characteristic in differentiating the BS2 spiked brains spectra, the BS1-spiked and control brains, with scores of 0.56 and 0.24, respectively (Table 3). In contrast to the un-spiked brains, those spiked with BS1 and BS2 found to exhibit a lower relative intensity 850/933 cm^{-1} ratio by 14 % and 37 %, respectively (Fig. 3C).

Similarities between the TBI biomarker spectra (Fig. 3A) and the biomarker-spiked brain samples (Fig. 3B) have been identified at the 805, 850, 933, 1004, 1130 and 1660 cm^{-1}. Symmetrical C-N-C stretching at 805 cm^{-1} is mainly a contributing factor of the BS2 spiked brains, with a SOMDI score of 0.45, directly linked to the higher protein content, (Socrates, 2004) which is characteristic to UCHL-1, D-Serine and GSH biomarkers (Fig. 3A). The increase in the 850 cm^{-1} SOMDI weight in BS2 samples relative to control and BS1 (Table 3) is attributed to the rocking of CH_2 bonds in proteins from leucine, determinative of UCHL-1 (Fig. 3B) (Freire et al., 2017). This biomarker is present only in the BS2 solution, this renders the 850 cm^{-1} as a potential predicative band of axonal damage observed through the presence of UCHL-1 post TBI. On the other hand, the S100B, which is only present in BS2, exhibits a characteristic feature peak at 936 cm^{-1} (Fig. 3A) (Harris et al., 2023)

Table 2
Outputs from finite element analysis including torque and the corresponding safety factors for titanium and nylon.

Material	Torque at Fracture [Nm]	Maximum Displacement [mm]	Stress [MPa]	Safety Factor
Titanium 6Al-4 V	0.8	0.002	82.55	10.69
	1.6	0.004	165.1	5.35
Nylon 6	0.228	0.025	23.5	3.00
	0.684	0.075	70.5	1

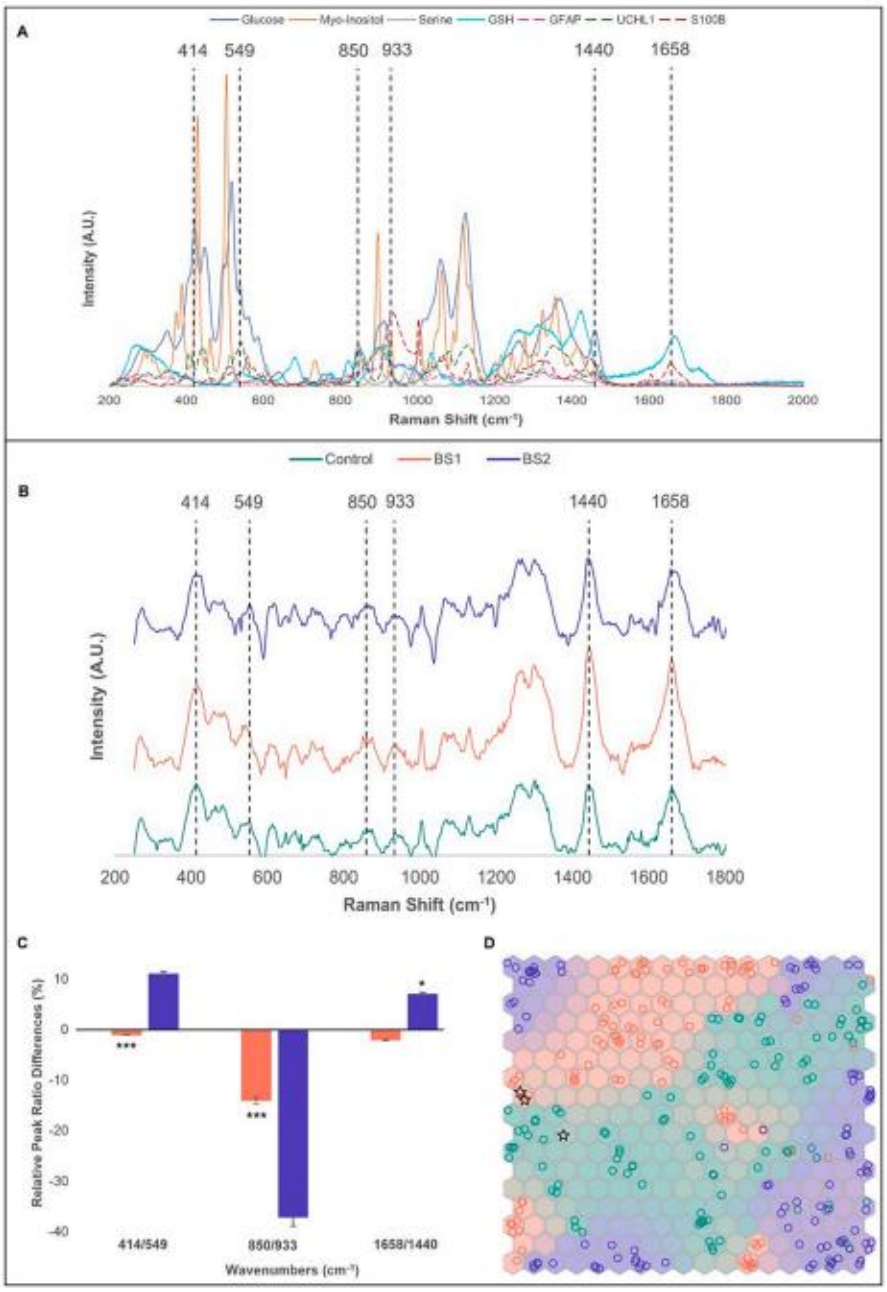

(caption on next page)

Fig. 3. Representative average superimposed spectra of (A) individual TBI biomarkers present in BS1 and BS2 solutions including Glucose (dark blue), Myo-Inositol (orange), Serine (grey), Glutathione (GSH, light blue), Glial Fibrillary Acidic Protein (GFAP, dashed pink), Ubiquitin C-terminal Hydrolase L1 (UCHL-1, dashed green) and S100B (dashed red). Solid line spectra represent biomarkers present both in BS1 and BS2, dashed line spectra are indicative of biomarkers exclusively present in BS2. (B). Averaged Raman spectra of control (green), BS1-spiked (red) and BS2-spiked (blue) brains with the highlighted Raman peaks at 414, 549, 850, 933, 1440 and 1658 cm^{-1} of key markers in the evaluation of (C) the relative differences in intensity ratios between the 549 and 414 cm^{-1}, the 933 and 850 cm^{-1} and the 1658 and 1440 cm^{-1} peaks for the BS1 (red) and the BS2 (blue) *versus* controls. (D). SOM clustering the characteristic features of each cohort for BS1, BS2 spiked brains and controls including the training data (circles) and the three BS1 test spectra (white stars). The SOM classifies healthy controls, BS1, and BS2 brain spectra correctly to an accuracy of 92 % ±0.04, and the BS1 brain spectra recorded through the model skull with an accuracy of 80 % ±0.21 ($^{*}p < 0.05$ and $^{***}p < 0.0001$, student's *t*-test). (For interpretation of the references to colour in this figure legend, the reader is referred to the web version of this article.)

Table 3
SOMDI scores for control, BS1 and BS2 brains with the corresponding assignments of the identified characteristic peaks.

Raman Band (cm^{-1})	SOMDI Scores			Assignment	Reference
	Control	BS1	BS2		
267	0.46	0.38	0.46	*Ring mode vibrations*	(Bock et al., 2020)
414	0.84	0.77	0.78	ν_{skel}(C—C)	(Socrates, 2004)
482	0.66	0.58	0.58	ν_{skel}(C—C)	(Socrates, 2004)
549	0.47	0.40	0.48	δ(C—S)	(Socrates, 2004)
612	0.44	0.31	0.48	ν(–C=CH)	(Socrates, 2004)
673	0.39	0.32	0.50	τ(C=C)	(Socrates, 2004)
716	0.34	0.33	0.49	ν_s(C—N)	(Pezzotti, 2021)
805	0.32	0.24	0.45	ν_s(O–P–O), ν_s(C–N–C)	(Socrates, 2004; Pezzotti, 2021)
850	0.38	0.37	0.50	ρ(CH_2)	(Freire et al., 2017)
857	0.38	0.34	0.52	ν_s(C–N–C)	(Socrates, 2004)
933	0.36	0.29	0.44	ν(C—C)	(Freire et al., 2017)
1004	0.45	0.39	0.50	δ(CH_2), Δ_{arom}(C—C)	(Guimarães et al., 2006)
1064	0.48	0.38	0.54	ν(C—O), ν (C—C), τ(NH_2)	(Pezzotti, 2021; Jahmani et al., 2021; Tfaili et al., 2012)
1129	0.51	0.39	0.55	ν(C—N), ν (C—C), ν_{skel}(C—C)	(Surmacki et al., 2017; Synytsya et al., 2014; Katsara et al., 2022)
1191	0.46	0.34	0.47	δ (CH), ω(CH_2)	(Babu et al., 2012)
1267	0.80	0.77	0.87	ν(C—O), δ (CH), *Amide III*	(Banbury et al., 2020; Cao et al., 2006; Movasaghi et al., 2007)
1302	0.83	0.81	0.88	τ(CH_2)	(Ricciardi et al., 2020)
1440	0.79	0.90	0.90	δ(CH_2), τ(CH_2)	(Staniszewska-Slezak et al., 2015; Farber et al., 2019)
1554	0.38	0.33	0.43	δ(NH_3^+)	(Socrates, 2004)
1580	0.37	0.29	0.41	Δ_{arom}(C—C), ν (C=O)	(Socrates, 2004; Tay et al., 2011)
1658	0.74	0.84	0.81	ν(C=O), ν(C=C)	(Galli et al., 2019; Timchenko et al., 2015)

ν = stretching; δ = bending; τ = twisting; ρ = rocking; s = symmetric; arom = aromatic; skel = skeletal.

for which the BS2-spiked brains are found to exhibit the highest scores compared to the control and BS1 (Table 3). The greater SOMDI score for the 850 and 933 cm^{-1} peaks in BS2-spiked brains, and these Raman shifts relating to biomarkers only present in BS2, demonstrate the probe's ability to detect simulated change in a complex biochemical environment. Further bands at 1004 and 1658 cm^{-1}, common to proteins, are attributed to the aromatic stretching of C—C bonds in the phenylalanine R group and the stretching of C=O bonds in the Amide *I* group, respectively (Galli et al., 2019; Timchenko et al., 2015; Guimarães et al., 2006). A lower SOMDI score for BS1- spiked brains compared to control and BS2 spiked brains to the 1004 cm^{-1} SOMDI score could be a result of the introduction of additional biomarkers not containing phenylalanine, consequently overshadowing the significance of this particular protein peak for characterising spectra of the BS1-spiked brains. This is further shown in Fig. 3A, in which the highest peak at 1004 cm^{-1} is produced by S100B, a biomarker only present in BS2.

Furthermore, the Intra-RSP probe was validated on unexposed rat brains, examining the brain directly through the skull. To ensure a uniform coverage, these were spiked with BS2 in two locations, once into the left cerebral hemisphere and once into the right. The skull itself was found to exhibit a sharp Raman spike at 960 cm^{-1} (Fig. 4A), due to the high density of PO_4 in bones (Ishimaru et al., 2018; Nyman et al., 2011). A complete separation is detected between the rat skull and the transcranial brain (TB) (Fig. 4B), with each test spectrum correctly identified on the SOM (99 % ± 0.03), indicating the unprecedented intracranial spectroscopy capability of penetrating the thin rat skull. Whilst the baseline subtracted spectra in Fig. 4A appear to show similar peaks at vastly different intensities, the normalized spectral data (**Supporting Information 2 A)** reveal Raman shifts primarily in the 600-800 cm^{-1} region for the TB, which are absent in the skull's spectra, representative of brain. Rat brains were subsequently spiked under the skull and spectra from these were acquired for comparison (Fig. 4C). Although a general homology is seen in Raman shifts, SKiNET successfully extracts the characteristic features, distinguishing the transcranial brains from spiked transcranial brains (sTB) with a classification accuracy of 92.8 % ±0.06 (Fig. 4D). Ultimately, the probe in conjunction with SKiNET (Fig. 4) demonstrates the capability to detect subtle changes in sample conditions without the direct exposure, which may be used as a crucial stepping stone into less invasive animal testing as well as paediatric TBI studies and technological developments.

To further assess the probe's ability to separate the various classes, a comparative analysis between brains extracted from SCI and uninjured rats was carried out. A traumatic injury to the spine can cause neuroinflammation and neurodegeneration in the brain, observable through axonal degeneration and cellular shrinkage, effectively simulating a mild TBI (Hains et al., 2003; Klapka et al., 2005; Wu et al., 2014). Fig. 5 establishes the probe's capacity to differentiate between the left cerebral hemispheres of rat brains with injured spines *versus* the healthy controls. Whilst the average spectra ($n = 100$) for each cohort (Fig. 5A) show a homology for control and SCI injured samples, the relative intensity ratios (Fig. 5B) exhibit certain differences. Firstly, the lipid to protein ratio detected *via* the 1444 and 1661 cm^{-1} bands, (Mowbray et al., 2021; Surmacki et al., 2017; Movasaghi et al., 2007) are found to be significantly increased ($p < 0.05$) in the SCI in contrast to the uninjured rat brains. This is in correspondence with the previously observed increased presence in lipids following damage to spinal cord tissue (Wu et al., 2014). Furthermore, the relative intensity ratio between the 533 and 409 cm^{-1} peaks is found to be decreased by 44 % in SCI compared to the uninjured brains, indicating an alteration of the disulfide bond concentration due to the changing levels of protein in the SCI brains (Socrates, 2004). There is a further 50 % relative ratio decrease in the 1004/864 cm^{-1} peaks between the control and the SCI brains, attributed to the phenylalanine residues and backbone peptide bonds (Pezzotti, 2021; Guimarães et al., 2006). Collectively, these detected changes not only cement the probe's ability to detect minute biochemical post injury variations but also establish the detection of the potential damage and protein dysregulation occurring in the brain as a result of SCI. The identified changes are found to be consistent throughout the analysed samples ($n = 100$) (Fig. 5C).

The additionally detected Raman shifts at 1213 and 1553 cm^{-1} are attributed to Haem groups in deoxygenated cells (Table 4 and

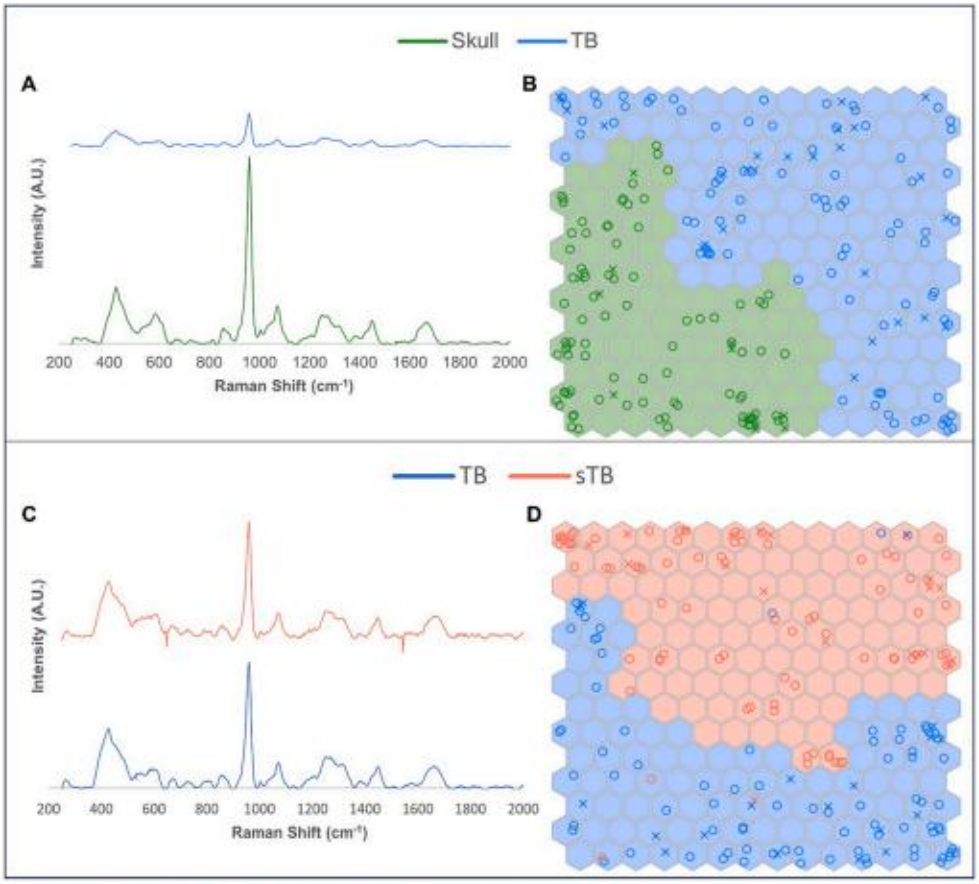

Fig. 4. Spectral Analysis of Transcranial Brains. (A). Analysis of the average spectra ($n = 100$) of raw skull (green) *versus* brains without removal of the skull (blue), *i.e.*, transcranial brain (TB). (B). Corresponding SOM, including the training spectra (dots) and test spectra (crosses) within a set of spectra to ascertain the differentiation of skull and skull covering rat brains with an accuracy of 99 % ± 0.03. (C). Average spectra of spiked transcranial brains (sTB) (red) spiked with BS2 solution *versus* TB (blue) with the corresponding (D) SOM with an accuracy of 92.8 % ±0.06. (For interpretation of the references to colour in this figure legend, the reader is referred to the web version of this article.)

Supporting Information S3) and the lipid C=C stretching and protein NH_3^+ bending, respectively (Socrates, 2004; Palings et al., 1987; Wood et al., 2007). The corresponding SOMDI scores exhibit a greater importance in SCI rat brains (0.60 for 1213 cm^{-1} and 0.63 for 1553 cm^{-1}) relative to controls (0.53 for 1213 cm^{-1} and 0.39 for 1553 cm^{-1}) (Table 4). These are indicative of a higher level of hypoxia from the injured rats (Wood et al., 2007; Doshi et al., 2015). Characteristic peaks at 688 and 1377 cm^{-1}, attributed to the stretching of C—S bonds in cysteine and carboxylic acid from amino acids, respectively (Socrates, 2004; Pezzotti, 2021; Marekha et al., 2015), are found to significantly contribute to the classification of SCI samples (Fig. 5C), showing an increase in protein content, which is in correspondence with the study by Wu et al. as a response to spinal cord trauma (Wu et al., 2014). This further validates the probe's ability to rapidly detect, and *in-situ* differentiate the biochemical changes within the brain's environment, with an accuracy of 94.5 % ±0.03. In addition to the 688 and 1377 cm^{-1} peaks, the 484 and 533 cm^{-1} arising from the disulfide bonds, the 1004 cm^{-1}, attributed to the aromatic C—C bonds from the phenylalanine R group, the 1661 cm^{-1}, attributed to the C=O stretching of Amide *I* groups and the 1258 cm^{-1} from the Amide III group are all found to be lower SOMDI weighted in the control relative to the injured cohorts (Table 4), collectively pointing to the occurrence of protein accumulation (Wu et al., 2014; Socrates, 2004; Galli et al., 2019; Timchenko et al., 2015; Pezzotti, 2021; Guimarães et al., 2006; Tong et al., 2019) post brain trauma.

Finally, the correlation between the SCI brains (Fig. 5A) and the TBI indicative biomarkers (Table 1) can be established. The acute phase response and neuroinflammation are identified through the detection of interleukin-6 (IL-6), exhibiting characteristic Raman shifts at 549, 1128, and 1066 cm^{-1} (Harris et al., 2023; Kumar et al., 2015). IL-6 is typically undetectable in healthy brain tissue, is upregulated as a result of trauma for neuron salvation (Schett, 2018). An increased S100B presence indicates mitochondrial structural damage as well as cellular death. S100B indicative Raman shifts present in the SCI brains at 938, 1066, and 1128 cm^{-1}, all exhibit higher SOMDI scores for the injured (0.52, 0.64 and 0.62, respectively) compared to the controls (0.38, 0.48 and 0.52)

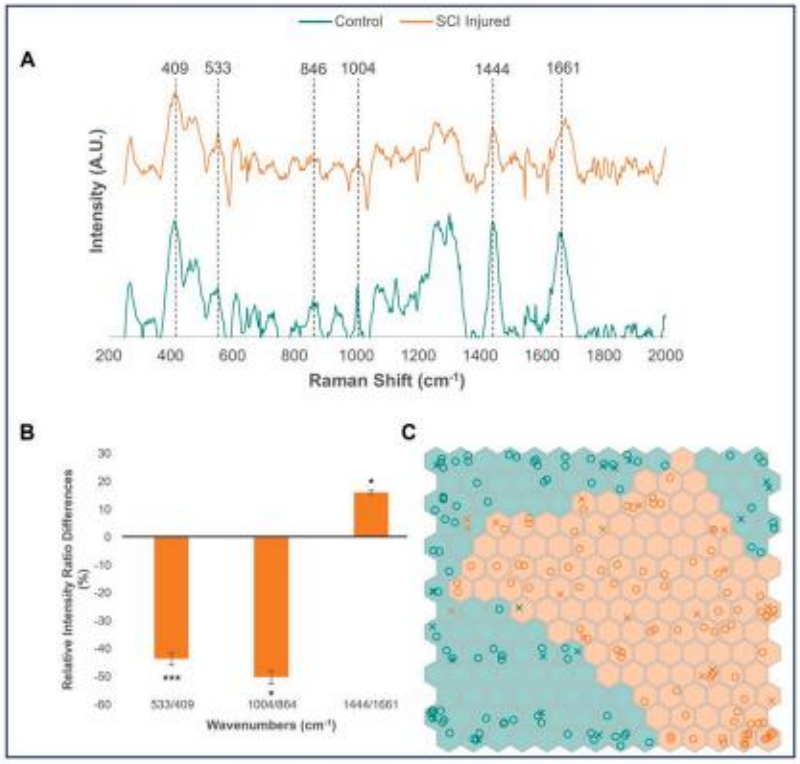

Fig. 5. Spectral Brain Analysis of SCI Injured Rodents. (A). Representative average Raman spectra of SCI injured (orange) rat brains *versus* the uninjured control cohort (green), with highlighted peaks used to investigate (B) the difference in relative intensity ratios between injured and uninjured rats using 533/409, 1004/864 and 1444/1661 cm^{-1} ratios. Error bars present the standard error. (C). SOM classification of uninjured control brain spectra (green) *vs.* SCI injured (orange), with training (circles) and test (crosses) data with an accuracy of 94.5 % ±0.03. (*$p < 0.05$ and ***$p < 0.0001$, student's *t*-test). (For interpretation of the references to colour in this figure legend, the reader is referred to the web version of this article.)

(Table 3) (Nishiyama et al., 2002). Shifts at 1066, 1128 and 1300 cm^{-1} are shared in common to both the SCI brains and sphingomyelin (with roles in cellular roles regulation and brain myelination (Alessenko and Albi, 2020)), gangliosides (which if disrupted, causes neurodegeneration (Sipione et al., 2020)) and sulfatides (which affect membrane functional properties (Takahashi and Suzuki, 2012)) (Harris et al., 2023). The 1066 cm^{-1} band is particularly indicative of GFAP, which if overexpressed leads to glial scars and delayed axonal regeneration (Tzeng et al., 2005; Sofroniew, 2009). UCHL-1 increases following axonal damage to aid in the removal of damaged axonal proteins exhibit a characteristic Raman band in common with the SCI at 1128 cm^{-1} (Shahjouei et al., 2018; Harris et al., 2023). Interleukin-18 (IL-18) with a characteristic peak at 1258 cm^{-1} (Harris et al., 2023) is an inflammatory cytokine inducer, which as a result of trauma causes a release of neurotoxic enzymes (Alboni et al., 2010). Cardiolipin plays key roles in mitochondrial metabolism and acts as a signal for mitophagy (Paradies et al., 2019; Chu et al., 2013). Its presence at 1300 cm^{-1} can therefore relate to mitochondrial damage in the SCI brains. Finally, a Raman shift common to *N*-acetyl aspartate at 1377 cm^{-1} is indicative in an inversely proportional manner to the degree of injury (Harris et al., 2012; Shannon et al., 2016). Overall probe's ability to detect the most dominant signature peak changes, representative of multiplex TBI biomarkers, is a promising technological development with the long-term potential to simplify the point-of-need neurological trauma detection process and enable *real-time* monitoring of the evolving injuries post TBI.

4. Conclusions

Herein, we design, engineer, optimize and establish Raman spectroscopy-based measurements utilising the specificity of inelastic scattering of light to assess TBI through standard clinically established cranial access techniques, undertaken in admissions to secondary care, showing the potential of tracking the pathology and injury evolution. This study demonstrates the efficacity of our developed and optimised biologically safe handheld Intra-RSP to distinguish changes in the brain's biochemical environment within TBI simulated samples. The development of a self-tapping three-dimensionally printed cranial bolt with mechanical stress test simulations for auto-tapping thread, when combined with the Intra-RSP, is established, and validated to be efficiently functional under conditions mimicking the *real-world* scenarios.

The developed probe-device is further validated in a rat model presenting mild TBI, as a result of SCI, differentiating between the CNS injured animals and the healthy controls, thus rapidly classifying injuries *via* SkiNET. Finite element analysis confirms that titanium is the most compatible and safe material, ensuring the bolts integrity even under high torques. The Intra-RSP accurately and rapidly detects and differentiates brains spiked with indicative biomarkers of sTBI from both direct and indirect brain surface exposure. Spectral signatures

Table 4
SOMDI scores for SCI injured rat brains and the corresponding spectral assignments.

Raman Band (cm^{-1})	SOMDI Scores		Assignment	References
	Control	Injured		
			Ring mode	
269	0.47	0.64	*vibrations*	(Bock et al., 2020)
409	0.83	0.95	ν_{skel}(C—C)	(Socrates, 2004)
484	0.63	0.78	ν(S—S)	(Socrates, 2004)
533	0.46	0.60	ν(S—S)	(Socrates, 2004)
549	0.48	0.65	δ(C—S)	(Socrates, 2004)
619	0.42	0.65	ν(–C=CH)	(Socrates, 2004)
				(Socrates, 2004; Pezzotti,
688	0.35	0.44	ν(C—S)	2021)
864	0.38	0.54	ν_s(C-N-C)	(Socrates, 2004)
938	0.34	0.52	ν(C—C)	(Freire et al., 2017)
			$\delta(CH_2)$,	(Pezzotti, 2021;
1004	0.47	0.52	Δ_{arom}(C—C)	Guimarães et al., 2006)
				(Socrates, 2004; Jahmani
			ν(C—O), ν(C—C),	et al., 2021; Tfaili et al.,
1066	0.48	0.64	$\tau(NH_2)$	2012)
				(Surmacki et al., 2017;
			ν(C—N), ν(C—C),	Synytsya et al., 2014;
1128	0.52	0.62	ν_{skel}(C—C)	Katsara et al., 2022)
1200	0.40	0.41	δ (CH), $\omega(CH_2)$	(Babu et al., 2012)
			ν(C=C),	
			Deoxygenated	(Palings et al., 1987;
1213	0.53	0.60	*cells*	Wood et al., 2007)
				(Movasaghi et al., 2007;
1258	0.67	0.69	*Amide III*	Tong et al., 2019)
1300	0.80	0.70	$\tau(CH_2)$	(Ricciardi et al., 2020)
				(Socrates, 2004; Wen
			δ(CH), ν(NH)	et al., 1994; Hadjiivanov
1314	0.73	0.68	Amide I Couplet	et al., 2020)
1377	0.27	0.44	$\nu_s(COO^-)$	(Marekha et al., 2015)
				(Staniszewska-Slezak
				et al., 2015; Farber et al.,
1444	0.79	0.74	$\delta(CH_2)$, $\tau(CH_2)$	2019)
1513	0.29	0.60	ν(NH)	(Socrates, 2004)
			$\delta(NH_3^+)$,	
			Deoxygenated	(Socrates, 2004; Wood
1553	0.39	0.63	*cells*	et al., 2007)
				(Galli et al., 2019;
1661	0.71	0.71	ν(C=O), ν(C=C)	Timchenko et al., 2015)

ν = stretching; δ = bending; τ = twisting; ρ = rocking; s = symmetric; arom = aromatic; skel = skeletal.

associated with these biomarkers are identified through an AI developed algorithm and the corresponding feature extraction discriminant index *i.e.*, SOMDI, provides insights into spectral features. By quantitatively attributing changes to the underlying biochemistry, it characterises the spiked brain by highlighting the dominant wavenumbers distinguishing TBI samples from controls. Similarly, brains from SCI injured rats are differentiated from the uninjured with an accuracy of 94.5 %. This not only solidifies the ability of the probe to separate representative TBI brains from non-TBI but also supports existing evidence of potential brain damage which accompanies SCI.

Further work is needed to include varying the concentration of the biomarker solutions to establish limits of detection as well as trials for *in-vivo* TBI models. With optimisation and *in-vivo* validation, Intra-RSP will be directly translatable for integration into currently available standards-of-neurological-care as a minimally invasive *in-situ* neuro-monitoring modality. *Real-time* spectroscopy of brain cortex TBI-monitoring *via* the developed Intra-RSP 'brain-optical' interface to track pathology and injury evolution, for which intra-cranial access is mandated at-hospital, will in the long-term improve target-management and understanding of injury heterogeneity, evolution, penetrance of pharmacological agents, identify novel targets for intervention and will lay the platform as the first modality for tactful therapeutic modifying therapies in TBIs.

CRediT authorship contribution statement

Clarissa A. Stickland: Writing – review & editing, Writing – original draft, Validation, Methodology, Investigation, Formal analysis. **Zoltan Sztranyovszky:** Writing – review & editing, Writing – original draft, Software, Formal analysis, Data curation. **Jonathan J.S. Rickard:** Writing – review & editing, Writing – original draft, Visualization, Supervision, Software, Resources, Methodology, Investigation, Formal analysis, Data curation. **Pola Goldberg Oppenheimer:** Writing – review & editing, Writing – original draft, Visualization, Validation, Supervision, Software, Resources, Project administration, Methodology, Investigation, Funding acquisition, Formal analysis, Data curation, Conceptualization.

Declaration of competing interest

Authors declare no competing interests.

Data availability

All data needed to evaluate the conclusions in the paper are present in the paper and the Supplementary Materials.

Acknowledgements

We acknowledge funding from the Wellcome Trust (Grant No. 174ISSFPP), the Engineering and Physical Science Research Council (Grant Refs: EP/V029983/1 and EP/L016346/1) and the National Institute for Health Research. We also acknowledge the funding by UK Research and Innovation (UKRI) under the UK Government's Horizon Europe Funding Guarantee (ERC Consolidator Grant, EP/Y030206/1). The authors thank A. Khan and Dr. Mr. D. Davies for helpful discussions about the technology and insights into clinical biomarkers aspects. Components of the developed device were fabricated using the facilities at the Cavendish Laboratory at the Department of Physics and the Nanoscience Centre for Fabrication, University of Cambridge.

Appendix A. Supplementary data

Supplementary data to this article can be found online at https://doi.org/10.1016/j.expneurol.2024.114960.

References

Alboni, S., Cervia, D., Sugama, S., Conti, B., 2010. Interleukin 18 in the CNS. J. Neuroinflammation 7 (1), 1–12.
Alessenko, A.V., Albi, E., 2020. Exploring sphingolipid implications in neurodegeneration. Front. Neurol. 11, 437.
Ashwal, S., Holshouser, B., Tong, K., Serna, T., Osterdock, R., Gross, M., et al., 2004. Proton spectroscopy detected myoinositol in children with traumatic brain injury. Pediatr. Res. 56 (4), 630–638.
Babu, P.C., Sundaraganesan, N., Sudha, S., Aroulmoji, V., Murano, E., 2012. Molecular structure and vibrational spectra of irinotecan: a density functional theoretical study. Spectrochim. Acta A Mol. Biomol. Spectrosc. 98, 1–6.
Banbury, C., Mason, R., Styles, I., Eisenstein, N., Clancy, M., Belli, A., et al., 2019. Development of the self optimising Kohonen index network (SKINET) for Raman spectroscopy based detection of anatomical eye tissue. Sci. Rep. 9 (1), 10812.
Banbury, C., Styles, I., Eisenstein, N., Zanier, E.R., Vegliante, G., Belli, A., et al., 2020. Spectroscopic detection of traumatic brain injury severity and biochemistry from the retina. Biomed. Opt. Express 11 (11), 6249–6261.
Banbury, C., Harris, G., Clancy, M., Blanch, R.J., Rickard, J.J.S., Goldberg, Oppenheimer P., 2023. Window into the mind: advanced handheld spectroscopic eye-safe technology for point-of-care neurodiagnostic. Sci. Adv. 9 (46), eadg5431.
Bock, P., Nousiainen, P., Elder, T., Blaukopf, M., Amer, H., Zirbs, R., et al., 2020. Infrared and Raman spectra of lignin substructures: Dibenzodioxocin. J. Raman Spectrosc. 51 (3), 422–431.
Cao, Y., Shen, D., Lu, Y., Huang, Y., 2006. A Raman-scattering study on the net orientation of biomacromolecules in the outer epidermal walls of mature wheat stems (*Triticum aestivum*). Ann. Bot. 97 (6), 1091–1094.
Chu, C.T., Ji, J., Dagda, R.K., Jiang, J.F., Tyurina, Y.Y., Kapralov, A.A., et al., 2013. Cardiolipin externalization to the outer mitochondrial membrane acts as an

elimination signal for mitophagy in neuronal cells. Nat. Cell Biol. 15 (10), 1197–1205.
Chung, P., Khan, F., 2013. Traumatic brain injury (TBI): overview of diagnosis and treatment. J. Neurol. Neurophysiol. 5 (1), 182–192.
Cordero, E., Latka, I., Matthäus, C., Schie, I.W., Popp, J., 2018. In-vivo Raman spectroscopy: from basics to applications. J. Biomed. Opt. 23 (7), 071210.
Dong, M., Fisher, C., Añez, G., Rios, M., Nakhasi, H.L., Hobson, J.P., et al., 2016. Standardized methods to generate mock (spiked) clinical specimens by spiking blood or plasma with cultured pathogens. J. Appl. Microbiol. 120 (4), 1119–1129.
Doshi, H., Wiseman, N., Liu, J., Wang, W., Welch, R.D., O'Neil, B.J., et al., 2015. Cerebral hemodynamic changes of mild traumatic brain injury at the acute stage. PLoS One 10 (2), e0118061.
Farber, C., Shires, M., Ong, K., Byrne, D., Kurouski, D., 2019. Raman spectroscopy as an early detection tool for rose rosette infection. Planta 250, 1247–1254.
Freire, P., Barboza, F.M., Lima, J.A., Melo, F., Mendes, Filho J., 2017. Raman spectroscopy of amino acid crystals. Raman Spectrosc. Appl. 201, 171.
Galgano, M., Toshkezi, G., Qiu, X., Russell, T., Chin, L., Zhao, L.-R., 2017. Traumatic brain injury: current treatment strategies and future endeavors. Cell Transplant. 26 (7), 1118–1130.
Galli, R., Meinhardt, M., Koch, E., Schackert, G., Steiner, G., Kirsch, M., et al., 2019. Rapid label-free analysis of brain tumor biopsies by near infrared Raman and fluorescence spectroscopy—a study of 209 patients. Front. Oncol. 9, 1165.
Goyal, A., Failla, M.D., Niyonkuru, C., Amin, K., Fabio, A., Berger, R.P., et al., 2013. S100b as a prognostic biomarker in outcome prediction for patients with severe traumatic brain injury. J. Neurotrauma 30 (11), 946–957.
Guimarães, A., Pacheco, M., Silveira Jr., L., Barsottini, D., Duarte, J., Villaverde, A., et al., 2006. Near infrared Raman spectroscopy (NIRS): a technique for doping control. Spectroscopy 20 (4), 185–194.
Hadjiivanov, K.I., Panayotov, D.A., Mihaylov, M.Y., Ivanova, E.Z., Chakarova, K.K., Andonova, S.M., et al., 2020. Power of infrared and raman spectroscopies to characterize metal-organic frameworks and investigate their interaction with guest molecules. Chem. Rev. 121 (3), 1286–1424.
Hains, B.C., Black, J.A., Waxman, S.G., 2003. Primary cortical motor neurons undergo apoptosis after axotomizing spinal cord injury. J. Comp. Neurol. 462 (3), 328–341.
Haris, M., Cai, K., Singh, A., Hariharan, H., Reddy, R., 2011. In vivo mapping of brain myo-inositol. Neuroimage 54 (3), 2079–2085.
Harris, J.L., Yeh, H.-W., Choi, I.-Y., Lee, P., Berman, N.E., Swerdlow, R.H., et al., 2012. Altered neurochemical profile after traumatic brain injury: 1H-MRS biomarkers of pathological mechanisms. J. Cereb. Blood Flow Metab. 32 (12), 2122–2134.
Harris, G., Stickland, C.A., Lim, M., Goldberg, Oppenheimer P., 2023. Raman spectroscopy spectral fingerprints of biomarkers of traumatic brain injury. Cells 12 (22), 2589.
Inc, I., RamanProbe II, T.M., 2022. InPhotonics.com [cited 2022 28/04]. Specification Flyer]. Available from: http://www.inphotonics.com/probeii.htm.
Ishimaru, Y., Oshima, Y., Imai, Y., Iimura, T., Takanezawa, S., Hino, K., et al., 2018. Raman spectroscopic analysis to detect reduced bone quality after sciatic neurectomy in mice. Molecules 23 (12), 3081.
Jahmani, M., Hammadeh, M., Al Smadi, M., Baller, M.K., 2021. Label-free evaluation of chromatin condensation in human normal morphology sperm using Raman spectroscopy. Reprod. Sci. 28, 2527–2539.
Jalloh, I., Carpenter, K.L., Helmy, A., Carpenter, T.A., Menon, D.K., Hutchinson, P.J., 2015. Glucose metabolism following human traumatic brain injury: methods of assessment and pathophysiological findings. Metab. Brain Dis. 30, 615–632.
Jensen, R., Marshak, D.R., Anderson, C., Lukas, T.J., Watterson, D.M., 1985. Characterization of human brain S100 protein fraction: amino acid sequence of S100β. J. Neurochem. 45 (3), 700–705.
Kajimoto, Y., Hashimoto, T., Shirai, Y., Nishino, N., Kuno, T., Tanaka, C., 1992. cDNA cloning and tissue distribution of a rat ubiquitin carboxyl-terminal hydrolase PGP9. 5. J. Biochem. 112 (1), 28–32.
Katsara, K., Psatha, K., Kenanakis, G., Aivaliotis, M., Papadakis, V.M., 2022. Subtyping on live lymphoma cell lines by raman spectroscopy. Materials 15 (2), 546.
Khatri, N., Thakur, M., Pareek, V., Kumar, S., Sharma, S., Datusalia, A.K., 2018. Oxidative stress: major threat in traumatic brain injury. CNS Neurol. Disord. Drug Targ. (Form. Curr. Drug Targ. CNS Neurol. Disord.) 17 (9), 689–695.
Kim, N.-H., Sankar, B.V., Kumar, A.V., 2018. Introduction to Finite Element Analysis and Design. John Wiley & Sons.
Klapka, N., Hermanns, S., Straten, G., Masanneck, C., Duis, S., Hamers, F.P., et al., 2005. Suppression of fibrous scarring in spinal cord injury of rat promotes long-distance regeneration of corticospinal tract axons, rescue of primary motoneurons in somatosensory cortex and significant functional recovery. Eur. J. Neurosci. 22 (12), 3047–3058.
Kohonen, T., 1982. Self-organized formation of topologically correct feature maps. Biol. Cybern. 43 (1), 59–69.
Koningstein, J.A., 2012. Introduction to the Theory of the Raman Effect. Springer Science & Business Media.
Koza, L., Linseman, D.A., 2019. Glutathione precursors shield the brain from trauma. Neural Regen. Res. 14 (10), 1701.
Kumar, R., Diamond, M., Boles, J., Berger, R., Tisherman, S., Kochanek, P., et al., 2015. Acute CSF interleukin-6 trajectories after TBI: associations with neuroinflammation, polytrauma, and outcome. Brain Behav. Immun. 45, 253–262.
Lek, S., Park, Y., 2008. Artificial Neural Networks. Encyclopedia of Ecology, Five-Volume Set. Elsevier Inc., pp. 237–245.
Lloyd, G.R., Wongravee, K., Silwood, C.J., Grootveld, M., Brereton, R.G., 2009. Self Organising maps for variable selection: application to human saliva analysed by nuclear magnetic resonance spectroscopy to investigate the effect of an oral healthcare product. Chemom. Intell. Lab. Syst. 98 (2), 149–161.
Long, D.A., Long, D., 2002. The Raman Effect: A Unified Treatment of the Theory of Raman Scattering by Molecules. Wiley Chichester.
López-Gambero, A.J., Sanjuan, C., Serrano-Castro, P.J., Suárez, J., Rodríguez de Fonseca, F., 2020. The biomedical uses of inositols: a nutraceutical approach to metabolic dysfunction in aging and neurodegenerative diseases. Biomedicines 8 (9), 295.
Maas, A.I., Menon, D.K., Adelson, P.D., Andelic, N., Bell, M.J., Belli, A., et al., 2017. Traumatic brain injury: integrated approaches to improve prevention, clinical care, and research. Lancet Neurol. 16 (12), 987–1048.
Marekha, B.A., Bria, M., Moreau, M., De Waele, I., Miannay, F.-A., Smirtsova, Y., et al., 2015. Intermolecular interactions in mixtures of 1-n-butyl-3-methylimidazolium acetate and water: insights from IR, Raman, NMR spectroscopy and quantum chemistry calculations. J. Mol. Liq. 210, 227–237.
Meister, A., Anderson, M.E., 1983. Glutathione. Annu. Rev. Biochem. 52 (1), 711–760.
Movasaghi, Z., Rehman, S., Rehman, I.U., 2007. Raman spectroscopy of biological tissues. Appl. Spectrosc. Rev. 42 (5), 493–541.
Mowbray, M., Banbury, C., Rickard, J.J., Davies, D.J., Goldberg, Oppenheimer P., 2021. Development and characterization of a probe device toward intracranial spectroscopy of traumatic brain injury. ACS Biomater. Sci. Eng. 7 (3), 1252–1262.
Nishiyama, H., Knöpfel, T., Endo, S., Itohara, S., 2002. Glial protein S100B modulates long-term neuronal synaptic plasticity. Proc. Natl. Acad. Sci. 99 (6), 4037–4042.
Nyman, J.S., Makowski, A.J., Patil, C.A., Masui, T.P., O'Quinn, E.C., Bi, X., et al., 2011. Measuring differences in compositional properties of bone tissue by confocal Raman spectroscopy. Calcif. Tissue Int. 89, 111–122.
Palings, I., Pardoen, J.A., Van den Berg, E., Winkel, C., Lugtenburg, J., Mathies, R.A., 1987. Assignment of fingerprint vibrations in the resonance Raman spectra of rhodopsin, isorhodopsin, and bathorhodopsin: implications for chromophore structure and environment. Biochemistry 26 (9), 2544–2556.
Paradies, G., Paradies, V., Ruggiero, F.M., Petrosillo, G., 2019. Role of cardiolipin in mitochondrial function and dynamics in health and disease: molecular and pharmacological aspects. Cells 8 (7), 728.
Pezzotti, G., 2021. Raman spectroscopy in cell biology and microbiology. J. Raman Spectrosc. 52 (12), 2348–2443.
Reeves, S.A., Helman, L.J., Allison, A., Israel, M.A., 1989. Molecular cloning and primary structure of human glial fibrillary acidic protein. Proc. Natl. Acad. Sci. 86 (13), 5178–5182.
Ricciardi, A., Piuri, G., Della Porta, M., Mazzucchelli, S., Bonizzi, A., Truffi, M., et al., 2020. Raman spectroscopy characterization of the major classes of plasma lipoproteins. Vib. Spectrosc. 109, 103073.
Safety factor result: Autodesk. Available from: https://help.autodesk.com/view/fusion360/ENU/?guid=GUID-8D0B2980-6854-4006-A89E-53C0C2E202B4.
Schett, G., 2018. Physiological effects of modulating the interleukin-6 axis. Rheumatology 57 (suppl_2), ii43–ii50.
Shahjouei, S., Sadeghi-Naini, M., Yang, Z., Kobeissy, F., Rathore, D., Shokraneh, F., et al., 2018. The diagnostic values of UCH-L1 in traumatic brain injury: a meta-analysis. Brain Inj. 32 (1), 1–17.
Shannon, R.J., van der Heide, S., Carter, E.L., Jalloh, I., Menon, D.K., Hutchinson, P.J., et al., 2016. Extracellular N-acetylaspartate in human traumatic brain injury. J. Neurotrauma 33 (4), 319–329.
Sipione, S., Monyror, J., Galleguillos, D., Steinberg, N., Kadam, V., 2020. Gangliosides in the brain: physiology, pathophysiology and therapeutic applications. Front. Neurosci. 14, 572965.
Smith, M., 2008. Monitoring intracranial pressure in traumatic brain injury. Anesth. Analg. 106 (1), 240–248.
Socrates, G., 2004. Infrared and Raman Characteristic Group Frequencies: Tables and Charts. John Wiley & Sons.
Sofroniew, M.V., 2009. Molecular dissection of reactive astrogliosis and glial scar formation. Trends Neurosci. 32 (12), 638–647.
Staniszewska-Sleszak, E., Malek, K., Baranska, M., 2015. Complementary analysis of tissue homogenates composition obtained by Vis and NIR laser excitations and Raman spectroscopy. Spectrochim. Acta A Mol. Biomol. Spectrosc. 147, 245–256.
Stevens, A.R., Hadis, M., Phillips, A., Thareja, A., Milward, M., Belli, A., et al., 2024. Implantable and transcutaneous photobiomodulation promote neuroregeneration and recovery of lost function after spinal cord injury. Bioeng. Transl. Med., e10674
Surmacki, J.M., Ansel-Bollepalli, L., Pischiutta, F., Zanier, E.R., Ercole, A., Bohndiek, S. E., 2017. Label-free monitoring of tissue biochemistry following traumatic brain injury using Raman spectroscopy. Analyst 142 (1), 132–139.
Synytsya, A., Judexova, M., Hoskovec, D., Miskovicova, M., Petruzelka, L., 2014. Raman spectroscopy at different excitation wavelengths (1064, 785 and 532 nm) as a tool for diagnosis of colon cancer. J. Raman Spectrosc. 45 (10), 903–911.
Takahashi, T., Suzuki, T., 2012. Role of sulfatide in normal and pathological cells and tissues. J. Lipid Res. 53 (8), 1437–1450.
Tapanes, S.A., Arizanovska, D., Díaz, M.M., Foloranso, O.O., Harvey, T., Brown, S.E., et al., 2022. Inhibition of glial D-serine release rescues synaptic damage after brain injury. Glia 70 (6), 1133–1152.
Tay, L.-L., Tremblay, R.G., Hulse, J., Zurakowski, B., Thompson, M., Bani-Yaghoub, M., 2011. Detection of acute brain injury by Raman spectral signature. Analyst 136 (8), 1620–1626.
Tfaili, S., Gobinet, C., Josse, G., Angiboust, J.-F., Manfait, M., Piot, O., 2012. Confocal Raman microspectroscopy for skin characterization: a comparative study between human skin and pig skin. Analyst 137 (16), 3673–3682.
Timchenko, E., Zherdeva, L., Timchenko, P., Volova, L., Ponomareva, U., 2015. Detailed analysis of the structural changes of bone matrix during the demineralization process using Raman spectroscopy. Phys. Procedia 73, 221–227.

Tong, D., Chen, C., Zhang, J., Lv, G., Zheng, X., Zhang, Z., et al., 2019. Application of Raman spectroscopy in the detection of hepatitis B virus infection. Photodiagn. Photodyn. Ther. 28, 248–252.
Tools, K., 2023. General Catalogue. Future Focus Precision Engineering, p. 270.
Tzeng, S.-F., Hsiao, H.-Y., Mak, O.-T., 2005. Prostaglandins and cyclooxygenases in glial cells during brain inflammation. Curr. Drug Targ. Inflam. Allergy 4 (3), 335–340.
Vespa, P.M., McArthur, D., O'Phelan, K., Glenn, T., Etchepare, M., Kelly, D., et al., 2003. Persistently low extracellular glucose correlates with poor outcome 6 months after human traumatic brain injury despite a lack of increased lactate: a microdialysis study. J. Cereb. Blood Flow Metab. 23 (7), 865–877.
Ward, J., Clarkson, J., Bishop, D., Fox, S., 2002. Good Design Practice for Medical Devices and Equipment–Design Verification. Institute for Manufacturing.
Wen, Z., Hecht, L., Barron, L., 1994. β-Sheet and associated turn signatures in vibrational Raman optical activity spectra of proteins. Protein Sci. 3 (3), 435–439.
Wongravee, K., Lloyd, G.R., Silwood, C.J., Grootveld, M., Brereton, R.G., 2010. Supervised self organizing maps for classification and determination of potentially discriminatory variables: illustrated by application to nuclear magnetic resonance metabolomic profiling. Anal. Chem. 82 (2), 628–638.
Wood, B.R., Caspers, P., Puppels, G.J., Pandiancherri, S., McNaughton, D., 2007. Resonance Raman spectroscopy of red blood cells using near-infrared laser excitation. Anal. Bioanal. Chem. 387, 1691–1703.
Wu, J., Zhao, Z., Sabirzhanov, B., Stoica, B.A., Kumar, A., Luo, T., et al., 2014. Spinal cord injury causes brain inflammation associated with cognitive and affective changes: role of cell cycle pathways. J. Neurosci. 34 (33), 10989–11006.
Yang, Z., Wang, K.K., 2015. Glial fibrillary acidic protein: from intermediate filament assembly and gliosis to neurobiomarker. Trends Neurosci. 38 (6), 364–374.

Update

Experimental Neurology

Volume 383, Issue , January 2025, Page

DOI: https://doi.org/10.1016/j.expneurol.2024.115046

Experimental Neurology 383 (2025) 115046

Contents lists available at ScienceDirect

Experimental Neurology

journal homepage: www.elsevier.com/locate/yexnr

Corrigendum to "Validation of optimised intracranial spectroscopic probe for instantaneous in-situ monitoring and classification of traumatic brain injury" [Experimental Neurology, 382 (2024) 1–12, 114960]

Clarissa A. Stickland [a], Zoltan Sztranyovszky [a], Jonathan J.S. Rickard [a,b], Pola Goldberg Oppenheimer [a,c,*]

[a] School of Chemical Engineering, College of Engineering and Physical Science, University of Birmingham, B15 2TT, UK
[b] Department of Physics, Cavendish Laboratory, University of Cambridge, JJ Thomson Avenue, Cambridge CB3 0HE, UK
[c] Institute of Healthcare Technologies, Mindelsohn Way, Birmingham B15 2TH, UK

The authors would like to add the following co-authors to the authorship list: Andrew R. Stevens, Zubair Ahmed, David J. Davies with the following affiliation: Department of Inflammation and Ageing, School of Infection, Inflammation and Immunology, University of Birmingham, Edgbaston, Birmingham, B15 2TT, UK.

The updated authors list is as following:

Clarissa A. Stickland, Zoltan Sztranyovszky, Andrew R. Stevens, Zubair Ahmed, David J. Davies, Jonathan J. S. Rickard and Pola Goldberg Oppenheimer.

The authors would like to apologise for any inconvenience caused.

DOI of original article: https://doi.org/10.1016/j.expneurol.2024.114960.
* Corresponding author at: School of Chemical Engineering, College of Engineering and Physical Science, University of Birmingham, B15 2TT, UK.
E-mail address: goldberp@bham.ac.uk (P.G. Oppenheimer).

https://doi.org/10.1016/j.expneurol.2024.115046

Available online 6 November 2024

Appendix C: Raman Spectroscopy as a Neuromonitoring Tool in Traumatic Brain Injury: A Systematic Review and Clinical Perspectives

cells

MDPI

Systematic Review

Raman Spectroscopy as a Neuromonitoring Tool in Traumatic Brain Injury: A Systematic Review and Clinical Perspectives

Andrew R. Stevens [1,2,*], Clarissa A. Stickland [3], Georgia Harris [3], Zubair Ahmed [1,2,4], Pola Goldberg Oppenheimer [3], Antonio Belli [1,2,4] and David J. Davies [1,2,4]

[1] Neuroscience, Trauma and Ophthalmology, Institute of Inflammation and Ageing, University of Birmingham, Birmingham B15 2TT, UK; z.ahmed.1@bham.ac.uk (Z.A.); a.belli@bham.ac.uk (A.B.); daviesdj@doctors.org.uk (D.J.D.)
[2] NIHR Surgical Reconstruction and Microbiology Research Centre, University Hospitals Birmingham, Birmingham B15 2TH, UK
[3] School of Chemical Engineering, University of Birmingham, Birmingham B15 2TT, UK; cas784@student.bham.ac.uk (C.A.S.); gxh975@student.bham.ac.uk (G.H.); p.goldbergoppenheimer@bham.ac.uk (P.G.O.)
[4] Centre for Trauma Science Research, University of Birmingham, Birmingham B15 2TT, UK
* Correspondence: a.stevens@bham.ac.uk

Abstract: Traumatic brain injury (TBI) is a significant global health problem, for which no disease-modifying therapeutics are currently available to improve survival and outcomes. Current neuromonitoring modalities are unable to reflect the complex and changing pathophysiological processes of the acute changes that occur after TBI. Raman spectroscopy (RS) is a powerful, label-free, optical tool which can provide detailed biochemical data in vivo. A systematic review of the literature is presented of available evidence for the use of RS in TBI. Seven research studies met the inclusion/exclusion criteria with all studies being performed in pre-clinical models. None of the studies reported the in vivo application of RS, with spectral acquisition performed ex vivo and one performed in vitro. Four further studies were included that related to the use of RS in analogous brain injury models, and a further five utilised RS in ex vivo biofluid studies for diagnosis or monitoring of TBI. RS is identified as a potential means to identify injury severity and metabolic dysfunction which may hold translational value. In relation to the available evidence, the translational potentials and barriers are discussed. This systematic review supports the further translational development of RS in TBI to fully ascertain its potential for enhancing patient care.

Keywords: traumatic brain injury; neuromonitoring; Raman spectroscopy; point-of-care diagnostics; neuroinflammation; oxidative stress; metabolic dysfunction

Citation: Stevens, A.R.; Stickland, C.A.; Harris, G.; Ahmed, Z.; Goldberg Oppenheimer, P.; Belli, A.; Davies, D.J. Raman Spectroscopy as a Neuromonitoring Tool in Traumatic Brain Injury: A Systematic Review and Clinical Perspectives. *Cells* **2022**, *11*, 1227. https://doi.org/10.3390/cells11071227

Academic Editors: Andrew Chih Wei Huang, Seong Soo A. An, Bai Chuang Shyu, Muh-Shi Lin and Anna Kozlowska

Received: 17 March 2022
Accepted: 4 April 2022
Published: 5 April 2022

1. Introduction

Traumatic brain injury (TBI) is a significant global health problem [1,2]. The incidence of TBI in Europe is estimated at 1012 cases per 100,000 people per year, and 939 per 100,000 globally [3]. The total annual cost globally is estimated in the region of EUR 55 billion [4]. At present, there are no disease-modifying treatments shown to improve outcomes [5], and it remains a leading cause of death and disability across age groups [6]. After an injury, survivors may develop a range of physical, cognitive, and behavioural symptoms which can have a significant and permanent impact on quality of life [7,8], and TBI is associated with an increased risk of neurodegeneration and dementia [9].

'Primary brain injury' is sustained from the trauma itself, whilst 'secondary brain injury' occurs after injury due to adverse sequelae resulting in further cell death and dysfunction [10]. In the early stage after injury, the development of cerebral oedema and expansion of surgical mass lesions result in increased intracranial pressure (ICP) and compromise of cerebral blood flow and oxygenation [11]. Contemporary therapeutic paradigms

are based on the correction and normalisation of these indices as supportive measures [5,11]. However, TBI has a complex pathophysiology, with a number of mechanisms contributing to the development of secondary injury [12]. Mitochondrial dysfunction [13], metabolic failure [14], excitotoxicity [15], oxidative stress [16], and neuroinflammation [17] are established mediators of ongoing neural injury burden after primary trauma and contribute to poor outcomes to an as-yet unquantified extent.

Current neuromonitoring strategies principally centre on ICP through the introduction of an invasive fibre optic probe into the parenchyma [5,11]. Growing evidence for partial brain tissue oxygen monitoring has increased its implementation in clinical practice [18,19]. Microdialysis of parenchymal tissue is implemented in some centres which provide some metabolic indices [20]. Beyond these modalities, few established means of interrogating the state of neural tissue exist in clinical practice. With the growing complexities of known pathophysiological mechanisms in TBI, there is an increasing need for neuromonitoring to increase in breadth, fidelity, and detail, particularly in monitoring tissue biochemistry.

Raman spectroscopy (RS) is a molecular monitoring technique, dependent on the inelastic scattering of photons detectable after excitation from a monochromatic light source. RS has gained interest in medical applications as a sensitive, label-free optical monitoring modality, capable of detecting molecular changes in real time [21–23]. The key to the suitability of RS is its non-destructive nature: it permits accurate tissue interrogation at a molecular level without compromising tissue integrity. RS has in recent years developed a growing interest in a number of potential medical diagnostic applications [22]. These include the diagnosis of atherosclerotic plaques during endovascular cardiac interventions, diagnosis of inflammatory bowel disease during endoscopy, and cancer diagnosis in a number of organs and tissue types.

RS is the technique in which the inelastically scattered light detectable from an excited molecule is exploited for information on the molecule's structure. Upon excitation by a monochromatic light source (e.g., a laser), electrons in a molecule are excited, inducing a dipole. The dipole interacts with the light and can hereafter be distinctly categorised as follows: elastic Rayleigh scattering and inelastic Stokes and anti-Stokes scattering. The Raman effect is observed through the latter two, in which the scattered light has either a higher or lower frequency than that of the laser. For the light to have a higher frequency, as in anti-Stokes scattering, the molecule will have been in an excited state prior to being exposed to light. As the molecule relaxes to its ground state, the emitted photon has more energy in comparison to the photon emitted from the laser. Most molecules, however, are found in their ground state at room temperature, making this event unlikely. For this reason, usually, only Stokes scattering is considered. Stokes scattering consists of a ground state molecule being raised to a higher energy state as a result of exposure to the laser. The molecule returns to an energy state above the ground state: as such, the photon has a lower energy value than that of the laser. RS data acquired are expressed as a function of the Raman wavenumber, the shift being the difference in frequency between the induced light and the scattered light. Each Raman shift is distinct due to the specific molecular vibration each molecule will have, dependent on the number of atoms present, bond lengths, atoms present, etc. The differences recorded provide each molecule a unique, label-free fingerprint, regardless of the concentration of sample present, and is non-destructive, making RS a powerful tool [24] and compatible with use in vivo.

The downfall of RS lies in its inherently weak nature. The number of photons inelastically scattered is comparatively small, compared with the elastically scattered light. This means the signal is easily overwhelmed by fluorescence, especially from organic molecules. To counter this, the lasers used tend to lie in the near-infrared range, the industrial standard being 785 nm, which allows for the least fluorescence without compromising on the resolution. Other approaches to improve outputs have been to take advantage of nanoscale features of surfaces such as gold or copper to chemically and electromagnetically enhance the sample. This is known as surface-enhanced Raman scattering (SERS) and is considered

the most effective way to increase the Raman signal. The need to place the sample on a specialised surface for the SERS procedure, however, limits its use to ex vivo applications.

RS has been the subject of growing interest in pre-clinical studies for the identification and study of a number of pathophysiological mechanisms. For example, RS has been used to detect oxidative stress-induced inflammation in human endothelial cells [25], excitotoxicity in epithelial cells [26], and tracking mitochondrial function [27]. Raman techniques have been utilised in alternative brain injury models, demonstrating consistent RS spectral changes in response to injury, including rat ischaemia–reperfusion injury [28], biochemical change in post-traumatic stress disorder rat models [29], and radiation damage to the brain in mice [30]. RS has been used in the identification of pathognomonic biochemical alterations in a number of neurodegenerative disorders in pre-clinical studies [31] and the identification of neoplasia in cerebral tissue [32]. RS has found applications and interest in neuro-oncological surgery in recent years [33–43]. For rapid intraoperative diagnosis of excised tissue, interest has grown in Raman histology, that is, the use of Raman microscopy with deep convolutional neural networks for rapid and accurate prediction of tissue diagnosis for use in the operating theatre [44]. The application of RS for intraoperative differentiation of normal brain tissue and glioma tissue demonstrates a proof of concept for monitoring applications in the human brain [33], but the exploration of this in the context of TBI has been limited.

The aim of this systematic review was to perform a literature search to identify the purpose of RS in TBI. We discuss the current literature on the utilisation of RS methods in pre-clinical and clinical development for monitoring in TBI and explore the translational challenges and the potential future clinical applications.

2. Materials and Methods

A systematic review of the literature was performed to identify relevant articles employing RS analysis in the setting of TBI. A comprehensive search was performed on 29 September 2021 following the methodology of the Cochrane Handbook for Systematic Reviewers and presented in accordance with the Preferred Reporting Items for Systematic Reviews and Meta-Analyses (PRISMA) [45].

Two authors (A.S. and Z.A.) systematically searched the following databases, from their respective inception to 29 September 2021: MEDLINE, EMBASE, Cochrane Central, Scopus, Google Scholar, and Web of Science. Reference lists of pertinent articles on the topic were hand-searched for suitable articles. Reference lists of identified articles for inclusion were also hand-searched for suitable articles. An example search strategy for Medline is given below:

1. Exp Traumatic brain injury;
2. Exp craniocerebral trauma;
3. Keywords 1 or 2;
4. Raman spectroscopy;
5. Exp spectrum analysis, Raman;
6. Keywords 4 or 5;
7. Keywords 3 and 6.

2.1. Study Selection

Studies were independently screened for inclusion by two reviewers (A.S. and Z.A.). Initial screening based on title and abstract was performed, followed by full-text screening. Inclusion criteria were defined as utilisation of RS methods (alone or in combination with other methods) for analysis of cerebral tissue from either in vitro or in vivo models of TBI, or clinical use in patients with TBI. Exclusion criteria were articles in which no RS methods were used, or no TBI tissue was utilised.

2.2. Data Extraction

Data were extracted from included reports using a piloted form. Data extracted included animal model used, number of replicates, Raman techniques used, the wavelength of the excitatory laser, any tissue fixing prior to analysis, reported outcome, analytical methods, spectral signatures identified, and author conclusions.

2.3. Risk of Bias

Risk of bias in individual studies was assessed using SYRCLE's tool for assessing the risk of bias [46], and the overall risk of bias was determined as low, moderate, or high for each included article.

2.4. Synthesis of Results

The heterogeneous nature of data collection and analysis methods precludes our ability to combine and synthesise results into a meta-analysis, and therefore, what follows is a qualitative summary of the results.

3. Results

3.1. Animal Models of TBI

The search identified 131 articles and after the removal of duplicates, 62 remained. Fifteen articles met our inclusion/exclusion criteria and, after full-text reading, seven studies were included in our final analysis (flow diagram in Figure 1). The included study characteristics are summarised in Table 1. Five additional studies utilised RS techniques for ex vivo biofluid assessment in the context of TBI, and four additional studies investigated RS in mechanistic models relevant to TBI. These are discussed separately in this review. Due to the heterogeneity in the data presented, a meta-analysis was not possible; hence, we performed a qualitative analysis of each study (Figure 1).

Table 1. Characteristics of the included studies. CCI = controlled cortical impact; FTIR = Fourier transform infrared spectroscopy; mTBI = mild traumatic brain injury; RS = Raman spectroscopy; sTBI = severe traumatic brain injury.

Author	Year	Type	Animal	Model Used	Raman Technique (Wavelength)	Overall Risk of Bias
Banbury et al.	2020	Article	Mouse	In vivo CCI mTBI/sTBI	Confocal RS (785 nm)	Moderate
Ercole et al.	2017	Abstract	Mouse	In vivo CCI sTBI	Confocal RS imaging (785 nm)	Moderate
Hu et al.	2016	Article	Rat	Stretch organotypic hippocampal slice cultures	Stimulated Raman scattering (720–990 nm pump beam, 1064 nm Stokes laser)	Moderate
Mowbray et al.	2021	Article	Rat	In vivo CCI sTBI	Confocal RS (785 nm)	Moderate
Surmacki et al.	2016	Article	Mouse	In vivo CCI	Confocal RS (785 nm)	Moderate
Tay et al.	2011	Article	Mouse	In vivo CCI	Confocal RS (785 nm)	Moderate
Kawon et al.	2021	Article	Rat	In vivo drill focal injury	Confocal RS (532 nm)—Additionally, FTIR-only Raman findings reported in this article	Moderate

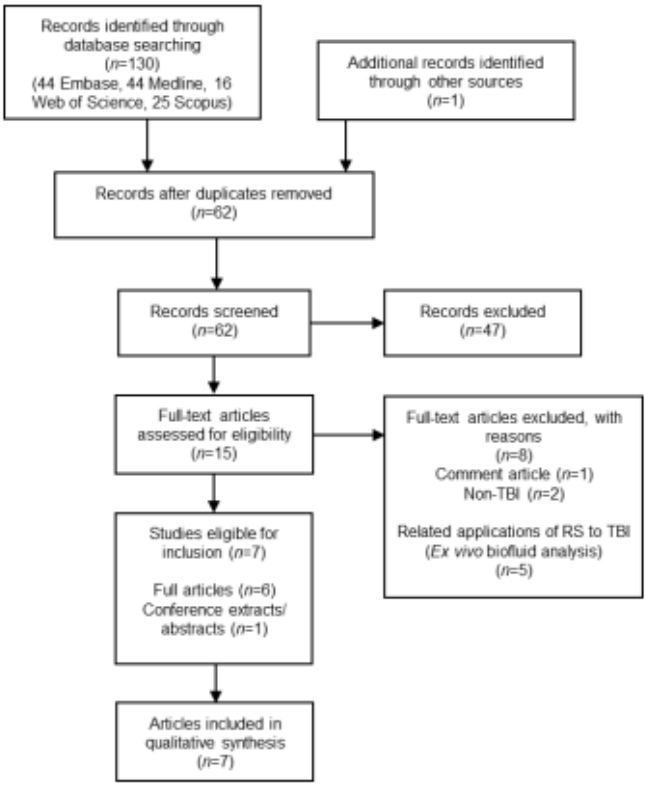

Figure 1. PRISMA flowchart of the systematic review process.

Banbury et al. [47] utilised a murine model of controlled cortical impact (CCI) to administer either a mild TBI, severe TBI, or no injury (sham). Three days post-injury, the animal was sacrificed. Brain and retina samples were prepared for confocal RS after paraformaldehyde fixation and air drying. 80% of spectral readings were used as input for a 'self-optimising Kohonen index network' (SKiNET [48]), a machine learning technique. The remaining 20% were utilised as 'test' spectra. With this, RS of the retina was able to 'predict' sTBI in 82% of cases and mild TBI in 75.1%. Brain tissue samples demonstrated a number of spectral changes between injury groups. Severe TBI resulted in a modest relative increase at 1447 cm^{-1}, accompanied by a significant decrease at 1660 cm^{-1}. Mild TBI demonstrated the same decrease at 1660 cm^{-1} but remained unchanged at 1447 cm^{-1} in comparison to sham. Both injury severities demonstrated a decrease in the band at 1266 cm^{-1}. Spectra retrieved were compared with a spectral library to ascertain possible biochemical candidates responsible for the spectral shift observed in injury. Cardiolipin and cytochrome c spectra from a library were identified to fit well and as potential candidates for the spectral effect.

Ercole et al. [49] utilised false colour imaging with a Raman microscope in fresh frozen sections of mouse brain tissue 2 and 7 days after severe TBI. Injured specimens demonstrated strong signals at 1003 and 1560 cm^{-1} persisting at 7 days. They also imaged ipsilateral corpus callosum and internal capsule sections from a site distant from the lesion. These demonstrated reductions in peaks at 1301 and 1440 cm^{-1}, partially recovering at 7 days. In a similar study by this group, reported by Surmacki et al. [50], they used these time points of 2 and 7 days in a CCI mouse model of TBI. In this study, they took spectroscopic readings from whole-brain specimens from the contralateral brain, ipsilateral

brain distant from contusion core, pericontusional tissue, and contusion core tissue, as well as comparison to sham injury. Their results demonstrated changes in the 1440/1660 cm^{-1} ratio both early (2 days) in the contusion core and late (7 days) in contralateral tissue, suggestive of both local and global biochemical changes in lipid/protein ratio content in response to TBI. The further principal component analysis identified changes in the 701/718 cm^{-1} ratio, corresponding with cholesterol/phospholipid. They hypothesised that the relative increase in cholesterol signal in the contusion core may relate to increasing amyloid-β formation. The group also noted striking features of haem protein in the Raman spectra in early samples from contusion core which resolved by day 7, demonstrating the potential of RS for identifying haemorrhagic conversion/resolution.

Mowbray et al. [51] utilised a controlled cortical impact model of TBI from Sprague Dawley rats. The group observed a fall in 1266 and 1660 cm^{-1} peaks in injured specimens when compared with control. Control specimens also had a relatively smaller 1447 cm^{-1} peak in comparison to TBI. The group utilised a handheld probe device (InPhotonics Raman Probe II, Norwood, MA, USA) with a novel transcranial bolt device fitted with a quartz 'window' to permit optical access to the parenchyma. The results of spectra gained from ex vivo animal tissue were obtained using this probe system, which demonstrates proof of concept for the translational ability of RS for in vivo human monitoring of brain issue biochemistry. Research by Tay et al. also identified spectral shifts associated with immunohistochemical findings of caspase-3 expression, adding further observations to support a role for RS as a monitoring modality for levels of cell death or survival after injury.

Kawon et al. [52] principally studied the use of Fourier transform infrared microspectroscopy, supplemented by RS to analyse rat brain samples 30 days after focal injury. They too noted RS changes at 1658 cm^{-1}, increasing in intensity associated with glial scarring which they postulated to correspond to matricellular protein release by astrocytes. They also observed reductions at 30 days in 2955 cm^{-1} bands which they hypothesised to be linked to reduced levels of lipids from the destruction of healthy tissue.

Hu et al. [53] utilised rat organotypic hippocampal slice cultures for 'live' qualitative imaging by stimulated Raman scattering. Slices after cultured were subjected to stretch mechanical injury and cultured with deuterated amino acids and lipids, which were then visualised with stimulated Raman scattering after 24 h. This was able to demonstrate that increased protein and lipid synthesis occurred in injured hippocampal slices in comparison with uninjured tissue. Due to the necessity of deuterated substrates added to culture media, this technique involves labelling. The 'label-free' potential of Raman spectroscopic methods is an attractive feature when considering the translational potential to in vivo settings and is not the case with the methods used here. However, this study demonstrates in principle the potential for Raman spectroscopic methods to be able to interrogate the biochemistry of living injured tissue.

3.2. *Risk of Bias*

All of the included studies stated their primary outcomes and described baseline characteristics (Figure 2). However, none of the studies reported whether they performed a sample size calculation, how incomplete data were dealt with, whether outcomes were randomly assessed, blinding of investigators, random housing of animals, whether the allocation of animals to groups was concealed, correct timing of randomisation, and whether a random sequence was generated in terms of study design. Therefore, there is potentially high risk of bias in all of these animal studies. However, future studies may avoid the apparent high risk of bias by following a set of standardised techniques in animal experiments based on the ARRIVE guidelines [54].

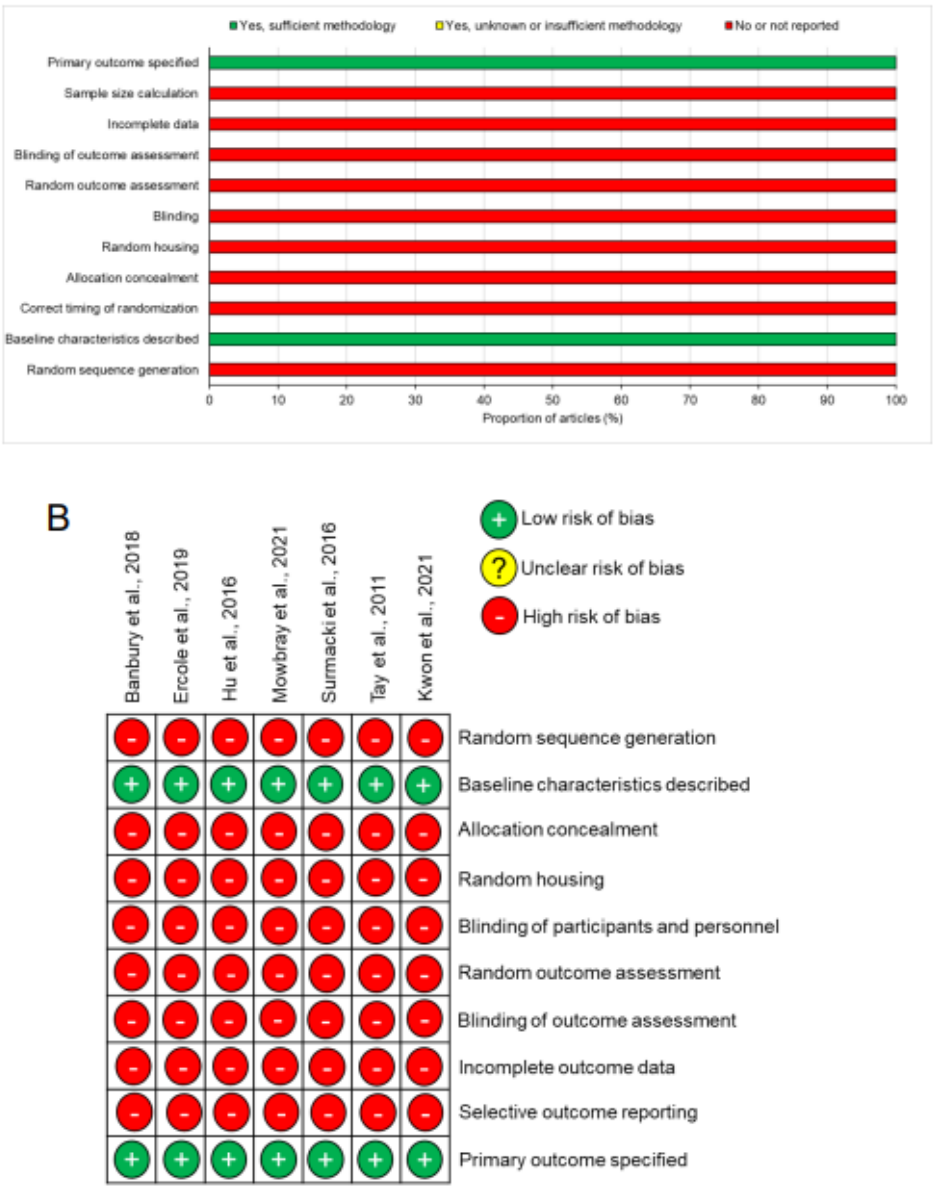

Figure 2. Risk of bias analysis for the included studies using the SYRCLE tool: (**A**) risk of bias summary in all studies; (**B**) risk of bias in individual studies.

3.3. *Analogous Animal Studies with Applicable Adverse Tissue Conditions*

Hackett et al. [55] utilised resonance RS for selective imaging of haem components in the lesion site and perilesional tissue in a collagenase model of intracerebral haemor-

rhage (ICH) in the rat. Whilst a model of primary haemorrhagic stroke, ICH models can be considered translatable to the TBI pathophysiology given the frequent incidence of contusion, an analogous pathology, in the traumatically injured cohort. This group was able to utilise haem signal intensity to quantitatively identify the haemorrhagic boundary, peri-haemorrhagic tissue, and normal tissue. This was utilised in a multimodal array, with RR, Fourier transform infrared imaging, and X-ray fluorescence imaging, to improve accuracy and quantitative assessment, and was further used to assess haematoma volume response to rehabilitative therapy [56].

Jung et al. [28] investigated RS in ischaemia–reperfusion injury in a rat model. Though an established model, their study had very small sample sizes, with one specimen in each arm. The group was able to gain spectral data from hippocampal (cornu ammonis area 1) tissue post-mortem ex vivo. In ischaemic versus control models, 1276 and 1658 cm^{-1} bands increased in injury, whereas 1300 and 1438 cm^{-1} bands decreased.

Dutta et al. [57] modelled oxidative stress in hippocampal primary network neuronal culture with the addition of hydrogen peroxide in the presence of Fe^{2+}. Oxidative stress is an established mechanism of secondary injury after TBI [58]. Based on their results, 725 cm^{-1} and 1320/40 cm^{-1} bands decreased progressively at the measured 20 min intervals over the 80 min post-exposure. This effect of oxidative stress was ameliorated by the addition of ascorbate, which correlated with live–dead cell counts. As such, the group further demonstrated the ability of RS to identify this therapeutic response.

Lakshmi et al. [30] conducted RS studies on radiation damage to the brain tissue in mice. After exposure to 10 Gy irradiation or control (anaesthesia alone), Raman spectra were obtained from both white and grey matter. These demonstrated early shifts in 1440 and 1660 cm^{-1} regions which were sustained over one-week post-exposure.

3.4. Biofluid Diagnostics

Detecting biochemical changes via TBI biomarkers using accessible samples such as blood, saliva and urine can provide early information in the vital acute phase (<24 h) of injury incidence [59] for triaging, monitoring, and diagnostics. Highly investigated TBI biomarkers include S100B, glial fibrillary acidic protein (GFAP), neuron-specific enolase (NSE), and ubiquitin C-terminal hydrolase-L1 (UCHL1) [60]. In 2007, the Scandinavian healthcare system introduced S100B into clinical practice guidelines to predict negative CT scans, thus reducing the number of unnecessary scans [61].

A popular modified RS technique is surface-enhanced Raman spectroscopy (SERS) which links the optimum excitation wavelength to the size, shape, composition, and dielectric environment of nanoparticles [62]. This method requires a rough, metal SERS active substrate to absorb the analyte or for the SERS substrate to be coated in nanostructures [63], via metal colloids in a thin film layer. Rickard et al. [64] developed an optofluidic device using SERS capable of detecting picomolar concentrations of *N*-acetylaspartate (NAA) [64]. NAA is an abundant molecule in the central nervous system (CNS) which is released following TBI and is believed to correlate with injury severity and poor prognosis [65]. The device was also able to detect and discriminate concentrations of S100B and GFAP, (glial fibrillary acidic protein) also recognised biomarkers of neurological injury burden [66]. Whilst this device is developed as an ex vivo tool for monitoring the presence of markers in biofluids, its ability to detect such biomarkers in minute concentrations represents the significant potential of RS for diagnostic resolution for biomarker monitoring.

Gao et al. [67,68] utilised SERS with a paper-based lateral flow assay system with a SERS labelled detection antibody to identify S100B in human blood samples. Using blood samples from patients with TBI, they demonstrated a good correlation with laboratory ELISA measured values of S100B concentration in the samples. Their system was developed to offer a reduced cost and time for the identification of biomarkers of TBI. Li et al. [69] similarly implemented SERS for the assessment of neuron-specific enolase (NSE), a biomarker of TBI, in diluted plasma samples from patients with TBI. With a 'lateral-flow glass-hemostix'-based SERS assay, the group identified a lower limit of detection of 0.74 ng/mL. These

studies demonstrate sufficient fidelity and performance of SERS-based assay in clinically relevant biomarker assay to suggest potential translatability to point-of-care testing.

O'Neal et al. [70,71] demonstrated the utility of SERS for the identification of excitatory amino acids in dialysate from a rat model of ischaemic brain injury after middle cerebral artery occlusion. Glutamate and aspartate in microdialysate were found to be distinguishable using SERS. A comparison of a SERS-based assay with high-performance liquid chromatography was able to identify concentrations of glutamate between 0.4 and 5 µmol/L.

3.5. Spectral Evidence from Animal Models

Understanding spectral data from RS in TBI is integral to identifying translatable value for clinical applications. Table 2 offers a summary of the literature on observed spectral changes in animal models of TBI and analogous mechanistic animal studies. Clear and reproducible shifts in peaks are identified across multiple studies and models. A notable contradiction is the 1660 cm^{-1} peak: TBI models have identified a consistent reduction in 1660 cm^{-1} intensity in comparison with control [48,51,52,72]. In contrast, an ischaemia–reperfusion model of brain injury identified an increase in the 1660 cm^{-1} intensity. The shift may alter between these pathologies; however, the validity of these results is highly questionable given the use of $n = 1$ specimen in control and test groups.

Table 2. Consolidation of Raman spectral data for noted wavenumbers which have demonstrated changes in TBI models or analogous mechanistic models. Assignment data are taken from corresponding references or alternative sources [43,47,50,57,72–97]. Peak assignments based on spectra from excitation with 785 nm laser unless otherwise stated. DNA = deoxyribonucleic acid; Hb = haemoglobin; A = adenine; C = cytosine; G = guanine; mTBI = mild traumatic brain injury; sTBI = severe traumatic brain injury; T = thymine.

Peak Wavenumber (cm^{-1})	Appropriation	TBI
426	Hb [50] Cholesterol [50]	Increasing in contusion core between 2 and 7 days [50]
491-2	Combination modes of the uracil ring plus ribose vibrations [92]	Increasing in contusion core between 2 and 7 days [50]
605	Cholesterol [50]	Increased in contusion core vs. contralateral hemisphere [50]
675	Hb [50], glycerol [93]	Decreasing in contusion core between 2 and 7 days [50]
701-2	Lipids (701 cm^{-1}) [50], cholesterol, cholesterol ester	Increasing in contusion core between 2 and 7 days [50]
718	Symmetric and anti-symmetric stretch vibrations of the choline group $N+(CH_3)_3$ in phospholipid, lipids [50]	Decreased in contusion core vs. contralateral hemisphere (2 and 7 days) [50]
725	nucleic acid (A) [57,94]	Reduced oxidative stress [57]
754	Hb [50]	Increased in contusion core vs. contralateral hemisphere (2 and 7 days) [50], decreasing in contusion core between 2 and 7 days [50]
782	DNA peak, cytosine (C), uracil (U), thymine (T), C, T, U-ring breathing [57,95]	Reduced oxidative stress [57]
801	Cyclohexane [74,75,98] (532 nm [96], 575 nm [73] and 785 nm [97] excitation)	Increased in contusion core vs. contralateral hemisphere [50]
850-2	C-H wagging [72] (850 cm^{-1}), C−C stretch in proline (collagen) [94]; ring breathing (tyrosine) [94]; C−O−C stretching (glycogen, polysaccharides) [57,94], albumin (852 cm^{-1}) [50]	Increased in mTBI and sTBI (3 days) [47]

Table 2. *Cont.*

Peak Wavenumber (cm^{-1})	Appropriation	TBI
970	Intralipid [50] haem aggregation marker bands, fibrin components [74]; C-C stretching mixed with C-H rocking, biliverdin, protoporphyrin IX [75]	Decreasing in contusion core between 2 and 7 days [50]
1002	Ring breathing mode of phenylalanine (1002 cm^{-1}) [50] and (1005 cm^{-1}) [57]	Decreasing in contusion core between 2 and 7 days [50], decreased in sTBI (3 days) [47,51], decreasing in contusion core between 2 and 7 days [50], weak or absent in injured samples [77]
1003	C-C skeletal [72], phenylalanine [76,94], Hb, albumin [50]	Decreasing in contusion core between 2 and 7 days [50], strong signal in pericontusional tissue (days 2 and 7) [49]
1079	Intralipid [50]	Decreasing in contusion core between 2 and 7 days [50]
1090	PO_2 stretch, phospholipids and nucleic acid [77]	Stable in oxidative stress [57]
1096-8	Phosphodioxy PO_2 [78], nucleic acid (1097 cm^{-1}) [94]	Increased in mTBI and sTBI (3 days) [47]
1154	Phenylalanine, tryptophan, hypro, tyr, phe, m(CC/CN) proteins (1155 cm^{-1}) [94] and (1156 cm^{-1}) [57]	Decreasing in contusion core between 2 and 7 days [50]
1175	Amide III vibration, cholesterol [77]	Band appears after injury [77]
1224	Hb [50]	Increased in contusion core vs. contralateral hemisphere (2 days) [50], decreasing in contusion core between 2 and 7 days [50]
1227-8	Amide III vibration, phospholipid [77] (1227 cm^{-1}); C-H methine bending vibration with changing methaemaglobin content (1228 cm^{-1}) [79]	Increased in contusion core vs. contralateral hemisphere [50], band after injury [77]
1266	CH bending modes [72]: amide groups in lipids and proteins [76], cardiolipin [47]	Decreased in mTBI and sTBI (3 days) [47,51], decreased in contusion core vs. contralateral hemisphere (2 and 7 days) [50]
1301	CH_2 twist/wag/deformation: phospholipid, mixed fatty acid chains, mixed amide III protein vibration [77], lipids [50]	Increasing in contusion core between 2 and 7 days [50], reduction in peak in ipsilateral corpus callosum and internal capsule (distant from lesion) at 2 days, partially recovering by 7 days [49]
1320	CH_2 CH_3 twisting; Proteins/lipids nucleic acid [57]	Reduced oxidative stress [57]
1337-1340	Nucleic acid (A,G) [57]; b protein CH_2 deformation [72], amide III [76] (1337 cm^{-1}); collagen (1338 cm^{-1}) [94]; albumin(1339 cm^{-1}) [50]; CH_2 scissors, C-OH bending [80]	Reduced in oxidative stress [57], increased in sTBI (3 days) [47,51]
1420	DNA peak, nucleic acid (A, G) [57]; -CH_2 bending mode for proteins and lipids, indicates change in cytochrome c, intracellular environment, and mitochondrial membrane structures [81]	Reduced oxidative stress [57]
1440	CH_2 twisting and bending [51,82,96], Lipid, cholesterol, phospholipid, mixed amide I protein, tyrosine [80,94]	Initially decreased in contusion core vs. contralateral hemisphere (2 and 7 days), increasing progressively in contralateral hemisphere and contusion core between 2 and 7 days, to above control levels [50], reduced after ischaemic injury
1447-50	CH_2 bending [72], mixed proteins and lipids [76] (1447 cm^{-1}) [94], albumin, CH_2 deformation from lipids and proteins (1450 cm^{-1}) [77]	Increased in sTBI (3 days) [47,51]
1462	Lipids [50]	Increasing in contralateral hemisphere between 2 and 7 days [50]

Table 2. *Cont.*

Peak Wavenumber (cm^{-1})	Appropriation	TBI
1547	Hb [50]	Decreased in contusion core vs. contralateral hemisphere (2 and 7 days), decreasing progressively over time [50]
1560	Associated with mitochondrial activity of cells [77]	Strong signal in pericontusional tissue (days 2 and 7) [49]
1562	Hb [50]	Increased in contusion core vs. contralateral hemisphere (2 days resolving by 7 days) [50]
1576	DNA peak, nucleic acid (A, G) [57]; Hb in red blood cells [82] (though not identified by dedicated erythrocyte RS at 785 nm [83]; N = N stretching vibration [84]	Reduced oxidative stress [57]
1586	Albumin [50]	Sharp band after injury [77]
1618-1620	Predominantly C = O stretch in protein, Hb, Amide I (1618 cm^{-1}) [77], tyrosine/tryptophan [94]	Sharp band after injury [77]
1620	Hb [50]	Increased in contusion core vs. contralateral hemisphere (2 days, resolving by 7 days) [50]
1648	Predominantly C = O stretch in protein, Amide I [57]	Decreased in contusion core vs. contralateral hemisphere (2 and 7 days), increasing progressively in contralateral hemisphere over time [50]
1660	Lipids [50], C = C stretching [72,76,82], amide I vibration [57,77], Tyrosine [80,94], mixed lipids and proteins [76], alpha-helix/random coil [94], cardiolipin [47]	Decreased in mTBI and sTBI (3 days) [47,51], decreased in contusion core vs. contralateral hemisphere (2 and 7 days) increasing progressively in contralateral hemisphere and contusion core between 2 and 7 days [50,77]. Increased after ischaemic injury.
1670	Cholesterol, C = C stretching [50]	Marginal increase in contusion core vs. contralateral to lesion [50]

Metrics offer a means of rationalising an otherwise arbitrary intensity measurement obtained from spectra. Table 3 offers a summary of the literature on ratio-based metrics from TBI animal studies. Identification of a consistent, unchanged 'reference' peak which is minimally altered in the context of injury, allows an internal comparator for a dynamic peak of interest. Based on the data, 1440 cm^{-1} is an example of a 'reference' peak, with minimal shift in TBI models; 1660 cm^{-1} operates as a 'dynamic' peak which alters in injury.

Table 3. Metrics utilised in the literature for ratio-based comparative analysis of spectral data [48,51,52]. TBI = traumatic brain injury.

Metrics cm^{-1}/cm^{-1}	Remark	Changes in Animal Models
701/718	Cholesterol/phospholipid	Statistically significant difference between the contralateral and pericontusional/contusional regions at 7 days after TBI [50]
1301/1250	Mixed fatty acid chains/amide III protein	Statistically significant difference between the contralateral and pericontusional/contusional regions at 7 days after TBI [50]
1440/1660	CH deformation/mixed amide I protein and C=C stretching of lipids	Statistically significant difference between the contralateral and pericontusional/contusional regions at 2, 3, and 7 days after TBI [48,51,52]
1301/1620	Mixed amide III protein and fatty acid chains/haemoglobin	Statistically significant difference between the contralateral and pericontusional/contusional regions at 7 days after TBI [50]

Resolution of early strong band signals from haem occurs between 2 and 7 days [50]. Whilst initial haem signal may obfuscate underlying metabolic tissue signal, identification of alterations in haem signal may be clinically advantageous to identify and monitor the temporal evolution of contusion. Utilisation of RS amongst other methods to delineate haematoma boundaries further suggests the potential for this application [55].

Dysfunctional mitochondrial lipid metabolism plays a role in both acute and chronic sequelae of TBI [99]. Tissue levels of free fatty acids are dynamic following TBI in rat models and may play a role in secondary tissue damage [98]. Differences between lipid concentrations between injured and uninjured brain tissue are also present after injury [100], and lipid composition changes can be identified with RS to discern such changes [50]. Oxidative states of cardiolipin and its interaction with cytochrome c are altered after injury and may be a mechanism for the production of reactive oxygen species [99]. Cardiolipin has been identified as a potential source for band shift after injury [47] and presents a potential for monitoring by RS, though there are consistent strong Raman bands from numerous brain lipids in the 1440 cm^{-1} region [91]. Whilst there is some overlap of lipid and protein signals, increased acquisition of data and utilisation of neural network analysis may provide means to differentiate and utilise such data.

Beyond this, bands in the 2600–3800 cm^{-1} region are able to identify the water content of the brain in the region of 0.75–0.95 to an accuracy of 0.01 [101–103]. Real-time assessment of the progression of brain oedema has clear clinical applications for guiding medical and surgical therapy for acute TBI in the intensive care unit setting.

4. Discussion

4.1. Translational Considerations

RS is a powerful, label-free, non-destructive modality for biochemical analysis. As demonstrated by early studies using ex vivo analysis of injured and normal brain tissue, it can produce relevant biochemical data relatable to tissue integrity, injury burden, and progression or resolution. Similarly, ex vivo techniques have found clinical utility in neuro-oncology settings for 'operating table-side' histological diagnostics. Clearly, in contrast to this application, the clinical setting of TBI is directed at maximal tissue salvage, rather than identifying tissue for excision. As such, in vivo RS would be necessary for providing clinically useful data in TBI. Whilst a number of the studies identified to use in vivo modelling of traumatic brain injury, the RS measurements have been taken ex vivo. In vivo applications of RS in TBI are yet to arise, though the technique has found applications in patients in neuro-oncological surgery [33,34,36–43]. Particularly, Jermyn and colleagues report the development of an intraoperative probe used for the detection of brain cancer tissue, compared with healthy brain tissue, and have demonstrated its safe and effective use in humans [34,41,43]. This concept has been further demonstrated with the development of a fibre optic probe for inclusion within a brain biopsy probe, which has been validated in human pilot studies [104]. The success of 'live-tissue' RS in vitro amongst included studies, though not in vivo, does further support the concept of gaining biochemical data from living brain tissue using RS.

There are a number of translational barriers to the effective application of RS for the benefit of patients. One consideration is the access to brain parenchyma: unlike near-infrared spectroscopy, the Raman scattering return signal does not display skull penetrance rendering a transcranial approach vulnerable to excessive 'noise' from extracranial tissue scatter, to the extent of rendering it impractical. Subsequently, there are three options: (1) intraoperative cortical access; (2) a probe device which allows optical passage across the skull via a 'window' [51]; (3) a temporarily implanted fibre optic probe array capable of excitation and detection, either as an intraparenchymal or cortical monitoring device.

4.2. Cranial Access

Proof of principle of utilising RS as an intraoperative means of brain tissue interrogation has been established in the field of neuro-oncology [34,41,43]. As described above,

numerous publications have described the developments required for the translation of an intraoperative application of RS—specifically, the localised differentiation between tumour tissue and normal parenchyma as a means to optimise maximal safe resection in glioma surgery. This demonstrates in vivo brain RS as a workable concept.

Whilst the intraoperative period provides cortical access opportunity, readings during surgery will be unable to avoid a degree of ambient light. Whilst the highly fluorescent direct lighting could be averted for readings, it is neither practical nor safe to be able to take cortical readings in circumstances at or nearing darkness. RS is a highly sensitive method but vulnerable to such background optical 'noise'. Adjustments to laser power and background reference measurements can be applied to overcome this potential [40].

Though the intraoperative period provides cortical access for RS monitoring in patients with traumatic brain injury, the majority of the acute phase of severe TBI is spent in the intensive care unit rather than the operating theatre. Single-time-point (intraoperative) biochemical interrogation with RS could provide clinically relevant data which may correlate with the burden of injury and thus prognosis. However, to permit longitudinal data throughout the acute phase, alternative means of access are required.

Our group has explored a quartz lens as a 'window' technique as a means for gaining optical access to the intracranial compartment [51]. Mowbray et al. [51] designed and engineered a novel device which functions as a means of eliminating extra- and cranial tissue, with a polished quartz disc as a transparent window to facilitate spectral interrogation of brain tissue intermittently. This carries a relative advantage that the RS is external and has, therefore, no requirement for sterilisation between patients and is reusable within the lifespan of the equipment, with the comparatively simple cranial access device as a single-patient 'consumable'.

Standard cranial access techniques to facilitate intracranial monitoring devices are well integrated into modern neurosurgical practice. Up to a fifth of patients with traumatic brain injury who require admission to secondary care facilities need such invasive placement of monitoring probes, principally for the monitoring of ICP as a key paradigm in the supportive management after severe injury. In recent years, additional modalities have become integrated, including brain tissue oxygen monitoring and the insertion of microdialysis probes for the sampling of small molecules of metabolic interest (such as glucose, lactate, pyruvate, etc). The standard of care, therefore, involves the invasive component required, and additional monitoring requires only adaptation of the systems already established, with minimal additional risk burden to patients. An example of this principle is the integration of a near-infrared spectroscopy probe with ICP monitoring [105]. This device has utilised existing intracranial access to introduce an optical monitoring modality for the assessment of cerebral haemodynamics, successfully implemented in a small pilot group without safety concerns.

4.3. Probe Development

Whilst a cranial window has been demonstrated as a technically feasible means to facilitate cortical RS, it holds a number of potential limitations. The device is too bulky and cumbersome for continual monitoring in clinical practice. Furthermore, obfuscation of the window with blood, inflammatory tissue, serous fluid, or other tissue may render the implanted device unusable for monitoring at depths beyond this layer which would inherently carry its own Raman signal.

An alternative means of facilitating RS monitoring in parenchyma is through the temporary implantation of a probe. This would require a fibre optic system for delivery of excitation wavelengths, and a further fibre optic system for collection and transmission of detected photons to a charge-coupled device (CCD) for spectroscopic analysis. The system at its most basic could comprise two optical fibres, one dedicated to each of these purposes. Filtering and focussing optics, too large for integration at a probe tip, are external to the probe tip and patient. More complex arrays, typically increasing the number of detection fibres or introducing lens tips, have been developed for endoscopic and probe-

based monitoring systems [34,41,43]. One difficulty with fibre optic RS is the inherent Raman signal of silica-based fibre optic surrounds, though this can be accounted for with computational methods. Data resolution may be compromised with a reductionist system, but similarly, computational methods have been demonstrated to achieve optimal data interpretation from such data [48].

Implanted cerebral devices are typically for single use. Cost effectiveness of disposable devices should be considered: minimising production costs of consumables and materials required would both increase the likelihood of cost-effective uptake, as well as achieve favourable sustainability in implementation.

4.4. Wavelength Selection

Raman signal is weak and is inversely proportional to the fourth power of the excitation wavelength: longer wavelengths result in reduced scatter and, therefore, reduced sensitivity [106]. Conversely, lower wavelengths (particularly in biological tissues) induce autofluorescence: this signal creates significant 'noise' alongside the Raman scatter, making achieving usable resolution more challenging. As such, 785 nm is a typically used wavelength as a 'middle ground' [22].

4.5. Potential Clinical Applications

4.5.1. In Vivo Monitoring: Detailed Biochemical Assessment

Current therapeutic paradigms in acute TBI are aimed at restoring physiological intracranial haemostasis to minimise secondary injury [5]. Most commonly, this involves measurement of ICP via an implanted probe and therapeutic intervention based on avoiding high ICP [11]. However, numerous further known and unknown mechanisms contribute to poor functional outcomes in secondary brain injury after trauma. These include neural apoptosis, glial scarring, axonal degeneration, excitotoxicity, metabolic failure, mitochondrial dysfunction, neuroinflammatory responses, and oxidative stress [12].

Detection of optical biomarkers in the injured brain could have prognostic value and guide further therapy in the acute phase. RS has demonstrated a pre-clinical aptitude for the assessment of aspects of these pathophysiological pathways, as outlined above. For example, metabolic failure from mitochondrial dysfunction is a key factor in poor outcomes from TBI, but the real-time assessment of this is minimally addressed with current standard neuromonitoring and therapeutic methods [107–110]. In vivo RS monitoring in the gastrocnemius muscle of the rat has been demonstrated to be able to detect early changes in mitochondrial redox states in response to sepsis, prior to any change detected in lactate levels. Translation of this concept to brain tissue as a single example would provide great potential for clinical applications; an illustration of a potential application and a general summary are given in Figure 3.

As described above, there are a number of possible methods of accessing brain tissue for optical interrogation. The standard of care in moderate-to-severe TBI routinely involves the invasive placement of probes into the brain parenchyma and would add a minimal excess risk burden to utilise such access for RS. This would permit 'online' or 'real-time' detailed biochemical assessment and response to therapy.

Further considerations are required for the utility of Raman spectra in clinical decision making. Given the currently sparse available data, it is not possible a priori to determine the exact influence RS may in the future have on the clinical care of patients with TBI. To consider ICP monitoring in comparison, since first-in-human measurements in 1951, and its integration into standard practice in the 1970s [111], further study and optimisation of the interpretation and clinical applications of the indices and derivatives of ICP are ongoing to this day [112]. However, it can be reasonably argued that a technique such as RS has the potential to offer molecular insights into the function and dysfunction of the human brain far beyond that of intraparenchymal pressure. In discerning the potential utility and clinical relevance of RS in acute traumatic brain injury, clinical studies to gain spectral data from humans with traumatic brain injury would be of tremendous benefit in the exploration of

future applications. A summary of commercially available probes which have been applied in neurosurgical settings is available in a review article from DePaoli et al. [113].

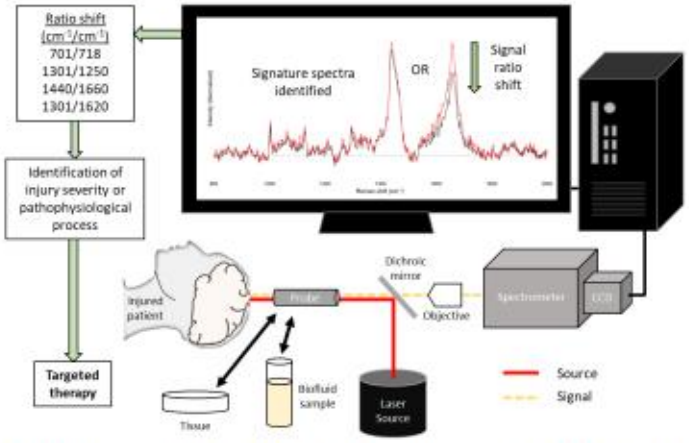

Figure 3. Illustration of a simplified Raman spectroscopy system and its potential application in clinical environments. CCD = charge-coupled device.

The spectral data from implanted fibre optics may be technically problematic. RS is sensitive to a number of factors which may adversely affect data quality and consequently, utility. Implanted fibre optic probes inherently are affected by 'background' spectra from silica fibre covering, and using small numerical aperture optics (as is preferable for minimising invasiveness) may further compromise the data. Previously, our research group has used machine learning tools to overcome such difficulties (SKiNET [47,51]). As demonstrated by SKiNET, it is possible to train such a system to accurately discern subtle modalities of biochemical derangement which correspond with differing adverse tissue conditions.

RS is able to identify a spectral 'signature' of normalisation of biochemical derangement. This effect has been observed in an oxidative stress model, with normalisation of deranged Raman signal with the addition of ascorbate [57]. Applied in vivo, this permits an immediate optical monitoring mechanism for oxidative stress states. Given the wide-ranging capabilities of RS to resolve spectral fingerprints of biochemical change at the molecular level, there is significant potential for such a concept to be applicable to other pathophysiological mechanisms in TBI. At present, outcome measures in TBI require at least three months of follow-up. Even with extensive longitudinal outcome assessments, the heterogeneity of injury necessitates vast numbers required in clinical trials to demonstrate clinical efficacy. Immediate biochemical feedback of normalisation of such mechanisms which may correspond to neural survival could provide such a proxy measure for early indication of effect.

4.5.2. Microdialysis Online Analysis

A microdialysis is a tool for neuromonitoring of cerebral metabolic function, used in limited centres in clinical practice [20]. Presently, samples of effluent dialysate are collected over intervals (one hour is typical) and intermittently analysed. This creates limitations in both clinical and research practice: changes in metabolite composition of the dialysate are not immediately recognisable, and any change is 'binned' into a mean sample for each hour. As such, establishing a true temporal relationship between patient or therapeutic variables and the metabolic observed effect is not possible [114]. RS-based methods have been established as effective in identifying clinically relevant quantitative information on metabolites [70,71]. Given the high sampling rate and accuracy of RS-based methods,

there is the potential for continuous analysis of passing dialysate: a bedside system for microdialysis with continuous 'online' analysis.

4.5.3. Pitchside/Bedside Concussion Assessment

A number of studies have utilised RS (or a variation thereof) in developing point-of-care applicable diagnostic devices for the recognition of biomarkers of TBI [64–69]. Point-of-care detection for TBI has the most relevance in mild TBI and particularly concussion. In severe TBI, the clinical condition of the patient (typified by impaired consciousness or seizure) or the severity of the injury mechanism necessitates urgent radiological diagnosis. However, clinical diagnosis of concussion can be more challenging, both for sportspeople and patients.

Currently, TBI point-of-care diagnostic and monitoring techniques routinely used by healthcare professionals are those of clinical examination and assessment. For moderate-to-severe injury with markedly altered levels of consciousness, the Glasgow Coma Scale (GCS) is the standard examination tool, alongside the assessment of pupillary responses to light. GCS is a fast and simple assessment method that can be performed by a healthcare professional of any level, by assessing the patient's motor, verbal, and eye responses [115]. Clinical assessment of suspected concussion and mild TBI can rely upon a more nuanced and detailed neurocognitive and symptomatology in addition to an assessment of consciousness, as in the Sports Concussion Assessment Tool, currently in its fifth version (SCAT5) [116].

Clinical examination methods are subjective, with moderate interrater reliability. There are inconsistencies between scores when undertaken by different healthcare workers and at varied timeframes [117]. GCS may also be affected by the presence of intoxicants, medication, sedation, and pre-morbid disability. SCAT5 assessments particularly require patient compliance and participation in both baseline and incident examinations. Attempts to develop objective bedside/pitchside diagnostics in recent years include pupillometry devices to improve interrater reliability of such clinical assessment [118], but as yet, a true point-of-care diagnostic device is not available to clinicians.

The available assessment methods have numerous limitations which highlight the need for an alternative point-of-care method that may be fulfilled by an RS diagnostic device. For maximal clinical utility, prospective diagnostic advice should be relatively portable and rapid for 'point-of-care' testing, in both geographical and temporal senses. As with any diagnostic test, the accuracy of the device (specificity and sensitivity) should also be appropriate to the cohort. For a pitch-side application, the ideal device would be user-friendly, such that a monitored first-aid provider would be able to take readings. In this context, the patient would also be outside of a hospital setting, so a pitch-side device would be capable of non-invasive measurements without incisions. RS has also been applied to non-invasive identification of traumatic brain injury diagnosis and severity stratification via examination of the retina [47] and may hold future potential with further development.

5. Conclusions

RS is a powerful diagnostic tool with the potential to provide detailed biochemical diagnostic information on the injured brain. This review highlights the success of RS in identifying biochemical changes after injury in tissue from in vivo models and holds significant potential for applications in in vivo or clinical settings for TBI diagnostics and monitoring. Potential applications in TBI are broad and include direct brain monitoring and biofluid diagnostics, with the opportunity to obtain detailed and temporally resolved detail of metabolic and biochemical shifts in response to injury which could increase understanding and inform clinical decision making. Novel spectral biomarkers of injury severity observed from in vivo models represent a significant opportunity for monitoring and treating the complex pathophysiological processes as yet uncaptured by neuromonitoring modalities. Further pre-clinical and clinical studies are required to fully recognise the potential for RS

in TBI. Whilst there are translational challenges, discussed examples from neuro-oncology and related optical monitoring modalities set a proof of concept for further investigation and application of RS in TBI.

Author Contributions: A.R.S. was responsible for conceptualisation and manuscript preparation. A.R.S. and Z.A. performed the searches and risk of bias assessments, extracted the data from the included articles, and performed the analysis. All authors contributed to the development of the ideas/writing/final review of the submitted article. All authors have read and agreed to the published version of the manuscript.

Funding: This article presents independent research funded by the National Institute for Health Research (NIHR) Surgical Reconstruction and Microbiology Research Centre (a partnership between University Hospitals Birmingham NHS Foundation Trust, the University of Birmingham, and the Royal Centre for Defence Medicine). The views expressed are those of the author(s) and not necessarily those of the NHS, the NIHR, or the Department of Health.

Institutional Review Board Statement: Ethical review and approval were waived for this study as per advice from the NHS Health Research Authority (UK) decision tool since it is a systematic review of published literature.

Informed Consent Statement: Patient consent was waived because no patients or members of the public were involved in the design, conduct of this study, or reporting of this research.

Data Availability Statement: All data generated as part of this study are included in the article.

Conflicts of Interest: The authors declare no conflict of interest. The funders had no role in the design of the study; in the collection, analyses, or interpretation of data; in the writing of the manuscript; in the decision to publish the results.

Abbreviations

CCI	Controlled cortical impact
FTIR	Fourier transform infrared spectroscopy
GCS	Glasgow coma scale
GFAP	Glial fibrillary acidic protein
ICP	Intracranial pressure
mTBI	Mild TBI
NAA	n-Acetyle aspartate
NSE	Neuron-specific enolase
RS	Raman spectroscopy
SCAT5	Sports concussion assessment tool 5
SERS	Surface-enhanced Raman scattering
SKiNET	Self-optimising Kohonen index network
sTBI	Severe traumatic brain injury
TBI	Traumatic brain injury
UCHL1	Ubiquitin C-terminal hydrolase-L1

References

1. Langlois, J.A.; Rutland-Brown, W.; Wald, M.M. The epidemiology and impact of traumatic brain injury: A brief overview. *J. Head Trauma Rehabil.* **2006**, *21*, 375–378. [CrossRef] [PubMed]
2. Jazayeri, S.B.; Beygi, S.; Shokraneh, F.; Hagen, E.M.; Rahimi-Movaghar, V. Incidence of traumatic spinal cord injury worldwide: A systematic review. *Eur. Spine J.* **2015**, *24*, 905–918. [CrossRef] [PubMed]
3. Dewan, M.; Rattani, A.; Gupta, S.; Baticulon, R.; Hung, Y.; Punchak, M.; Agrawal, A.; Adeleye, A.; Shrime, M.; Rubiano, A.; et al. Estimating the global incidence of traumatic brain injury. *J. Neurosurg.* **2018**, *130*, 1080–1097. [CrossRef] [PubMed]
4. Xiong, Y.; Mahmood, A.; Chopp, M. Emerging treatments for traumatic brain injury. *Expert Opin. Emerg. Drugs* **2009**, *14*, 67–84. [CrossRef]
5. Bullock, M.R.; Chesnut, R.; Ghajar, J.; Gordon, D.; Hartl, R.; Newell, D.W.; Servadei, F.; Walters, B.C.; Wilberger, J. Surgical management of traumatic brain injury. *Neurosurgery* **2006**, *58*, 16–24.
6. Faul, M.; Coronado, V. Epidemiology of traumatic brain injury. *Handb. Clin. Neurol.* **2015**, *127*, 3–13. [CrossRef]

7. Polinder, S.; Haagsma, J.A.; van Klaveren, D.; Steyerberg, E.W.; van Beeck, E.F. Health-related quality of life after TBI: A systematic review of study design, instruments, measurement properties, and outcome. *Popul. Health Metr.* **2015**, *13*, 4. [CrossRef]
8. Pavlovic, D.; Pekic, S.; Stojanovic, M.; Popovic, V. Traumatic brain injury: Neuropathological, neurocognitive and neurobehavioral sequelae. *Pituitary* **2019**, *22*, 270–282. [CrossRef]
9. Graham, N.S.N.; Sharp, D.J. Understanding neurodegeneration after traumatic brain injury: From mechanisms to clinical trials in dementia. *J. Neurol. Neurosurg. Psychiatry* **2019**, *90*, 1221–1233. [CrossRef]
10. Chesnut, R.M.; Chesnut, R.M.; Marshall, L.F.; Klauber, M.R.; Blunt, B.A.; Baldwin, N.; Eisenberg, H.M.; Jane, J.A.; Marmarou, A.; Foulkes, M.A. The role of secondary brain injury in determining outcome from severe head injury. *J. Trauma* **1993**, *34*, 216. [CrossRef]
11. Brain Trauma Foundation Guidelines for the Management of Severe TBI, 4th Ed. Available online: https://braintrauma.org/guidelines/guidelines-for-the-management-of-severe-tbi-4th-ed#/ (accessed on 26 August 2021).
12. Ng, S.Y.; Lee, A.Y.W. Traumatic Brain Injuries: Pathophysiology and Potential Therapeutic Targets. *Front. Cell. Neurosci.* **2019**, *13*, 528. [CrossRef] [PubMed]
13. Cheng, G.; Kong, R.H.; Zhang, L.M.; Zhang, J.N. Mitochondria in traumatic brain injury and mitochondrial-targeted multipotential therapeutic strategies. *Br. J. Pharmacol.* **2012**, *167*, 699–719. [CrossRef] [PubMed]
14. Belli, A.; Sen, J.; Petzold, A.; Russo, S.; Kitchen, N.; Smith, M. Clinical Article Metabolic failure precedes intracranial pressure rises in traumatic brain injury: A microdialysis study. *Acta Neurochir.* **2008**, *150*, 461–470. [CrossRef] [PubMed]
15. Chamoun, R.; Suki, D.; Gopinath, S.P.; Goodman, J.C.; Robertson, C. Role of extracellular glutamate measured by cerebral microdialysis in severe traumatic brain injury: Clinical article. *J. Neurosurg.* **2010**, *113*, 564–570. [CrossRef] [PubMed]
16. Deng, Y.; Thompson, B.M.; Gao, X.; Hall, E.D. Temporal relationship of peroxynitrite-induced oxidative damage, calpain-mediated cytoskeletal degradation and neurodegeneration after traumatic brain injury. *Exp. Neurol.* **2007**, *205*, 154–165. [CrossRef] [PubMed]
17. Semple, B.D.; Bye, N.; Rancan, M.; Ziebell, J.M.; Morganti-Kossmann, M.C. Role of CCL2 (MCP-1) in traumatic brain injury (TBI): Evidence from severe TBI patients and CCL2−/− mice. *J. Cereb. Blood Flow Metab.* **2010**, *30*, 769–782. [CrossRef]
18. Okonkwo, D.O.; Shutter, L.A.; Moore, C.; Temkin, N.R.; Puccio, A.M.; Madden, C.J.; Andaluz, N.; Chesnut, R.M.; Bullock, M.R.; Grant, G.A.; et al. Brain tissue oxygen monitoring and management in severe traumatic brain injury (BOOST-II): A phase II randomized trial. *Crit. Care Med.* **2017**, *45*, 1907. [CrossRef]
19. Chesnut, R.; Aguilera, S.; Buki, A.; Bulger, E.; Citerio, G.; Cooper, D.; Arrastia, R.; Diringer, M.; Figaji, A.; Gao, G.; et al. A management algorithm for adult patients with both brain oxygen and intracranial pressure monitoring: The Seattle International Severe Traumatic Brain Injury Consensus Conference (SIBICC). *Intensive Care Med.* **2020**, *46*, 919–929. [CrossRef]
20. Carpenter, K.; Young, A.; Hutchinson, P. Advanced monitoring in traumatic brain injury: Microdialysis. *Curr. Opin. Crit. Care* **2017**, *23*, 103–109. [CrossRef]
21. Ercole, A.; Magnoni, S.; Vegliante, G.; Pastorelli, R.; Surmacki, J.; Bohndiek, S.; Zanier, E. Current and Emerging Technologies for Probing Molecular Signatures of Traumatic Brain Injury. *Front. Neurol.* **2017**, *8*, 450. [CrossRef]
22. Cordero, E.; Latka, I.; Matthäus, C.; Schie, I.; Popp, J. In-vivo Raman spectroscopy: From basics to applications. *J. Biomed. Opt.* **2018**, *23*, 071210. [CrossRef] [PubMed]
23. Hanlon, E.B.; Manoharan, R.; Koo, T.W.; Shafer, K.E.; Motz, J.T.; Fitzmaurice, M.; Kramer, J.R.; Itzkan, I.; Dasari, R.R.; Feld, M.S. Prospects for in vivo Raman spectroscopy. *Phys. Med. Biol.* **2000**, *45*, R1. [CrossRef] [PubMed]
24. Demtröder, W. Laser Raman Spectroscopy. In *Laser Spectroscopy2*; Springer: Berlin/Heidelberg, Germany, 2015; pp. 149–181. [CrossRef]
25. Bik, E.; Mateuszuk, L.; Stojak, M.; Chlopicki, S.; Baranska, M.; Majzner, K. Menadione-induced endothelial inflammation detected by Raman spectroscopy. *Biochim. Biophys. Acta Mol. Cell Res.* **2021**, *1868*, 118911. [CrossRef] [PubMed]
26. Zhang, W.; Rhodes, J.S.; Garg, A.; Takemoto, J.Y.; Qi, X.; Harihar, S.; Tom Chang, C.W.; Moon, K.R.; Zhou, A. Label-free discrimination and quantitative analysis of oxidative stress induced cytotoxicity and potential protection of antioxidants using Raman micro-spectroscopy and machine learning. *Anal. Chim. Acta* **2020**, *1128*, 221–230. [CrossRef]
27. Lalonde, J.W.; O'Connor, S.P.; Noojin, G.D.; Gonzales, C.C.; Yakovlev, V.V.; Denton, M.L. Measuring cytochrome c redox state using resonance Raman spectroscopy to determine metabolic rates in electron transport chain when exposed to light. In *Mechanisms of Photobiomodulation Therapy XIV*; Hamblin, M.R., Carroll, J.D., Arany, P., Eds.; SPIE: Bellingham, WA, USA, 2019; Volume 10861, p. 18. [CrossRef]
28. Jung, G.; Kang, S.; Lee, G.; Kim, D. Biochemical Characterization of the Brain Hippocampal Areas after Cerebral Ischemia-Reperfusion Using Raman Spectroscopy. *Appl. Spectrosc.* **2018**, *72*, 1479–1486. [CrossRef]
29. Chaichi, A.; Hasan, S.; Mehta, N.; Donnarumma, F.; Ebenezer, P.; Murray, K.; Francis, J.; Gartia, M. Label-free lipidome study of paraventricular thalamic nucleus (PVT) of rat brain with post-traumatic stress injury by Raman imaging. *Analyst* **2021**, *146*, 170–183. [CrossRef]
30. Lakshmi, R.; Kartha, V.; Krishna Murali, C.; Solomon, J.; Uma Devi, P. Tissue Raman Spectroscopy for the Study of Radiation Damage: Brain Irradiation of Mice. *Radiat. Res.* **2002**, *157*, 175–182. [CrossRef]
31. Devitt, G.; Howard, K.; Mudher, A.; Mahajan, S. Raman Spectroscopy: An Emerging Tool in Neurodegenerative Disease Research and Diagnosis. *ACS Chem. Neurosci.* **2018**, *9*, 404–420. [CrossRef]

32. Aguiar, R.P.; Silveira, L.; Falcão, E.T.; Pacheco, M.T.T.; Zângaro, R.A.; Pasqualucci, C.A. Discriminating Neoplastic and Normal Brain Tissues in Vitro Through Raman Spectroscopy: A Principal Components Analysis Classification Model. *Photomed. Laser Surg.* **2013**, *31*, 595–604. [CrossRef]
33. Desroches, J.; Jermyn, M.; Pinto, M.; Picot, F.; Tremblay, M.; Obaid, S.; Marple, E.; Urmey, K.; Trudel, D.; Soulez, G.; et al. A new method using Raman spectroscopy for in vivo targeted brain cancer tissue biopsy. *Sci. Rep.* **2018**, *8*, 1792. [CrossRef]
34. Livermore, L.; Isabelle, M.; Bell, I.; Edgar, O.; Voets, N.; Stacey, R.; Ansorge, O.; Vallance, C.; Plaha, P. Raman spectroscopy to differentiate between fresh tissue samples of glioma and normal brain: A comparison with 5-ALA-induced fluorescence-guided surgery. *J. Neurosurg.* **2020**, *135*, 469–479. [CrossRef] [PubMed]
35. Koljenović, S.; Schut, T.; Vincent, A.; Kros, J.; Puppels, G. Detection of meningioma in dura mater by Raman spectroscopy. *Anal. Chem.* **2005**, *77*, 7958–7965. [CrossRef] [PubMed]
36. Zhang, J.; Fan, Y.; He, M.; Ma, X.; Song, Y.; Liu, M.; Xu, J. Accuracy of Raman spectroscopy in differentiating brain tumor from normal brain tissue. *Oncotarget* **2017**, *8*, 36824–36831. [CrossRef] [PubMed]
37. Hollon, T.; Lewis, S.; Freudiger, C.; Sunney Xie, X.; Orringer, D. Improving the accuracy of brain tumor surgery via Raman-based technology. *Neurosurg. Focus* **2016**, *40*, E9. [CrossRef] [PubMed]
38. Depciuch, J.; Tołpa, B.; Witek, P.; Szmuc, K.; Kaznowska, E.; Osuchowski, M.; Król, P.; Cebulski, J. Raman and FTIR spectroscopy in determining the chemical changes in healthy brain tissues and glioblastoma tumor tissues. *Spectrochim. Acta. A. Mol. Biomol. Spectrosc.* **2020**, *225*, 117526. [CrossRef]
39. Kalkanis, S.; Kast, R.; Rosenblum, M.; Mikkelsen, T.; Yurgelevic, S.; Nelson, K.; Raghunathan, A.; Poisson, L.; Auner, G. Raman spectroscopy to distinguish grey matter, necrosis, and glioblastoma multiforme in frozen tissue sections. *J. Neurooncol.* **2014**, *116*, 477–485. [CrossRef]
40. Jermyn, M.; Mok, K.; Mercier, J.; Desroches, J.; Pichette, J.; Saint-Arnaud, K.; Bernstein, L.; Guiot, M.; Petrecca, K.; Leblond, F. Intraoperative brain cancer detection with Raman spectroscopy in humans. *Sci. Transl. Med.* **2015**, *7*, 274ra19. [CrossRef]
41. Jermyn, M.; Desroches, J.; Mercier, J.; St-Arnaud, K.; Guiot, M.; Leblond, F.; Petrecca, K. Raman spectroscopy detects distant invasive brain cancer cells centimeters beyond MRI capability in humans. *Biomed. Opt. Express* **2016**, *7*, 5129. [CrossRef]
42. Desroches, J.; Jermyn, M.; Mok, K.; Lemieux-Leduc, C.; Mercier, J.; St-Arnaud, K.; Urmey, K.; Guiot, M.; Marple, E.; Petrecca, K.; et al. Characterization of a Raman spectroscopy probe system for intraoperative brain tissue classification. *Biomed. Opt. Express* **2015**, *6*, 2380. [CrossRef]
43. Galli, R.; Meinhardt, M.; Koch, E.; Schackert, G.; Steiner, G.; Kirsch, M.; Uckermann, O. Rapid Label-Free Analysis of Brain Tumor Biopsies by Near Infrared Raman and Fluorescence Spectroscopy—A Study of 209 Patients. *Front. Oncol.* **2019**, *9*, 1165. [CrossRef]
44. Hollon, T.; Pandian, B.; Adapa, A.; Urias, E.; Save, A.; Khalsa, S.; Eichberg, D.; D'Amico, R.; Farooq, Z.; Lewis, S.; et al. Near real-time intraoperative brain tumor diagnosis using stimulated Raman histology and deep neural networks. *Nat. Med.* **2020**, *26*, 52–58. [CrossRef] [PubMed]
45. Moher, D.; Liberati, A.; Tetzlaff, J.; Altman, D.G. Preferred reporting items for systematic reviews and meta-analyses: The PRISMA statement. *BMJ* **2009**, *339*, 332–336. [CrossRef] [PubMed]
46. Hooijmans, C.R.; Rovers, M.M.; De Vries, R.B.M.; Leenaars, M.; Ritskes-Hoitinga, M.; Langendam, M.W. SYRCLE's risk of bias tool for animal studies. *BMC Med. Res. Methodol.* **2014**, *14*, 43. [CrossRef] [PubMed]
47. Banbury, C.; Styles, I.; Eisenstein, N.; Zanier, E.R.; Vegliante, G.; Belli, A.; Logan, A.; Oppenheimer, P.G. Spectroscopic detection of traumatic brain injury severity and biochemistry from the retina. *Biomed. Opt. Express* **2020**, *11*, 6249–6261. [CrossRef] [PubMed]
48. Banbury, C.; Mason, R.; Styles, I.; Eisenstein, N.; Clancy, M.; Belli, A.; Logan, A.; Goldberg Oppenheimer, P. Development of the Self Optimising Kohonen Index Network (SKiNET) for Raman Spectroscopy Based Detection of Anatomical Eye Tissue. *Sci. Rep.* **2019**, *9*, 10812. [CrossRef]
49. Ercole, A.; Surmaki, J.; Ansel-Bollepalli, L.; Pischiutta, F.; Bohndiek, S.; Zanier, E. Mapping spatial biochemical changes in a mouse model of traumatic brain injury with Raman imaging. *Intensive Care Med. Exp.* **2017**, *5*.
50. Surmacki, J.M.; Ansel-Bollepalli, L.; Pischiutta, F.; Zanier, E.R.; Ercole, A.; Bohndiek, S.E. Label-free monitoring of tissue biochemistry following traumatic brain injury using Raman spectroscopy. *Analyst* **2017**, *142*, 132. [CrossRef]
51. Mowbray, M.; Banbury, C.; Rickard, J.J.S.; Davies, D.J.; Goldberg Oppenheimer, P. Development and Characterization of a Probe Device toward Intracranial Spectroscopy of Traumatic Brain Injury. *ACS Biomater. Sci. Eng.* **2021**, *7*, 1252–1262. [CrossRef]
52. Kawon, K.; Setkowicz, Z.; Drozdz, A.; Janeczko, K.; Chwiej, J. The methods of vibrational microspectroscopy reveals long-term biochemical anomalies within the region of mechanical injury within the rat brain. *Spectrochim. Acta A Mol. Biomol. Spectrosc.* **2021**, *263*, 120214. [CrossRef]
53. Hu, F.; Lamprecht, M.; Wei, L.; Morrison, B.; Min, W. Bioorthogonal chemical imaging of metabolic activities in live mammalian hippocampal tissues with stimulated Raman scattering. *Sci. Rep.* **2016**, *6*, 39660. [CrossRef]
54. Du Sert, N.P.; Ahluwalia, A.; Alam, S.; Avey, M.T.; Baker, M.; Browne, W.J.; Clark, A.; Cuthill, I.C.; Dirnagl, U.; Emerson, M.; et al. Reporting animal research: Explanation and elaboration for the ARRIVE guidelines 2.0. *PLoS Biol.* **2020**, *18*, e3000411. [CrossRef]
55. Hackett, M.J.; Desouza, M.; Caine, S.; Bewer, B.; Nichol, H.; Paterson, P.G.; Colbourne, F. A New Method To Image Heme-Fe, Total Fe, and Aggregated Protein Levels after Intracerebral Hemorrhage. *ACS Chem. Neurosci.* **2015**, *6*, 761–770. [CrossRef] [PubMed]
56. Williamson, M.R.; Dietrich, K.; Hackett, M.J.; Caine, S.; Nadeau, C.A.; Aziz, J.R.; Nichol, H.; Paterson, P.G.; Colbourne, F. Rehabilitation Augments Hematoma Clearance and Attenuates Oxidative Injury and Ion Dyshomeostasis After Brain Hemorrhage. *Stroke* **2017**, *48*, 195–203. [CrossRef] [PubMed]

57. Dutta, A.; Gautam, R.; Chatterjee, S.; Ariese, F.; Sikdar, S.K.; Umapathy, S. Ascorbate Protects Neurons against Oxidative Stress: A Raman Microspectroscopic Study. *ACS Chem. Neurosci.* **2015**, *6*, 1794–1801. [CrossRef]
58. Khatri, N.; Thakur, M.; Pareek, V.; Kumar, S.; Sharma, S.; Datusalia, A.K. Oxidative Stress: Major Threat in Traumatic Brain Injury. *CNS Neurol. Disord. Drug Targets* **2018**, *17*, 689–695. [CrossRef]
59. Mehta, T.; Fayyaz, M.; Giler, G.E.; Kaur, H.; Raikwar, S.P.; Kempuraj, D.; Selvakumar, G.P.; Ahmed, M.E.; Thangavel, R.; Zaheer, S.; et al. Current Trends in Biomarkers for Traumatic Brain Injury. *Open access J. Neurol. Neurosurg.* **2020**, *12*, 86.
60. Wang, K.K.; Yang, Z.H.; Zhu, T.; Shi, Y.; Rubenstein, R.; Tyndall, J.A.; Manley, G.T. An update on diagnostic and prognostic biomarkers for traumatic brain injury. *Expert Rev. Mol. Diagn.* **2018**, *18*, 165–180. [CrossRef]
61. Calcagnile, O.; Anell, A.; Undén, J. The addition of S100B to guidelines for management of mild head injury is potentially cost saving. *BMC Neurol.* **2016**, *16*, 200. [CrossRef]
62. Granger, J.H.; Schlotter, N.E.; Crawford, A.C.; Porter, M.D. Prospects for point-of-care pathogen diagnostics using surface-enhanced Raman scattering (SERS). *Chem. Soc. Rev.* **2016**, *45*, 3865–3882. [CrossRef]
63. McNay, G.; Eustace, D.; Smith, W.E.; Faulds, K.; Graham, D. Surface-enhanced Raman scattering (SERS) and surface-enhanced resonance raman scattering (SERRS): A review of applications. *Appl. Spectrosc.* **2011**, *65*, 825–837. [CrossRef]
64. Rickard, J.J.; Di-Pietro, V.; Smith, D.; Davies, D.; Belli, A.; Goldberg Oppenheimer, P. Rapid optofluidic detection of biomarkers for traumatic brain injury via surface-enhanced Raman spectroscopy. *Nat. Biomed. Eng.* **2020**, *4*, 610–623. [CrossRef] [PubMed]
65. Osier, N.; Ziari, M.; Puccio, A.; Poloyac, S.; Okonkwo, D.; Minnigh, M.; Beers, S.; Conley, Y. Elevated cerebrospinal fluid concentrations of N-acetylaspartate correlate with poor outcome in a pilot study of severe brain trauma. *Brain Inj.* **2019**, *33*, 1364–1371. [CrossRef] [PubMed]
66. Toman, E.; Harrisson, S.; Belli, T. Biomarkers in traumatic brain injury: A review. *J.R. Army Med. Corps* **2016**, *162*, 103–108. [CrossRef] [PubMed]
67. Gao, X.; Zheng, P.; Kasani, S.; Wu, S.; Yang, F.; Lewis, S.; Nayeem, S.; Engler-Chiurazzi, E.; Wigginton, J.; Simpkins, J.; et al. Paper-Based Surface-Enhanced Raman Scattering Lateral Flow Strip for Detection of Neuron-Specific Enolase in Blood Plasma. *Anal. Chem.* **2017**, *89*, 10104–10110. [CrossRef]
68. Gao, X.; Boryczka, J.; Zheng, P.; Kasani, S.; Yang, F.; Engler-Chiurazzi, E.; Simpkins, J.; Wigginton, J.; Wu, N. A "hot Spot"-Enhanced paper lateral flow assay for ultrasensitive detection of traumatic brain injury biomarker S-100β in blood plasma. *Biosens. Bioelectron.* **2021**, *177*, 112967. [CrossRef]
69. Li, D.; Yang, M.; Li, H.; Mao, L.; Wang, Y.; Sun, B. SERS based protocol using flow glass-hemostix for detection of neuron-specific enolase in blood plasma. *New J. Chem.* **2019**, *43*, 5925–5931. [CrossRef]
70. O'Neal, P.; Motamedi, M.; Lin, W.; Chen, J.; Coté, G. Feasibility study using surface-enhanced Raman spectroscopy for the quantitative detection of excitatory amino acids. *J. Biomed. Opt.* **2003**, *8*, 33. [CrossRef]
71. O'Neal, D.P.; Motamedi, M.; Chen, J.; Cote, G.L. Surface-enhanced Raman spectroscopy for the in-vitro and ex-vivo detection of excitatory amino acids. In *Biomedical Applications of Raman Spectroscopy*; SPIE: Bellingham, WA, USA, 1999; Volume 3608, pp. 211–216. [CrossRef]
72. Larkin, P. IR and Raman Spectra-Structure Correlations. In *Infrared Raman Spectrosc*; Elsevier: Amsterdam, The Netherlands, 2011; pp. 73–115. [CrossRef]
73. Kang, D.G.; Woo, K.C.; Kang, D.H.; Park, C.; Kim, S.K. Improved spectral resolution of the femtosecond stimulated Raman spectroscopy achieved by the use of the 2nd-order diffraction method. *Sci. Rep.* **2021**, *11*, 3361. [CrossRef]
74. Lemler, P.; Premasiri, W.R.; DelMonaco, A.; Ziegler, L.D. NIR Raman spectra of whole human blood: Effects of laser-induced and in vitro hemoglobin denaturation. *Anal. Bioanal. Chem.* **2014**, *406*, 193–200. [CrossRef]
75. Thomas, D.B.; Hauber, M.E.; Hanley, D.; Waterhouse, G.I.N.; Fraser, S.; Gordon, K.C. Analysing avian eggshell pigments with Raman spectroscopy. *J. Exp. Biol.* **2015**, *218*, 2670–2674. [CrossRef]
76. Talari, A.C.S.; Movasaghi, Z.; Rehman, S.; Rehman, I.U. Raman Spectroscopy of Biological Tissues. *Appl. Spectrosc. Rev.* **2014**, *50*, 46–111. [CrossRef]
77. Tay, L.; Tremblay, R.; Hulse, J.; Zurakowski, B.; Thompson, M.; Bani-Yaghoub, M. Detection of acute brain injury by Raman spectral signature. *Analyst* **2011**, *136*, 1620–1626. [CrossRef] [PubMed]
78. Girard, A.; Cooper, A.; Mabbott, S.; Bradley, B.; Asiala, S.; Jamieson, L.; Clucas, C.; Capewell, P.; Marchesi, F.; Gibbins, M.P.; et al. Raman spectroscopic analysis of skin as a diagnostic tool for Human African Trypanosomiasis. *PLoS Pathog.* **2021**, *17*, e1010060. [CrossRef]
79. Journal, A.I.; Lu, M.; Zhao, L.; Wang, Y.; You, G.; Kan, X.; Zhang, Y.; Zhang, N.; Wang, B.; Guo, Y.-J.; et al. Measurement of the methemoglobin concentration using Raman spectroscopy, Artificial Cells. *Nanomed. Biotechnol.* **2014**, *42*, 63–69. [CrossRef]
80. Sacharz, J.; Wesełucha-Birczyńska, A.; Zięba-Palus, J.; Lewandowski, M.H.; Kowalski, R.; Palus, K.; Chrobok, Ł.; Moskal, P.; Birczyńska, M.; Sozańska, A. Epileptic rat brain tissue analyzed by 2D correlation Raman spectroscopy. *Spectrochim. Acta-Part A Mol. Biomol. Spectrosc.* **2018**, *188*, 581–588. [CrossRef]
81. Shin, H.J.; Lee, J.H.; Kim, Y.D.; Shin, I.; Sim, T.; Lim, D.K. Raman-Based in Situ Monitoring of Changes in Molecular Signatures during Mitochondrially Mediated Apoptosis. *ACS Omega* **2019**, *4*, 8188–8195. [CrossRef] [PubMed]
82. Codrich, D. Applications and Limits of Raman Spectroscopy in the Study of Colonic and Pulmonary Malformations. Ph.D. Thesis, Universita' Degli Studi di Trieste, Trieste, Italy, 2006.

83. Wood, B.R.; Caspers, P.; Puppels, G.J.; Pandiancherri, S.; McNaughton, D. Resonance Raman spectroscopy of red blood cells using near-infrared laser excitation. *Anal. Bioanal. Chem.* **2007**, *387*, 1691–1703. [CrossRef] [PubMed]
84. Castro, M.A.; Pereira, F.J.; Aller, A.J.; Littlejohn, D. Raman spectrometry as a screening tool for solvent-extracted azo dyes from polyester-based textile fibres. *Polym. Test.* **2020**, *91*, 106765. [CrossRef]
85. Bankapur, A.; Krishnamurthy, R.S.; Zachariah, E.; Santhosh, C.; Chougule, B.; Praveen, B.; Valiathan, M.; Mathur, D. Micro-Raman Spectroscopy of Silver Nanoparticle Induced Stress on Optically-Trapped Stem Cells. *PLoS ONE* **2012**, *7*, e35075. [CrossRef]
86. Yao, H.; Tao, Z.; Ai, M.; Peng, L.; Wang, G.; He, B.; Li, Y.-Q. Raman spectroscopic analysis of apoptosis of single human gastric cancer cells. *Vib. Spect.* **2009**, *50*, 193–197. [CrossRef]
87. Notingher, I.; Green, C.; Dyer, C.; Perkins, E.; Hopkins, N.; Lindsay, C.; Hench, L. Discrimination between ricin and sulphur mustard toxicity in vitro using Raman spectroscopy. *J.R. Soc. Interface* **2004**, *1*, 79–90. [CrossRef] [PubMed]
88. Krafft, C.; Knetschke, T.; Funk, R.; Salzer, R. Studies on stress-induced changes at the subcellular level by Raman microspectroscopic mapping. *Anal. Chem.* **2006**, *78*, 4424–4429. [CrossRef] [PubMed]
89. Muthuselvi, C.; Pandiaraja, S.S.; Ravikumar, B.; Athimoolam, S.; Srinivasan, N.; Krishnakum, R.V. FT-IR and FT-Raman Spectroscopic Analyzes of Indeno Quinoxaline Derivative Crystal. *Asian J. Appl. Sci.* **2018**, *11*, 83–91. [CrossRef]
90. Kumar, V.; Panikar, Y.; Palafox, M.A.; Vats, J.; Kostova, I.; Lang, K.; Rastogi, V. Ab-initio calculations, FT-IR and FT-Raman spectra of 2-chloro-6-methyl benzonitrile. *Indian J. Pure Appl. Phys.* **2010**, *48*, 85–94.
91. Krafft, C.; Neudert, L.; Simat, T.; Salzer, R. Near infrared Raman spectra of human brain lipids. *Spectrochim. Acta-Part A Mol. Biomol. Spectrosc.* **2005**, *61*, 1529–1535. [CrossRef] [PubMed]
92. Farquharson, S.; Gift, A.; Shende, C.; Inscore, F.; Ordway, B.; Farquharson, C.; Murren, J. Surface-enhanced Raman Spectral Measurements of 5-Fluorouracil in Saliva. *Molecules* **2008**, *13*, 2608. [CrossRef] [PubMed]
93. De Gelder, J.; De Gussem, K.; Vandenabeele, P.; Moens, L. Reference database of Raman spectra of biological molecules. *J. Raman Spectrosc.* **2007**, *38*, 1133–1147. [CrossRef]
94. Staniszewska-Slezak, E.; Malek, K.; Baranska, M. Complementary analysis of tissue homogenates composition obtained by Vis and NIR laser excitations and Raman spectroscopy. *Spectrochim. Acta-Part A Mol. Biomol. Spectrosc.* **2015**, *147*, 245–256. [CrossRef]
95. Clemens, G.; Butler, H.J.; Ashton, K.M.; Brodbelt, A.; Dawson, T.P.; Fullwood, L.M.; Jenkinson, M.D.; Stables, R.; Baker, M.J.; North, L.; et al. Feature Driven Classification of Raman Spectra for Real-Time Spectral Brain Tumour Diagnosis Using Sound. *Analyst* **2017**, *142*, 98–109.
96. Acosta-Maeda, T.E. Raman Spectroscopy for Planetary Exploration and Characterization of Extraterrestrial Materials. Ph.D. Thesis, University of Hawai'i at Manoa, Honolulu, HI, USA, 2016.
97. Mccreery, R.L.; Chalmers, J.M.; Griffiths, P.R. Photometric Standards for Raman Spectroscopy. In *Handbook of Vibrational Spectroscopy Photometric Standards for Raman Spectroscopy*; John Wiley & Sons Ltd: Chichester, UK, 2002.
98. Demediuk, P.; Faden, A.I.; Romhanyi, R.; Vink, R.; Mcintosh, T.K. Traumatic Brain Injury in the Rat: Effects on Lipid Metabolism, Tissue Magnesium, and Water Content. *J. Neurotrauma* **1988**, *5*, 105–119. [CrossRef]
99. Lamade, A.M.; Anthonymuthu, T.S.; Hier, Z.E.; Gao, Y.; Kagan, V.E.; Bayır, H. Mitochondrial Damage & Lipid Signaling in Traumatic Brain Injury HHS Public Access. *Exp. Neurol.* **2020**, *329*, 113307. [CrossRef] [PubMed]
100. Mallah, K.; Quanico, J.; Trede, D.; Kobeissy, F.; Zibara, K.; Salzet, M.; Fournier, I. Lipid Changes Associated with Traumatic Brain Injury Revealed by 3D MALDI-MSI. *Anal. Chem.* **2018**, *90*, 10568–10576. [CrossRef] [PubMed]
101. Tashibu, K. Analysis of water content in rat brain using Raman spectroscopy. *Brain Nerve* **1990**, *42*, 999–1004.
102. Kitajima, T.; Tashibu, K.; Tani, S.; Mizuno, A.; Nakamura, N. Analysis of water content in young rats brain edema by Raman spectroscopy. *No Shinkei* **1993**, *45*, 519–524.
103. Wolthuis, R.; van Aken, M.; Fountas, K.; Robinson, J.S.; Bruining, H.A.; Puppels, G.J. Determination of water concentration in brain tissue by Raman spectroscopy. *Anal. Chem.* **2001**, *73*, 3915–3920. [CrossRef] [PubMed]
104. Desroches, J.; Lemoine, E.; Pinto, M.; Marple, E.; Urmey, K.; Diaz, R.; Guiot, M.; Wilson, B.; Petrecca, K.; Leblond, F. Development and first in-human use of a Raman spectroscopy guidance system integrated with a brain biopsy needle. *J. Biophotonics* **2019**, *12*, e201800396. [CrossRef]
105. Seule, M.; Sikorski, C.; Sakowitz, O.; von Campe, G.; Santos, E.; Orakcioglu, B.; Unterberg, A.; Keller, E. Evaluation of a New Brain Tissue Probe for Intracranial Pressure, Temperature, and Cerebral Blood Flow Monitoring in Patients with Aneurysmal Subarachnoid Hemorrhage. *Neurocrit. Care* **2016**, *25*, 193–200. [CrossRef]
106. Tuschel, D. Selecting an Excitation Wavelength for Raman Spectroscopy. *Spectroscopy* **2016**, *31*, 14–23.
107. Signoretti, S.; Marmarou, A.; Aygok, G.; Fatouros, P.; Portella, G.; Bullock, R. Assessment of mitochondrial impairment in traumatic brain injury using high-resolution proton magnetic resonance spectroscopy. *J. Neurosurg.* **2008**, *108*, 42–52. [CrossRef]
108. Adjunctive therapies in lifethreatening CNS infections. *Eur. J. Neurol.* **2015**, *22*, 19. [CrossRef]
109. Nordström, C.; Nielsen, T.; Schalén, W.; Reinstrup, P.; Ungerstedt, U. Biochemical indications of cerebral ischaemia and mitochondrial dysfunction in severe brain trauma analysed with regard to type of lesion. *Acta Neurochir.* **2016**, *158*, 1231–1240. [CrossRef] [PubMed]
110. Stovell, M.; Mada, M.; Helmy, A.; Carpenter, T.; Thelin, E.; Yan, J.; Guilfoyle, M.; Jalloh, I.; Howe, D.; Grice, P.; et al. The effect of succinate on brain NADH/NAD + redox state and high energy phosphate metabolism in acute traumatic brain injury. *Sci. Rep.* **2018**, *8*, 11140. [CrossRef] [PubMed]

111. Sonig, A.; Jumah, F.; Raju, B.; Patel, N.V.; Gupta, G.; Nanda, A. The Historical Evolution of Intracranial Pressure Monitoring. *World Neurosurg.* **2020**, *138*, 491–497. [CrossRef] [PubMed]
112. Tas, J.; Beqiri, E.; van Kaam, C.; Ercole, A.; Bellen, G.; Bruyninckx, D.; Cabeleira, M.; Czosnyka, M.; Depreitere, B.; Donnelly, J.; et al. An Update on the COGiTATE Phase II Study: Feasibility and Safety of Targeting an Optimal Cerebral Perfusion Pressure as a Patient-Tailored Therapy in Severe Traumatic Brain Injury. *Acta Neurochir. Suppl.* **2021**, *131*, 143–147. [CrossRef] [PubMed]
113. DePaoli, D.; Lemoine, E.; Ember, K.; Parent, M.; Prud'homme, M.; Cantin, L.; Petrecca, K.; Leblond, F.; Côté, D. Rise of Raman spectroscopy in neurosurgery: A review. *J. Biomed. Opt.* **2020**, *25*, 050901. [CrossRef] [PubMed]
114. Stevens, A.R.; Ng, I.H.X.; Helmy, A.; Hutchinson, P.J.A.; Menon, D.K.; Ercole, A. Glucose Dynamics of Cortical Spreading Depolarization in Acute Brain Injury: A Systematic Review. *J. Neurotrauma* **2019**, *36*, 2153–2166. [CrossRef]
115. Teasdale, G.; Maas, A.; Lecky, F.; Manley, G.; Stocchetti, N.; Murray, G. The Glasgow Coma Scale at 40 years: Standing the test of time. *Lancet Neurol.* **2014**, *13*, 844–854. [CrossRef]
116. Echemendia, R.J.; Meeuwisse, W.; McCrory, P.; Davis, G.A.; Putukian, M.; Leddy, J.; Makdissi, M.; Sullivan, S.J.; Broglio, S.P.; Raftery, M.; et al. The sport concussion assessment tool 5th edition (SCAT5): Background and rationale. *Br. J. Sports Med.* **2017**, *51*, 851–858. [CrossRef]
117. Gill, M.R.; Reiley, D.G.; Green, S.M. Interrater reliability of Glasgow Coma Scale scores in the emergency department. *Ann. Emerg. Med.* **2004**, *43*, 215–223. [CrossRef]
118. Stevens, A.R.; Su, Z.; Toman, E.; Belli, A.; Davies, D. Optical pupillometry in traumatic brain injury: Neurological pupil index and its relationship with intracranial pressure through significant event analysis. *Brain Inj.* **2019**, *33*, 1032–1038. [CrossRef]